Diffractive Dijet Production in $\sqrt{s} = 7$ TeV pp collisions at the ATLAS Experiment

Hardeep Singh Bansil

Thesis submitted for the degree of
Doctor of Philosophy

Particle Physics Group,
School of Physics and Astronomy,
University of Birmingham.

Supervisors:
Prof. Paul Newman
Dr. Juraj Braciník

September 26, 2013

Abstract

A data sample of pp collisions with an integrated luminosity of 6.75 nb^{-1} was collected using a combination of a minimum bias trigger and a single jet trigger at $\sqrt{s} = 7$ TeV using the ATLAS detector at the Large Hadron Collider. It is analysed to study diffractive dijet production, i.e. events with a hadronic system containing at least two jets in addition to a large region of pseudorapidity devoid of hadronic activity. The cross section is presented differentially with respect to $\Delta\eta^F$, the largest continuous region of pseudorapidity which extends from the edge of the detector at $\eta = \pm 4.9$ and contains no final state particles above threshold momentum cuts, over the region $0 < \Delta\eta^F < 6.5$. It is also presented differentially in the variable $\xi^{\pm}$, which estimates the fractional momentum loss of the proton in single diffractive dissociation ($pp \to pX$) events. Comparing the data distributions with a Monte Carlo model suggest that fluctuations in the hadronisation process allow non-diffractive dijets to look like diffractive events, but that the data cannot be described solely by non-diffractive dijet production. In addition, the monitoring of the electromagnetic and jet efficiencies for the ATLAS Level-1 Calorimeter Trigger is described.

Author's Contribution

The work in this thesis relies on the design, construction and operation of the ATLAS detector and the Large Hadron Collider, as well as the results of a number of individual researchers and analysis subgroups. This thesis is the result of my own work, except where explicit reference is made to the work of others. The contributions by the author are outlined below.

This document includes an overview of the LHC and ATLAS, as well as diffraction and general Standard Model physics, which is based on my interpretation of existing reports, with focus given to areas in which I have contributed. My service position was monitoring the efficiencies of electrons, photons and jets for the Level-1 Calorimeter Trigger. The analysis of diffractive dijets was performed jointly with two colleagues from the Institute of Physics of the Academy of Sciences of the Czech Republic in Prague. Working independently, towards the same ultimate goal, resulted in an improvement in quality of the analysis. However the analysis presented here is entirely my own.

For my family

Acknowledgements

First, thanks go to the Birmingham Particle Physics group as a whole for allowing me an opportunity to do a PhD and for the numerous interesting discussions and pieces of advice provided. To all my fellow post-graduate students, especially those in West 316 and 327, thanks for making the days more interesting! A special mention to Juergen Thomas and Simon Head for the technical support they have provided me with. I would also like to thank the Science & Technology Facilities Council (STFC) for supporting my research.

A massive thank you goes to Paul Newman and Juraj Braciník for being excellent supervisors, and for the time they were able to offer me. Thanks to Paul for guiding me over these past years, including the final year undergraduate project, and for getting me to produce a physics measurement. Juraj, thanks for all those times I would enter your office without knocking, get useful advice and some laughs as well.

Thank you to the Level-1 Calorimeter Trigger collaboration for their all of their help, expertise and enthusiasm. It is a great group to join, making me feel very welcome and that I was contributing to the ATLAS experiment straight away. In particular, I want to recognise the efforts of Alan Watson, Steve Hillier and Pete Faulkner from Birmingham as well as Rainer Stamen, Michele Dieli, Bruce Barnett, Martin Wessels and Ivana Hristova. From the Egamma Trigger Signature Group, I would like to thank Monika Wielers and Hauqiao Zhang for many useful discussions.

Thanks to the Soft QCD working group for their advice. I am grateful for the expertise that Tim Martin shared based on the soft diffractive analysis. I would also like to acknowledge the help from Prague (Oldřich Kepka, Vlastimil Kůs, Marek Taševský) in terms of advice and independent measurements that improved the quality of the analysis.

Finally, I must give thanks to my family for all of their love and support - I could not have done it without you.

We may regard the present state of the universe as the effect of its past and the cause of its future. Given, for one instant, an intelligence which could comprehend all the forces by which nature is animated and the respective situation of the beings who compose it - an intelligence sufficiently vast to submit these data to analysis - it would embrace in the same formula the movements of the greatest bodies of the universe and those of the lightest atom. For it, nothing would be uncertain and the future, as the past, would be present to its eyes.

Pierre-Simon Laplace - *A Philosophical Essay on Probabilities* (translated into English) [1]

Contents

List of Figures

List of Tables

Outline

This thesis consists of three sections; an introductory section (Chapters 1 - 3), a section related to the ATLAS Level-1 Calorimeter Trigger (Chapters 4 - 6), and a section covering the analysis of diffractive dijets (Chapter 7 - 11).

Chapter 1 is a brief review of the Standard Model of particle physics and potential candidates of physics beyond the Standard Model, both of which provide important physics motivations for the LHC experiments. Chapter 2 describes the LHC and the CERN accelerator complex, and Chapter 3 gives an overview of the ATLAS detector and its performance.

A more detailed overview of the Level-1 Calorimeter Trigger is provided in Chapter 4. Next, the reconstruction of electrons, photons and jets in ATLAS is described in Chapter 5, with the work done to measure the efficiency of the electromagnetic and jet triggers described in Chapter 6.

Chapter 7 provides an introduction to the physics of diffraction, and diffractive dijets in particular. Chapter 8 explains how Monte Carlo event generators for inclusive and diffractive dijets produce their samples and Chapter 9 describes the event selection and measurement. Chapters 10 and 11 present the final results and conclusions, respectively.

CHAPTER 1

Standard Model of Particle Physics

The Standard Model (SM) is a theory, or set of theories, that provide the current understanding of how fundamental particles behave at the subatomic scale, leading to an understanding of the nature of matter, space and time. The model has been developed using theoretical advances stimulated by and confirmed through experimental discoveries created from high-energy particle interactions, such as those seen at the Large Hadron Collider (LHC).

1.1 Standard Model

The Standard Model (SM) is a unified description of the Strong and Electroweak forces combined in a SU(3)⊗SU(2)⊗U(1) gauge theory for massless particles [2], describing how the strong, weak and electromagnetic forces act on the elementary particles. Gravity is not included in the Standard Model as on the scale of elementary particles, it is negligible when compared to the other forces. For instance, for two electrons the ratio of the

electrostatic force compared to the gravitational force is about 10^{42}.

This model classifies all elementary particles into two types: fermions, with a half-integer quantum number of the quantum mechanical property called spin, and bosons with integer spin. The fermions make up matter and interact by exchanging the force-carrying bosons.

There are two types of fermions: quarks and leptons. There are 12 fermions in total, grouped into three generations of leptons and quarks, as summarised in Table 1.1. Each fermion has its own anti-fermion and is considered to be point-like, as there is currently no experimental evidence suggesting they have structure. Quarks combine together to make composite particles such as the proton and neutron, which are the components of atomic nuclei. The electron, the lightest charged lepton, combines with nuclei to make up atoms.

Symmetries are important in explaining the mathematics of how elementary particles interact and how the strong, weak and electromagnetic forces arise. The bosons mediating these forces are listed in Table 1.2. Leptons interact via the weak and electromagnetic forces, from which the photon and the $W^{\pm}$ and Z bosons are produced as a result of electroweak symmetry breaking (EWSB). Quarks can also interact via these forces and also through the strong interaction (Quantum Chromodynamics, QCD), which is mediated by gluons. Quarks and gluons carry an additional charge, related to the symmetry of the SU(3) group, known as colour (see Section 7.1).

Fermion	Generation			Q
	1	2	3	
Lepton	e^- (electron)	μ^- (muon)	τ^- (tau)	-1
	ν_{e} (electron neutrino)	ν_μ (muon neutrino)	ν_τ (tau neutrino)	0
Quark	u (up)	c (charm)	t (top)	$+2/3$
	d (down)	s (strange)	b (bottom)	$-1/3$

Table 1.1: The fermions of the Standard Model and their electric charges, expressed in units of absolute electron charge. All fermions have a corresponding anti-fermion partner. All quarks exist in one of three colour states: red, green or blue.

Protons are made up of two up quarks and a down quark. These quarks produce associated gluons and quark-anti-quark pairs via the strong interaction, and are collectively known as partons. When protons at LHC energies collide into each other, any of the partons of

Boson	Spin	Charge	Interaction	Mass (GeV)
γ (photon)	1	0	Electromagnetic	0
W^+, W^-	1	$+1$, -1	Weak (charged current)	80.385 ± 0.015
Z	1	0	Weak (neutral current)	91.1876 ± 0.0021
g (gluon)	1	0	Strong	0

Table 1.2: The bosons of the Standard Model along with their main properties. The masses of the W and Z bosons are taken from [3].

one proton can interact with the partons from another. These partons contain a fraction, x (Bjorken-x), of the total proton momentum, meaning that partons interact with each other at energies less than the total of centre of mass energy of the two protons. Parton Density Functions (PDFs, see Section 7.1) are used to describe the quark and gluon content of the proton of the probabilities of finding partons carrying different fractions of the total momentum.

Some of the first tasks of the LHC experiments have been to 'rediscover' these Standard Model particles and make precise measurements of known Standard Model phenomena at higher energies than those previously explored. This includes measuring the production rates of W and Z bosons and studying the top quark. The top quark is the last of the quarks to be discovered experimentally, as it is approximately 172 times heavier than the proton and much heavier than the other quarks. The LHC can generate sufficient numbers of top quarks to study them precisely.

It must be first verified that the response of the LHC experiments to known phenomena is well understood and matches what is expected from Monte Carlo simulations, which generate events based on random numbers and probabilities related to the current understanding of particle physics interactions. The tests include studies of photons, electrons, muons and jets (collimated streams of particles that originate from the emissions of energetic quarks or gluons from colliding particles). Many different Monte Carlo models are available with varying underlying models, based on a knowledge of the PDFs.

1.1.1 Electroweak Symmetry Breaking

Table 1.2 shows that the photon and gluon do not have mass, but the weak force carriers (W^+, W^- and Z) do. For symmetry reasons, the Standard Model requires massless particles, unless some mechanism is incorporated to distort the model. The favoured mechanism is that of 'spontaneous electroweak symmetry breaking' [4], caused by a scalar field that is associated to the Higgs Boson (H). Spontaneous symmetry breaking keeps the gauge field SU(2)×U(1) invariant, producing the γ, $W^{\pm}$, and Z gauge bosons as linear combinations of its generators as a consequence. Gauge invariance, defined as the invariance of the theory under local gauge transformations, is required in order to make the gauge field renormalisable so that the calculations of all observable quantities remain finite. The quanta of the invariant gauge fields are the gauge bosons.

Through spontaneous symmetry breaking, the fermions acquire a mass proportional to the vacuum expectation value of the Higgs field, the average value it takes throughout the universe. The more the fermions interact with the Higgs field through the Yukawa interaction, the larger their mass becomes. If the vacuum expectation value of the field were zero then the fermions would be massless, making it impossible for atoms and nuclei to form. In addition to providing a mechanism for giving the particles mass, it also solves other problems such as the unsustainable growth of the W^+W^- (longitudinally polarised vector boson) scattering cross section with increasing centre of mass energies.

The Higgs boson can be produced in proton-proton collisions via a number of mechanisms, as shown in Figure 1.1. At LHC energies, the proton contains a large number of gluons, making gluon-gluon fusion the dominant method for producing the Higgs.

The Higgs boson decays very quickly into a number of different possible channels. The probability for decaying in each way depends on the Higgs coupling to different particles, which in turn depends only on what the Higgs mass is. These probabilities, known as branching ratios, can be seen as a function of Higgs mass in Figure 1.2.

In July 2012, a neutral boson consistent with a Standard Model Higgs boson was discovered by ATLAS [7] and CMS [8]. Using the data collected in 2011 and 2012, ATLAS used combined results from the $\gamma\gamma$ and $ZZ \rightarrow 4l$ decay channels, the channels with best mass

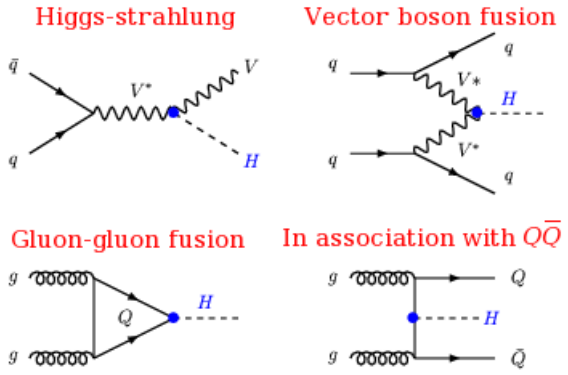

Figure 1.1: Production mechanisms for the Standard Model Higgs boson at hadron colliders [5].

resolution, and determined the mass to be $m_H = 125.5 \pm 0.2$ (stat) $^{+0.5}_{-0.6}$ (sys) GeV [9]. The mass distribution for the $H \to ZZ \to 4$ leptons channel ($4e$, 4μ, $2e2\mu$) in shown in Figure 1.3. Additional data has made it look increasingly more likely that this is the Standard Model Higgs. For example, a Higgs boson is postulated to have no spin, and in the Standard Model its parity (a measure of how its "mirror image" behaves) should be positive. CMS and ATLAS have compared a number of options for the spin-parity of this particle with data, and these all prefer no spin and positive parity [10, 11].

More data are required to fully understand the quantum properties of the new particle and to determine whether this is the one and only Higgs boson of the Standard Model of particle physics, or possibly the lightest of several bosons predicted in some theories that go beyond the Standard Model. The most important measurements will involve precisely determining the rate at which the boson decays into other particles, characterising all of the decay modes and comparing the results to predictions.

1.2 Beyond the Standard Model

While the Standard Model is successful in describing the majority of particle physics, it is not capable of describing all experimental observations. For example, it does not contain any mechanisms to generate neutrino masses (or explain neutrino oscillations). Additionally, matter and antimatter are thought to have existed in equal amounts at

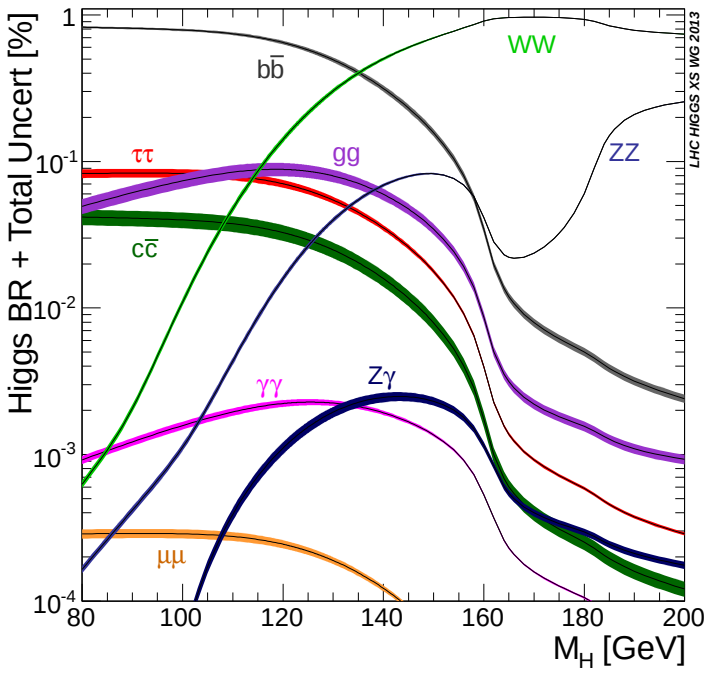

Figure 1.2: The branching ratios, with uncertainties, of the Standard Model Higgs as a function of Higgs mass M_H between 80 and 200 GeV. The discovered Higgs mass is around 125 GeV [6].

the beginning of the universe, but as the universe expanded and cooled, an asymmetry developed between them, leaving a universe that appears to be composed entirely of matter. The Standard Model predicts a matter-antimatter asymmetry, but at a level which is too small to explain the observed asymmetry in the universe without additional physics. There is also a strong desire to have a theory which unifies gravity with the other fundamental forces. This leads many to believe that the Standard Model is an effective theory, related to a deeper theory in a manner comparable to how the Newtonian theory of classical mechanics is an approximation to special and general relativity at small speed, although the energies at which the Standard Model breaks down are not known yet.

Evidence from astronomy also suggests that the Standard Model is incomplete, accounting for only approximately 5% of all of the mass-energy that can be currently inferred to exist [12]. The remaining 95% consists of dark matter and dark energy, for which dark matter has potential candidates which might be producible at the LHC. This has required other theories to be developed to provide potential solutions, involving new particles and symmetries, new forces or additional spatial dimensions.

One of the biggest problems with the Standard Model, as it currently stands, is why the

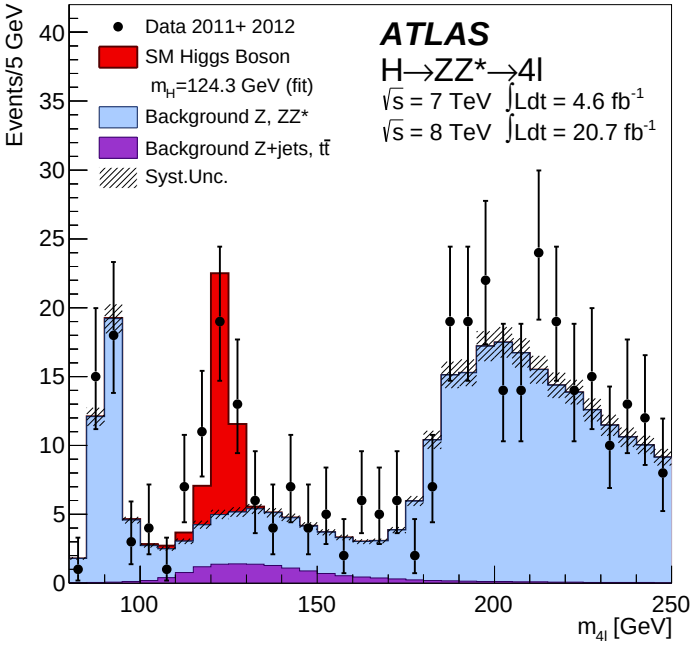

Figure 1.3: The distribution of the four-lepton invariant mass, m_{4l}, for the selected $H \to ZZ \to$ 4 lepton candidates in combined ATLAS 2011 and 2012 data. The estimated background, as well as the expected SM Higgs boson signal for $m_H = 124.3$ GeV (scaled by the signal strength obtained from fits to the data), are also shown [9].

weak nuclear force is 10^{32} times stronger than gravity, with even larger factors for the other forces. This is known as the hierarchy problem. The Higgs boson "bare mass" (m_0) comes from its self interaction and the non-zero Higgs field vacuum expectation value. All massive Standard Model particles can produce virtual loops interacting with the Higgs, producing quantum corrections to its mass (Δm), which cause it to diverge to infinity, or at least a scale large enough where the Standard Model must break down. These parameters have to be finely tuned to cancel out, such that $m_0 + \Delta m \simeq 125$ GeV, the observed Higgs mass.

One of the more promising theories that solves the hierarchy and fine tuning problems is that of Supersymmetry (SUSY) [13]. In SUSY, each fermion and boson has a partner supersymmetric particle (sparticle) which differs from it by half a unit of spin and is generally heavier. The loop contributions of the Standard Model particles to the Higgs mass are cancelled out by the contributions from the superpartners.

SUSY would generate several Higgs bosons as well as natural candidates for dark matter

and could also make the unification of the strong, weak, and electromagnetic forces a reality. In some models, the lightest supersymmetric particle (LSP), a 'neutralino', is a candidate for dark matter. If the neutralino exists it will likely be stable, heavy, neutral and will not interact electromagnetically, making it possible to be present in large quantities in the universe and not easily observable directly. Decay signatures for SUSY particles are expected to be combinations of leptons and quarks as well as neutralinos which, as the LSP, will not be detected.

Many of the simpler models, in which assumptions are made to reduce the number of free parameters, have already been ruled out by LHC data at the 95% confidence level [14]. The data have excluded large regions of phase space in which SUSY particles could exist (up to around 1 TeV in most channels) apart from the stop, as it has a large overlap with the signals produced by the top particle.

As well as SUSY, other models of new physics are being studied. These models would imply new particles such as a new generation of heavier fermions, heavier W and Z bosons (W' and Z') or leptoquarks (quark-lepton bound systems). Other theories involve quark and lepton compositeness, extra spatial dimensions, technicolour and contact interactions. As well as direct observation of new particles, new physics could also be found indirectly through its influence on rare processes. There are no hard expectations on what will be seen at the TeV scale, so the LHC and its experiments must be capable of searching for a wide range of possible signatures.

CHAPTER 2

CERN and the Large Hadron Collider

CERN (European Organization for Nuclear Research) was established in 1954 and operates the world's largest laboratory for particle physics, located on the Franco-Swiss border. CERN operates a series of particle accelerators, designed to accelerate particles to increasingly higher energies, as well as data processing facilities in order to carry out research in particle physics.

In this chapter, the basics of how accelerators for particle physics experiments are described before discussing the CERN accelerator complex leading up to the LHC, the LHC itself and some of its experiments.

2.1 Basic Principles of Particle Acceleration

In a linear accelerator (linac), particles are accelerated in a straight line either to collide with a target of interest or to provide an initial acceleration stage to particles before they are injected into circular accelerators.

Linear high-energy accelerators use a linear array of plates (or drift tubes) to which an alternating high-energy electric field is applied. The plates use an opposite charge to the particle being accelerated, to attract the particle as it approaches the plate. After the particle passes through a hole in the plate, the charge on the plate is switched to repel the particle, assisting the acceleration of the particle towards the next plate.

Circular accelerators use electromagnets to keep particles in circular motion to reach their desired energy. In maintaining circular motion and depending on the energy of the particle, particles emit synchrotron radiation tangentially to the circle. The amount of radiation varies proportionally to m^{-4}, where m is the mass of the particle. For high energy physics, synchrotron accelerators are used. They use rings of constant diameter and the magnetic field is applied only over the particle orbit.

Radio Frequency (RF) cavities replace plates in higher energy machines. This is important as the rate at which the charge needs to be switched corresponds to the radio frequency region once the particles are close to the speed of light. The cavities are typically on the order of tens of centimetres in length, generating a longitudinal oscillating voltage to an isolated gap in the vacuum chamber to induce an electric field within it. A standing wave is produced at a frequency designed to apply an accelerating voltage to particles that pass through. A particle exactly synchronised with the RF frequency is called a synchronous particle. All of the other particles in the accelerator will oscillate longitudinally around the synchronous particles under the influence of the RF system.

In circular accelerators, groups of particles get "clumped" around the synchronous particles in a "bunch" rather than being spread uniformly along an accelerator. For each bunch of particles to be accelerated, a carefully controlled AC voltage has to be applied at each plate for the process to be repeated. For a synchrotron this is important, as to maintain the curvature of the orbit, the B-field has to be adjusted according to the particle energies - a continuous stream of particles would be harder to maintain around the circumference of the accelerator. Each bunch is contained in an RF bucket, which can be thought of as a virtual segment along the circumference of the accelerator ring.

For a synchrotron, the final energy is dependent on the particles maintaining an orbit within the beam pipe. Dipole magnets create a homogeneous magnetic field over some

distance, applying a force that bends charged particles perpendicular to the direction of the field in order to go around their circular path, so the final energy is also directly related to the size of the magnetic field used to maintain the orbit, the number of orbits and the radius of the ring. In order for particles to be accelerated each time they approach an RF cavity within the synchrotron, the RF frequency must be an integer multiple of the revolution frequency. This factor is known as the harmonic number, h.

On attaining the energy required for the experiments, the beams are focused using quadrupole magnets located around the experiments. These magnets have the property of focusing charged particles in one plane and defocusing them in the orthogonal plane. A succession of alternate quadrupole magnets have the net effect of focusing the particle beam in both directions. The beams are then defocused with an additional set of quadrupole magnets in order to get them back to the original beam size after passing the experimental interaction point.

2.2 Pre-LHC Accelerator Chain

The full CERN accelerator complex is shown in Figure 2.1. It is used to accelerate protons and heavy ions. These are used directly in collisions at experiments on the accelerators or fired into targets, generating different types of particle that can be studied. The description of particle acceleration before the Proton Synchrotron is based on information in [15].

Protons are made by ionising hydrogen atoms, taken from a standard hydrogen bottle, with a Duoplasmatron source. Lead ions, are formed by heating a pure lead sample up to 550 °C and then ionising the resultant lead vapour up to Pb^{27+}. For both particle types, the accelerator chain begins with acceleration through a linear accelerator before passing through a succession of synchrotrons to achieve their desired energies.

Protons are accelerated by LINAC2, a multi-chamber resonant cavity, up to 50 MeV to be injected into the PS Booster (PSB). The beam line to the PSB from LINAC2 is 80 m long, using 20 pulsed quadrupole magnets to focus the beam along the line with 2 bending

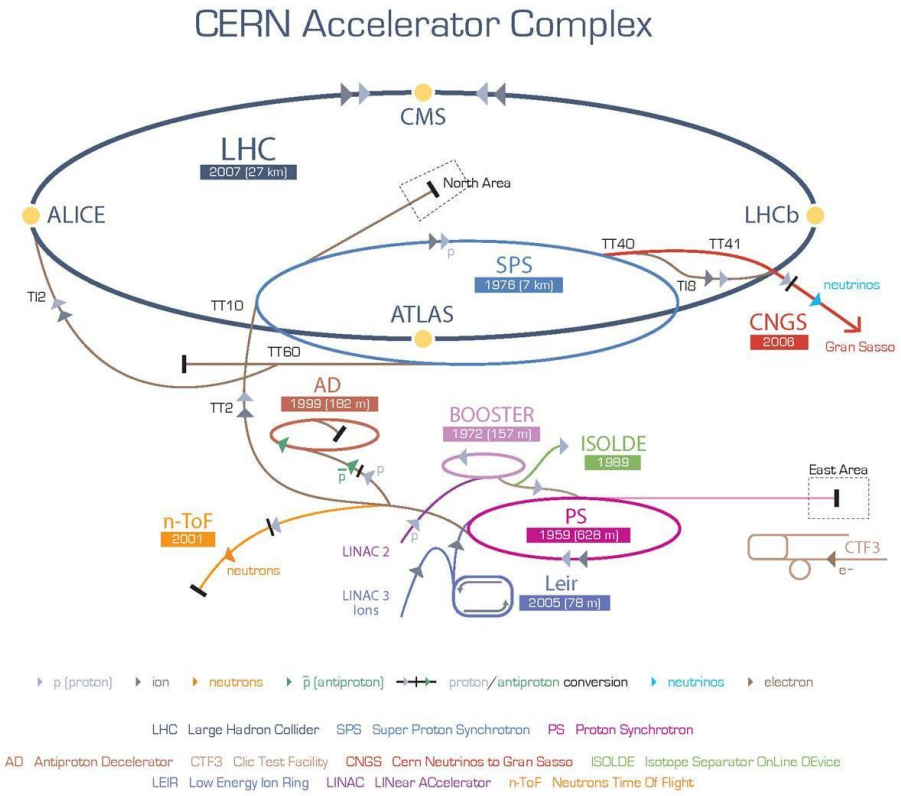

Figure 2.1: The LHC accelerator complex including the four major LHC experiments [16].

and 8 steering magnets to direct the beam. The PSB splits protons with an intensity of 3×10^{13} protons per pulse. The PS Booster accelerates the protons to 1.4 GeV (a factor of 28) in 530 ms, then after less than a microsecond they are injected into the Proton Synchrotron (PS).

The lead ions are accelerated in LINAC3 to 4.2 MeV/u (energy per nucleon) to be injected into the Low Energy Ion Ring (LEIR). LEIR splits the lead ions into 4 bunches, each containing around 2.2×10^8 lead ions. The ions are accelerated from 4.2 MeV/u to 72 MeV/u, in approximately 2.5 seconds, before being injecting into the PS.

The Proton Synchrotron (PS) [17] is a 628 m circumference ring and contains 277 conventional magnets to accelerate particles to 25 GeV, to be fed into the SPS. The PS can accelerate, manipulate and extract protons in 1025 ms. If the protons are from the first PSB batch to the PS, it takes an additional 1.2 seconds to be accelerated. By using RF technology for the acceleration, the PS is responsible for bunching groups of protons (or heavy ions) together along the rest of the acceleration process, using 81 bunch packets

with 25 ns spacing as required for the LHC.

The Super Proton Synchrotron (SPS) is a circular accelerator with a diameter of 2.2 km. Like the PS, the SPS operates with room-temperature magnets. 1317 electromagnets, including 774 dipoles to bend the particle beam around the ring. Since 2008, it has been used to accelerate and inject protons and heavy ions into the Large Hadron Collider (LHC). The protons arrive into the LHC at 450 GeVwith the total time from the source to LHC injection taking between 5.86 and 17.86 seconds.

2.3 Large Hadron Collider

The Large Hadron Collider (LHC) [18] is a high-energy particle accelerator housed in a 27 km circumference tunnel, previously used by the Large Electron-Positron Collider (LEP). By using superconducting dipole magnets, producing a magnetic field of up to 8.33 T, it bends two counter-rotating beams of protons (or lead ions) in separate vacuum tubes, kept to very low pressures in order to minimise interactions between the beam and residual gas. It then uses quadrupole magnets to focus the beams and produce collisions at the four different interaction points around the ring.

The energy of the collisions is dependent on the energy of the protons in the beam. This can be up to 7 TeV, leading to collisions of up to a centre of mass energy, $\sqrt{s}$, of 14 TeV[1].

The LHC is not a perfect circle but instead consists of eight 2.45 km long arcs, and eight 545 m long straight sections. Each arc contains 23 arc cells, which are 106.5 m long and have a FODO (focusing-defocusing, [19]) structure made from the main dipole magnets as well as quadrupole magnets and higher order multipole magnets that help in beam focussing and counteracting other interactions that each beam suffers. The dipoles are 14.3 m long and use liquid helium to sustain the large currents passing through the superconducting windings. The cross section of a dipole magnet is shown in Figure 2.2.

An insertion consists of a long straight section plus transition regions at the end to connect back into the arcs. The layout of the insertions, as shown in Figure 2.3, depends on the

[1] s is a kinematic Mandelstam variable equal to the square of the centre of mass energy.

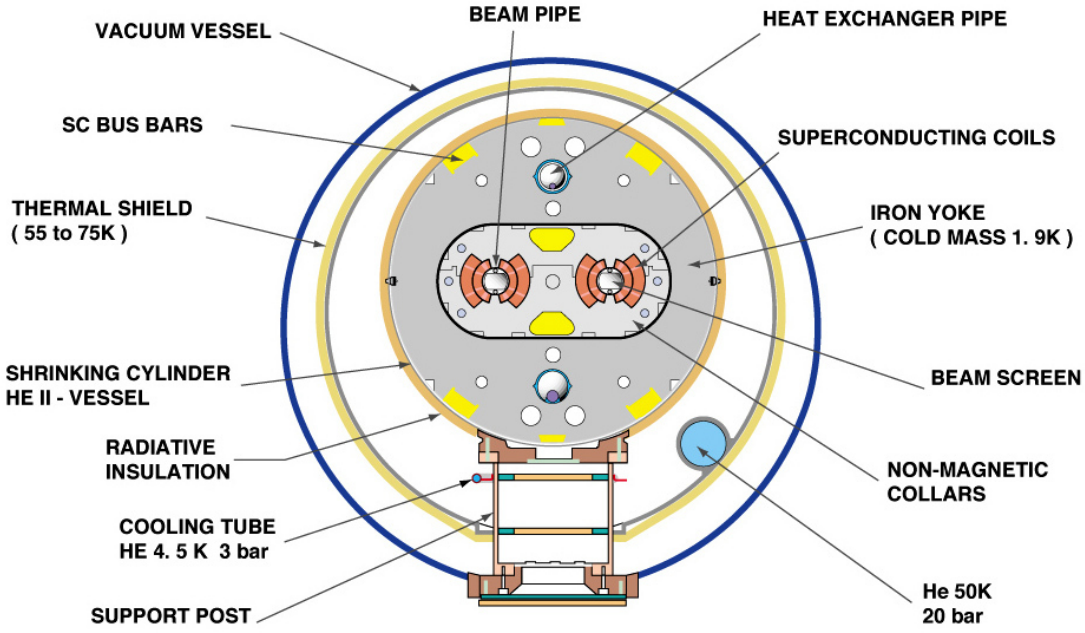

Figure 2.2: Schematic diagram of one the LHC cryodipoles [20].

purpose of the insertion: physics (beam collisions within an experiment), injection, beam dumping or beam cleaning. More properties of the accelerator are shown in Table 2.1.

The LHC first created proton-proton collisions at $\sqrt{s} = 0.9$ TeV on November 23rd 2009, then for a few days at 2.36 TeV starting on 14 December 2009. Between 30 March 2010 and December 2011, the collisions were at $\sqrt{s} = 7$ TeV, half of the design energy, and since 30 March 2012, the energy of the beams has increased to produce collisions at $\sqrt{s} = 8$ TeV. There have also been heavy ion collisions for approximately a month per year at the end of 2010, 2011 and 2012.

The luminosity, $\mathcal{L}$, of an accelerator is an important property as it determines how many events, N, are produced (per unit time) for a process of a given cross section, σ, of a particular physics process, according to

$$\frac{dN}{dt} = \mathcal{L}\sigma \ . \tag{2.1}$$

This relationship implies that for processes with small cross sections to be observed, very high luminosities are required. The cross sections for selected Standard Model processes

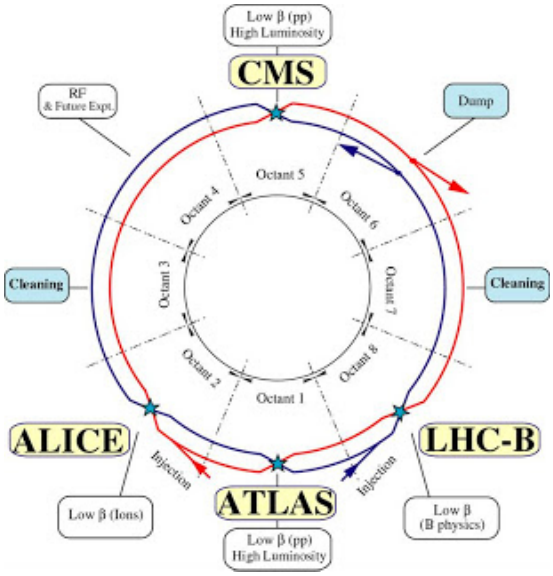

Figure 2.3: Schematic of the LHC showing where the beams are injected and which apparatus are installed in each of the octants [20].

produced in proton-proton collisions at different centre of mass energies are shown in Figure 2.4.

For a storage ring accelerator, such as the LHC, operating at a revolution frequency f_r and with n_b bunch pairs colliding per revolution and μ being the average number of inelastic interactions per bunch crossing, the luminosity could be written as

$$\mathcal{L} = \frac{\mu n_b f_r}{\sigma_{inel}} \tag{2.2}$$

where σ_{inel} is the pp inelastic cross-section.

High instantaneous luminosities are achieved by using beams made of bunches of protons (with each bunch containing approximately 100 billion protons) squeezed to minimise their transverse dimensions in order to increase the likelihood of interactions. The instantaneous design luminosity is $\mathcal{L} = 10^{34}$ cm^{-2} s^{-1}, obtainable by using bunches spaced out by 25 ns with an average of 23 collisions per crossing at peak design performance, leading to a potential proton-proton interaction rate approaching 1 GHz at each interaction point. The choice of pp collisions is related to the high design luminosity of the LHC - it could not be achieved with $p\bar{p}$ collisions, because the production of the necessary amounts of antiprotons is problematic with current technology.

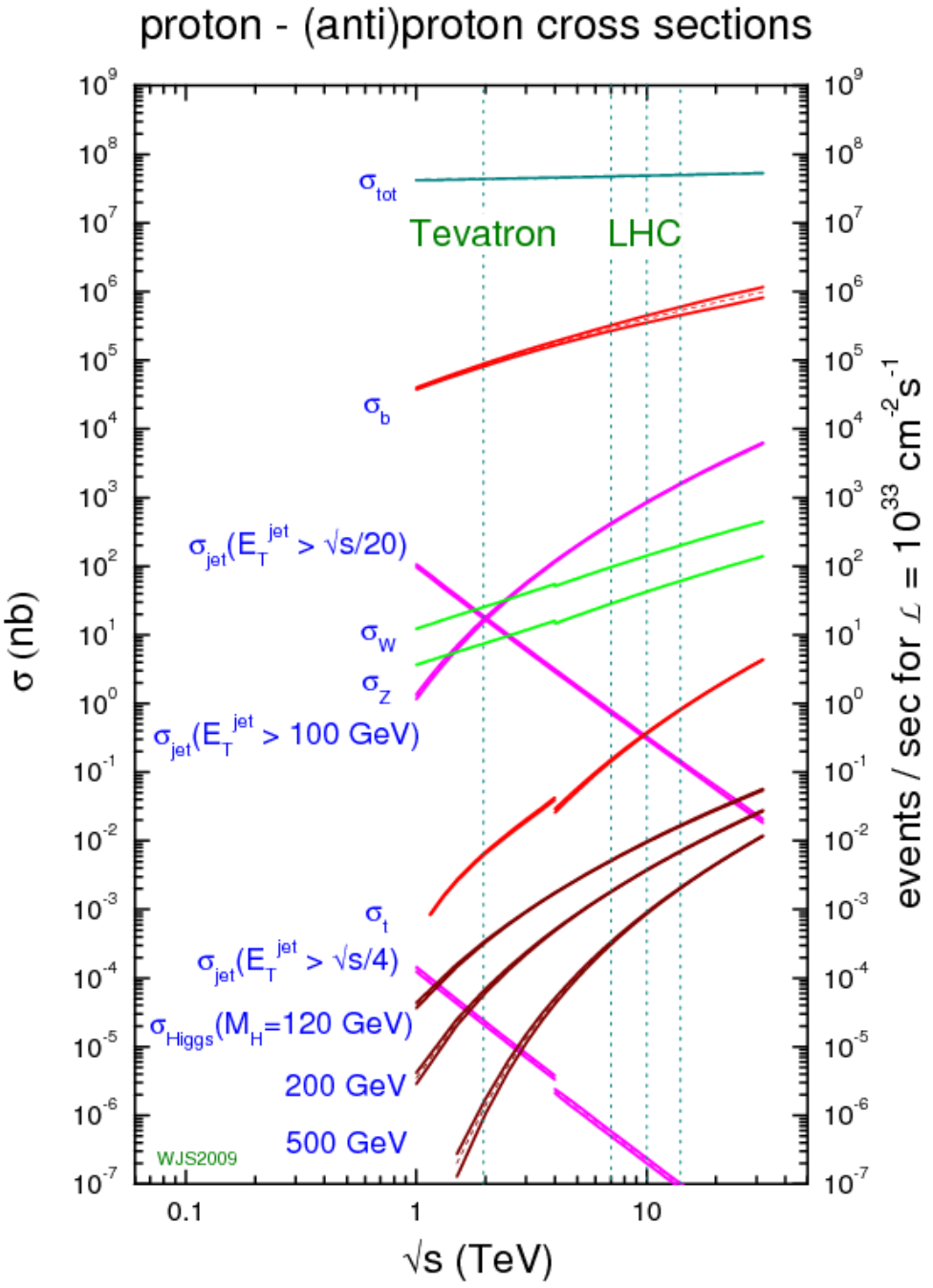

Figure 2.4: Production rates for signal and background processes at hadron colliders. The discontinuity at $\sqrt{s} = 4$ TeV is due to the Tevatron being a proton-antiproton collider while the LHC is a proton-proton collider. The Tevatron corresponds to a centre of mass energy of 2 TeV and the LHC corresponds to energies between 7 TeV and 14 TeV [21].

Parameter	Value
Circumference	26659 m
Injected proton beam energy	450 GeV
Nominal proton beam energy	7 TeV
Magnetic field at 7 TeV	8.33 Tesla
Operating temperature	1.9 K
Number of main dipoles	1232
Current at nominal field	11.85 kA
Number of quadrupoles	858
Number of correcting magnets	6208
Number of RF cavities	8 per beam
Field strength at top energy	5 MV/m
RF frequency	400 MHz
Revolution frequency	11.2455 kHz
Nominal beam pipe pressure	1.3×10^8 Pa

Table 2.1: Parameters of the Large Hadron Collider.

	Design	2010	2011	2012
Energy ($\sqrt{s}$)	14 TeV	7 TeV	7 TeV	8 TeV
Peak luminosity ($\mathrm{cm^{-2}s^{-1}}$)	10^{34}	2×10^{32}	3.5×10^{33}	6×10^{33}
# Protons (10^{11} p/bunch)	1.15	1.2	1.5	1.6-1.7
Number of bunches	2808	368	1380	1380/1374
Interactions per bunch crossing	23	3	19	35
Bunch spacing (ns)	25	150	75/50	50
Bunch crossing rate (MHz)	40	6.67	13.3/20	20
Off-line storage rate (Hz)	200	200	400	400

Table 2.2: LHC design and running conditions in 2010, 2011 and 2012.

The commissioning speed of the LHC has been remarkable and unprecedented. Despite not reaching the design bunch crossing rate, the other parameters and conditions for colliding beams have been optimised over the space of three years. This can be seen from both the LHC running conditions in Table 2.2 and the integrated luminosity as seen by the ATLAS experiment in Figure 2.5. Over this time, the conditions for running have been regularly changing, meaning that the experiments have had to continually re-optimise their data taking strategies to extract the most physics possible.

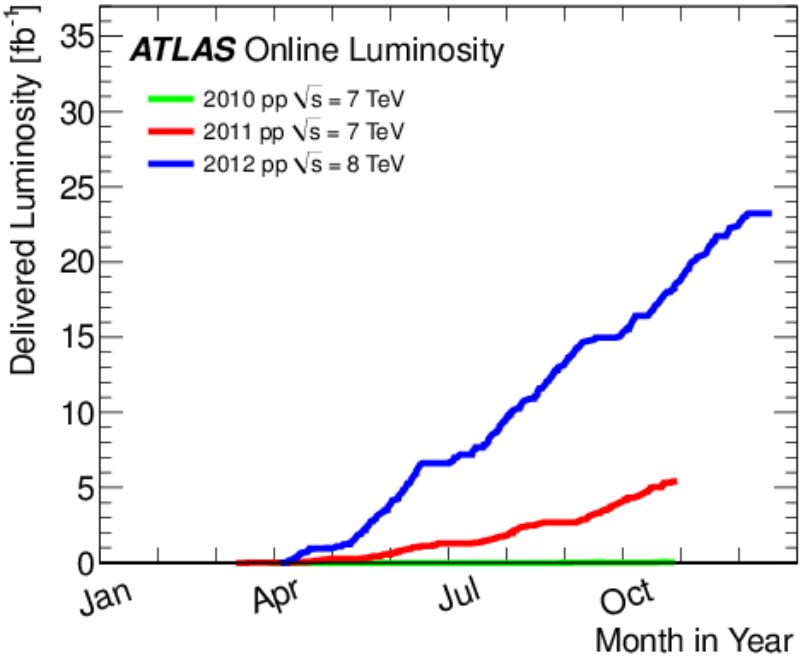

Figure 2.5: Cumulative luminosity versus day delivered to the ATLAS experiment during stable beams for *pp* collisions. This is shown for 2010 (green), 2011 (red) and 2012 (blue) running. [22].

2.3.1 LHC Bunch Structure

The RF frequency used in the LHC is 400 MHz and the revolution frequency for particles is 11.2455 kHz, resulting in a harmonic number, $h = 35640$. This provides the maximum number of LHC RF-buckets, meaning the LHC might accelerate a beam made up of 35640 bunches. A bucket can be empty or hold a bunch of protons. The LHC is designed so that approximately one tenth of the buckets accelerating protons around the ring contain a proton bunch at any given time, spacing the bunches out by 25 ns. This amount of time, based on a bunch being positioned at an interaction point, defines the bunch crossing (BC) frequency. For proton-proton collisions, the design LHC operation contains 3564 bunch crossings per revolution, with each bunch crossing assigned to a unique bunch-crossing identifier (BCID).

It is not possible for all of the BCIDs to be filled by proton bunches. In reality the number of occupied buckets in the LHC is 2808 at most. In case the beam needs to be dumped, an abort gap is always made available for the beam to be diverted into, meaning that there needs to be a series of consecutive buckets kept empty. The way buckets are

filled determines where the beams cross and collide, as some experiments require fewer collisions and lower luminosities than others. In early 2010, bunches were injected into the LHC ring individually, with long gaps between bunches. After this, the filling was done in bunch-trains, which consist of a predefined number of nearby bunches spaced out evenly, followed by a long gap to allow protons to be inserted or ejected from the LHC ring.

The beams circulate around the LHC at high energy for 10 hours. This duration is known as the beam lifetime and the beam is dumped after this time has elapsed. After the beam dump, the dipole magnets are ramped down to 0.5 T for between 20 and 40 minutes. Beam injection is repeated before the magnets are ramped up again to 8.3 T in order to repeat the cycle of proton collisions. It takes approximately 45 minutes for ramping up the magnets and getting the protons to their final energy.

2.3.2 Pile-up

Pile-up is a situation in which the experiments observe multiple proton-proton collisions in a single bunch crossing. A significant increase in the number of collisions is important to increase the amount of data collected, but the physics can only be understood in terms of the individual collisions and the resultant products. Pile-up increases as the number of protons per bunch increases, creating secondary interactions in a given bunch crossing (in-time pile-up).

The luminosity and BC spacing affect the in-time pile-up, which can be expressed as an average number of proton-proton collisions per BC. At design luminosity and performance, there is a Poisson mean of 23 collisions on top of any signal processes that occur at each bunch crossing in ATLAS. These additional collisions are dominated by so-called minimum bias collisions, which are dominated by soft interactions and low transverse energy parton scattering processes. Individual soft interactions need to be studied in order to understand high pile-up environments accurately.

The overall pile-up effect at interaction points is enhanced by out-of-time pile-up. This is due to the superimposition of signals in a detector that come from different bunch

crossings, when the signal response of a detector component (e.g. calorimeters) is much longer than the bunch crossing frequency.

In 2012, the LHC reached a peak instantaneous luminosity of 7.73×10^{33} cm^{-2}s^{-1}. Although the bunch spacing was at 50 ns, the number of protons per bunch exceeded design parameters meaning the beam intensity was very high. Over this time, the mean number of interactions per BC was around 37 and peaked close to 50 [22].

2.4 LHC Experiments

There are four major LHC experiments at the LHC, located in large caverns excavated at points along the tunnel where the beams are designed to interact. They are ALICE (A Large Ion Collider Experiment), ATLAS (A Toroidal LHC Apparatus), CMS (Compact Muon Solenoid) and LHCb (LHC-beauty). There are also two smaller experiments, TOTEM (TOTal cross section, Elastic scattering and diffraction dissociation Measurement at the LHC) and LHCf (LHC-forward). The ATLAS experiment is described in detail in Chapter 3. The remaining experiments are briefly reviewed below.

2.4.1 ALICE

ALICE [23] is an experiment optimised to study heavy ion collisions at a peak luminosity of $\mathcal{L} = 10^{27}$ cm^{-2} s^{-1} and at a centre of mass energy of 2.76 TeV per nucleus, with the aim of generating the ideal temperature and energy density levels to study a state of matter called the quark-gluon plasma, in which quarks and gluons are no longer confined, and which is believed to have existed shortly after the creation of the Universe.

2.4.2 LHCb

LHCb [24] is the experiment dedicated to b-quark physics at the LHC. Its primary goal is to look for indirect evidence of new physics in CP violation and rare decays of B-mesons, to help understand the matter-antimatter asymmetry in the Universe.

2.4.3 CMS

CMS [25] is comparable to ATLAS in its goals. It is a general purpose detector used to study physics at high energies with a particular focus on exotica and signs of new physics. ATLAS and CMS are designed to have a different detector geometry and systematics.

2.4.4 TOTEM

TOTEM [26] is designed to take precise measurements of the total proton-proton interaction cross section at LHC energies as well as studying proton structure from elastic and diffractive collisions. TOTEM uses 3 different detector types, spread over 440 m, two of which are inside of CMS.

2.4.5 LHCf

The LHCf experiment [27] is for studying particles produced at large pseudorapidities from collisions in order to simulate high-energy cosmic rays in laboratory conditions. It is located ±140 m from the ATLAS interaction point, measuring cascades from particles (typically forward photons, neutral pions and neutrons) in the region $|\eta| > 8.7$. These forward going particles are similar to those in cosmic ray showers and LHCf studies are used to help with calibrating and interpreting results from large scale cosmic-ray experiments.

2.5 The Grid

The amount of data produced by each of the experiments is much too large for everyone to download their own copy locally. The LHC uses a distributed computing grid to access the data and allows computing resources to be shared worldwide.

The Grid [28] uses a multi-tiered structure with the central hub (Tier-0) being the CERN Data Centre. It is used to safely keep all of the raw data for each LHC detector, recon-

structs the raw data into usable information and then distributes these data to Tier-1 sites. The Tier-1 sites are large regional computer centres responsible for storing raw and reconstructed LHC data, performing data reprocessing to be stored and distributing data. Tier-2 sites are places that can store sufficient data and provide computing resources for analysis (e.g. scientific institutes or universities), including production and reconstruction of simulated events. Individual scientists can access the Grid through local (or Tier-3) computing resources e.g. a university department PC cluster. This allows scientists to submit analysis algorithms to many Tier-2 and Tier-3 sites, depending on where the required data are located.

CHAPTER 3

The ATLAS Experiment

The ATLAS Experiment [29] is a general purpose detector designed to be sensitive to a wide range of potential physics signals at the TeV energy scale, including the Higgs boson and supersymmetry, as well as exploring the Standard Model at higher energies than those that have been achieved at other colliders.

As to how the different theories that extend the Standard Model will manifest themselves, as they contain many free parameters that affect observables, means that ATLAS must cast its "search net" far and wide. However, it is from the possible decay channels of the Standard Model Higgs boson, as shown in Figure 1.2, that stringent bounds have been put on the requirements of the detector. This chapter provides an overview of the ATLAS experiment and the different sub-detectors within it as well as its trigger and data acquisition systems.

3.1 Detector Overview

An overview cut-away image of the ATLAS detector can be seen in Figure 3.1. It is a 'cylindrical' detector which is 44 m long, 25 m in diameter and weighs approximately 7000 tonnes, making it by far the largest LHC detector by volume. It has nearly 4π of angular coverage, making it a hermetic detector, which is sensitive to a wide range of physics processes.

When protons collide at the LHC, a large number of different particle types are produced. Detectors such as ATLAS are made of a number of layers, each layer with a different functionality, acting like cameras to produce 3D photographs of the events that take place within them by identifying and measuring the particles that come out of the collisions.

The ATLAS detector layout in the central part of the detector (barrel) is made of concentric layers of detectors around the beam. The barrel lies between two end-caps where the different layers are arranged perpendicular to the beam. The different layers comprise several sub-detectors, designed to work together in identifying and measuring different particles. The innermost regions consist of a tracking system, known as the Inner Detector (ID), housed in a 2 T solenoidal magnetic field. Beyond this there are electromagnetic and hadronic calorimeters followed by muon detectors interleaved between air-core toroids, producing a toroidal magnetic field. The rest of this chapter describes the sub-detector systems of ATLAS in more detail, based on the ATLAS detector paper [30].

3.2 ATLAS Coordinate System

ATLAS is designed to be symmetric around the collision interaction point (IP) at the centre of the detector. It uses a right handed coordinate system in which the positive x-direction points from the interaction point to the centre of LHC ring, with the positive y-direction being vertically upwards and the z-axis being along the beam line, as shown in Figure 3.2. Conventionally, the side of ATLAS from which the incoming clockwise LHC beam 1 arrives ($+z$-direction) is known as the A side and the side of the incoming anti-clockwise LHC beam 2 is the C side ($-z$-direction). In cylindrical polar coordinates,

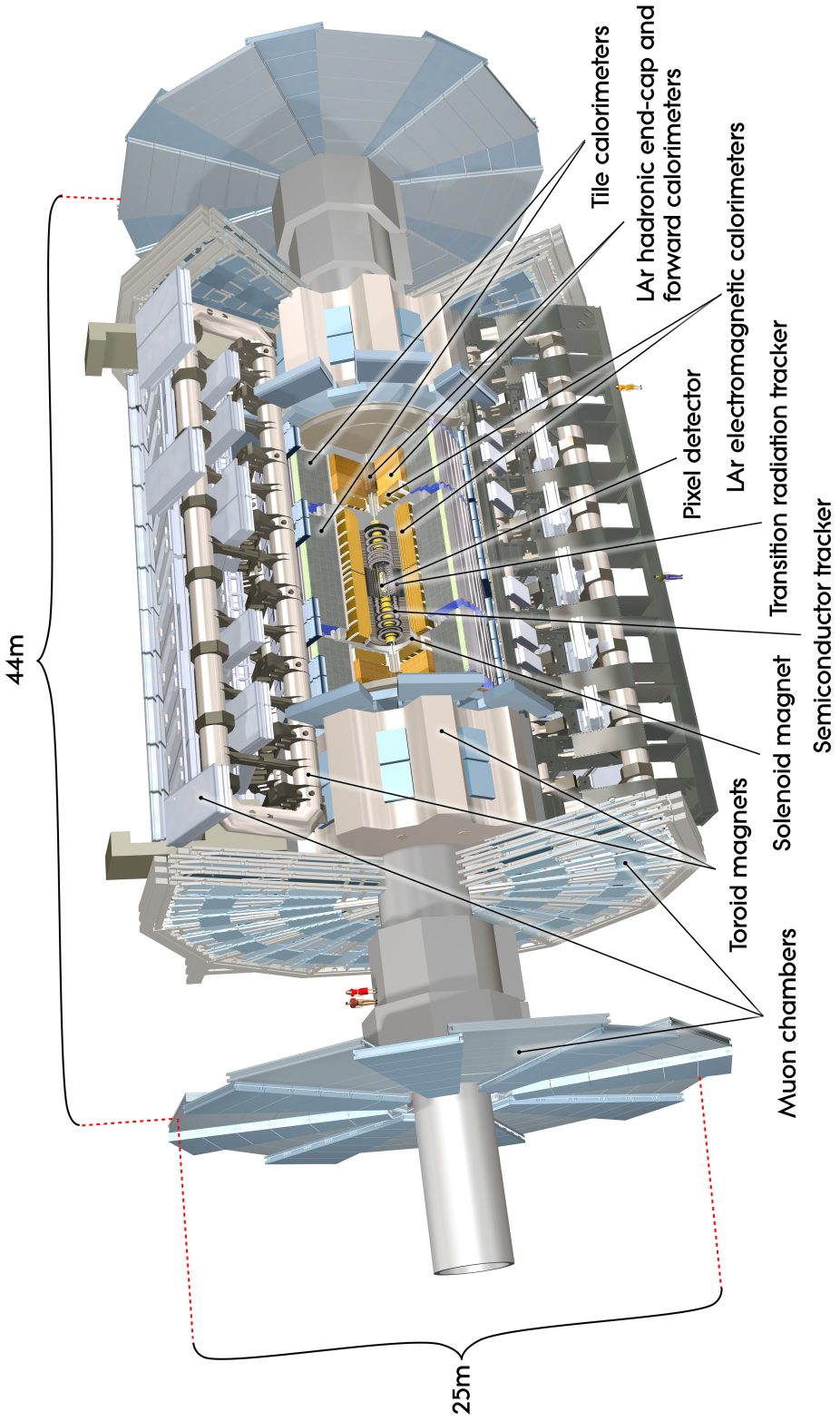

Figure 3.1: A computer generated image of the ATLAS detector with a section taken out to reveal the sub-detector systems [30].

R is defined as $\sqrt{x^2 + y^2}$, the azimuthal angle ϕ is measured with respect to the x-axis and the polar angle θ is measured relative to the $+z$ beam axis. Any quantity described as being transverse e.g. transverse momentum (p_{T}), transverse energy (E_{T}), total transverse energy (ΣE_{T}) and missing transverse energy ($E_{\mathrm{T}}^{\mathrm{miss}}$) is evaluated in the x-y plane.

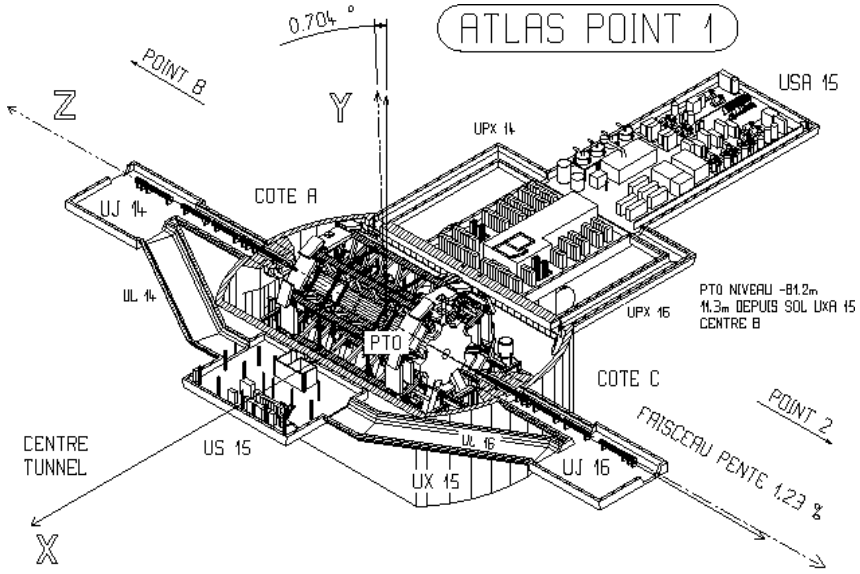

Figure 3.2: The ATLAS detector is located in the UX 15 underground cavern, with further caverns holding supporting ATLAS electronics and services. The coordinate system used in this thesis is also indicated [31].

The rapidity, y, of a particle is defined as $y = \frac{1}{2} \ln \left(\frac{E+p_z}{E-p_z} \right)$, where E and p_z are the particle's energy and longitudinal momentum, respectively. In the ultra-relativistic limit ($p^2 \gg m^2$), it can be assumed that a particle is massless and y reduces to the pseudorapidity, η, defined as $\eta = -\ln \tan \frac{\theta}{2}$. Rapidity (and pseudorapidity) are useful variables as particle production is almost constant as a function of rapidity, unlike θ, and the rapidity differences remain invariant under Lorentz boosts along the beam axis.

3.3 Inner Detector and Solenoid Magnet

The Inner Detector (ID) is used as a tracker of charged particles. The ID consists of three different sub-detector systems, as seen in Figure 3.3, combining high-precision detectors close to the interaction point with continuous tracking elements further outward. In the barrel (up to $|\eta| \leq 1.0$), these systems are arranged in concentric cylinders and in the

end-caps, they are mounted on disks perpendicular to the beam axis to provide tracking coverage for $|\eta| < 2.5$.

The combined sub-detectors are required to reconstruct the charged particle trajectories along the whole track length, with good resolution for determining primary interaction vertices as well as pile-up vertices from additional pp collisions in an event. The resolution needs to be good enough to reconstruct secondary decay vertices, such as those involving hadrons containing b-quarks.

The ID is surrounded by a solenoid magnet which is 5.3 m long and has a 2.4 m diameter bore. The solenoid provides a 2 T axial field in the central tracking volume, needed for the paths of charged particles to bend in the transverse plane. The solenoid being shorter than the ID means that the field becomes inhomogeneous in the forward regions. The strong field allows the particle momenta to be measured over a wide p_{T} range. As all the charged particles are influenced by the magnetic field, the lower limit in p_{T} to which tracks can be reconstructed is 100 MeV. Charged particles with a transverse momentum less than 400 MeV are affected enough by magnetic field that they typically do not reach the calorimeters.

The momentum resolution of the inner detector is: $\frac{\sigma(p_{\mathrm{T}})}{p_{\mathrm{T}}} = 0.05\% \times p_{\mathrm{T}} \oplus 1\%$ (p_{T} in GeV). It also has to have good b-tagging performance to distinguish between b-jets and jets from lighter quarks. This requires that the impact parameter of tracks is measured accurately. Over the range $0.25 < |\eta| < 0.5$, the impact parameter resolution as a function of track p_{T} is designed to be $\sigma(d_0) = 10(1 \oplus 14\ \mathrm{GeV}/p_{\mathrm{T}})\ \mu\mathrm{m}$.

For the ID and solenoid magnet, the materials used must be as thin and light as possible. This is so that the tracking detectors, including the services and electronics necessary for the ID to work, have little effect on the path of the particles. Additionally, as they both lie inside the calorimeters, too much material would have a significant affect on energy measurements.

Additionally, being so close to the beam line, the levels of radiation in the ID are extremely high. It is a challenge to make the sub-detectors radiation hard as radiation can damage the silicon detectors, degrade the electronics and introduce a larger rate of background in

sensitive areas.

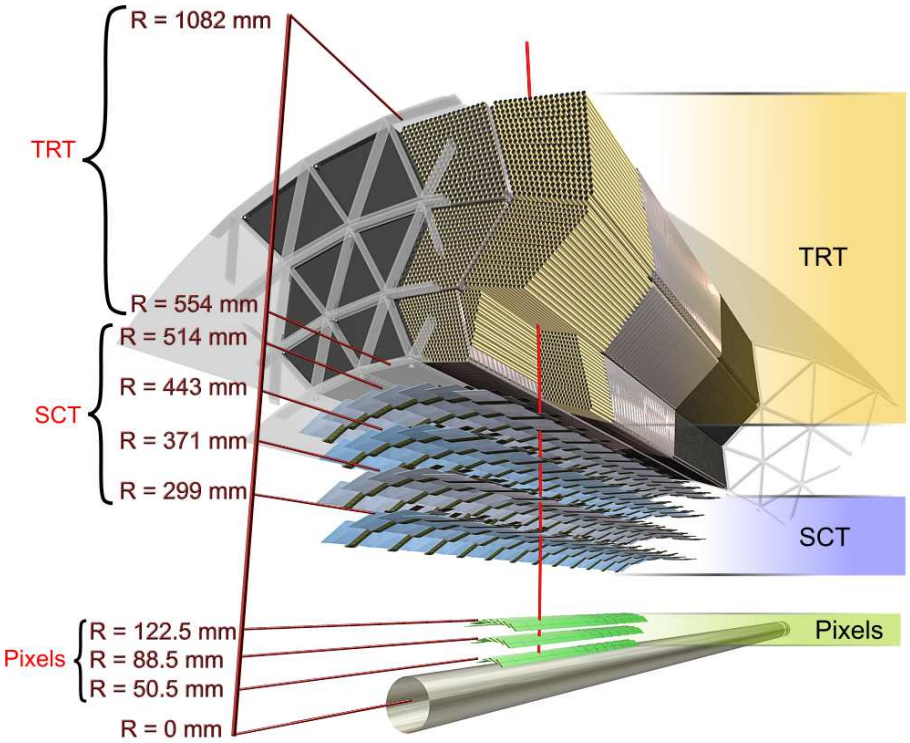

Figure 3.3: Scheme of the ATLAS Inner Detector barrel being crossed by one high-energy particle, labelled and showing the radial distance, R, of the different sub-detectors away from the beam line [30].

3.3.1 Pixel Detector

The Pixel detector is designed to provide high granularity and be very radiation hard due to the large particle density produced at the interaction point. There are 3 barrel layers at 50.5, 88.5 and 122.5 mm away from the beam line and 3 disks in each of the end-caps. The innermost layer of the Pixel Detector barrel region is known as the B-layer, since it provides the critical vertexing information used to reconstruct the displaced vertices from b-quark decays (and any other short-lived particles, including c-quarks and τ-leptons).

Both the barrel layers and end-cap disks use very high granularity silicon modules. The pixels are of nominal size 50 μm$\times$400 μm. Each of the 1744 modules consists of 160$\times$24 pixels, covering an area of 60.8 mm$\times$16.4 mm, read out by 16 chips and the modules have a resolution of 10 μm in R-ϕ and 115 μm in z.

The pixels use a charge-depleted layer of silicon to collect and detect the charge carriers generated by ionising particles passing through. For each pixel, the signal time-over-threshold is used to determine the amount of charge deposited and the distribution of charge across a pixel determines the position of the particle hit.

3.3.2 Semiconductor Tracker

In the intermediate radial range, the Semiconductor Tracker (SCT) provides four precision measurements per track using silicon strip sensors. The SCT has four layers in the barrel, at radii of 299, 371, 443 and 514 mm, providing coverage up to $|\eta| = 1.4$, and the end-caps each use nine disks. In the barrel, each layer uses sensor modules of size 6.36 cm$\times$6.40 cm, with each having 768 strips with 80 μm pitch. In the end-cap the pitch varies between 57 and 94 μm. To make precision measurements, modules are placed back to back in each ring, with a small stereo angle (about 2.3°, 40 mrad) with respect to each other and an overlap of 1% in ϕ to increase the hermicity of the detector.

Being a silicon detector, it operates in the same way as the pixel layers in measuring current as a charged particle passes through its sensors. Instead of reading out information about the current, the signals from the SCT sensors are amplified and then passed through discriminators to store hits above threshold. The spatial resolution is 16 μm in R-ϕ and 580 μm in z. Tracks can be distinguished if separated by more than 200 μm.

3.3.3 Transition Radiation Tracker

The outer tracking system is the Transition Radiation Tracker (TRT) which is a combined straw tube and transition radiation detector. This produces a poorer spatial resolution than silicon detectors, but has the advantage of a much smaller material budget.

As charged particles traverse the TRT, their trajectories are measured with 36 straw tube hits per track on average. These cylindrical straws (4 mm diameter) are filled with a mixture containing Xenon gas such that as the particle passes through the gas, the atoms are ionised. The resulting ions and electrons drift in the electric field and signals are

produced at the anode wire in the centre of the tube. The resolution of the TRT drift tubes is around 130 μm in R-ϕ. The larger number of measurements and the higher average radius compensate the lower precision per point of the TRT compared to the precision trackers used by the Pixel detectors and SCT.

Transition radiation is electromagnetic radiation produced when charged particles pass through inhomogeneous media. For the TRT, the layers of straws are interleaved with the polypropylene foils, acting as radiators. The Xenon gas is good at absorbing photons . The Xenon gas acts as a radiating medium so photons are radiated by charged particles as they pass through. It is capable of distinguishing between electrons and charged hadrons based on the Lorentz boost ($\gamma \equiv E/m$) of the particle e.g. for a fixed particle energy, an electron with low mass and hence high γ would produce more radiation and larger signals than charged hadrons with higher masses.

3.4 Calorimeters

Calorimeters can be of two types: homogeneous and sampling. Homogeneous calorimeters are ones where the calorimeter is both the absorber and the active material, but are only really used in electromagnetic calorimetry (a homogeneous hadronic calorimeter would need to be extremely large). Performing both roles means that the full shower can be measured, leading to good energy resolution but often at the expense of limited spatial resolution, particularly in the longitudinal direction. A sampling calorimeter uses separated layers of active material and absorber material, and is used for both electromagnetic and hadronic calorimetry. The layers of absorber mean that the full energy deposit is not measured and sampling calorimeters tend to have a more limited energy resolution but provide good spatial resolution. They produce an output signal proportional to the input energy.

Calorimeter systems are normally split into an electromagnetic and a hadronic calorimeter due to the differences in how electrons and photons shower when compared to hadrons in large amounts of dense absorber material.

An electromagnetic shower is produced when an electron or photon is incident on the calorimeter. The characteristic mean amount of material traversed before an electron radiates a bremsstrahlung photon ($e \rightarrow e\gamma$) or a photon produces an electron-positron pair ($\gamma \rightarrow e^+e^-$) is known as a radiation length, X_0. Within the shower, electrons radiate bremsstrahlung photons which convert into e^+e^- pairs. These continue to bremsstrahlung more photons until a threshold is reached where the electrons become more likely to ionize the atoms in the dense material then to radiate photons and the photons no longer have the 2×511 keV required to pair-produce an electron-positron pair.

Hadronic showers are produced by the interaction of high energy hadrons incident on the absorber material. Hadronic showers are more complicated than EM showers, as they usually involve the production of many lower energy hadrons, mainly pions and nucleons. The decay of some hadrons will produce electrons and photons, e.g. neutral pions decaying into two photons, so the hadronic shower will have an electromagnetic component. Additionally, a small fraction of particles within the shower decay will produce neutrinos which cannot be measured. For hadronic showers, the characteristic distance scale of the decay is expressed by the nuclear interaction length, λ. Hadronic calorimeters should ideally give an equal response to the hadronic, h, and electromagnetic, e, parts of the shower (an e/h ratio = 1) although designers may choose between a compensating calorimeter (e.g. using uranium as an absorber) or software corrections to produce this response.

The ATLAS calorimeter system is split into an electromagnetic calorimeter followed by a hadronic calorimeter, as shown in Figure 3.4. Both of the calorimeters are designed such that there is a large difference between the radiation length and the nuclear radiation length in order to separate the showers.

3.4.1 Electromagnetic Calorimeter

The electromagnetic calorimeter (ECAL) precisely measures the energy of high energy electrons and photons by containing the electromagnetic shower produced.

The ECAL is a sampling calorimeter that is 24 X_0 deep and consists of 3 separate modules, the barrel ($|\eta| < 1.45$), and two end-caps ($1.35 < |\eta| < 3.2$). The detector utilises lead

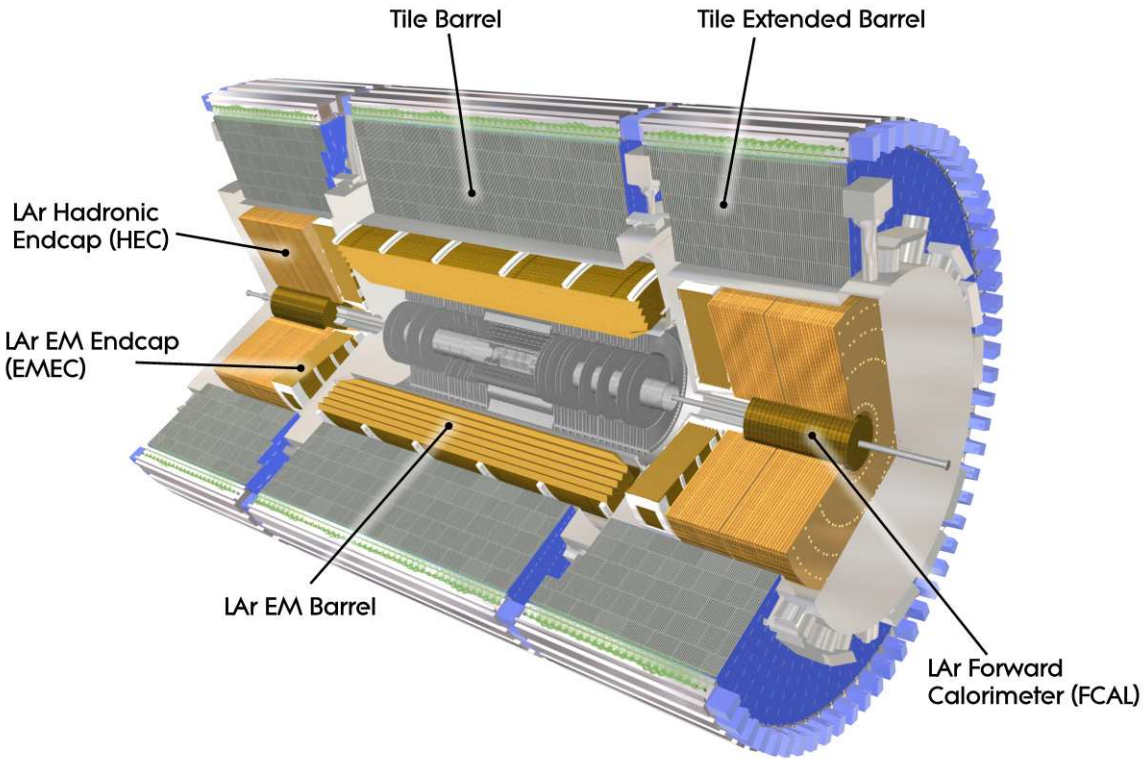

Figure 3.4: An image of the combined electromagnetic and hadronic ATLAS calorimeter system [30].

sheets, clad in stainless steel, as absorbers with liquid argon (LAr) chosen for its intrinsic radiation hardness, used in the space between the sheets forming the active medium to collect the signal. The energy signal in the active medium is read out by layers of conductive copper sheets. A honeycomb spacer arrangement is provided to maintain the size of the LAr gap between layers.

To provide full hermetic coverage, the calorimeter has an 'accordion' geometry to remove gaps in ϕ. It consists of three different layers, as shown in Figure 3.5 [32]. The first sampling layer has very fine granularity in η to distinguish between γ/π^0 and $e/\pi^{\pm}$ and produce a precise η measurement. The second sampling layer is then very deep to contain as much of the electromagnetic shower as possible and produce a precise measurement of the energy. The final sampling layer has reduced granularity but is primarily there to measure any remaining part of the shower that was not contained in the second layer.

In the region $|\eta| < 1.8$, an additional pre-sampler provides a first sampling of the showers

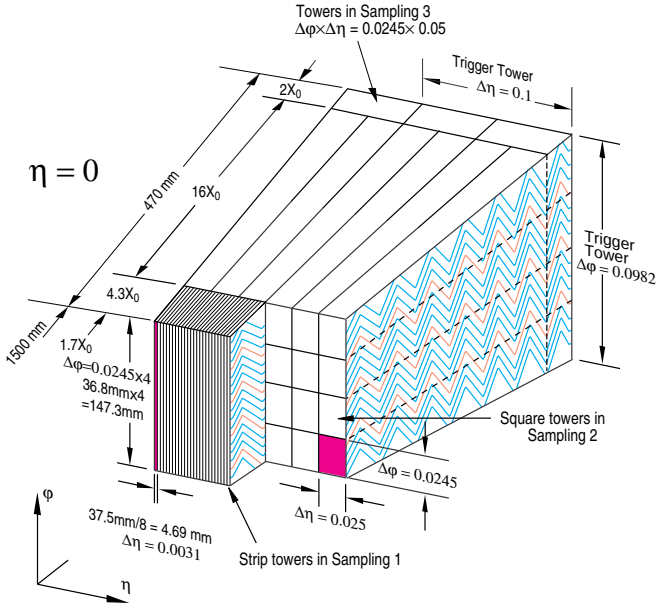

Figure 3.5: A section of the electromagnetic calorimeter. For each layer of the calorimeter, the thickness in radiation lengths and the size of the cells in $\Delta\phi \times \Delta\eta$ is shown [32].

in front of the electromagnetic barrel and end-cap calorimeters. This allows the reconstruction to correct for energy lost in inactive material upstream of the calorimeters (see Section 5.3.1). Figure 3.6 shows the typical amount of inactive material (e.g. from the Inner Detector and solenoid magnet) that has to be traversed before reaching the calorimeters.

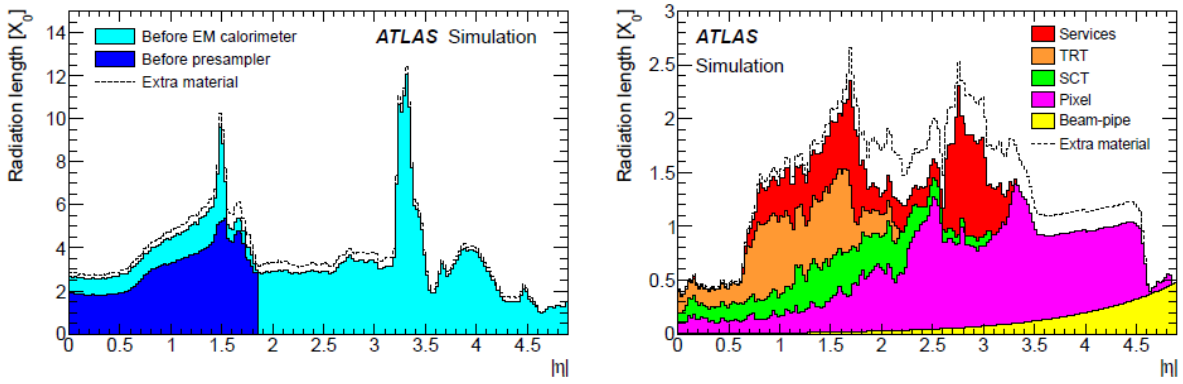

Figure 3.6: Amount of material, in units of radiation length X_0, traversed by a particle as a function of η: (left) material in front of the presampler detector and the ECAL, and (right) material up to the ID boundaries. The contributions of the different detector elements, including the services and thermal enclosures are shown separately by filled colour areas. The extra material used for systematic studies is indicated by dashed lines [33].

For the EM calorimeter, there are areas with significant dead material that prevent energy

deposits from being directly measurable. In particular, the cracks between the EM barrel and end-caps ($1.4 < |\eta| < 1.5$) have many services (cryostat walls for the barrel and end-caps, cabling for the inner detector) passing through them. At $\eta = 0$, there is also a very small gap where the two parts of the barrel join together.

3.4.2 Hadronic Calorimeter

The hadronic calorimeter (HCAL) is also a sampling calorimeter made of two different technologies for different pseudorapidity ranges. The main tasks required from it are the reconstruction of jets from hadronic showers and the reconstruction of missing transverse momentum ($E_{\mathrm{T}}^{\mathrm{miss}}$), which requires a large coverage in η. It also needs to be large enough to measure the whole shower and prevent particles producing 'punch-throughs', where energy leaks out of the calorimeter, but it must not be so dense such that muons scatter regularly within the calorimeter (multi-Coulomb scattering).

The Tile Calorimeter (TileCal) is used at central pseudorapidity ($|\eta| < 1.7$). There are three modules, one barrel module covering $|\eta| < 1.0$ with two extended barrel modules covering $0.8 < |\eta| < 1.7$. The calorimeter has an inner radius of 2.28 m and the outer radius of 4.23 m. The layout of a TileCal module can be seen in Figure 3.7, with a steel absorber structure used with plastic scintillator tiles as the active medium. The tiles have a 3 mm thickness and are staggered in depth, in planes perpendicular to the colliding beams, to achieve good sampling homogeneity behind the electromagnetic calorimeters. The opposite sides of the scintillating tiles are read out by wavelength shifting (WLS) fibres into two separate photomultipliers (PMTs). The modules are grouped in sets of 64 for building the integrated signals from the central barrel and extended barrel.

In the hadronic end-caps (HEC), spanning the range $1.5 < |\eta| < 3.2$, LAr is used as the active medium, due to its radiation hardness, with copper plates used as the absorber. The HEC shares the two end-cap cryostats together with the EMEC and forward calorimeter (FCAL). The HECs are composed of 2 wheels per end, of outer radius 2.03 m, with 32 modules per wheel. The front and rear wheels have copper plates of 25 mm and 50 mm thickness, respectively, with gaps of 8.5 mm between the copper plates. The gap between

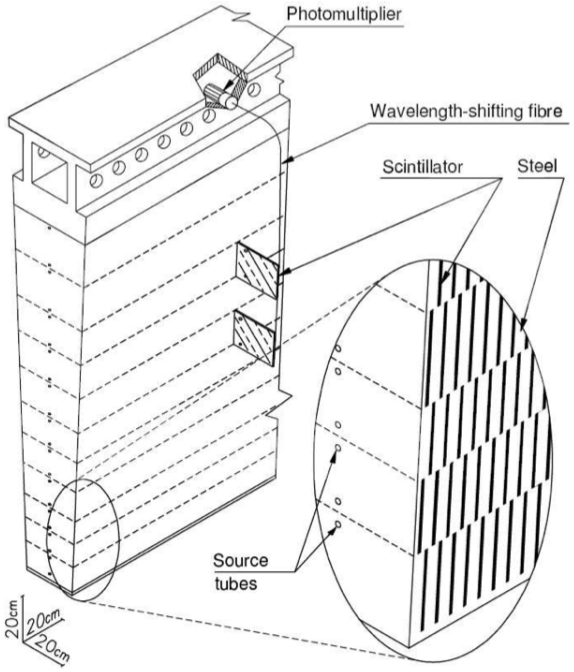

Figure 3.7: Details of a TileCal module in which tile plastic scintillators are sandwiched with iron absorbers. The photomultipliers at the top of the modules collect scintillation light via wavelength-shifting fibres. [34]

plates is filled with three parallel electrodes and uses an electrostatic transformer (EST) readout structure.

For the HCAL, similarly to the ECAL, there are regions where signals need to be corrected due to upstream and in-detector dead material. This affects the jet reconstruction efficiency and resolution and can generate fake $E_{\mathrm{T}}^{\mathrm{miss}}$ contributions, resulting in topology dependencies for the reconstruction of missing energy. The EM barrel shares its cryostat with the superconducting solenoid and the ID, such that there is some dead material between the LAr barrel and Tile calorimeter. Between the Tile barrel and extended barrels, there is a gap of 680 mm used to house the electronics cables and cryogenics services for the inner detector and LAr calorimeters. Intermediate Tile Calorimeter (ITC) scintillators are also placed in the gap, corresponding to the range $0.8 < |\eta| < 1.6$ to sample the showers after passing through the services. For $0.8 < |\eta| < 1.0$, the ITCs are arranged as plugs made of thin layers of steel and scintillator to sample showers downstream of the TileCal central barrel. For $1.0 < |\eta| < 1.6$, the space is too narrow and only scintillators are used to sample the showers downstream of the LAr barrel.

3.4.3 Forward Calorimeter

In the range $3.1 < |\eta| < 4.9$, a forward calorimeter (FCAL) is installed in each end-cap cryostat using liquid argon as the active medium. At these values of η, there is not any tracking information and η granularity is limited so the resolution for precision physics analysis is reduced. Instead, the large coverage in η aids in the determination of the total and missing energy in the event, as well as the reconstruction of forward electrons, photons and jets.

The FCAL is a small yet high density sub-detector which sits in a region with very large energy fluxes from forward particles. It is approximately 10λ deep, consisting of one module with a copper absorber optimised for electromagnetic measurements and two modules with a tungsten absorber for hadronic interactions as shown in Figure 3.8. An uninstrumented brass plug is placed at the back of the modules to prevent punch through to the muon systems.

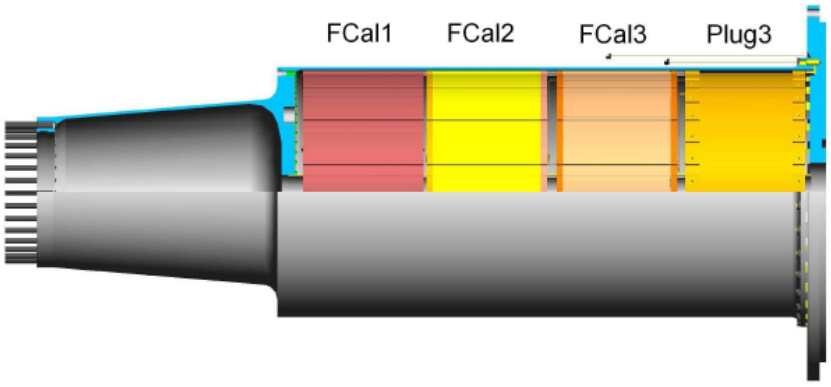

Figure 3.8: Cut away image of the FCAL modules and uninstrumented brass plug in their cryostat. This FCAL is located at positive η with the interaction point to the left [35].

To measure the energy deposited in each module, cylindrical electrodes are built, parallel to the beam pipe, into an absorber matrix. The electrodes are made of an outer tube (cathode) and an inner rod (anode), separated by a very narrow gap filled with LAr (Figure 3.9). Very narrow LAr gaps are required for a well defined energy measurement in the forward region due to the high ionisation density. The LAr gap in the EM FCAL layer is 250 μm and then goes to 375 μm and 500 μm in the following hadronic modules, respectively, as the ionisation density from showers becomes lower.

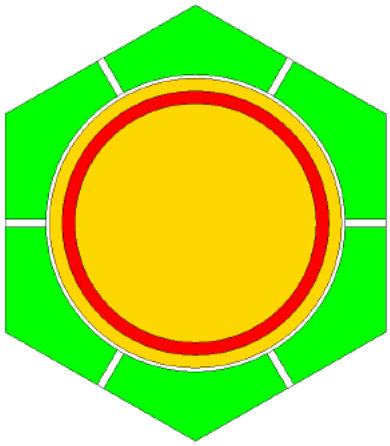

Figure 3.9: Representation of a cell in an ATLAS FCAL module. The absorber matrix (green) houses the electrodes (yellow) which consist of an outer tube and inner rod, separated by a narrow liquid argon gap (red) [35].

3.4.4 Energy Resolution

The resolution of a sampling calorimeter is typically of the form $\frac{\Delta E}{E} = \frac{a}{\sqrt{E}} \oplus \frac{b}{E} \oplus c$ [36], although the three parameters a, b and c all typically vary as a function of η in practice. For a sampling calorimeter, the 'sampling' statistical term a is affected by the number of interfaces between the absorber and active medium layers, the thickness of layers and choices of material and is dominant for intermediate energies between 10 and 100 GeV. The 'noise' term, b, is defined by the electronic noise and is dominant for low energies, typically around 400 MeV, and so does not often get displayed for the ATLAS calorimeters. The constant term, c, affects the resolution for high energy deposits and accounts for effects such as energy leakage. It is then determined by the depth of the calorimeter, as well as the cracks and dead material (non-uniformity) of it.

The design energy resolution for both the EM barrel and end-cap is given as $\frac{\Delta E}{E} = \frac{10\%}{\sqrt{E(\text{GeV})}} \oplus 0.7\%$. The EM calorimeter performance was measured with an electron test beam of energies up to 300 GeV. The ratio of the reconstructed to the beam electron energy was found to be consistent with unity to better than 1% and the energy resolution of the EM barrel at $\eta = 0.9$ was measured to be $\frac{\Delta E}{E} = \frac{10.1\%}{\sqrt{E(\text{GeV})}} \oplus \frac{0.2}{E(\text{GeV})} \oplus 0.4\%$ [37].

The energy resolution decreases in the region between the EM barrel and end-cap due to the large amount of dead material in these regions, preventing energy deposits from

being well measured. There is a similar effect in the transition for the forward region around $|\eta| = 3.2$. The distributions of signals nearby can be used as a guide to evaluate the influence of the cracks, but the energy losses could require signal corrections on the order of 10% depending on the nature of the energy deposit.

The design energy resolution of the hadronic calorimeter [34] is

$$\frac{\Delta E}{E} = \begin{cases} \frac{50\%}{\sqrt{E(\mathrm{GeV})}} \oplus 3\%, & \text{for } |\eta| < 3 \\ \frac{100\%}{\sqrt{E(\mathrm{GeV})}} \oplus 10\%, & \text{for } 3 < |\eta| < 5 \end{cases} \tag{3.1}$$

where the constant term is dominated by the different response to the hadronic and electromagnetic part of the shower as a larger fraction of the total energy ends up as an electromagnetic shower at high energies.

The Tile and HEC performances were studied using test beams consisting of single pions. For Tile, with pions of energy between 20 and 350 GeV, the energy resolution was determined to be $\frac{\Delta E}{E} = \frac{52.7\%}{\sqrt{E(\mathrm{GeV})}} \oplus 5.7\%$ [38]. The HEC resolution, for pions between 5 and 200 GeV was measured as $\frac{\Delta E}{E} = \frac{71\%}{\sqrt{E(\mathrm{GeV})}} \oplus 6\%$ [39].

3.5 Muon Spectrometer

The ATLAS Muon Spectrometer (MS) serves a double purpose as a trigger to select events with high energy muons and as an independent precision muon spectrometer for muon reconstruction. The aim is for a momentum resolution of 2% for 100 GeV muons and 10% for 1 TeV muons. This is achieved by the use of a large toroidal magnet system together with high precision tracking chambers and dedicated trigger chambers. The arrangement is shown in Figure 3.10.

The muon spectrometer covers the outermost layers of the ATLAS detector. Before entering the muon spectrometer, muons have to pass a large amount of material corresponding to about 100 X_0. As muons are roughly 200 times heavier than electrons, they are unlikely to undergo bremsstrahlung processes, in which the total radiated energy goes as

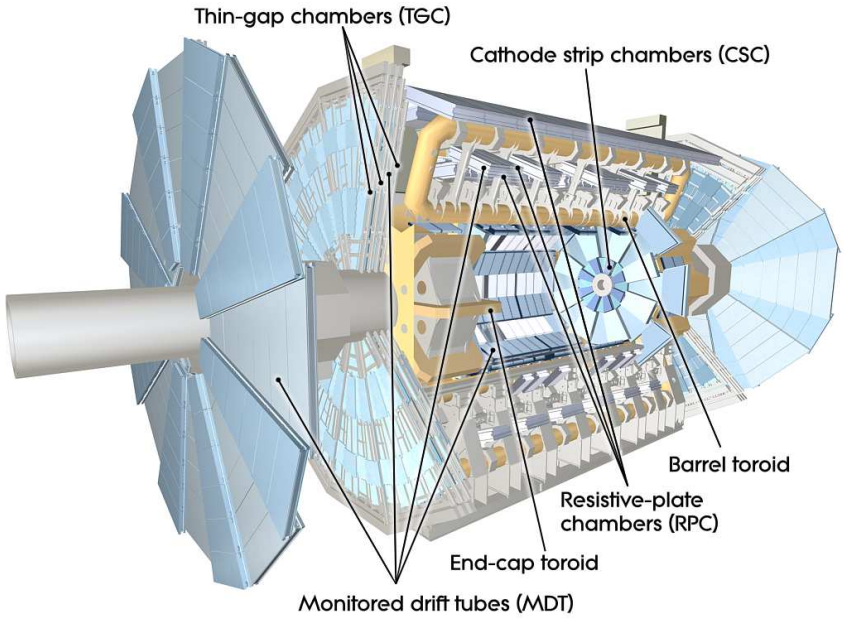

Figure 3.10: Overview of the ATLAS Muon Spectrometer with labelled components [30].

m^{-4}. They will thus pass through the Inner Detector and calorimeters leaving only tiny amounts of ionisation energy. Also by this point all other particles, except neutrinos, will have been absorbed in the detector material.

The toroid magnet system is divided into one barrel part and two forward systems. With a toroid field, particles across the complete pseudorapidity range will be almost perpendicular to the field. This means that the field integral $\int B\ dl$, a measure of the bending power of the magnetic field (the important factor for track momentum measurements), can be kept high even in the forward direction.

In the pseudorapidity range $|\eta| < 1.0$, magnetic bending is provided by 8 independent coils positioned symmetrically around the ATLAS calorimeters, each in separate cryostats. These coils are 25 m long, and have an inner and outer radius of 4.7 m and 10 m, respectively. In the forward direction, $1.4 < |\eta| < 2.7$, the toroid field is also formed by 8 superconducting coils placed in a common cryostat. The arrangements of the toroid magnets, as well as the solenoid surrounding the Inner Detector, can be seen in Figure 3.11. In the interval $1.0 < |\eta| < 1.4$, referred to as the transition region, magnetic deflection is provided by a combination of barrel and end-cap fields. The low number of coils used to form the toroid field results in a field strength that varies strongly with the

ϕ coordinate. The field integral varies in the barrel from 2 to 6 Tm and in the end-caps from 4 to 8 Tm.

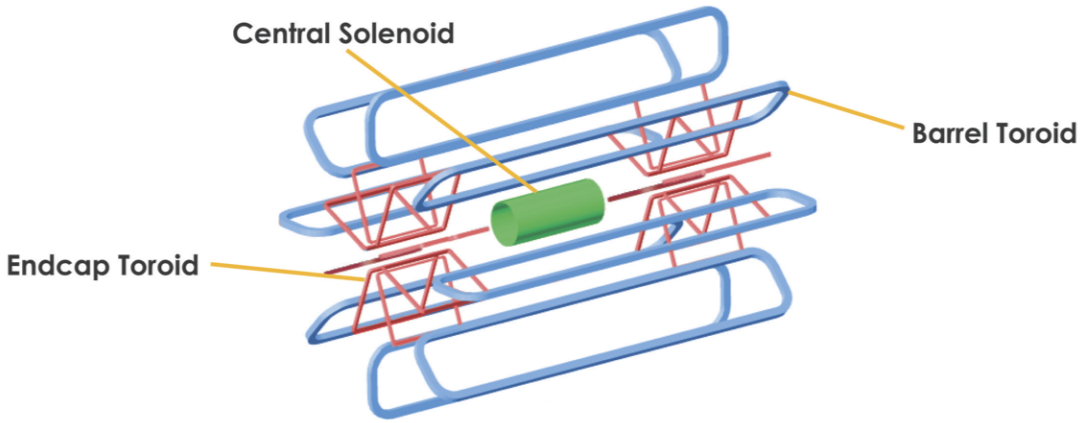

Figure 3.11: Arrangement of the solenoid and toroidal magnet systems in the ATLAS detector (other sub-detectors not shown) [40].

3.5.1 Monitored Drift Tubes

The Monitored Drift Tube (MDT) chambers are proportional chambers made of aluminium tubes of 30 mm diameter, containing a central wire, and lengths varying from 70 cm to 630 cm. To measure the coordinate in the bending plane of the magnet the tubes are placed transverse to the beam axis. Each set of MDTs consists of 2 major layers each containing 3 or 4 smaller layers of tubes. The large number of tubes in each set reduce the number of fake tracks reconstructed from background hits.

A muon that crosses a tube frees electrons by ionisation, which drift to the anode. The distance between the muon track and the anode is determined by measuring the drift time of the primary ionisation clusters that reach the anode with respect to the start time of the bunch crossing. The resolution on the drift distance is around 80 μm but the drift time can be up to 480 ns. MDT chambers are used both in the barrel and end-caps of the muon system. In the barrel region, $|\eta| < 1.05$, MDT chambers are situated in three layers at radii of 5, 7.5 and 10 m from the beam axis. In the end-cap region the chambers are divided over three wheels located at z-positions of 7.5, 13 and 20 m. The MDT end-cap wheels cover the region $1.05 < |\eta| < 2.7$, except in the innermost layer, where the MDT chambers are only used up to $|\eta| = 2.0$.

3.5.2 Cathode Strip Chambers

Cathode Strip Chambers (CSCs) replace the MDTs in the inner end-cap wheel, $2.0 < |\eta| < 2.7$, as they are designed to withstand the higher particle fluxes in this region. They are multi-wire proportional chambers with a wire spacing of 2.5 mm, giving them a high spatial resolution and an electron drift time of less than 30 ns.

The precision coordinate is determined from the charge distribution measured on the cathode strips. A second coordinate is read out using strips which are parallel to the anode wires (orthogonal to the cathode strips). The spatial resolution on the precision coordinate is around 60 μm and for the second coordinate the resolution is around 5 mm.

3.5.3 Resistive Plate Chambers

Special layers of muon chambers are implemented for triggering purposes, which is necessary due to the large drift time of the MDTs in comparison to the design bunch crossing spacing.

Resistive Plate Chamber (RPC) detectors are placed in every MDT barrel layer. The basic detector unit employs a thin gap formed by two resistive plates with metal strips filled with a gas mixture in which ionisation is produced by the passage of a charged particle. The plates are covered with two orthogonal read-out strips. The η strips are parallel to the MDT wires (and help provide a fast p_{T} estimate in the trigger) and the ϕ strips are orthogonal to the MDT wires and provide a position measurement along the MDT wire. The spatial resolution of the RPC is around 10 mm for both strips and the time resolution is around 1 ns.

3.5.4 Thin Gap Chambers

The Thin Gap Chambers (TGCs) provide the trigger signal and second coordinate measurement in the end-cap region. The TGCs use an array of wire anodes and cathode strips with a thin gap in order to produce a short drift time and momentum estimate

for triggering. The anode wires are arranged parallel to the MDT wires and the cathode strips are arranged orthogonally to provide the position measurement along the MDT wire. The spatial resolution of the TGC is around 2-7 mm for both measurements.

3.6 Minimum Bias Trigger Scintillators

The primary triggers for selecting all types of inelastic interactions with as little bias as possible are the Minimum Bias Trigger Scintillators (MBTS). These are arranged in two disks, located on the inner faces of each of the end-cap calorimeter cryostats at either side of the detector, ±3560 mm from the interaction point. As seen in Figure 3.12, each disk is split into an inner and outer ring covering different pseudorapidity ranges, $2.82 < |\eta| < 3.84$ and $2.09 < |\eta| < 2.82$, respectively. Each ring is segmented in ϕ into 8 independent polystyrene scintillator counters of 2 mm thickness.

As charged particles pass through the counters, the light emitted is read out via wavelength-shifting (WLS) fibres connected to photomultiplier tubes (PMTs). The signals are shaped and amplified by the Tile calorimeter electronics and passed through Leading Edge (LE) discriminators. For a counter to have registered a hit, the signal must be above a discriminator threshold. This information is sent to the Central Trigger Processor (Section 4.5) which determines the multiplicity of counter hits independently for both sides of the detector.

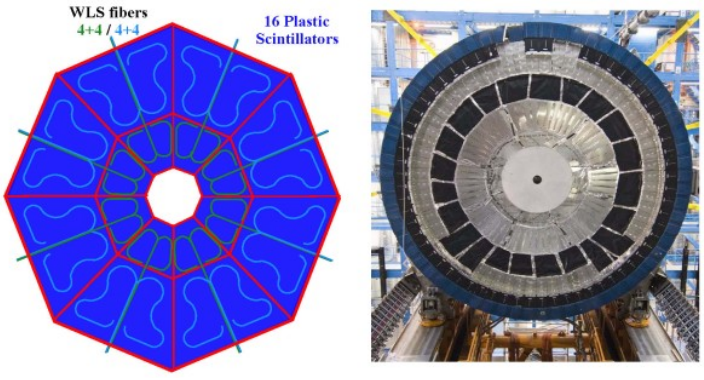

Figure 3.12: Layout of scintillator tiles on one set of the Minimum Bias Scintillator Triggers [41].

3.7 Forward Sub-detectors

The final components of the ATLAS detector are forward detectors located in the LHC tunnel. The roles of these detectors include studying forward physics as well as performing luminosity monitoring and providing an absolute luminosity measurement for ATLAS.

3.7.1 LUCID

LUCID (Luminosity measurement using Čerenkov Integrating Detector) is used as the primary detector for monitoring the instantaneous luminosity as seen by ATLAS. On each side of ATLAS, the detector consists of a set of 20 individual aluminium tubes, each 1.5 m in length and 15 mm in diameter. The detectors are installed in the end-cap regions, 17 m away from the IP, with the tubes situated 10 cm away from the beam line (covering the range $5.6 < |\eta| < 5.9$).

Each tube is filled with C_4F_{10} gas, which produces Čerenkov radiation as charged particles (pointing to the primary pp collisions) pass through it, at thresholds of 10 MeV and 2.8 GeV for electrons and pions, respectively. The Čerenkov light is collected by photomultipliers directly coupled to the tubes with a signal output accuracy of 100 ps. The height of the pulses seen by the PMTs allows the number of particles passing through a tube to be determined. The instantaneous luminosity is measured from the rate of inelastic pp collisions as seen by LUCID, assuming the number of inelastic interactions in a bunch crossing is proportional to the number of particles detected in the tubes.

The luminosity monitoring can be performed on individual bunch crossings, and importantly, this is done independently of the Level 1 trigger which is constrained by dead-time and the data acquisition systems (see Sections 3.8 and 4.5.1). If LUCID were to be used as a minimum bias trigger at high $|\eta|$, the signals would be sent to the trigger but this does not affect the luminosity monitoring.

3.7.1.1 van der Meer Scans

Following from Equation 2.2, ATLAS measures the luminosity from the observed interaction rate per bunch crossing, μ_{vis}, such that the luminosity can be expressed as

$$\mathcal{L} = \frac{\mu_{vis} n_b f_r}{\sigma_{vis}} \ , \tag{3.2}$$

where $\sigma_{vis} = \epsilon\sigma_{inel}$, $\mu_{vis} = \epsilon\mu_{inel}$ and ϵ is the efficiency of measuring σ_{vis} using a particular sub-detector and algorithm [42]. The detectors that can be used for the luminosity determination include the Inner Detector, MBTS and FCAL but LUCID provides the primary measurement due to its fast timing characteristics (allowing for a bunch by bunch luminosity determination) and its large acceptance.

Calibrating σ_{vis} is important in constraining the uncertainty on the luminosity. This is done using van der Meer (vdM) scans, in which the beams are separated with respect to one another and then made to overlap in known horizontal and vertical distance steps. The delivered luminosity, in terms of the accelerator parameters, is given as

$$\mathcal{L} = \frac{n_b f_r n_1 n_2}{2\pi \Sigma_x \Sigma_y} \tag{3.3}$$

where n_1 and n_2 are the numbers of protons per bunch in beam 1 and 2, respectively, and Σ_x and Σ_y are the horizontal and vertical beam widths, respectively, that overlap from the beam crossing. By performing a scan where the beam positions are adjusted in steps by known amounts and by using an external measurement of n_1 and n_2, the luminosity of unseparated beams, and also beams with a small crossing angle, can be determined.

3.7.2 ZDC

The ZDC (Zero Degree Calorimeter) consists of two modules located on either side of ATLAS in the LHC tunnel, 140 m from the interaction point (IP) where the beam pipe is split back into two vacuum tubes in order to circulate the protons correctly around the LHC ring again.

The aim is to detect neutrons and photons with $|\eta| > 8.3$ in pp and heavy ion collisions. The ZDCs are housed in a slot in the TAN (Target Absorber Neutral) absorber, an inert block for used for shielding, and they consist of one electromagnetic module and three hadronic modules, 9 cm by 9 cm perpendicular to the beam and 15 cm thick. The thickness for the EM module is $29X_0$ and 1.14λ for the HAD modules. The modules are composed of tungsten with an embedded matrix of quartz rods which are read out via photomultiplier tubes (PMTs) to measure the position of the particle. The time resolution of the ZDCs is roughly 100 ps, important for associating ZDC signals with the correct bunch crossing.

For heavy ion collisions the ZDCs play an important role in determining the centrality[1] of the collisions, which is strongly correlated with the number of very forward (spectator) neutrons. During the early LHC running (pp collisions with $\mathcal{L} = 10^{32}$ cm^{-2} s^{-1} or smaller), the ZDC modules increase the acceptance for forward and diffractive physics. They can also be used to reduce beam induced backgrounds[2] by asking for coincident signals from both ZDCs. It is not used for high luminosity pp collisions.

3.7.3 ALFA

The Absolute Luminosity For ATLAS (ALFA) detectors are located at ± 240 m from the interaction point. Their purpose is the measurement of elastic pp-scattering (discussed in Section 7.2) at small angles (3.5 μrad), corresponding to $10.6 < |\eta| < 13.5$. The set-up consists of four Roman Pot stations (with upper and lower pots), two on each side of the interaction point, each housing two vertically movable detectors. Each pot is equipped with 1500 scintillating fibres arranged in 20 horizontal/vertical detection planes, providing a spatial resolution of 30 μm.

By measuring the impacts of elastically scattered protons, the absolute luminosity of the LHC at the ATLAS IP is measured to a precision of $\Delta\mathcal{L}/\mathcal{L} \backsim 3.5\%$ in 2010, improving

[1] The centrality is a measure of how much of the cross section of the colliding nuclei overlap each other.

[2] Beam induced backgrounds come from 'beam-gas collisions' in which there are collisions of one of the proton beams with some of the residual beam gas within the beam pipe over the length of ATLAS and 'beam-halo collisions' from muons or pions created in interactions in the tertiary collimators of the LHC upstream of ATLAS that then travel in the halo of the beam.

to $\Delta\mathcal{L}/\mathcal{L} \backsim 2\%$ in 2011. The luminosity calibration is done in special runs where the beam has a much larger transverse profile than normal (high-β^* optics[3]). The choice of β^* affects the momentum transfer, t, range[4] that can be reached with $t_{min} \propto 1/\beta^*$ e.g. for $\beta^* = 1000$ m, the t range $-t \geq 6 \times 10^{-4}$ GeV^2, making the Coulomb-Nuclear Interference (CNI) region accessible. For $\beta^* = 90$ m, the t range accessible is reduced to $-t \geq 10^{-2}$ GeV^2.

3.8 Trigger and Data Acquisition

For proton-proton collisions with a centre of mass energy of 14 TeV, the total pp interaction rate seen in ATLAS at the design luminosity of $\mathcal{L} = 10^{34}$ cm^{-2} s^{-1} is approximately 1 GHz. More relevant to the actual recording of data is the bunch crossing rate of 40 MHz as events are produced in bunch crossings at this frequency. Data handling is one of the most important problems for all of the LHC experiments. For ATLAS, if all data channels are recorded per event, the raw data rate is around 40 TB/s. However, due to resource limitations, the event storage rate is limited to between 200-400 Hz, with events averaging 1.5 MB in size. The ATLAS trigger system [43], divided into three levels as shown in Figure 3.13, is responsible for reducing this rate whilst keeping events which contain physics processes of interest.

3.8.1 Architecture

The trigger dictates the physics reach of the experiment. A flexible trigger menu is used in ATLAS to allow different types of data to be selected for further analysis. The emphasis is on high p_{T} signatures, covering selected Standard Model physics and all discovery physics that ATLAS plans to study.

The decision at each trigger level is based on the fulfilment of requirements imposed on

[3] $\beta(z)$ is a function related to the transverse size of the particle beam at a location z along the beam trajectory. The value of $\beta(z)$ at an interaction point (where the beam should be most focussed) is referred to as β^*, with $\beta(z) = \beta^* + z^2/\beta^*$.

[4] t is a Mandelstam variable equal to the squared four-momentum transfer between the colliding particles.

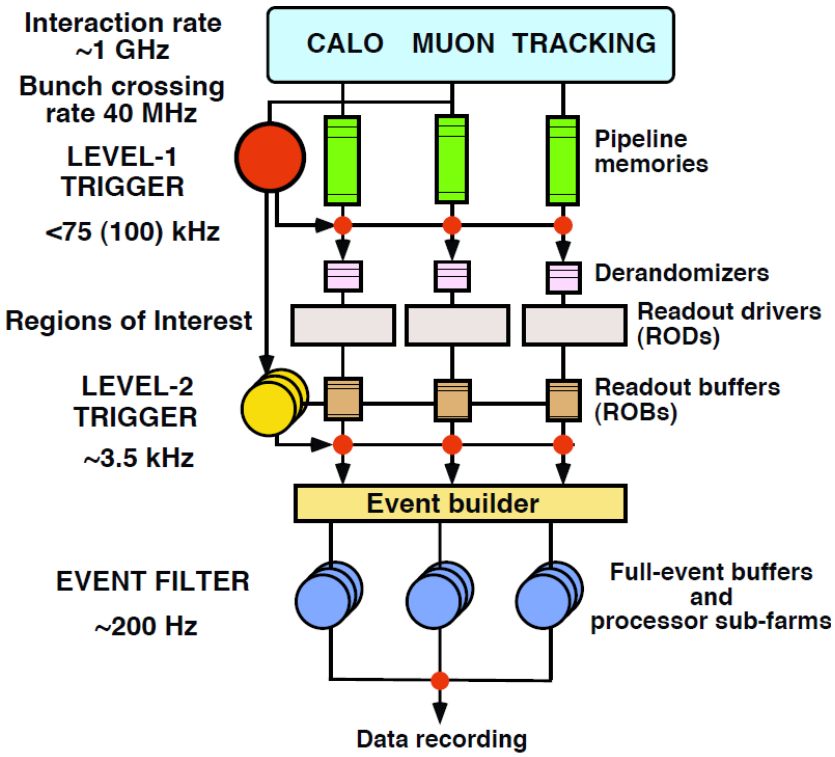

Figure 3.13: Block diagram of the 3-level ATLAS trigger. For each level, the level to which the event rates can be reduced is shown, according to design specifications [43].

event properties e.g. the minimum energy in a calorimeter, a certain number of tracks in tracking chambers or a muon above a defined p_{T} threshold. These pieces of trigger logic are called trigger elements. Within one level the trigger elements are combined into logical expressions (using AND, OR, etc.) called trigger items.

At each level an event is accepted if it fulfils at least one trigger item. The rate of events collected by a trigger item can be scaled down by a prescale factor p, such that on average only every p^{th} selected event is kept by the system. In the three-level system, individual trigger items from several levels are further combined into chains. Events fulfilling all trigger items within a chain are finally accepted by the trigger system.

3.8.2 First Level Trigger

The hardware based Level-1 (L1) Trigger consists of the Level-1 Calorimeter Trigger (L1Calo) and Level-1 Muon Trigger (L1Muon). It also accounts for activity in the forward detectors such as MBTS, ZDC, LUCID and ALFA.

Using purpose built electronics which receive a small subset of all the detector information, the L1Calo and L1Muon triggers search for signatures from high-p_{T} muons, electrons and photons, jets and τ-leptons. They also select events with large $E_{\mathrm{T}}^{\mathrm{miss}}$ and ΣE_{T} using reduced granularity information. In an event, if one of these signatures is found and successfully passes the L1 trigger selection, a Region of Interest (RoI) is sent to the High Level Trigger (HLT) with details of the location of the object in η-ϕ and the type of signature to expect.

The data from the different sub-detectors are stored in data pipelines to be read out to the data acquisition systems once an event is accepted by the L1 trigger. The maximum L1 accept rate which the detector readout systems can handle is 75 kHz, which is limited by their bandwidth. The L1 latency, defined as the time from the pp collision taking place to the trigger decision being available to the front-end electronics, is designed to be less than 2.5 μs after the bunch crossing with which it is associated.

3.8.3 Higher Level Trigger

The HLT consists of two parts. These are the Level-2 Trigger (L2) followed by the Event Filter (EF). Both levels use software based selection algorithms run on computer farms.

The L2 trigger is seeded by RoI objects created by L1 and is optimised to look near to those regions but this time with the full granularity of the detector, to search for objects of interest. L2 processes a single event in 40 ms in order to reduce the rate to 3.5 kHz.

The EF uses the full detector information available after the event building stage as well as algorithms used for off-line reconstruction to reduce the final data-taking rate to approximately 200 Hz. Selection and classification of events in the EF takes 3-4 seconds.

3.9 Data Streaming and Formats

All events passing the HLT are written to permanent storage. Depending on what type of trigger was passed, the data are put into physics streams for specific types of physics

analysis e.g. events passing Minimum Bias trigger selections go into the $MinBias$ stream, events passing the electron or photon selections go into the $Egamma$ stream and events triggering on jets go into the $JetTauEtmiss$ stream. There are also other streams for data checking and calibration as shown in Figure 3.14.

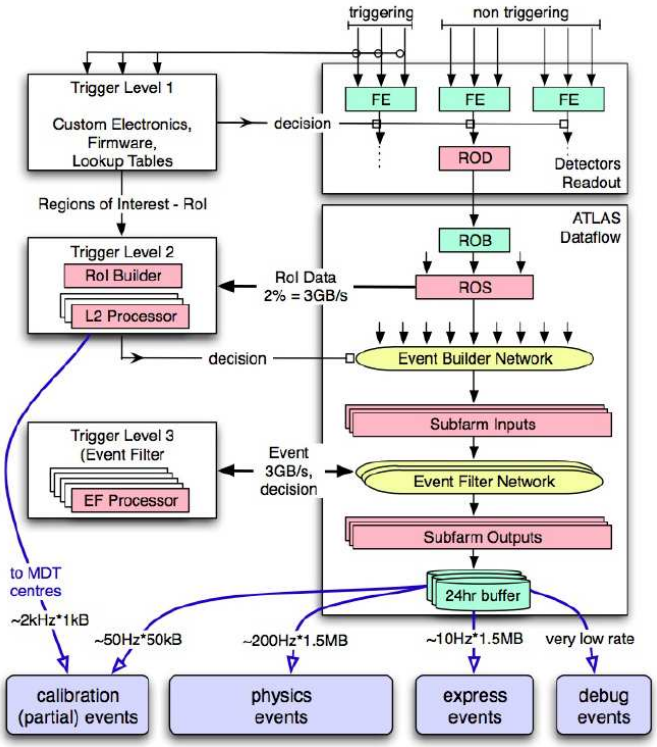

Figure 3.14: Schematic diagram of the trigger and data acquisition systems. On the left hand side the data processing components are shown and on the right hand side the data acquisition components, resulting in different calibration and physics data streams [44].

The ATLAS experiment has adopted the inclusive streaming model, so an event passing the criteria of multiple trigger items may be directed to several streams but the overlap been streams needs to be kept low. There are also special streams used for prompt reconstruction and monitoring of the data and error checking.

CHAPTER 4

The ATLAS Level-1 Calorimeter Trigger and Central Trigger Processor

The Level-1 Calorimeter Trigger [45] (L1Calo) and Central Trigger Processor [46] (CTP) are two of the key components of the ATLAS Level-1 Trigger. In this chapter, the L1Calo components and algorithms for identifying physics objects are discussed in more detail along with how the CTP makes the overall L1 decision.

4.1 Level-1 Calorimeter Trigger System Architecture

L1Calo is a fixed latency, pipelined processor system using bespoke custom built hardware. The calorimeters contain over 200,000 channels, too many to have them all processed at the LHC BC frequency. Therefore, the calorimeter signals are summed within the calorimeter front-end electronics to provide reduced granularity information with which to identify electrons, photons, τ-leptons and jets as well as sums of total and missing energy. Schematics of the electronics that perform the summing of the calorimeter signals

are shown in Figure 4.1.

The L1Calo electronics are located off the detector in a separate electronics cavern called USA15. For L1Calo, the analogue signals are received from the calorimeters via individually shielded 16-way twisted-pair cables with an average length of 50 m. With the signals having to pass through several stages from the calorimeter front-ends including amplifiers, receivers, being transmitted along cables and then going through the L1Calo electronics, the different contributions can add up to 500 MeV per channel of RMS noise to the analogue signals.

The architecture of L1Calo is shown in Figure 4.2. Including the time for the transmission of data, L1Calo can make a decision with a latency of about 2.1 μs. Extensive work has been undertaken to make sure the results from the stage of having digital signals through to producing a final L1 decision agree between off-line simulations and the hardware [48].

4.2 Pre-processor

The analogue signals, summed over calorimeter cells, are collected by the receivers and then passed into the first stage of L1Calo, the Pre-processor system (PPr). The PPr has a number of roles including providing inputs of E_{T} sums to the Cluster Processor (CP, see Section 4.3) and Jet/Energy Processor (JEP, see Section 4.4) Systems for object identification, identifying the LHC bunch crossing from which a signal originates and providing readout to the ATLAS Data Acquisition systems if it is decided that there is something interesting in the event.

The PPr receives 7168 analogue signals, known as Trigger Towers (TTs). Half of these are from the electromagnetic (EM) calorimeters and half are from the hadronic (HAD) calorimeters (including the FCAL). The towers are processed in groups by modules known as Pre-processor Modules (PPMs). Figure 4.3 shows the coverage in η and ϕ for a single EM quadrant in ϕ. For $|\eta| < 2.4$, each trigger tower is 0.1×0.1 in $\eta \times \phi$ and each PPM processes 64 TTs. For $|\eta| > 2.4$, the TTs have coarser granularity and so fewer PPMs are required to cover the granularity. For $2.4 < |\eta| < 2.9$, only half of the channels on the

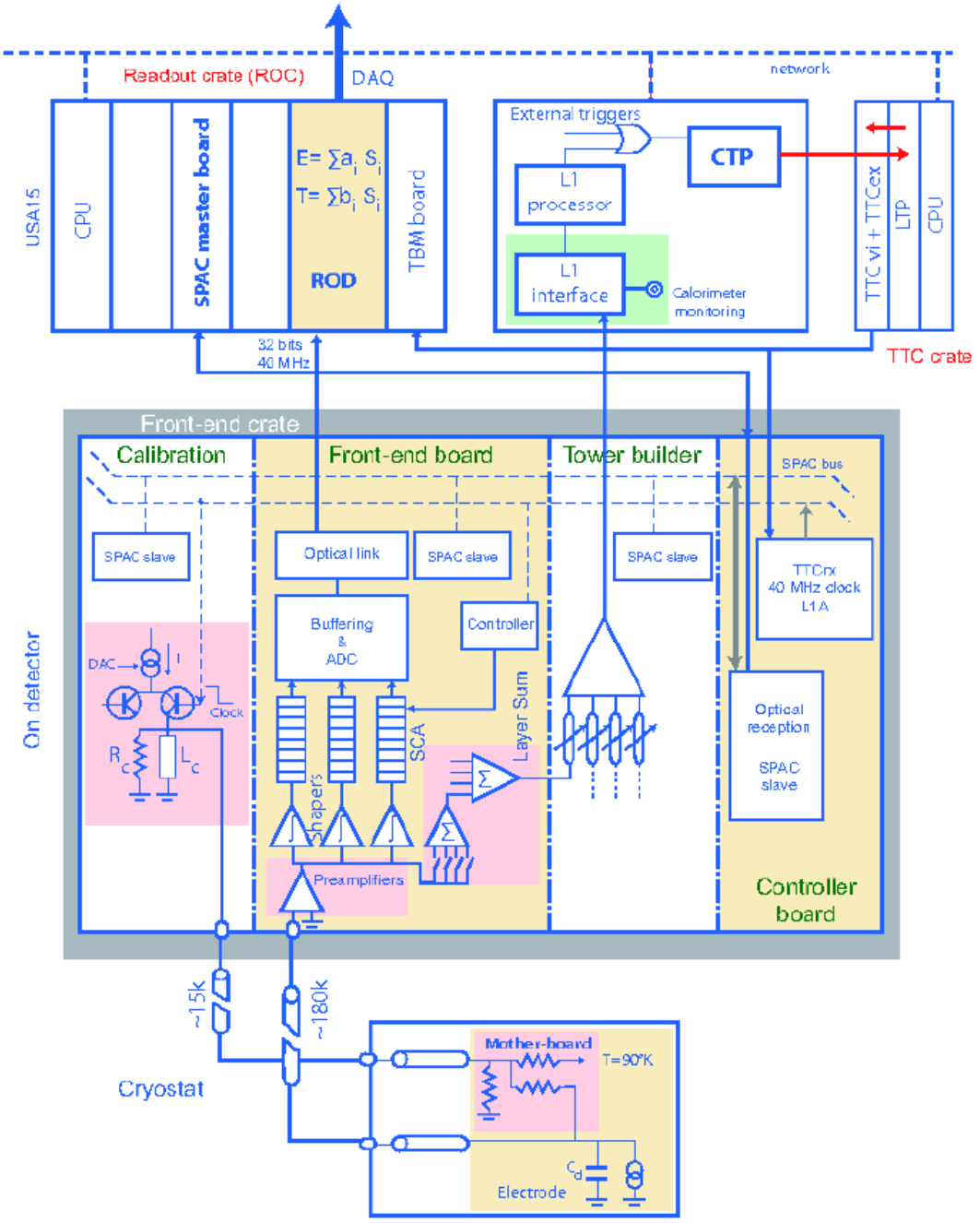

Figure 4.1: Schematic illustration of the electronics associated with the ATLAS Liquid Argon calorimeters. The lower box depicts the calorimeters installed in their respective cryostats. The central box illustrates the functionality of the calibration, front-end, controller and tower builder boards located in front-end crates on the detector. The upper box shows the off-detector back-end electronics mounted in Readout crates, as well as trigger and control crates [47].

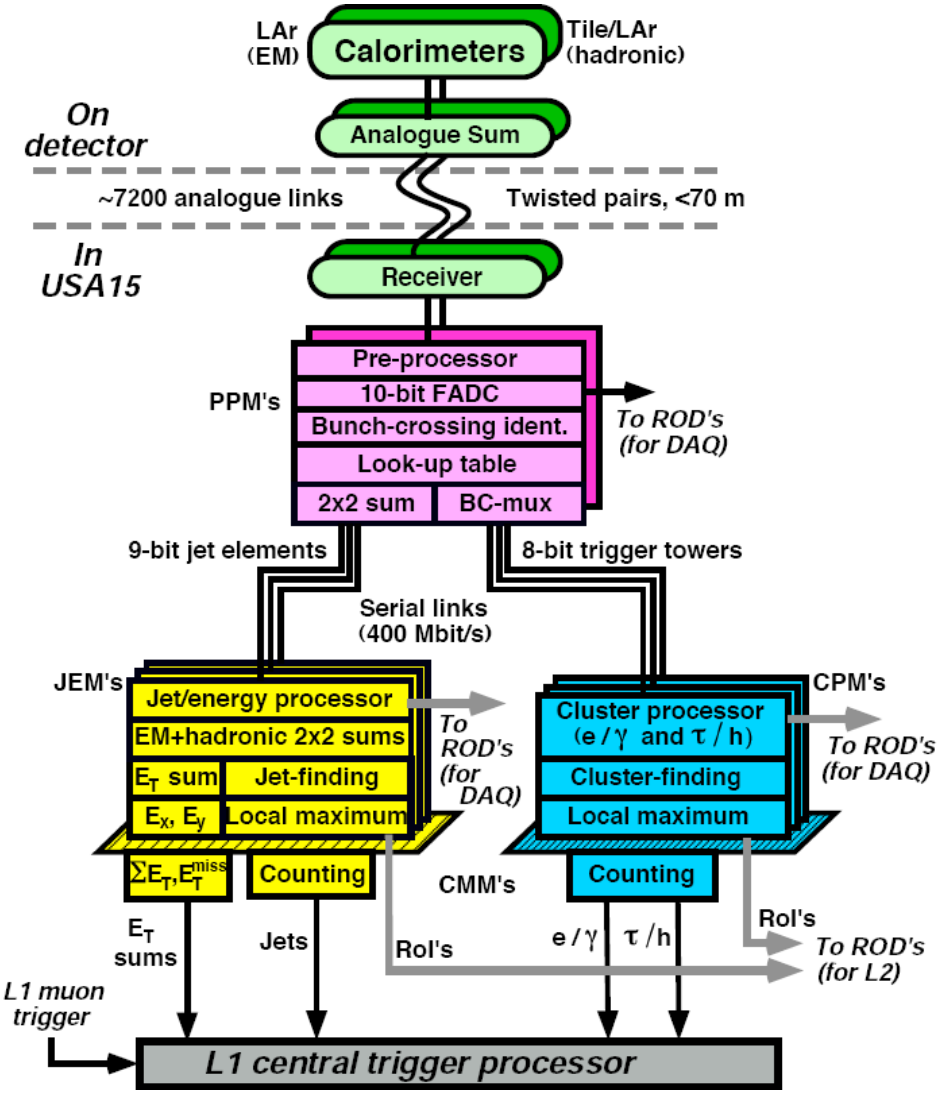

Figure 4.2: Architecture of the Level-1 Calorimeter Trigger. Analogue data from the calorimeters are digitised and associated with the correct bunch-crossing in the Pre-processor and then sent to two algorithmic processors, the Jet/Energy Processor and the Cluster Processor. The resulting hit counts and energy sums are sent to the Central Trigger Processor. [45]

PPM are used and for $2.9 < |\eta| < 3.2$, one PPM covers two quadrants.

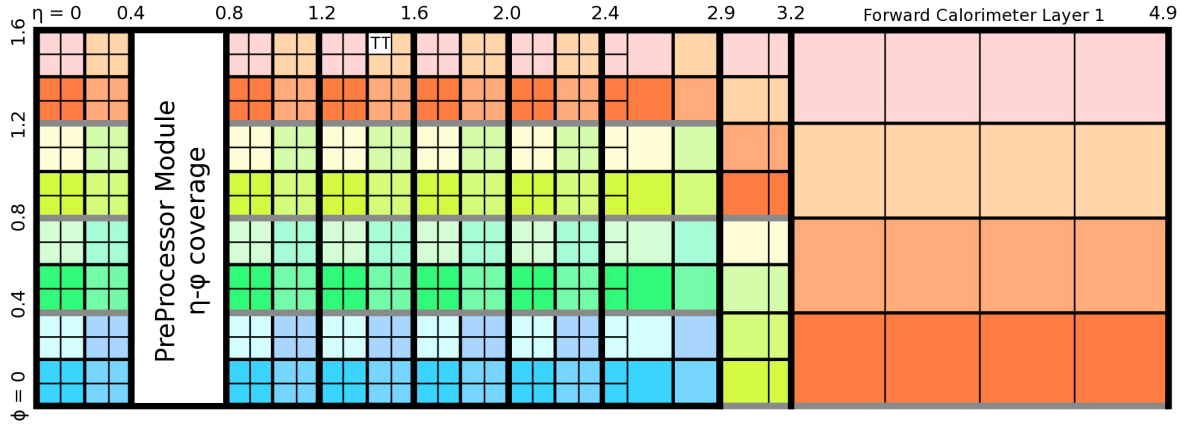

Figure 4.3: Trigger tower distribution in η and ϕ within one quadrant of the Electromagnetic Calorimeter. The areas covered by each PPM and Trigger Tower (TT) are shown. TTs, grouped in 4, of the same colour are summed by a single Multi-Chip Module (MCM) to form a single jet element. In the range $2.9 < |\eta| < 3.2$ only half of a PPM gets used and for $3.2 < |\eta| < 4.9$ only quarter of a PPM is used per quadrant as the granularity gets reduced. [49]

In the FCAL, in the range $3.2 < |\eta| < 4.9$, only one PPM is necessary to cover all four quadrants in ϕ. In this region, the different layers of the FCAL send separate signals, with the innermost layer, FCAL1, represented as EM trigger towers of size 0.4×0.4 in $\eta \times \phi$. The latter regions, FCAL2 and FCAL3, are seen as HAD TTs with coarser granularity and so they are approximately of size 0.8×0.4.

Examples of TT signals from the LAr and Tile calorimeters are shown in Figure 4.4. The shaped pulses from the calorimeters extend over several bunch-crossings. The signals have peaks which are proportional to the total E_{T} within the tower. The Tile signals are made of a single peak (unipolar) and the LAr signals are made of half waves (bipolar), with the first half having a sharp peak and the second half being a negative shallow trough of equal area. In both cases the peak is the part used for triggering. These pulses are digitised by using flash analogue-to-digital converters (FADCs) with 10-bit precision. This corresponds to turning the signals into E_{T} values in steps of approximately 250 MeV per FADC count, between 0 and 255 GeV.

As the pulses span multiple bunch-crossings, it is important to determine which pulses correspond to the signal being analysed. This is known as Bunch Cross Identification (BCID). There are three types of BCID used by the PPM, one using an external signal

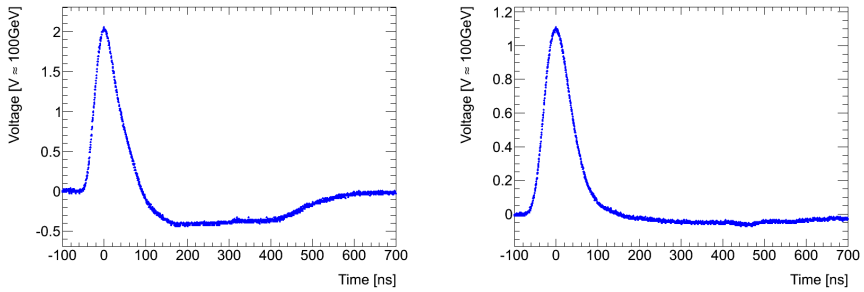

(a) (b)

Figure 4.4: Example Trigger Tower signals arriving at the PreProcessor Module from the (a) Liquid Argon EM calorimeter layer and (b) Tile Hadronic calorimeter layer. [49]

and two based on algorithms applied to the signals seen in the TTs.

The Peak-Finder BCID method applies a Finite Impulse Response (FIR) Filter to the 10-bit values. The FIR Filter, as shown in Figure 4.5, takes five analogue-to-digital converter (ADC) values, d_i, for each BC as well as for the two previous and two following BCs. Five coefficients, a_i are applied to these values as

$$f = \sum_{i=1}^{5} a_i d_i \tag{4.1}$$

to determine the resultant FIR output, f, for each BC. The coefficients a_i are tuned to optimise the signal-to-noise ratio, per TT, by being proportional to the signal heights for expected pulse shapes in the LAr, Tile and FCAL calorimeters, assuming non-correlated white Gaussian noise. To determine the correct BC, this output must pass the condition, $f_{-1} \leq f_0 < f_{+1}$, where f_0 is the FIR output for the current BC, f_{+1} is for the next BC, and f_{-1} from the previous BC. The BCID efficiency using the FIR filter reaches 100% for towers with $E_{\mathrm{T}} > 3$ GeV.

If the incoming values, d_i, reach the 10-bit maximum limit, equivalent to 255 GeV, then the Saturated BCID algorithm determines which BCID the pulses belong to based on the rest of the signal peak shape. Regardless of the BCID method used, if the signals correspond to the correct BC then the transverse energies from the trigger towers are sent in parallel as inputs to the Cluster Processor and Jet/Energy Processor. The processing of individual TTs is done independently so that the energy of a TT in the identified BC is sent onwards.

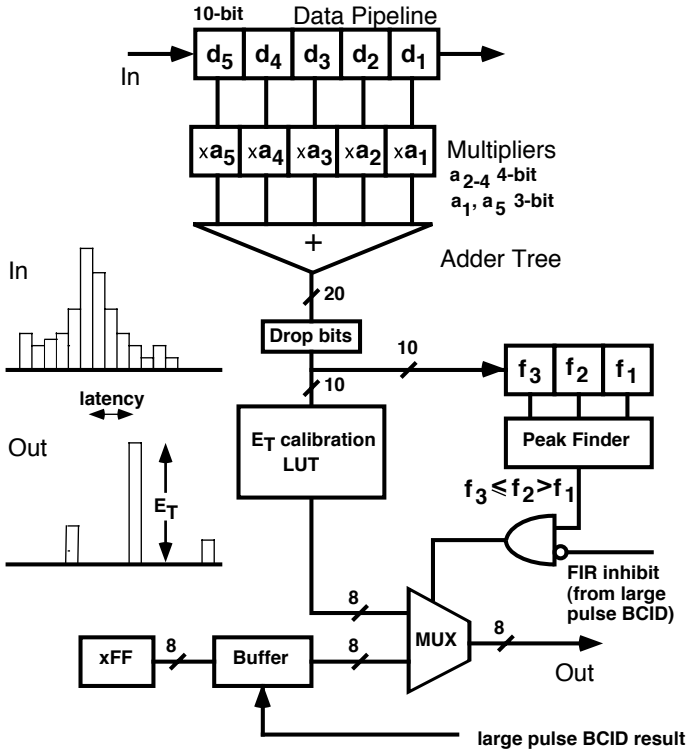

Figure 4.5: Finite Impulse Response Filter used for bunch crossing identification. A typical input pulse and its resulting output are shown. [45]

4.3 Cluster Processor

The Cluster Processor uses four crates of electronics, each crate handling one quadrant of the calorimeter system in ϕ and containing 14 Cluster Processor Modules (CPMs). This can be seen in Figure 4.6. The CP system identifies electron/photon and hadron (e.g. jets or hadronically decaying τ-leptons) candidates. The calorimeter data covers the range $|\eta| < 2.5$ from which there are precision data from the EM calorimeter and Inner Detector. Each CPM covers a core set of 16×4 towers ($\phi \times \eta$) and the CPMs also share data in order to provide full coverage of trigger towers for the cluster finding algorithm.

4.3.1 Algorithm for Cluster Finding

The Cluster Processor algorithm, illustrated in Figure 4.7, is based on a window of 4×4 trigger towers in both the electromagnetic and hadronic calorimeters. The algorithm identifies 2×2 clusters of nearest neighbour trigger towers that are local transverse energy

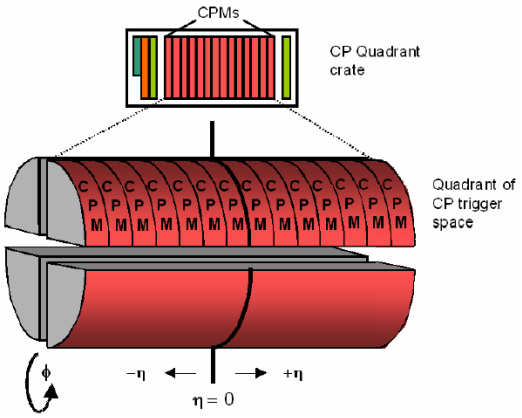

Figure 4.6: Layout of one crate of Cluster Processor Modules, covering one quadrant in ϕ. [45]

(E_{T}) maxima for all possible 4×4 windows.

Within the EM trigger towers, any of the four possible 1×2 or 2×1 component sums in a window that exceeds a predefined energy threshold is known as the EM cluster. The hadronic trigger towers directly behind the EM 2×2 window are known as the hadronic inner core, which in the selection of electrons and photons can be used to check for hadronic leakage. For τ-leptons and hadrons, the EM cluster and hadronic inner core combine to produce a HAD cluster. The twelve EM towers surrounding the EM 2×2 central window are known as the EM isolation ring and the 12 hadronic towers behind this ring are known as the HAD isolation ring. Energy deposits in these regions around a cluster may be used to distinguish between isolated electron/photon candidates and hadrons.

For a candidate object to satisfy the cluster finding, it must satisfy the following criteria:

- For electron and photon candidates, the EM cluster must have an E_{T} greater than the electromagnetic threshold under consideration. For τ/hadron candidates, the HAD cluster (τ/hadron) must have an E_{T} greater than the hadronic threshold.
- The E_{T} in the EM isolation ring must be less than the electromagnetic isolation threshold.
- The E_{T} in the HAD isolation ring must be less than the hadronic isolation threshold.
- For EM clusters, the total E_{T} in the hadronic inner core must be less than a thresh-

old.

If these requirements are passed, a Region of Interest (RoI) corresponding to a electron, photon or τ candidate is produced, known as an EmTau RoI.

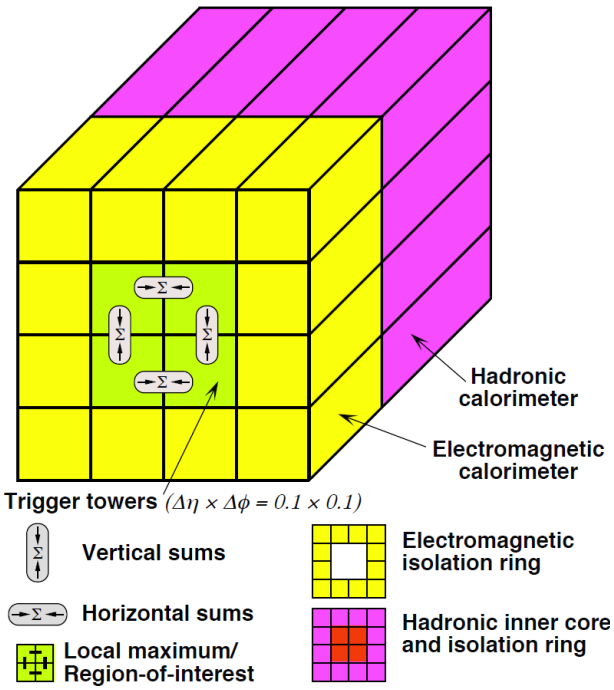

Figure 4.7: Trigger tower selection for the Cluster Processor algorithm. [50]

4.3.2 Electromagnetic Trigger Thresholds

For EmTau RoIs, 16 trigger thresholds are implemented in the hardware with 8 being exclusively for L1 electromagnetic trigger thresholds and the remainder being used either for L1 electromagnetic or hadronic trigger thresholds. This means that a CPM can identify 16 independent cluster types for the trigger towers it has access to. Up to the end of 2011, these were split equally with 8 EM thresholds and 8 L1 HAD thresholds in the data. In 2012, this changed to 9 EM thresholds and 7 HAD thresholds. If an EmTau RoI is produced, it will indicate which of the 16 trigger thresholds are passed and provide the location on the CPM. To reduce the information sent, the transverse energy of the EmTau RoI is not sent any further.

An example EM trigger threshold is L1_EM10. This threshold requires that an EmTau

RoI is produced with a transverse EM energy greater than 10 counts, where 1 count is approximately 1 GeV, and there are no isolation requirements. An electron or photon candidate would require approximately $E_{\mathrm{T}} \geq 11$ GeV to create this RoI. An example of an EM trigger threshold with isolation is L1_EM10I. For this threshold, as well as asking that the EmTau RoI had an EM E_{T} greater than 10 counts, the E_{T} in the electromagnetic isolation ring has to be less than 4 GeV, that in the hadronic isolation ring less than 3 GeV and there must be less than 2 GeV in the hadronic core.

From 2011, these thresholds were replaced by new isolation requirements on the hadronic calorimeter and core rather than the electromagnetic isolation ring in order to trigger on electron and photon candidates without additional hadronic activity nearby. L1_EM10VH as an example would have a cut on the hadronic core E_{T} less than or equal to 1 GeV. The 'V' part of the trigger threshold provides a varied threshold as a function of η for different towers, in order to provide coarse dead-material corrections, accounting for differences across the detector. Table 4.1 shows how the threshold on the EM cluster E_{T} varies in steps of $|\eta| = 0.4$. The 'H' part puts a cut on the hadronic core $E_{\mathrm{T}} \leq 1$ GeV, effectively placing a hadronic leakage requirement on candidates[1].

$\lvert\eta\rvert$ range	EM10VH Threshold	EM16VH Threshold
$\lvert\eta\rvert \leq 0.4$	11	18
$0.4 < \lvert\eta\rvert \leq 0.8$	11	18
$0.8 < \lvert\eta\rvert \leq 1.2$	10	17
$1.2 < \lvert\eta\rvert \leq 1.6$	10	16
$1.6 < \lvert\eta\rvert \leq 2.0$	10	17
$2.0 < \lvert\eta\rvert \leq 2.4$	11	18
$2.4 < \lvert\eta\rvert \leq 2.5$	10	18

Table 4.1: Variation in η of the threshold E_{T} counts necessary for the EM cluster to produce an EmTau RoI as used for L1_EM10VH and L1_EM16VH trigger thresholds in 2011 data. [51]

Each CPM determines the number of objects passing each trigger threshold for the trigger towers it is able to access and then sends these results, in real-time, to the Common Merger Module (CMM), still located within the L1Calo electronics. The CMM produces an event level result to send to the CTP, while RoIs are sent to L2 for further processing, provided

[1] At L2 and EF the software is designed to work with calorimeter cells rather than trigger towers, meaning HLT triggers seeded by L1 thresholds with a hadronic veto have a cut applied on the total transverse energy of the electron/photon candidate leaking out into the hadronic calorimeters, as there is no direct equivalent of a hadronic core.

the CTP accepts the event for further study.

4.4 Jet Energy Processor

The Jet/Energy Processor (JEP) has to handle the full set of calorimeter input signals and analyse them very quickly. To do this, the JEP contains two crates that split the calorimeter systems into four quadrants, with each JEP crate handling the opposite quadrants in ϕ. Each quadrant is analysed by 8 Jet/Energy Modules (JEMs).

The JEP system uses jet elements, as shown in Figure 4.3, with 0.2×0.2 in $\eta \times \phi$ up to $|\eta| = 3.2$, becoming coarser in the FCAL. Each JEM receives the jet elements, summed up from both the electromagnetic and hadronic calorimeters, using dedicated Input Processor FPGAs. These Input Processors allow the JEMs to share data across JEM boundaries in order to find jets (Section 4.4.1). Accounting for the overlapping, each JEM processes 11×7 jet elements in η-ϕ.

For the jet elements that do not get duplicated across JEM boundaries, each JEM calculates sums of E_{T} and also determines the E_x and E_y components of this based on the η and ϕ of jet elements for the missing energy calculation. The three energy values from each JEM are sent to a CMM, dedicated to merging jet information and energy sums only, to form the final $E_{\mathrm{T}}^{\mathrm{miss}}$ and ΣE_{T} quantities to send on to the CTP.

4.4.1 Algorithm for Jet Finding

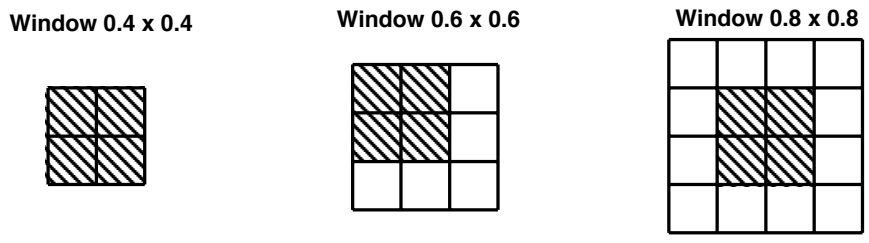

Figure 4.8: Sliding window algorithm for jet identification using either a 2×2, 3×3 or 4×4 jet window. A Region of Interest for the candidate jet is selected based on the central 2×2 set of jet elements (a jet element has a granularity of $\Delta\eta \times \Delta\phi = 0.2 \times 0.2$). [50]

The jet algorithm identifies clusters of energy deposition within overlapping windows of 2×2, 3×3 or 4×4 jet elements, as shown in Figure 4.8. The segmented jet elements cover the region $|\eta| < 3.2$, which is the acceptance limit of the hadronic end-caps. In the forward calorimeters (FCAL), the full η range $3.2 < |\eta| < 4.9$ is treated as a single jet element. Jet Regions of Interest (Jet RoIs) are determined by sliding the jet window in steps of 0.2 in the η and ϕ directions (equivalent to moving across by one jet element) to locate local maxima in regions of 2×2 jet elements. The programmable window size is then used to measure the E_{T} of the jet and if this exceeds a predefined threshold a Jet RoI is created.

Hadronic showers leave energy deposits in both the electromagnetic and hadronic calorimeters. Therefore, the algorithm for jets uses both the 2×2 central HAD tower energies and EM towers directly above them in order to see if the HAD energy threshold was exceeded. As a consequence, an electron or photon with sufficient E_{T}, which may have triggered by the CP, is also triggered as a jet.

4.4.2 Jet Trigger Thresholds

The jet trigger thresholds are far simpler than their electromagnetic counterparts in that they only have a requirement on exceeding an energy threshold, that depends on the size of the window, with no additional isolation requirements. Example jet trigger thresholds are L1_J10 and L1_FJ10. They require that a Jet RoI is produced with a transverse energy greater than 10 counts, in the central detector and forward detector, respectively.

Since the start of running in 2009 there have been 8 L1 jet trigger thresholds in the trigger menu and 4 L1 forward jet trigger thresholds. The majority of the time the window size is 4×4 jet elements. On each JEM, the numbers of jets above the different programmable E_{T} thresholds are sent to a Common Merger Module (CMM) to determine jet multiplicities and energy sums to be sent to the CTP.

4.5 Central Trigger Processor

The CTP consists of a a number of different modules including those for timing, data input and output, bunch monitoring and trigger formation and read-out.

The CP and JEP system information is merged and summarised in terms of the number of identified objects observed passing the different trigger thresholds, in their respective CMMs, for each bunch-crossing. The results from L1Calo, as well as from L1Muon and the L1 minimum bias triggers, are sent to the Central Trigger Processor (CTP) to make a final decision for the whole of the Level-1 Trigger. In addition to the trigger inputs from the L1 triggers, the CTP also includes two random triggers, L1_RDO (high rate) and L1_RD1 (low rate). The CTP has to synchronise the inputs from different sources so that all of the trigger decisions, and the processing performed on the data, all belong to the same BC.

The BCs are organised in bunch groups by the CTP. The bunch group definition is programmable and adapted to the actual bunch pattern of each LHC fill. The purpose of the bunch group is to characterise the proton bunches; the CTP combines them with the trigger signal to define specific trigger requirements, such as colliding bunches for physics signals, or single beam bunches for non-collision background studies. There are eight different bunch group conditions, of which the main four conditions are:

- Paired (Filled) - both LHC beams in the same BC contain a bunch of protons.
- Unpaired isolated - a bunch in only one LHC beam with no bunch in the other beam within 3 BCs.
- Unpaired non-isolated - a bunch in only one LHC beam with a nearby (within 3 BCs) bunch in the other beam.
- Empty - no proton bunches in either beam within a BC.

The CTP implements a trigger menu based on logical combinations of results from L1Calo and L1Muon, the MBTS triggers, other forward detectors and bunch group information. This means that each of the thresholds programmed into the L1Calo hardware e.g.

L1_EM3 exist as trigger items within the menu that are checked to see if they have passed. The trigger menu also allows coincidences of triggers (and/or of trigger combinations). The number of items in the menu are limited to 256 by the hardware.

Prescales are applied to each trigger item by the CTP (this is also performed in both HLT levels by trigger chains seeded on L1 trigger items) such that for a trigger item with a prescale p, the prescaled item will pass 1 in every p events that it triggered. After prescaling individual trigger elements, in order to make efficient use of the allowable bandwidth as the luminosity and background conditions change, if there are still trigger items that have passed in the BC a Level 1 Accept (L1A) is produced and sent out to the different sub-detectors.

For each sub-detector the raw event data are stored in digital pipelines as the trigger decisions are taking place. The digital pipeline length allows for 100 BCs worth of data to be stored. The Read Out Drivers (RODs) on each sub-detector receive the L1A and get the data stored in the pipeline memories to the Read Out Buffers (ROBs). This data plus the event level information from the CTP, L1Muon and L1Calo (PP, CP, JEP) are sent to the Read Out System (ROS) to be made accessible to the HLT.

The RoI data from L1Calo and L1Muon are sent to the Region of Interest builder (RoIB) of the Level-2 trigger system, which the L2 trigger algorithms use to investigate trigger objects with more accuracy. This is used for electron, photon and muon searches. It is also done for jets but during 2011, the L2 jet trigger was redesigned in order to improve the efficiency of the L1 jet sliding window algorithm for jets produced from the splitting and merging of existing jets. This is achieved by running the same jet finding algorithms as used by the Event Filter (EF) and offline reconstruction (see Chapter 5) directly over the trigger towers rather than all calorimeter cells.

4.5.1 Dead-time

During the time that the detector is busy reading out the information from an event in the detector to the ROBs, it is unable to process any other events that take place in the detector regardless of whether they contain physics of interest or not. Preventative

dead-time is built into the CTP in order to limit the frequency of L1As to a rate that the sub-detector front-end electronics can support.

There are two types of dead-time that the CTP uses: simple and complex. For the simple dead-time, there are a programmable number of bunch crossings after each L1A for which there can be no new L1A. The complex dead-time is based on a 'leaky bucket' model, with L1As filling the bucket with events that then leak out at a fixed rate. When the bucket is full, no further L1A can be generated thus representing dead-time. Using the definitions that the bucket size (buffer) is X, in units of L1A, and the time to leak an L1A being R, in BC, then the average trigger rate is limited to X triggers in a time period of $X \times R$ bunch crossings. Typical ATLAS dead-time settings in 2010 were 5 BC (simple) and $X = 7$, $R = 415$ BC (complex) [52] but these numbers were changed with luminosity. In addition to the prescale stored for each trigger item, there is also a priority level stored as either high or low to allow higher or lower priority triggered events to pass through the bucket.

CHAPTER 5

Electron, Photon and Jet Reconstruction in ATLAS Software

Excellent particle reconstruction and identification is required at LHC. Therefore, the reconstruction of electrons, photons and jets at the event building stage requires sophisticated algorithms within software to be applied to the signals received from the calorimeters and the inner detector.

5.1 ATHENA Framework

To simulate and reconstruct events from Monte Carlo and reconstruct collision events from data in ATLAS needs many software applications, all provided under a common software framework known as ATHENA (ATlas realization of a High Energy and Nuclear physics data analysis Architecture) [53]. ATHENA is an implementation of GAUDI [54], a software framework for High Energy Physics, and uses a collection of algorithms to perform specific tasks, e.g. track reconstruction. The algorithms make use of code to perform the tasks, acting on detector components and particles that are represented as

data objects in C++.

Monte Carlo events are necessary to determine the expected detector response to various physics process and to test the ability to reconstruct individual particles. This is done in several steps - event generation, detector simulation, digitisation and reconstruction.

Event generation involves simulating an underlying physics processes from a proton-proton collision designed to replicate the LHC running conditions. Event generators simulate the particles produced in a collision, expressing the energy, momentum and mass of the outgoing stable leptons, photons and hadrons as four-vectors.

The detector simulation is created using GEANT4 [55] and includes a detailed model of the detector geometry and materials used by the different sub-detectors and services. This takes the input of the generated particles, recreating how they would interact with the detector. This is updated regularly to better reproduce particle responses in ATLAS.

Digitisation involves simulating the response of the detector electronics to the analogue signals. The simulated detector response here will register the appropriate hits and signals expected from particles passing through various parts of the detector. The output of the simulation is designed to be identical in format to real data at the end.

Reconstruction takes the detector hits, either from simulated or real data, and applies many software algorithms to them in order to identify different particles within an event based on reconstructing vertices, tracks, calorimeter deposits and muon chamber activity. The reconstruction makes use of calibration constants, stored in various conditions databases, for all of the detectors in order to convert the hits into momentum, energy and position values.

5.2 Track and Vertex Reconstruction

Proton-proton collisions happen in ATLAS in a small region around the nominal interaction point at the centre of detector. This region is known as the beam spot and can be described by Gaussians in the R-z plane (with $\sigma_z \sim 50$ mm and $\sigma_R \sim 20$ μm).

Track reconstruction, from particles originating from the collisions, can be done with a number of algorithms, with the typical approach being to start from the Pixel hits and SCT space points and work outwards to the TRT, using a Kalman-fitter/smoother to determine the trajectory [56]. The resulting tracks are parametrised in terms of key parameters, as shown in Figure 5.1.

- q/p_T: inverse transverse momentum, multiplied by the charge of the particle,
- d_0: transverse impact parameter, the (signed) distance of closest approach to the beam line in the x-y plane,
- z_0: longitudinal beam parameter (value of z of the point on the track that determines d_0),
- ϕ_0: the angle relative to the x-axis at the distance of closest approach to the beam line in the x-y plane,
- θ_0: the angle in the R-z plane of the track relative to the z-axis.

In 2010, tracks could be reconstructed with $p_T > 100$ GeV. This increased to $p_T > 400$ GeV in 2011 and $p_T > 500$ GeV in 2012 in order to reduce the amount of data output per event.

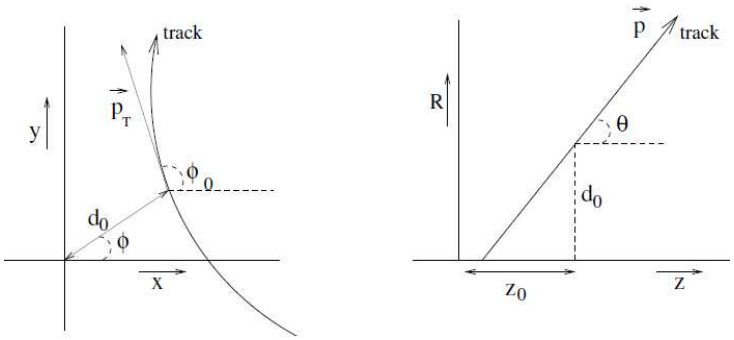

Figure 5.1: Track parametrisation [57].

Vertices are reconstructed using an iterative vertex finding algorithm [56]. This makes vertex seeds based on the z_0 positions of the reconstructed tracks. A χ^2 fit is performed by iterating over nearby tracks and trying to match them to seeds. Tracks displaced by

more than 7σ from existing seeds are then used to produce new seeds for vertices, and the process is repeated until all of the reconstructed tracks are matched to a seed. A vertex needs to have two intersecting tracks associated to it and the vertex positions are constrained by the beam spot location.

The primary vertex in an event is the point of intersection of the most reconstructed tracks, and determines the location of the collision. A primary vertex can be reconstructed from as few as two intersecting tracks but typically this number is around 20-30. It is also possible to have no reconstructed primary vertex in a physics event. If a hadron containing a heavy quark is involved in an event, it will decay at a finite distance from the beam line, characterised by a larger d_0, away from the primary vertex interaction. Tracks intersecting away from the beam line are used to reconstruct secondary vertices.

5.3 Electron and Photon Reconstruction

The ATLAS electron/photon reconstruction and identification algorithm [58] is designed to provide various levels of background rejection optimized to provide high identification efficiencies for calorimeter energy deposits with $E_{\mathrm{T}} > 20$ GeV, over the full acceptance of the inner detector system ($|\eta| < 2.5$).

The process of reconstruction can be split into three steps. This first step involves finding energy deposits in the calorimeter to seed cluster production. This is followed by reconstructing tracks and matching them to the cluster seeds and finally reconstructing full clusters from the seeds.

The cells in the EM barrel and end-caps are projected onto a fixed grid of 0.025×0.025 in $\Delta\eta \times \Delta\phi$, based on the granularity of the second layer of the EM calorimeter, in which the energies of all of the cells are summed to create the tower energies. A sliding window (SW) of size 0.075×0.125 is moved about the grid and the sum of the transverse energy is calculated within it. If $\Sigma E_{\mathrm{T}} > 2.5$ GeV within a window then a pre-cluster is formed at this point. The 2.5 GeV threshold is chosen to select the optimum number of pre-clusters while removing fakes produced due to noise and pile-up.

To determine whether the SW clusters originate from electrons or photons requires the use of the inner detector. Tracks with $p_{\mathrm{T}} > 0.5$ GeV are matched with $\Delta\eta < 0.05$ and $\Delta\phi < 0.10$ from the extrapolated position in η and ϕ to the barycentre of the cluster in the second layer of the EM calorimeter. If there is a matched track then the cluster is classified as an electron. If no tracks are matched then the cluster is classified as an unconverted photon candidate unless a reconstructed conversion vertex, where the photon splits into two electrons, can be matched instead and the cluster is classified as a conversion photon candidate. Conversion vertices are measured with high efficiency in the inner detector provided the conversion vertex radius is less than 800 mm from the beam pipe. ATLAS also reconstructs 'single-track' conversions in which only one track gets reconstructed and there is no hit in the B-layer. This is common in the TRT but the lack of information from the more precise Pixel or SCT layers leads to candidates with poorer momentum and η measurements.

The final clusters are made by summing up rectangular windows in η-ϕ space. The windows are of different sizes, optimised depending on the location of the cluster and the distinction between electrons and photons, to collect all of the deposited energy while minimising signals from pile-up and noise. The cluster energy for electron and converted photon candidates is filled from cells using towers of 0.075×0.175 in $\eta \times \phi$ in the barrel EM calorimeter and 0.125×0.125 for the candidates in the end-caps. Unconverted photon candidates use clusters of 0.075×0.125 in the barrel and end-caps.

From this point onwards, the properties of the electron and photon candidates are fixed. The final step of applying quality cuts to electron and photon candidates is discussed in Section 5.3.2.

5.3.1 Cell, Cluster and Physics Calibrations

Calibrations are performed at the cell, cluster and final reconstructed object level to account for energy losses and variations in the detector geometry (particularly from the accordion structure of the electromagnetic calorimeter).

For the LAr calorimeters, the ionisation electrons in the LAr gaps are collected by high

voltage (HV) between the layers of absorber and electrodes, with the peak current proportional to the energy deposited. The signal pulse is pre-amplified and shaped, sampled at the bunch crossing frequency and digitised. Samples of the signal pulse (s_j) are taken, with the values in ADC counts, to determine the maximum amplitude of the pulse, A_{max}, as

$$A_{max} = \sum_{j=1}^{N_{samples}} a_j(s_j - p) \tag{5.1}$$

where $N_{samples} = 5$ for physics runs, p is the pedestal (average noise value), and the a_j are Optimal Filtering Coefficients (OFC) [59]. The a_j are determined to minimise the effects of electronic and pile-up noise.

The cell energy is calculated from A_{max} as

$$E_{cell} = F_{DAC\rightarrow\mu A} \cdot F_{\mu A\rightarrow MeV} \cdot \left(\frac{M_{phys}}{M_{calib}}\right)^{-1} \cdot G \cdot A_{max} \tag{5.2}$$

where $F_{DAC\rightarrow\mu A}$ and $F_{\mu A\rightarrow MeV}$ are conversion factors [59]. G is the gain used to convert from ADC to DAC (digital-to-analogue converter) and is derived using calibration pulses, meaning that corrections have to be applied based on the ratio between the maximum of a typical physics pulse (M_{phys}) and typical calibration pulse (M_{calib}).

The calibration at the cell level is at the intrinsic EM scale, which has no specific corrections for energy that is lost due to leakage or deposits in dead matter, but involves measuring the factors for Equation 5.2 accurately. Pedestal runs measure the calorimeter response when there are no beams circulating to determine noise, ramp runs use different DAC input currents to determine the gain variation and delay runs use a known input current signal made from simulated pulses to measure calibration pulse shapes and determine physics pulse predictions. Together these runs help to determine the a_j values and take place with the frequency of once per day/week to make sure the calibration is stable. This process takes account of HV corrections and dead/noisy cells as the translation of a signal to a cell energy can cause a negative value of energy to be reconstructed. This is more likely to occur for noisy cells, which receive a signal pulse that is very different in shape than that used to derive the optimal filtering coefficients.

The cluster corrections (for sliding window clusters and LAr cells in TopoClusters, Section

5.4) involve first correcting the position measurements, relative to the cluster barycentre. The energy is then corrected based on the lateral and longitudinal shower shapes, "out of cluster" deposits and finally accounting for η and ϕ modulations due to the accordion structure of the calorimeter.

The initial calibration scheme used for electrons and photons is obtained from simulation and compares the Monte Carlo truth level information of isolated electron and photons at fixed energies to the energy deposited in the detector. The truth energy is restored based on the following parameters:

- The energy deposited in the material in front of the electromagnetic calorimeter, estimated from the energy seen in the presampler, or from the longitudinal barycentre where there is no presampler. One of the difficulties for electrons, in particular, is that they can radiate up to 50% of their energy within the Inner Detector volume via Bremsstrahlung.
- The energy deposited in the individual layers of the EM calorimeter by the shower.
- The energy leakage out of the back of the EM calorimeter.

The correction is obtained as

$$E_{\text{corr}} = scale \times (offset + W_0 E_0 + E_1 + E_2 + W_3 E_3) \tag{5.3}$$

where $scale$, $offset$, W_0 and W_3 are functions of η only. E_0 is the energy in the presampler and E_1, E_2 and E_3 are the energies in the three sampling layers of the EM calorimeter.

With higher luminosities, the calibrations of electrons and photons have been refined by studying prompt electrons from Z, W and J/ψ decays [33]. For example, by constraining the invariant mass distribution of the electron-positron pairs to follow the line shape of the Z boson as determined using Monte Carlo, and fitting the distributions, the energies in the central and forward calorimeters can be calibrated more precisely. In the central region of the detector, the difference in energy between Monte Carlo and data is now on the order of 0.5%. The area with the worst calibration is the transition between the EM barrel and the end-cap ($1.37 < |\eta| < 1.52$), due to the large amounts of dead material.

5.3.2 Electron and Photon Quality

The expected ratio of isolated electron candidates to QCD jets is approximately 10^{-5}. As a result, electron and photon candidates are checked for how well they agree with an expected signal from an isolated electron or photon, using a function called isEM. Three reference sets of requirements (*loose*, *medium* and *tight*) have been chosen, providing progressively stronger jet rejection at the expense of some identification efficiency loss.

The cuts look at the electromagnetic shower shapes in the EM calorimeter, as well as track quality and track-cluster matching for electrons. For instance the *loose* cuts place requirements on the shower shape variables (shower width, lateral shower containment) in the second EM calorimeter layer and hadronic leakage variables. The *medium* cuts are for electrons only and in addition to the *loose* cuts, they place requirements on the shower shape variables in the first layer of the EM calorimeter, as well as track quality requirements (the number of hits in the Pixel trackers and SCT, and a transverse impact parameter cut) and track-cluster matching in η. The *tight* cuts, in addition to the *medium* cuts (*loose* for photons), place requirements on a B-layer hit, track-cluster matching in ϕ, no secondary candidates produced from conversions, the ratio of the cluster energy to the track momentum and the ratio of high threshold TRT hits to total TRT hits.

In 2010, a sample of approximately 1 nb^{-1}, containing 128,909 preselected electrons, was compared to templates derived from non-diffractive minimum bias MC, in order to break the electron sample up into different components [60]. The percentages of electrons classified as fakes, created from photon conversions or created promptly are listed in Table 5.1. Although the *tight* cuts select a greater fraction of prompt electrons, still over half of the *tight* candidates were classified as either fake or conversion electrons. This has to be accounted for, potentially with additional isolation requirements on the cluster or track, depending on the analysis.

Jets can often pass the electron identification cuts and this can be due to a number of physics processes taking place within the detector. The most common reasons are for semi-leptonic b-decays and c-decays, charged pions produced early in the shower development and conversions, such as $\pi^0 \rightarrow \gamma\gamma \rightarrow e^+e^- + X$, where a hadronic contribution (X)

isEM Level	% Hadrons	% Conversions	% Prompt
Preselected	82.1±0.1	16.3±0.1	1.6±0.1
loose	67.5±0.3	28.4±0.3	4.1±0.1
medium	66.5±0.5	22.8±0.4	10.7±0.3
tight	29.6±1.1	22.4±1.0	48.1±1.2

Table 5.1: Percentage of preselected electrons classified as hadrons faking electrons, electrons produced from conversions and prompt electrons for the different isEM levels - *loose*, *medium* and *tight* in 2010 data based on comparisons with MC templates [60].

gets produced alongside an electron-positron pair. Similarly to how charged pions mimic electrons, jets can often pass photon identification cuts where they fragment into a single π^0 or η, decaying into diphotons.

From 2011, for both electrons and photons, all of the cuts were re-optimised to produce new *loose*++, *medium*++ and *tight*++ cuts, in order to select candidates more efficiently in an increased pile-up environment. In 2012, an intermediate *medium* level cut was introduced for photons by only using the shower shape cuts on the first EM calorimeter layer, as was already used by *medium* electrons.

5.4 Topological Clustering

TopoClusters are three-dimensional objects designed to capture and measure the shower development from particles. Unlike the fixed sized sliding window clusters used in electron and photon identification, these clusters contain varying numbers of cells, selecting those cells with energies that are significant compared to the expected noise.

Clusters are formed by selecting a seed cell with an energy significance, $S = E/\sigma$, where E is the energy deposited in a cell and σ is the standard deviation of the noise distribution per cell, which is above a large threshold t_{seed}. The noise σ is measured from randomly triggered events. Neighbouring cells are then added to the cluster if they have a significance above a medium threshold, $t_{neighbour}$. Finally, a set of cells directly surrounding the neighbouring cells are added to the cluster if their significance is above a low threshold t_{low}. The current significance thresholds are set for t_{seed}, $t_{neighbour}$ and t_{low} at 4, 2 and 0 (420), respectively, which is designed to make sure that electronics and pile-up noise

are suppressed while the tails of showers are still measured. Figure 5.2 shows which cells within a sampling layer contribute to a 420 TopoCluster, but the clustering algorithm also finds neighbouring cells in the sampling layers before and in front of the seed layer, regardless of whether it is an adjacent layer in the same calorimeter or another calorimeter system. Typically, energy deposits in the calorimeter with higher E_{T} are formed from a larger number of cells.

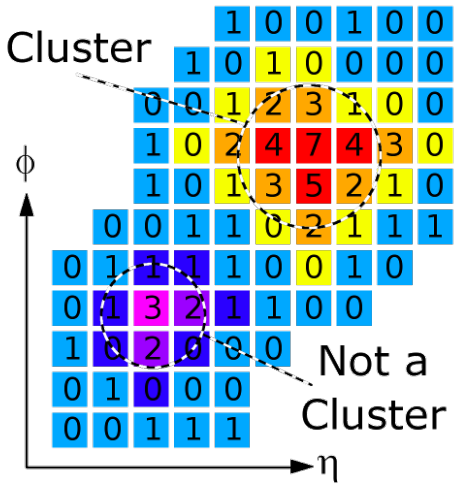

Figure 5.2: TopoCluster reconstruction using a group of seed cells (red) with neighbouring cells (orange) and surrounding cells (yellow) in a single sampling layer of the calorimeters [61].

The default option is to use $|E|$ rather than E to identify seed cells and to take σ as the sum in quadrature of the electronics and pile-up noise rather than electronics noise only. When clusters are combined e.g. to form jets or other quantities, applying the cut on $|E|/\sigma$ ensures that the tails of the noise energy distributions cancel on average. Seed cells with negative energy result in clusters with negative E_{T} and p_{T}. The contributions of electronics noise and total noise (electronics plus pile-up noise) can be seen in Figure 5.3. The electronics noise varies based on the granularity of cells and the pile-up noise varies based on luminosity.

The calorimeter contains 187652 cells in total. From Poisson statistics, it is expected that there will be 11.9 clusters formed, with the 420 thresholds, from just electronic noise in an event (see Section 9.5.1.1). The distribution of these pure noise clusters as a function of η follows the average granularity in each region, as shown in Figure 5.4.

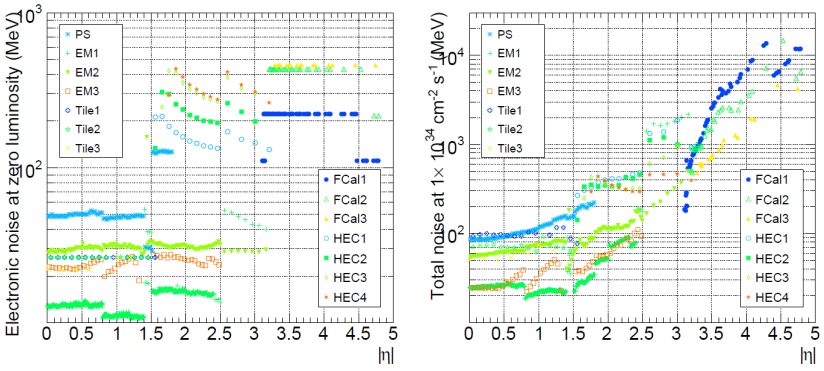

Figure 5.3: Per-cell electronics noise (left) and total noise at high luminosity (right), in MeV, for each calorimeter layer [62].

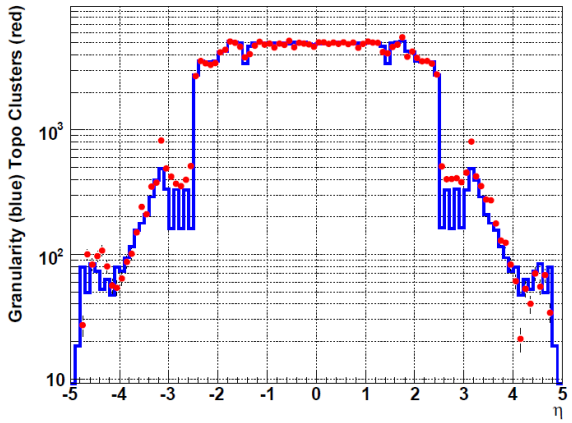

Figure 5.4: Average cell granularity (number of cells per $\Delta\eta = 0.1$) as from the detector geometry (blue histogram) compared with from the distribution of topological clusters in simulated noise-only events (red points) [62].

5.5 Jet Reconstruction

ATLAS can use a number of different inputs to reconstruct jets based on particles interacting in the detector [63]. These are either tracks, calorimeter towers (CaloTowers, similar to those for the EM reconstruction but spanning the electromagnetic and hadronic calorimeters, or noise suppressed towers, TopoTowers) or three-dimensional topological clusters (TopoClusters) based on the calorimeter cells. Some of these inputs are seen in Figure 5.5.

The CaloTowers include every cell spanning the depth of the EM and HAD calorimeters within a grid of size 0.1×0.1 in $\Delta\eta \times \Delta\phi$, regardless of whether they have negative energy

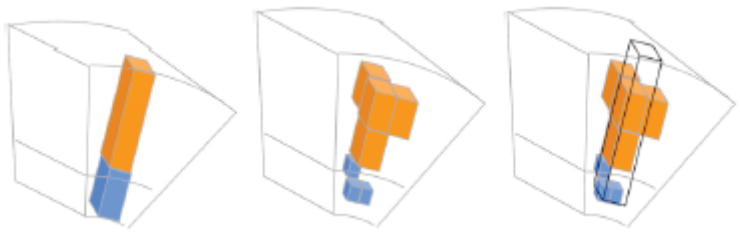

Figure 5.5: Calorimeter based inputs for reconstructing jets. From left to right, these are calorimeter towers (CaloTowers), three-dimensional topological clusters (TopoClusters) or calorimeter towers made from topologically selected seeds (TopoTowers). Jets can also be reconstructed from tracks [64].

constituents. The TopoTowers only take the cells within the original CaloTowers that passed the TopoCluster noise suppression requirements.

5.5.1 Jet Algorithm

The selected jet inputs, typically topological clusters, are used as inputs into the infrared-safe anti-k_t algorithm [65] to reconstruct jets with two clustering parameters, $R = 0.4$ and $R = 0.6$, with full momentum information, noting that the jets are reconstructed to have mass but the reconstructed inputs (TopoClusters, CaloTowers etc.) are massless. This algorithm constructs, for each input object i and j, the distances d_{ij} and d_{iB}, where B is the beam, as

$$d_{ij} = min(k_{Ti}^{-2}, k_{Tj}^{-2}) \frac{(\Delta R)_{ij}^2}{R^2} \ , \tag{5.4}$$

$$d_{iB} = k_{Ti}^{-2} \tag{5.5}$$

where

$$(\Delta R)_{ij}^2 = (y_i - y_j)^2 + (\phi_i - \phi_j)^2 \tag{5.6}$$

and k_{Ti}, y_i, ϕ_i are the transverse momentum, rapidity and azimuth of particle i, respectively.

A list containing all the d_{ij} and d_{iB} values is compiled. If the smallest entry is a d_{ij}, objects i and j are combined and the list is remade. If the smallest entry is a d_{iB}, this object is considered a complete "jet" and is removed from the list. As defined above, d_{ij} and d_{iB} are distance measures between two objects, thus the variable R is a resolution

parameter which sets the relative distance at which jets are resolved from each other.

5.5.2 Jet Calibrations

The jets reconstructed from calorimeter information are reconstructed at the electromagnetic (EM) scale. The EM scale is the intrinsic energy scale of the calorimeters, determined from test-beam measurements for the response of electrons in both the EM and hadronic calorimeters.

There are many instrumental effects in the reconstruction that have to be accounted for. These include:

- Energy lost in material upstream of the calorimeters such as the inner detector
- Energy lost in dead material such as services, gaps and other uninstrumented regions (shower leakage)
- Calorimeter response to hadrons being lower than response to electrons and photons (non-compensation)
- Bending of jet constituents within the magnetic field, particularly soft charged particles
- Energy not collected in the jet reconstruction ("out of cone")
- Inefficiencies in calorimeter clustering and jet reconstruction
- Pile-up

The end result is that the raw energy of the reconstructed jet is usually less than that of the actual jet. The process of correcting the jet energy for these losses is usually referred to as determining the Jet Energy Scale (JES).

By default, jets in ATLAS are calibrated with 'EM+JES', which is relatively simple, applying correction factors as a function of the electromagnetic scale jet η and p_{T}. The correction factors are derived by performing p_{T} balancing with data and Monte Carlo

simulations of QCD dijets and can also include additional adjustments from in-situ measurements for isolated hadrons and pile-up [61].

5.5.3 Jet Quality

Jet quality cuts [66] are provided to reduce three different types of contributions for misconstructed jets due to fake or out-of-time energy depositions.

Jets created from sporadic noise bursts within the HEC are responsible for the majority of fake jets. The jet energy comes mainly from single calorimeter cells, which then affect neighbouring HEC cells due to cross-talk. LAr noise jets are the result of noise bursts within the electromagnetic calorimeter, creating coherent noise across a number of cells. Out-of-time deposits, e.g. those generated by cosmic ray muons or beam backgrounds, can be rejected by comparing the timing of the jet signal compared to the overall event timing.

Similarly to electrons and photons, there are three levels of fake jet rejection: *loose*, *medium* and *tight*. The different cuts and the *loose*, *medium* and *tight* levels were optimised using samples of fake and real jets. They are also tested by studying the missing energy distributions as fake jets often produce events with large $E_{\mathrm{T}}^{\mathrm{miss}}$ due to not having a jet opposite that would balance it in p_{T}.

There is an additional class of jet, known as *ugly*, due to real energy depositions in cells where the energy measurement is not accurate, requiring many software-based corrections. This classification of jets is applied if a jet contains a large fraction of their energy deposited in the Inter Tile Calorimeter scintillators or have a significant fraction of energy fall in problematic cells classed as dead or masked within the detector database.

CHAPTER 6

Monitoring of Level-1 Calorimeter Trigger Electromagnetic and Jet Efficiencies

Some combination of electrons, photons and jets must be identified as final state objects for most interesting physics processes so the ability to correctly trigger on them is essential to ATLAS physics. In particular, certain processes that have been studied in great detail at previous experiments such as $Z \rightarrow e^{+}e^{-}$ and $W \rightarrow e\nu_{\mathrm{e}}$ (so called 'standard candles'), as well as γ-jet and dijet events, are very important for the calibration of the calorimeters and accurately determining the missing transverse energy in an event.

In this chapter, studies were performed using existing and newly devised methods for measuring the efficiencies of the electromagnetic and jet trigger items using electrons, photons and jets reconstructed offline in the event building stage, to understand and improve the Cluster Processor and Jet Energy Processor hardware performance in identifying Regions-of-Interest (RoIs) for reconstructed particle candidates at different transverse energies.

6.1 Typical Methods for Measuring Efficiencies

In order to avoid bias in the efficiency calculations, the electron and photon candidates must be from a sample triggered independently of electromagnetic trigger items and jet samples must be triggered independently of jet trigger items. The *Egamma* stream contains electrons and photons known to have been triggered by L1Calo and the HLT, so despite containing the best statistics for electrons and photons it is not the best stream to use for this analysis. Likewise, for jets, the *JetTauEtmiss* stream cannot be used.

The Minimum Bias Trigger Scintillators (MBTS) produce *MinBias* stream data as they select events independently of the calorimeters. A Minimum Bias sample is one which contains (almost) all possible processes in proportion to their cross section, essentially without any triggers dedicated to search for rare processes [67]. With increasing luminosity, the MBTS trigger items are increasingly more prescaled at all trigger levels, so this method can only be used in early 2010 data. Muon triggers can also be used provided there are enough electron, photon and jet candidates to make it worthwhile, as the muon triggers have minimal correlation with calorimeter based triggers.

For the L1_EM triggers, it is possible to measure their performances using data-driven techniques [51, 68]. A $Z \rightarrow ee$ Tag-and-Probe method tags electrons passing the lowest unprescaled single electron trigger and then probes a second electron if the invariant mass of the pair corresponds to a Z mass window ($80 < m_{ee} < 100$ GeV). This sets a lower limit on the p_{T} of the electrons of around 10 GeV, such that the trigger items with the smallest energy thresholds cannot be completely studied. To access the lower p_{T} range, a $J/\psi \rightarrow ee$ Tag-and-Probe can be derived, but this can only cover electrons with $p_T \leq 15$ GeV.

Other types of jet selection can be provided by triggering on $W/Z \rightarrow$ jets, or using photon-jet events with the photon as a tag.

6.1.1 New Methods for Independently Triggered Samples

To create an independent sample that covers the full p_{T} and η spectrum and provides significant statistics on a run-by-run basis, new methods to obtain independently triggered

samples are necessary. This is because in 2010 and 2011 data, even with low pile-up, it is more likely to obtain multiple jets in an event than to have multiple electrons or photons due to the nature of proton-proton collisions.

6.1.1.1 Jet Tag-and-Probe for Electron and Photon Candidates

Unbiased samples of electrons and photons are obtained by triggering on particular Event Filter (EF) trigger chains. The main selection comes from a jet Tag-and-Probe method which requires that the event was triggered by any of the exclusive EF single-jet triggers. This works since the jet sliding window algorithms automatically count electrons and photons as jets. From studies of the *JetTauEtmiss* stream with 2011 and 2012 data triggering on an EF single-jet trigger, it was verified by matching offline jets to L1 Jet Region of Interests (Jet RoI) and then jets reconstructed at L2 and EF levels, that the offline jet with the highest transverse energy is most often the one that triggered the single-jet trigger chain up to EF level.

To avoid biasing the results, a check is made to ensure that the electromagnetic object being studied is not the cause of the triggered jet by demanding a separation of $\Delta R > 0.4$ between the Jet RoI that triggered the event up to EF level and the offline raw cluster being probed[1].

The jet Tag-and-Probe efficiencies with *loose++*, *medium++* and *tight++* isEM cuts are expected to be stable with increased pile-up. In 2011 and 2012, L1Calo studies have shown that pile-up influences the FCAL regions and the calculation of $E_{\mathrm{T}}^{\mathrm{miss}}$ but in the region $|\eta| < 2.5$, there is no equivalent effect [69].

6.1.1.2 EM Tag-and-Probe for Jet Candidates

Independent selections of jets are obtained using an EM Tag-and-Probe method. This involves using events that triggered on Event Filter trigger chains involving single electrons or single photons. By looking at events in the *Egamma* stream triggered on an EF single-

[1] $\Delta R = \sqrt{(\Delta\eta)^2 + (\Delta\phi)^2}$ is a quantity that defines the separation between two objects in pseudorapidity-azimuthal angle space.

electron or single-photon trigger, it is possible to match L1 EmTau RoIs with electrons or photons reconstructed at the L2 and EF levels and to verify that the L1 EmTau RoI with the highest transverse energy is the one that triggered the complete single-electron or single-photon trigger chain. Additionally, if the highest EF single-electron or single-photon trigger contains a hadronic veto requirement then the EmTau RoI needs to meet this requirement too.

Distinguishing between electron and photon trigger chains aids in identifying which object triggered the event (tag). To study a probe jet within an event, it must have a separation of $\Delta R > 0.5$ from the tag object.

6.2 Studies of L1 Electromagnetic Efficiencies in Early 2010 Data

The analysis was performed with proton-proton collision data at low luminosity (up to $\mathcal{L} = 10^{32}$ cm^{-2} s^{-1}), where the standard candle processes were not readily available due to their relatively small cross sections, but where there was still a need to look at the trigger efficiencies of the electromagnetic trigger items relative to the calorimeter deposits (clusters) that come from electrons and photons, reconstructed offline in the event building stage. The aim of this was to understand and improve the L1Calo (Cluster Processor) hardware performance in producing EmTau RoIs for electron and photon candidates with different transverse energies. The efficiencies produced in these studies quantify how well the trigger worked and were important for identifying regions of the calorimeter (or L1Calo) with poor performance in physics analyses in 2010.

6.2.1 Method

Trigger efficiencies, ϵ, are calculated with respect to independently triggered offline electron and photon clusters for the electromagnetic trigger items according to

$$\epsilon\,(\text{L1\_EM}x) = \frac{\text{N}^{\text{o}}(\text{Offline Cluster \& } \Delta R \text{ to RoI} < 0.15 \text{ \& RoI passes L1\_EM}x)}{\text{N}^{\text{o}}(\text{Offline Cluster})} \quad (6.1)$$

where L1_EMx is the name of a trigger item, with x being the value of the transverse energy threshold that goes into the L1Calo hardware.

The requirement of the offline cluster having $\Delta R < 0.15$ to an EmTau RoI matches that used in the CP algorithm. As the EmTau RoI is based on a local energy maximum from a 2×1 (or 1×2) cluster of trigger towers (each of 0.1×0.1 in $\Delta\phi \times \Delta\eta$), an offline cluster with $\Delta R < 0.15$ should have matched to it[2].

To make these efficiencies relevant for physics analyses, cuts were applied to the offline cluster positions. For electron clusters, the calorimetry and tracking provides precision measurements up to $|\eta| = 2.5$, so any electron clusters with $|\eta| > 2.47$ are excluded to avoid studying showers that are not fully contained within the barrel and end-caps. For photon clusters, the selection only studies clusters with $|\eta| < 2.37$ to contain showers within the region of the finely segmented first layer ($|\eta| \leq 2.4$), used to distinguish between photons and neutral pions, which undergo the decay $\pi^0 \rightarrow \gamma\gamma$.

In addition, the raw electromagnetic cluster under study must not fall into the transition regions between the barrel and end-caps ($1.37 < |\eta| < 1.52$). Across these regions there are significant amounts of dead material present, affecting the energy measurement of electron and photon candidates. Before Summer 2011, another problem in the transition regions came from the summation of the trigger towers across the barrel and end-caps not being in time (see Section 6.2.5). Therefore the trigger towers in the barrel or end-cap across these η ranges are deliberately masked and these transition regions are studied separately.

An independent problem that affected cluster selection came from groups of channels

[2]In the unlikely, but not impossible, case of there being two EmTau RoIs within 0.15 of an offline cluster, the closer RoI to the cluster is assumed to be the one to have been created from it.

which could not be read out. These problematic channels existed due to failed optical transmitters (OTXs) [70] that are designed to transmit data from the electronics on the front end boards (FEBs) of the electromagnetic calorimeters to the data acquisition (DAQ) systems. Despite being designed to be radiation-hard, the OTXs had a significant mortality rate in 2009 and 2010. This meant that digitised signals from the calorimeters could not be sent to DAQ, although L1Calo was unaffected as it receives analogue signals through a different set of electronics. Faulty OTXs cause 128 neighbouring channels to stop providing measurements of energy. The reconstruction and measurement of $E_{\mathrm{T}}^{\mathrm{miss}}$ as well as electron, photon and jet energies deteriorate in the presence of such failures, as well as if a high voltage (HV) power supply (in the calorimeters) becomes non-operational. In particular for electrons and photons, if the faulty OTX affects the second sampling layer, in which the bulk of the energy is collected, no offline objects are reconstructed. Regions in η and ϕ surrounding the faulty OTX are masked off in offline analyses.

6.2.2 Effect of Cluster Calibration on Matching to Offline Clusters

Studies have involved extracting the energy and position response of EmTau RoIs to see how closely they match the offline clusters. This tests the effects of the reduced granularity information available to L1Calo as well as the effect of energy calibrations.

The transverse energy response and position responses in η and ϕ are calculated as

$$E_T \text{ Response } = \frac{\text{Offline Cluster } E_{\mathrm{T}} \text{ } - \text{ EmTau RoI } E_{\mathrm{T}}}{\text{Offline Cluster } E_{\mathrm{T}}} \tag{6.2}$$

$$\eta, \phi \text{ Position Response } = \text{ Offline Cluster } \eta, \phi \text{ } - \text{ EmTau RoI } \eta, \phi \tag{6.3}$$

In Equation 6.2, the offline cluster E_{T} goes into the denominator as it is more precisely defined than the EmTau RoI E_T which is restricted to integer values (GeV).

The responses are fitted to a Gaussian over the peak area to study the mean (bias) and standard deviation (resolution) of the fit for both raw and calibrated clusters. Ideally

the mean of the fit will be equal to zero so that despite the reduced granularity of the L1Calo trigger towers, it will match well to the clusters available offline. A small standard deviation corresponds to a good resolution.

The results for the energy response are shown in Figure 6.1 for $MinBias$ stream data and a minimum bias Monte Carlo sample, scaled to have the same overall normalisation value as the data. The E_T response of L1Calo relative to calibrated offline clusters are very similar between the data and Monte Carlo. For raw clusters, the fits are not as similar with the fit to the Monte Carlo having a mean further away from zero than for the data.

As raw clusters are better matched in terms of the input L1Calo receives, the fits for raw clusters have mean values closer to zero than for the calibrated clusters. L1Calo studies are therefore usually done relative to raw cluster energies but for physics analyses, the calibrated cluster quantities are more interesting. The standard deviations of all four fits are similar, suggesting that on average the calibration will add energy to that of the raw cluster without influencing the width of the distribution.

There is a significant tail in the resolution data towards negative values, where the cluster E_{T} is much less than that of the EmTau RoI. This has been attributed to wrong matches between clusters and EmTau RoIs, as the matching allows any cluster with $\Delta R < 0.15$ to avoid biasing the results (see Section 6.2.4). This tail is more significant for the data than the Monte Carlo sample, indicating that this matching effect is more common in real data.

For the η resolution (not shown), the Gaussian fit to the raw clusters[3] gave $\mu = -0.042$, $\sigma = 0.024$ and that to the calibrated clusters the result produced $\mu = -0.047$, $\sigma = 0.028$. For the ϕ resolution, the fit to raw clusters gave $\mu = -0.037$, $\sigma = 0.018$ and for calibrated clusters gave $\mu = -0.043$, $\sigma = 0.026$. The means of these fits are non-zero due to the reduced granularity of the trigger towers used to create an EmTau RoI. Again the raw η and ϕ mean values are closer to zero than for calibrated clusters but the difference in position resolution is very small between the raw and calibrated clusters in terms of position resolution with respect to L1Calo.

[3]The errors in the mean and standard deviation for the Gaussian fits to the resolutions are not given, as the statistical errors on the fits were negligible.

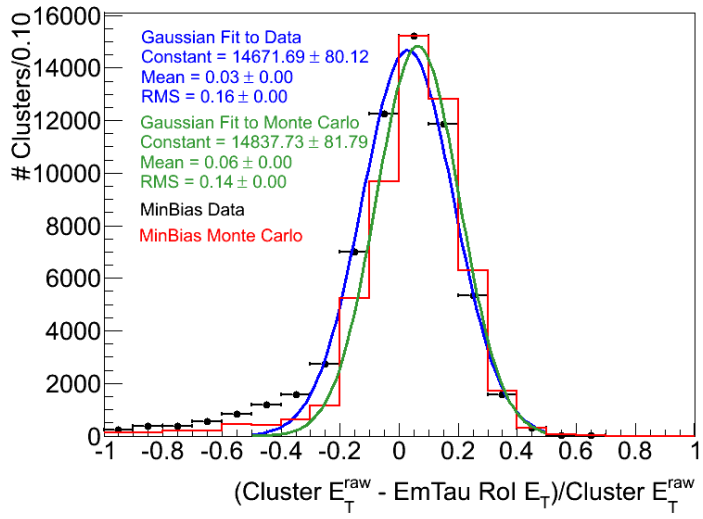

(a) Raw Clusters

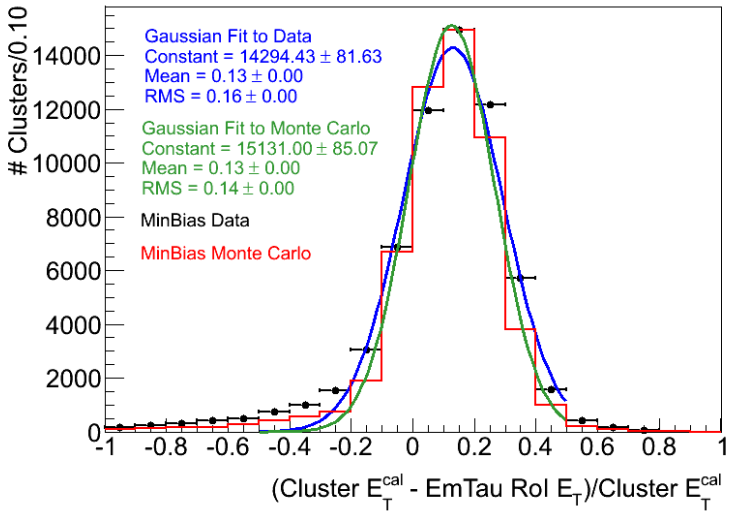

(b) Calibrated Clusters

Figure 6.1: Transverse energy response for L1Calo relative to raw and calibrated offline clusters using *MinBias* stream data and Monte Carlo. Each sample is fitted with a Gaussian over the peak region and the results of each fit are shown.

6.2.3 Efficiencies

Perfect efficiency results (as a function of E_{T}) would produce a step function which switches on at a given energy, but in reality it is similar to a sigmoid function, often referred to as a turn-on curve. Ideally the efficiency turn-on curves for each trigger item reaches 100% within a few GeV of the energy threshold and then stays at 100% as the energy increases.

The results below are for the 2010 ATLAS data taking period E (taken from the 29 June

to 18 August 2010), corresponding to an integrated luminosity of 1118 ± 112 nb^{-1}. For this period the EM thresholds set in the hardware were: L1_EM2, L1_EM3, L1_EM5, L1_EM10, L1_EM10I, L1_EM14, L1_EM14I and L1_EM85. The data are compared to a minimum bias Monte Carlo sample [71], containing approximately 20 million events, for which the ATLAS detector response is simulated.

The trigger efficiencies are shown for L1_EM2, L1_EM3 and L1_EM5 using $MinBias$ stream data in Figure 6.2(a) which may be compared with those from ATLAS Public Results [72] in Figure 6.3, made from an earlier data sample of smaller integrated luminosity. The public results were produced with the first 2010 data by the ATLAS Electron and Photon performance group, with the aim of verifying the trigger performance primarily for physics analysis purposes. The trigger efficiencies calculated here have been used to extend this study and provide a detailed check of the hardware performance. Trigger efficiencies are also shown from this analysis for L1_EM10 and L1_EM14 in Figure 6.4. With the statistics of electron and photon candidates available, it was not possible to calculate the efficiency for the L1_EM85 trigger item. For all plots, the statistical uncertainties in the efficiency calculation become large at energies greater than around 15 GeV.

The calculated efficiencies for the L1_EM2, L1_EM3 and L1_EM5 thresholds are in very good agreement with the public results produced with a much smaller data sample, especially when it is noted that between 0-2 GeV, the public results use a bin width of 1 GeV compared to 0.5 GeV for the calculated efficiencies here. It should be noted that for the L1_EM2 threshold, and less so for L1_EM3 and L1_EM5, the behaviour of the efficiency curve for $E_{\mathrm{T}}^{\mathrm{raw}} < 3$ GeV is no longer described by a sigmoid function as many candidates below the lowest energy threshold are able to trigger (see Section 6.2.4 for a discussion of this effect). A difference between the calculated and public results is that for the Monte Carlo L1_EM3 and L1_EM5 thresholds the efficiency at low E_{T} is not the same between the sets of results. In the public results there are bins in the plateau region beyond the turn-on curve where very small inefficiencies are observed (see Section 6.2.5). These are also present in the results obtained here but are far less pronounced, as the period E data was produced after several updates (improved timing, repairs, etc.) to the L1Calo hardware.

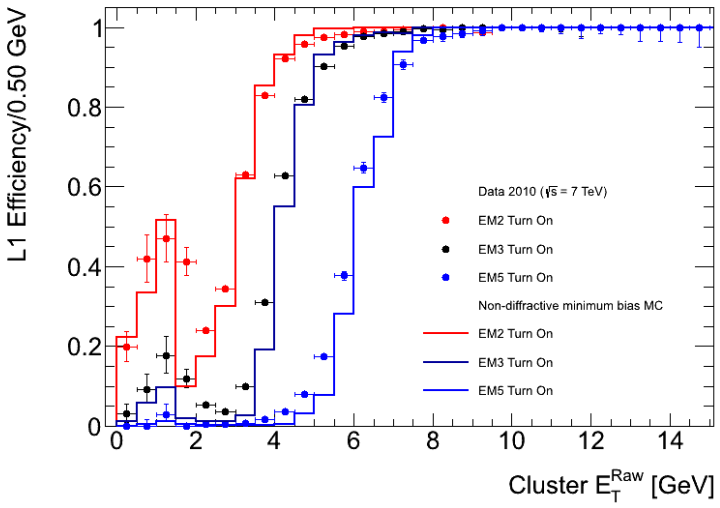

(a) Comparison to Monte Carlo

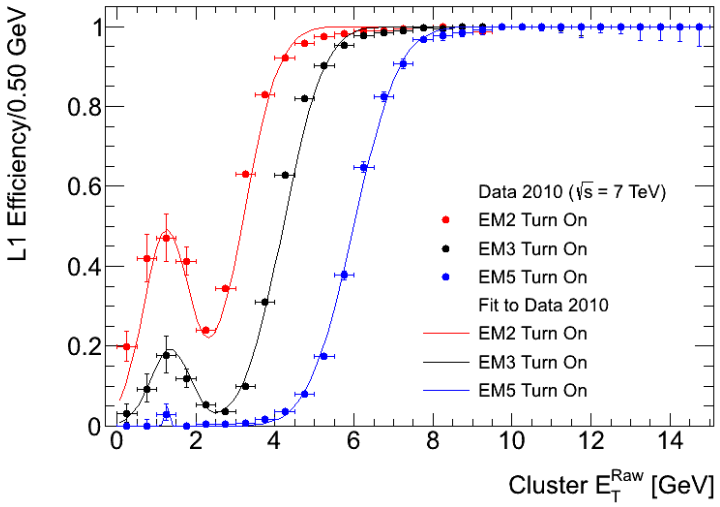

(b) Fitted with sum of error function and Gaussian

Figure 6.2: Efficiency as a function of $E_{\mathrm{T}}^{\mathrm{raw}}$ for the L1_EM2, L1_EM3 and L1_EM5 electromagnetic trigger items with respect to the clusters of isEM *loose* electrons and photons using $MinBias$ stream data.

To characterise the performance of the trigger efficiencies, data for the lower energy thresholds (L1_EM2, L1_EM3 and L1_EM5) were fitted with a modified version of a sigmoid known as the error function ($Erf(x) = \frac{2}{\sqrt{\pi}} \int_0^x e^{-t^2}\,\mathrm{d}t$) of the form $f(x) = a_0(1 + Erf((x - a_1)/a_2)$, where the a_i are fit parameters, summed with a Gaussian of the standard form $f(x) = b_0 e^{-(x-b_1)^2/2b_2^2}$ (Figure 6.2(b)). Higher transverse energy thresholds were fitted solely with the error function, as in Figure 6.4(b). As the range of $Erf(x)$ is from -1 to $+1$ by default, $a_0 = 0.5$ produces a fit between 0 and 1 for $(1 + Erf(x))$. The results of the fit to L1_EM2, L1_EM3 and L1_EM5 can be seen in Table 6.1 and the fit parameters

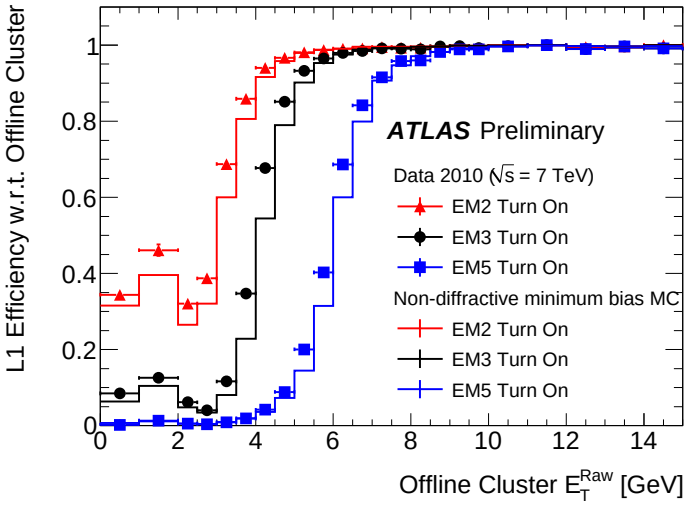

Figure 6.3: ATLAS Public Results for the efficiency with respect to offline clusters as a function of the raw cluster E_{T} for the L1_EM2, L1_EM3 and L1_EM5 electromagnetic trigger items, taken in early 2010 data [72].

for L1_EM10 and L1_EM14 are seen in Table 6.2.

Parameter	L1_EM2 [GeV]	L1_EM3 [GeV]	L1_EM5 [GeV]
$Erf\ a_0$	0.50 ± 0.01	0.50 ± 0.01	0.50 ± 0.01
$Erf\ a_1$	3.16 ± 0.10	4.21 ± 0.06	5.99 ± 0.02
$Erf\ a_2$	1.04 ± 0.12	1.17 ± 0.14	1.29 ± 0.02
Gaussian b_0	0.49 ± 0.05	0.19 ± 0.02	0.05 ± 0.01
Gaussian b_1	1.25 ± 0.10	1.35 ± 0.12	1.26 ± 0.04
Gaussian b_2	0.58 ± 0.06	0.51 ± 0.04	0.05 ± 0.01

Table 6.1: Fit parameters for the combined Gaussian and error function to the efficiencies for L1_EM2, L1_EM3 and L1_EM5.

Parameter	L1_EM10 [GeV]	L1_EM14 [GeV]
$Erf\ a_0$	0.50 ± 0.01	0.50 ± 0.01
$Erf\ a_1$	10.91 ± 0.06	14.24 ± 0.10
$Erf\ a_2$	1.96 ± 0.13	2.45 ± 0.19

Table 6.2: Fit parameters for the error function to the efficiencies for L1_EM10 and L1_EM14.

A trigger item of the form L1_EMx requires that a 2×1 set of trigger towers see a total of at least $(x+1)$ GeV of transverse energy to produce an EmTau RoI. In this case the error function parameter a_1, which corresponds to the $E_{\mathrm{T}}^{\mathrm{raw}}$ that give 50% efficiency is usually within a GeV of the $(x+1)$ GeV design. The sharpness of the turn-on curve, characterised

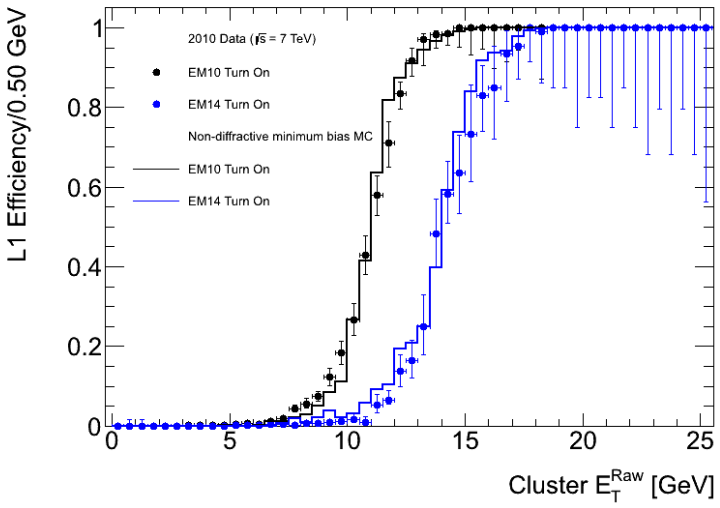

(a) Comparison to Monte Carlo

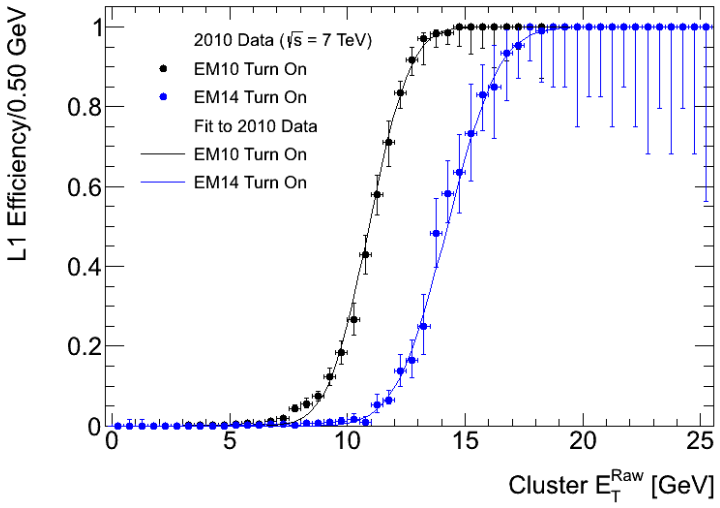

(b) Fitted with error function

Figure 6.4: Efficiency as a function of $E_{\mathrm{T}}^{\mathrm{raw}}$ for the L1_EM10 and L1_EM14 electromagnetic trigger items with respect to the clusters of isEM *loose* electrons and photons using $MinBias$ stream data.

by a_2, also decreases slightly as the threshold increases. The efficiencies reach 100% at typically $E_{\mathrm{T}}^{\mathrm{raw}} = (x + 5)$ GeV.

The effect of isolation can be seen in Figure 6.5(a) through a direct comparison of the L1_EM10 and L1_EM10I trigger items. The rise of the turn-on curves is similar but in the plateau region, the behaviour is very different. This is attributed to the fact that as the energy gets larger, the electromagnetic showers develop broader widths, so that there is greater energy deposited in the isolation regions, making the L1_EM10I efficiency decrease with increasing E_{T}. Parametrising using a fit to an error function, the results are shown

in Figure 6.5(b) for L1_EM10I but only to characterise the fit to the turn on curve. Only points with $E_{\mathrm{T}}^{\mathrm{raw}} \leq 13.5$ GeV are included in this fit (a solid blue line), and then a blue dotted line shows the extrapolation of the fit to larger $E_{\mathrm{T}}^{\mathrm{raw}}$. Selecting isolated candidates will become very important once higher instantaneous luminosities are achieved, and it is therefore essential that isolation criteria are carefully chosen to avoid the high E_{T} losses identified here.

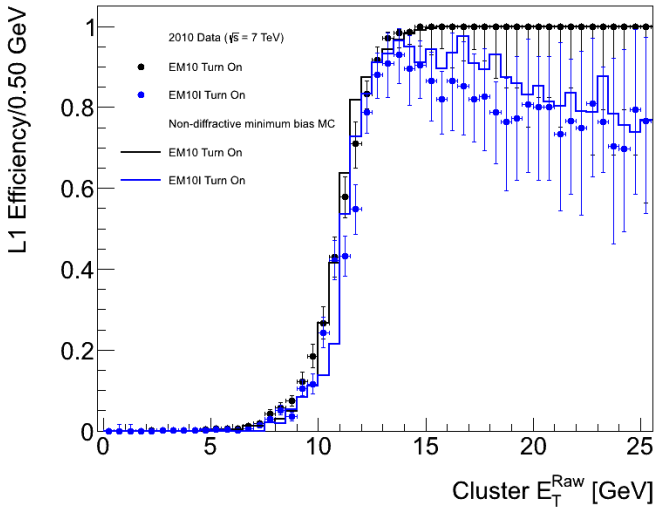

(a) Comparison to Monte Carlo

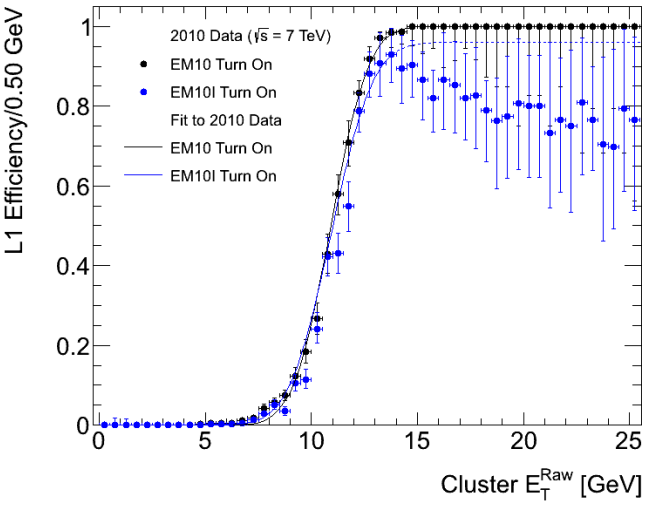

(b) Fitted with error function

Figure 6.5: Efficiency as a function of $E_{\mathrm{T}}^{\mathrm{raw}}$ for the L1_EM10 and L1_EM10I electromagnetic trigger items with respect to the clusters of isEM *loose* electrons and photons using $MinBias$ stream data.

A comparison of the L1_EM5 efficiencies produced by the MBTS and jet tag-and-probe methods was performed to see how compatible the two event selection methods were in

providing independently triggered offline clusters. Figure 6.6 and Table 6.3 show that the jet Tag-and-Probe method does not produce an efficiency turn-on curve which is as sharp as those produced by the MBTS method, although the candidates studied here have much lower E_{T} than the reconstruction was optimised for. In addition, the smaller statistical errors at high transverse energy show that the jet Tag-and-Probe method is capable of selecting a greater number of higher energy electron and photon candidates.

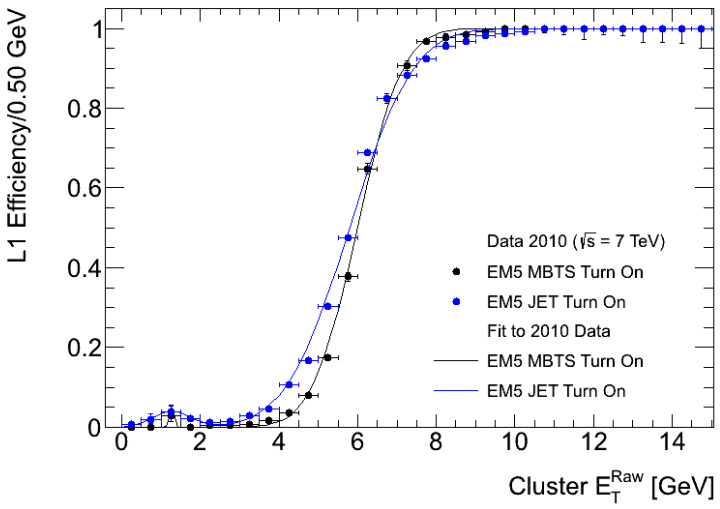

Figure 6.6: Efficiency with respect to clusters of isEM *loose* electrons and photons as a function of the raw cluster E_{T} for the L1_EM5 electromagnetic trigger items calculated using samples triggered with either MBTS triggers or Jet triggers using a Tag-and-Probe method.

Parameter	MBTS Triggered L1_EM5 [GeV]	Jet Triggered L1_EM5 [GeV]
$Erf\ a_0$	0.50 ± 0.01	0.50 ± 0.01
$Erf\ a_1$	5.99 ± 0.02	5.79 ± 0.03
$Erf\ a_2$	1.29 ± 0.02	1.29 ± 0.02
Gaussian b_0	0.05 ± 0.01	0.07 ± 0.01
Gaussian b_1	1.26 ± 0.04	1.26 ± 0.04
Gaussian b_2	0.05 ± 0.01	0.49 ± 0.05

Table 6.3: Fit parameters for the combined Gaussian and error function to the efficiencies for L1_EM5 selected using the MBTS method and the Jet Tag-and-Probe method.

To first order these methods should produce the same trigger efficiencies. However, the streaming and trigger selection may produce some higher order effects. For example, between the two event selection methods, the fraction of candidates that are fakes (hadrons reconstructed as electromagnetic candidates) is different. Additionally, events selected in a jet sample may have a higher level of hadronic content in general.

To improve the results from the jet Tag-and-Probe method, the number of fakes must be reduced. This can be achieved by using a tighter selection of offline electrons and photons than that used by the isEM *loose* selection, providing enough statistics are available to measure the full transverse energy range sufficiently. This was done in later analyses as the instantaneous luminosity increased.

6.2.4 "Bump" in Trigger Efficiencies at Low Transverse Energy

Electron and photon clusters with transverse energy of at least 3 GeV are capable of producing an EmTau RoI as intended in the trigger design. In the efficiencies shown in Figure 6.2, it can be seen that clusters with lower energies than this can also sometimes be triggered, creating a small peak (referred to as the "bump" by ATLAS experts) in the efficiencies around $E_{\mathrm{T}}^{\mathrm{raw}} = 1$ GeV. This is a strong effect for L1_EM2 and becomes smaller for higher threshold triggers. For an in-depth study of the bump, an effect only significant in 2010, see [73].

The first public ATLAS results, Figure 6.3, assumed that this was purely an artefact of having reduced granularity trigger towers and the choice of matching algorithm allowing matching of low energy clusters within $\Delta R < 0.15$ of an EmTau RoI produced by a higher energy cluster ('bad matching').

By selecting candidates on an event-by-event basis with $E_{\mathrm{T}}^{\mathrm{raw}} < 3$ GeV that contributed to the bump and investigating why they triggered, it was possible to classify the causes and develop an algorithm to do this classification automatically over larger samples.

In addition to 'bad matching', the other contributions to the bump are hardware and software related. These include:

- Electronics noise: The propagation of the summed analogue signals seen in the calorimeter cells to the CPMs is affected by the intrinsic noise of calorimeter and the thermal noise of the amplifiers, receivers and cables. This is the dominant cause with up to 500 MeV of RMS noise added to the individual signals [43].
- E_T miscalibration: Difference between the calibration of the digitised signals studied

in L1Calo and those digitised to be sent to the data acquisition systems.

- Cluster combination: Two clusters within 0.15 of an EmTau RoI are positioned such that their energies are combined into the reduced granularity trigger towers making the RoI cluster. The EmTau RoI usually has more than 3 GeV having matched to both clusters.

- Multiple reconstruction of offline clusters: Subset of the noise and miscalibration effect involving an electron and photon that have been reconstructed from the same offline cluster, most likely from a photon conversion.

- Offline cluster calibration: An unusual situation where the calibration in the offline reconstruction made the calibrated cluster energy much smaller than that of the raw cluster.

The percentages of how much these various effects contribute to the bump for *MinBias* stream are shown in Figure 6.7 as a function of the offline cluster $E_{\mathrm{T}}^{\mathrm{raw}}$ to see how much the individual effects contribute to these low energy candidates triggering as a function of the cluster energy. The results are dependent on the data stream used and the cuts applied to the offline clusters.

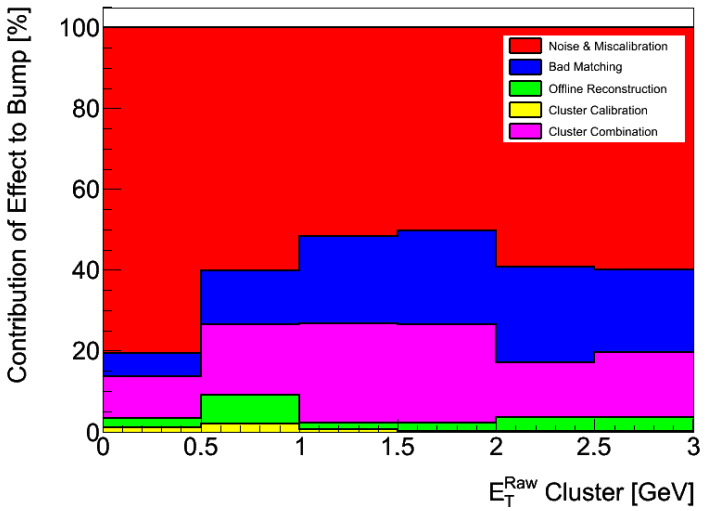

Figure 6.7: Relative contributions, as a function of the offline cluster $E_{\mathrm{T}}^{\mathrm{raw}}$, of the effects enabling electron or photon candidates with $E_{\mathrm{T}}^{\mathrm{raw}} < 3$ GeV to be triggered by L1Calo for *MinBias* stream data.

In the MC sample, the collective noise and E_T miscalibration term made up (97.61 ± 1.34)% (statistical error only) of the bump, indicating a big difference in the simulation of the particle response in the sample. Figure 6.7 also has this as the dominant contribution to the total (59.83 ± 0.35)% but the bad matching and cluster combination terms contribute (20.65 ± 0.18)% and (16.00 ± 0.15)%, respectively, with the remaining terms making up less than 4%.

The noise term dominates for L1_EM2 and becomes less significant for L1 EM triggers with increasing energy thresholds. The already high rate for L1_EM2 was not helped by being triggered in events with a large amount of noise. L1_EM2 was already very highly prescaled by 2010 Period E and was dropped from the trigger menu before the end of 2010 data taking. L1_EM3 was still being used during 2012 data taking as a highly prescaled physics trigger but helped by improved L1Calo noise cuts to handle the large amount of pile-up. Improved offline selection of electron and photon candidates has allowed the other reasons for producing the bump to be minimised or removed.

6.2.5 Missing Electromagnetic Trigger Events

A trigger efficiency energy dependence shaped like a sigmoid function implies that both below and above the nominal energy threshold there are electron and photon candidates that do not get triggered. With the first data taken with ATLAS, the detector as a whole was still technically in development. It was expected that hardware problems would occur during this time, resulting in small areas with reduced efficiency.

At energies much higher than the threshold it would be expected that a RoI would always be created, but the trigger efficiency results show small dips in efficiency well above the energy threshold, implying some small inefficiency in a region where physics analyses rely on L1Calo to obtain samples.

For an EmTau RoI not to be produced for an electron or photon candidate, the electromagnetic trigger towers near the object must have seen insufficient energy and consequently the L1Calo PPr produces a smaller output energy than expected. The energy can be lost in several places prior to this stage so finding the underlying causes for this was important.

For the low energy trigger items (L1_EM2, L1_EM3), electron and photon candidates were studied if their offline cluster $E_{\mathrm{T}}^{\mathrm{raw}}$ was greater than 10 GeV, so that they lie in the plateau beyond these efficiency turn-on curves, but an EmTau RoI was not produced. This involved looking at the different parts of L1Calo, primarily the PPr and CP, as well as the calorimeter cells nearby, to determine the causes of not producing RoIs.

To determine the reason why there was no EmTau RoI for a candidate, trigger towers within 0.2 units in both η and ϕ from an electron or photon candidate were investigated. For each selected tower, the FADC (flash analogue-to-digital converter), the BCID (bunch crossing identification), LUT (look-up table) and trigger tower electromagnetic and hadronic transverse energy values are extracted and studied. It is also useful to look at the summed transverse energies of the calorimeter cells that are combined to make the trigger tower as a check of the analogue signal going into L1Calo. In doing this, all of the individual steps up to and including the L1Calo PPr are known, making it easier to determine why the CP did not produce a RoI.

The Atlantis event display [74], as seen for an example event in Figure 6.8, was also used in a configuration optimised for L1Calo to aid in understanding the whole event and the reasons for why there are offline candidates without EmTau RoIs.

The most common reasons for an electron or photon with an energy of at least 10 GeV not to produce an EmTau RoI include:

- The trigger tower has been switched off due to faulty electronics or for being too noisy. The latter case is called a 'hot tower' and is capable of producing very high trigger rates, thereby reducing the bandwidth available for other processes.
- The electromagnetic shower from the electron or photon candidate was sufficiently broad that it spread across many trigger towers (more than 3) so there was not enough E_{T} seen in a single tower.
- The FIR filter indicates the candidate came in a bunch crossing out of time with the LHC beam so the trigger tower will not measure any E_{T} for the correct bunch crossing. In early data, the timing was not yet finalised as it was based on calorimeter delay runs (discussed in Section 5.3.1), which do not represent the timing of signals

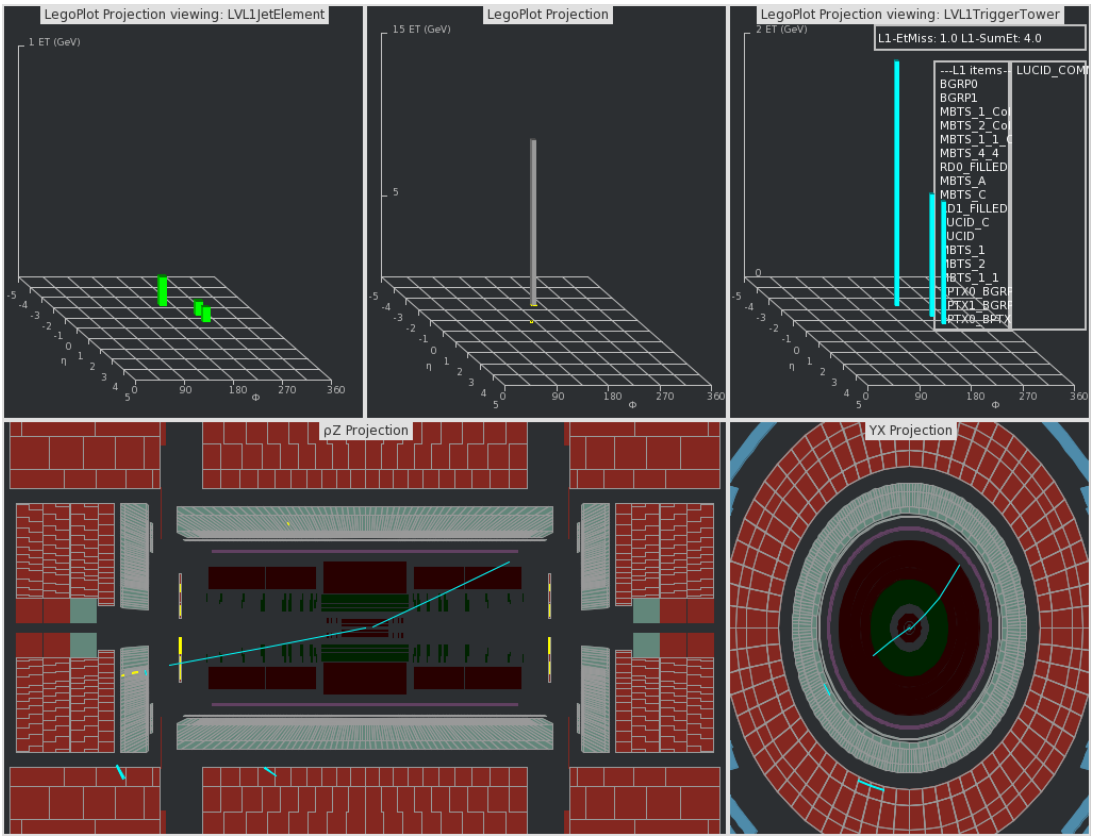

Figure 6.8: An Atlantis event display picture of an event containing an electron candidate at $\eta = -2.41$, $\phi = -2.64$ with no corresponding EmTau RoI in L1Calo. The electron cluster has $E_{\mathrm{T}} = 10.38$ GeV (top middle) but the only trigger tower nearby (top right) has $E_{\mathrm{T}} = 2$ GeV.

in recent collision data as accurately as possible.

A problem at all transverse energies came from the transition region for the electromagnetic calorimeters, classified for offline analyses as $1.37 < |\eta| < 1.52$. From 2009 and for all of 2010, the trigger towers that overlap across this region between the barrel and end-caps were not timed in correctly, meaning that the trigger towers in either the barrel or the end-caps were deliberately masked. This meant that the full shower in the calorimeter could not be summed correctly and so less energy was seen in L1Calo than offline. This was a common enough effect to ignore candidates in this region. The data taken in 2010 provided enough information to get a common timing across all these towers but this was not implemented until 2011 running.

Using all of the data, an η-ϕ efficiency map is made for a given threshold with the sizes of the 2-dimensional η-ϕ bins corresponding to individual electromagnetic trigger towers.

This map can then be used to test the ability of the trigger towers to produce EmTau RoIs and identify regions with poor performance. This was done with and without the OTX cuts being applied as shown in Figures 6.9 and 6.10, respectively. These efficiencies were plotted for offline clusters with $E_{\mathrm{T}}^{\mathrm{raw}} > 5$ GeV for the L1_EM3 trigger item. The reason for this choice was that by 5 GeV, the plateau for L1_EM3 is close to being reached, meaning the majority of the candidates will be triggered, whilst the relatively low 5 GeV cut provides sufficient statistics to cover the whole map. By analysing these figures, it is possible to keep track of problematic trigger tower regions so that the L1Calo hardware experts can be made aware of them.

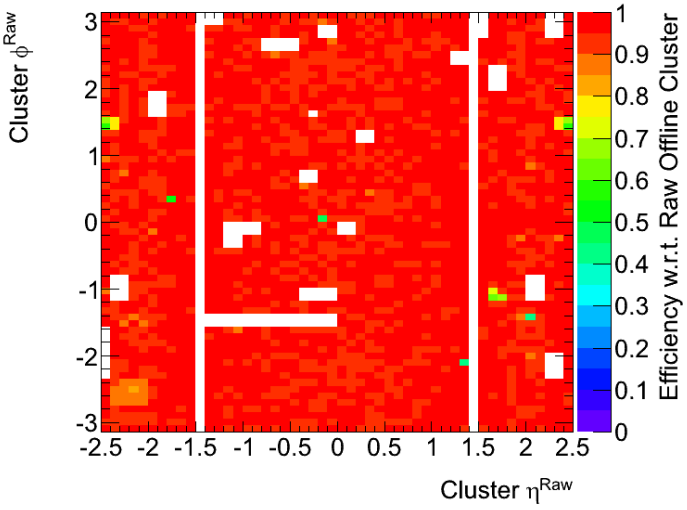

Figure 6.9: L1_EM3 efficiency map in η-ϕ for raw offline clusters with E_{T} greater than 5 GeV after applying the electromagnetic calorimeter optical transmitter (OTX) cuts.

If the OTX fails in producing a readout for the second layer of the electromagnetic calorimeter where most of the energy of a shower is measured, there are very few particles reconstructed in these areas. The EmTau RoIs used in this analysis also have to be reconstructed offline[4] meaning that these areas have very low efficiencies with respect to the offline clusters, as there are no EmTau RoIs reconstructed offline in these regions and electron and photon candidates reconstructed nearby have few EmTau RoIs to match to. To recover the lost energy in OTXs for offline analyses, a strategy was developed which used the independent energy readout from L1Calo to estimate the energy deposited in those regions, particularly for $E_{\mathrm{T}}^{\mathrm{miss}}$ reconstruction. However, the strategy took signifi-

[4]EmTau RoIs are reconstructed offline using the equivalent of the Cluster Processor sliding window algorithm on the reconstructed calorimeter signals.

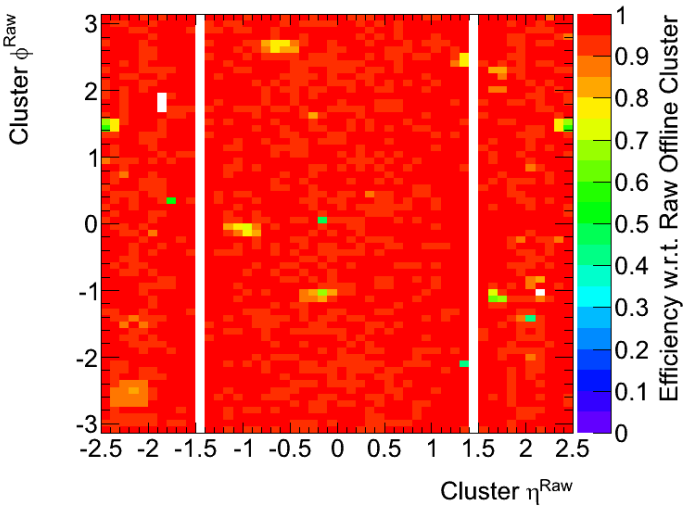

Figure 6.10: L1_EM3 efficiency map in η-ϕ for raw offline clusters with E_{T} greater than 5 GeV without applying the electromagnetic calorimeter optical transmitter (OTX) cuts.

cant time to be developed and had limited accuracy due to the reduced granularity of the trigger towers [75].

If the OTX problem does not relate to the readout from the second layer of the calorimeter, the efficiency with respect to the offline clusters for the affected trigger towers is similar to towers where there are no known problems. For L1Calo monitoring, it would be more suitable not to apply OTX cuts around these areas to then determine if there are actual problems with the L1Calo hardware.

Table 6.4 gives a list of the trigger towers with less than 90% efficiency in Figure 6.9. This list was prepared and sent to L1Calo experts who investigated the suggested problematic towers in more detail by studying the signals with oscilliscopes. In the majority of cases, the problem was fully understood and eventually fixed.

A killed tower is one that was switched off by L1Calo for being too noisy and a dead tower is one for which it was observed that the analogue signal from the calorimeter was lost before it reached the L1Calo receivers. The miscabling on the electromagnetic calorimeter meant that in the affected regions, the incorrect analogue signals were being summed together so these towers did not see as much energy as they should have done [76]. The HV (high voltage) problems appear to arise where the electromagnetic calorimeter is not able to operate at the nominal voltage for collecting signals within the active

medium. This can be corrected for in the offline reconstruction. However the signals sent independently to L1Calo are smaller than usual, reducing the potential to trigger. The loose input cable to L1Calo has been reconnected since it was spotted and so this area was more efficient in following data.

Tower η	Tower ϕ	Probable cause of reduced efficiency
-2.45	1.42	ECAL HV problem
-2.45	1.52	ECAL HV problem
-2.35	1.42	ECAL HV problem
-2.35	1.52	ECAL HV problem
-2.25	-1.52	Miscabling on ECAL electronics
-2.15	-1.42	Miscabling on ECAL electronics
-2.05	-1.52	Miscabling on ECAL electronics
-1.75	0.34	Trigger tower killed for being too noisy
-0.15	0.05	Known dead trigger tower
1.35	-2.11	Known dead trigger tower
1.65	-1.13	Input cable to trigger tower came loose
1.65	-1.03	Input cable to trigger tower came loose
1.75	-1.13	Input cable to trigger tower came loose
2.05	-1.42	Known dead trigger tower
2.35	1.42	ECAL HV problem
2.35	1.52	ECAL HV problem
2.45	1.42	ECAL HV problem
2.45	1.52	ECAL HV problem

Table 6.4: Causes for reduced efficiency in trigger towers, as determined by studying the tower signals with oscilloscopes, with respect to offline clusters when regions affected by failed electromagnetic calorimeter optical transmitters are excluded (see Figure 6.9).

For problems related to reduced calorimeter HV, it is possible to improve the trigger tower performance by adjusting the gains on the L1Calo receivers. However, there are still other trigger towers in Figure 6.9, where the efficiency falls between 80%-90%, where the result could not be associated directly to any hardware problem. For some individual towers that did not fall into faulty OTX regions, it is still possible that efficiencies just below 90% could occur within statistical fluctuations, as the plateau of the turn on curve is not reached by 5 GeV.

The group of trigger towers around the coordinates $\eta = -2.2$, $\phi = -2.6$ for which the efficiency was reduced could not be explained as easily. The efficiencies improved across this set of towers in later 2010 data and by the time the hardware was checked, separately by both the LAr and L1Calo experts, no problems could be associated to the results seen.

The size of the area over which the efficiencies were reduced potentially indicates that there could have been some small hardware miscalibration or mis-timing at the time.

6.2.6 Extension of Studies of L1 Electromagnetic Efficiencies to Later 2010 Periods

Having seen that there were areas of reduced efficiency in Period E, it was important to check the trigger towers corresponding to these areas in later data taking periods in 2010, and also to identify if other areas produced reduced efficiencies. The details of data taking periods E, F, G, H, I are listed in Table 6.5.

Period	Int. luminosity (nb^{-1})	Peak $\langle\mu\rangle$
E	1118	1.52
F	1980	2.05
G	9070	2.82
H	9300	3.21
I	23000	3.82

Table 6.5: Luminosity information for 2010 data taking periods E, F, G, H and I.

The data are compared against the `L1CaloChannelMappingTool`, which takes the database records of the towers known to be affected by the faulty OTX readout to the DAQ systems, disabled by L1Calo experts or classified as unusual/dead.

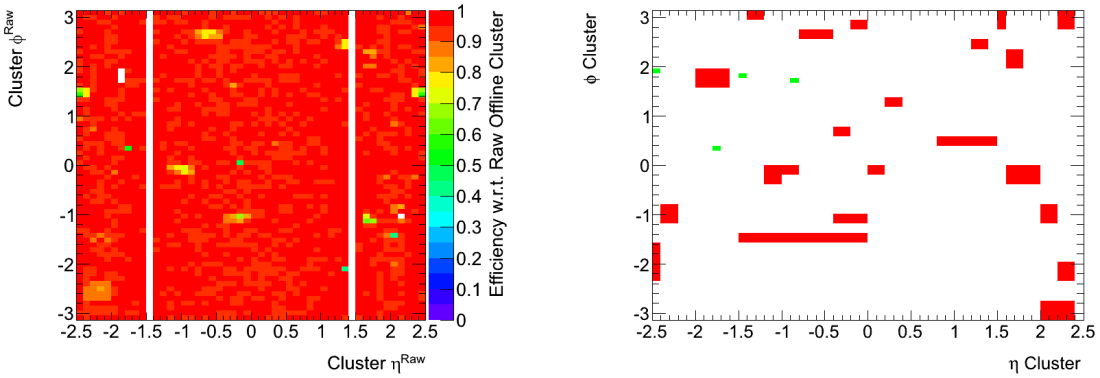

(a) Calculated L1_EM5 efficiency

(b) Bad Calorimeter/Disabled EM Towers

Figure 6.11: η-ϕ maps of L1_EM5 efficiency with respect to 10 GeV clusters and EM Trigger Towers classified as disabled or with bad calorimeter problems (according to the database) for 2010 Period E.

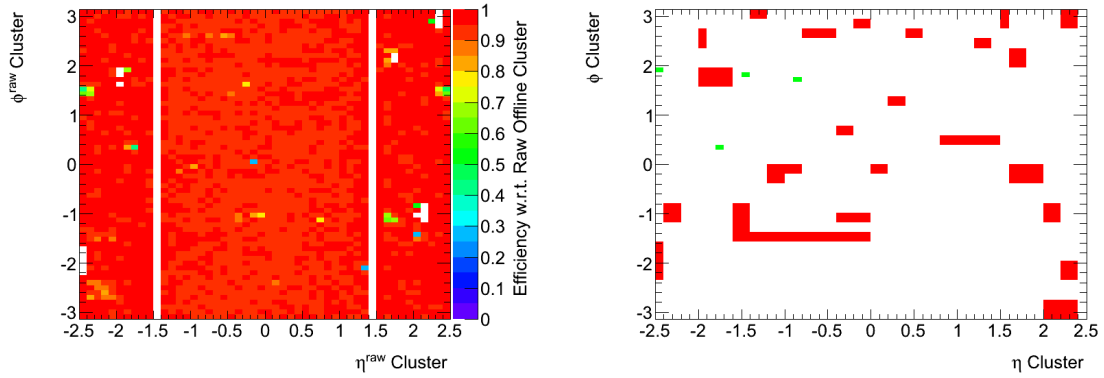

(a) Calculated L1_EM5 efficiency (b) Bad Calorimeter/Disabled EM Towers

Figure 6.12: η-ϕ maps of L1_EM5 efficiency with respect to 10 GeV clusters and EM Trigger Towers classified as disabled or with bad calorimeter problems (according to the database) for 2010 Period F.

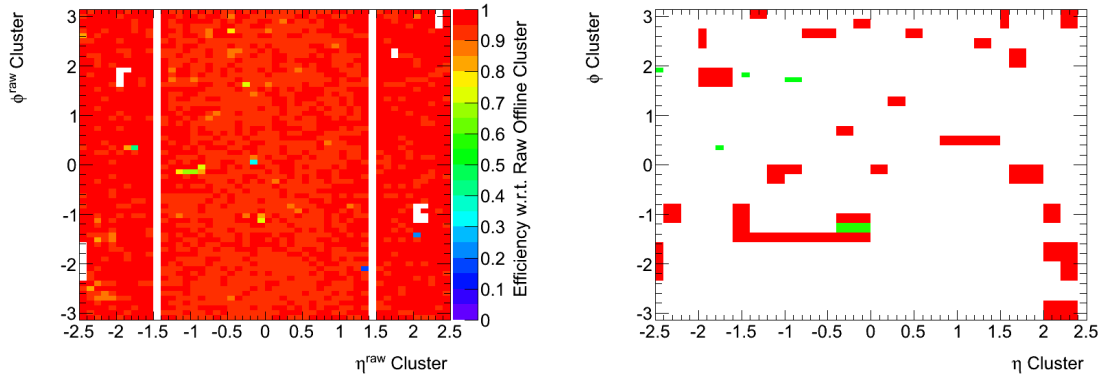

(a) Calculated L1_EM5 efficiency (b) Bad Calorimeter/Disabled EM Towers

Figure 6.13: η-ϕ maps of L1_EM5 efficiency with respect to 10 GeV clusters and EM Trigger Towers classified as disabled or with bad calorimeter problems (according to the database) for 2010 Period G.

Figures 6.11-6.15 show that there are some discrepancies between the areas of reduced efficiency seen in the Trigger Towers, using the method described in Section 6.2.5 (left-hand side plots), and those stored in the databases (right-hand side plots). During this time, the most complete information regarding disabled towers was located on the L1Calo web pages. In addition, the `L1CaloChannelMappingTool` only kept a record of towers that were affected by OTX problems but does not distinguish between the calorimeter sampling layers that are actually affected. If the OTX problem was in the second layer where most of the energy is deposited, then the efficiencies are strongly impacted, but in other layers the effects on efficiencies are small. The implementation of the `L1CaloChannelMappingTool` tool gives the impression that efficiencies are fine even when towers are affected by OTX

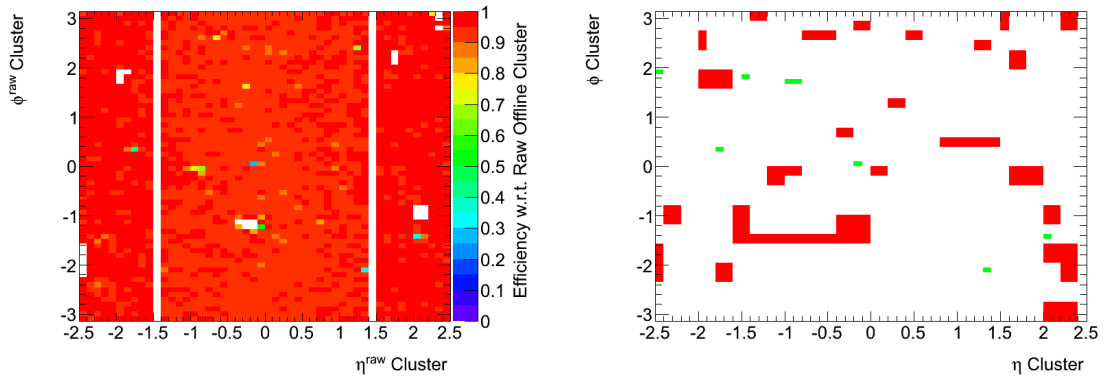

(a) Calculated L1_EM5 efficiency (b) Bad Calorimeter/Disabled EM Towers

Figure 6.14: η-ϕ maps of L1_EM5 efficiency with respect to 10 GeV clusters and EM Trigger Towers classified as disabled or with bad calorimeter problems (according to the database) for 2010 Period H.

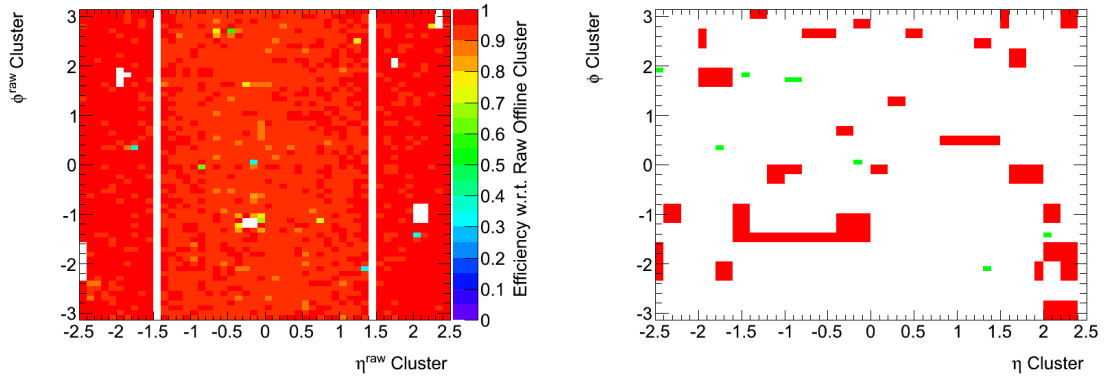

(a) Calculated L1_EM5 efficiency (b) Bad Calorimeter/Disabled EM Towers

Figure 6.15: η-ϕ maps of L1_EM5 efficiency with respect to 10 GeV clusters and EM Trigger Towers classified as disabled or with bad calorimeter problems (according to the database) for 2010 Period I.

issues. This provided good evidence that the databases needed improving and updating more frequently and that the response to areas with poor efficiency should occur with more urgency.

6.3 Studies of L1 Jet Efficiencies in 2011

Jet efficiencies are studied in both the central and forward parts of the detector in 2011 data. In this case, the central region covers the trigger towers up to $|\eta| = 2.9$, and the efficiencies for the L1 jet trigger items are calculated with respect to independently

triggered offline jets according to

$$\epsilon\,(\text{L1\_J}x) = \frac{\text{N}^{\text{o}}(\text{Jet \& } \Delta R \text{ to Jet RoI} < 0.3 \text{ \& RoI passes L1\_J}x)}{\text{N}^{\text{o}}(\text{Jet})} \tag{6.4}$$

where x is the transverse energy threshold (in GeV) for the given trigger item that needs to be exceeded in order to create a Jet RoI and ΔR is the separation in η-ϕ space between the jet and Jet RoI. The ΔR cut value is double that for matching electrons to EM RoIs as the granularity of the jet elements is double that of the trigger towers.

In the forward region, $3.2 < |\eta| < 4.9$, the whole range of the FCAL in η is used for jet elements so very little η information is available. As a result the efficiencies in this region only use a $\Delta\phi$ cut and a check ensuring that the forward jet and Jet RoI are on the same side of the detector. The efficiencies for the forward jet trigger items are calculated as

$$\epsilon\,(\text{L1\_FJ}x) = \frac{\text{N}^{\text{o}}(\text{Forward Jet \& } \Delta\phi \text{ to Jet RoI} < 0.4 \text{ \& RoI passes L1\_FJ}x)}{\text{N}^{\text{o}}(\text{Forward Jet})}\ . \tag{6.5}$$

The intermediate region between the central and forward parts of the detector, $2.9 < |\eta| < 3.2$, uses a combination of these two methods to determine whether the forward or central jet triggers are chosen. At the end of the hadronic end-caps, some of the energy of the jet may be deposited in the FCAL, potentially causing the Jet RoI to be created in either of these detectors.

The jets used in the analysis are reconstructed with the anti-k_{t} algorithm from topological clusters (Section 5.5.1) using a resolution parameter $R = 0.4$ and are required to pass a tight quality cleaning cut. Jets with $R = 0.4$ are favoured over those with $R = 0.6$ as the energy deposited will be contained more easily in the set of 2×2 jet elements that produce a Jet RoI. In addition, at Level 2 and the EF, jets are reconstructed using $R = 0.4$ rather than $R = 0.6$ as is usually the case in offline analyses. The jets are calibrated to the ATLAS electromagnetic scale, again to match more closely with what L1Calo observes in its raw data.

The results of typical jet efficiency studies can be found in Section 6.4.3.2.

6.4 Tier-0 Monitoring of Electromagnetic and Jet Trigger Items

Having run over the data for individual runs and periods for 2010 and 2011 proton-proton collisions, it was deemed more appropriate to automate the process for each run in order to identify potential new areas of the detector with reduced efficiency more easily and quickly.

To do this, the analyses to calculate the efficiencies were migrated to Tier-0 (CERN central data hub, see Section 2.5). At Tier-0, monitoring of new data is achieved by running different analyses over them automatically. This produces histograms that are checked by L1Calo on-call experts to monitor all of the different components of L1Calo. Much of the text that follows was originally written in an ATLAS internal note [77].

6.4.1 Running at Tier-0

At Tier-0, the electromagnetic and jet efficiencies are calculated using separate analyses. For the electromagnetic efficiencies, the analysis runs over full event information (Event Summary Data, ESD) with the $JetTauEtmiss$, $Muons$ and $express$ streams for every proton-proton run. For the jet efficiencies, the analysis runs over ESDs with the $Egamma$, $Muons$ and $express$ streams. For heavy ion runs, only the $express$ stream ESDs are used.

The ESDs are processed in two separate passes. The first pass (ES1) involves express processing at Tier-0 and then the second pass (BLK) is for prompt bulk reprocessing at Tier-0 [78]. The $express$ stream, used exclusively by ES1, has smaller statistics of electrons, photons and jets to analyse, but the results are available sooner and can give a fast, crude measure of whether there are any problems or not. The $JetTauEtmiss$ and $Egamma$ streams, the main streams to look at for the electromagnetic and jet efficiencies respectively, can then be studied to identify any potential problems in greater detail.

For the processing of BLK ESDs, events with noise bursts and data integrity errors in the LAr calorimeter can be identified [79]. This means that between the ES1 and BLK

express stream ESD results for a given run, it is possible to see in the ES1 sample if there were regions of the detector affected by noise bursts as these will typically appear to have reduced efficiency.

To quantify the performance of L1Calo for data quality (DQ) purposes [80], automated checks are applied to selected histograms. The DQ algorithm applied to turn-on curves determines how many data points between $0 < E_T < 100$ GeV, in units of 1 GeV, have an efficiency below a predefined threshold across the displayed E_{T} range of the histogram. The DQ classification of *Green*, *Yellow* or *Red* for each efficiency depends on additional thresholds.

The efficiency threshold for all trigger items is currently set to 90%. This means that currently any efficiency drop bigger than 10% can be spotted automatically and anything smaller than this will have to be viewed. The DQ classification thresholds are tailored for each trigger item having a different energy at which the plateau is reached. Taking the L1_EM12 efficiency for example, to have a *Green* DQ flag less than 45 of the 100 data points must be below the efficiency threshold and 85 of the 100 for a *Yellow* flag. The efficiency and bin thresholds are set to account for runs with low statistics.

6.4.2 List of Plots

For each L1Calo electromagnetic and jet trigger item, the efficiencies are created as two separate distributions. These are presented as a turn-on curve or as an η-ϕ map.

The η-ϕ maps are produced above selected transverse energy thresholds for the offline object studied (e.g. jets above 50 GeV). This is also done for each L1 jet trigger item with the addition that if it shares an energy threshold with a corresponding forward jet trigger item then a separate set of η-ϕ maps and turn-on curves are produced for the combination of the matching jet and forward jet trigger items (e.g. L1_J30 & L1_FJ30). The plots and thresholds are optimised for the electromagnetic and jet trigger configurations as the trigger menu changes.

Additionally for the η-ϕ maps, to help distinguish between histogram bins corresponding

to trigger towers with poor performance and those with low statistics, if any of the bins have fewer entries than a threshold then these are automatically set to 100%. The threshold is currently set to 3 entries per bin for all EM η-ϕ maps and 6, 4 and 2 bins for Jet η-ϕ maps at 50, 100 and 200 GeV, respectively.

The efficiencies are produced for each data-taking run and the histograms can be accessed either from the Data Quality Monitoring (DQM) web page [78] or by downloading the files from the Grid. The histograms used to make the efficiencies (numerator and denominator) are also available as well as plots of EM and HAD trigger towers flagged as being 'dead'/'miscalibrated' channels or having other hardware problems to compare against, as stored in the conditions databases.

6.4.2.1 Electromagnetic Efficiencies

The electromagnetic efficiencies produced as η-ϕ maps have a cut applied on the raw cluster E_{T} at thresholds of 10, 20 and 30 GeV. For each data-taking run, it is suggested that the on-call experts study the turn-on curves for each L1 electromagnetic trigger item, not containing a hadronic veto[5], to see if they have a *Green* DQ flag and if there is any reduction in efficiency once the plateau of curve has been reached. η-ϕ maps are also suggested to be studied to look for trigger towers with low efficiency.

6.4.2.2 Jet Efficiencies

The jet efficiencies produced as η-ϕ maps have a cut applied on the jet electromagnetic scale E_{T} at thresholds of 50, 100 and 200 GeV. For each data-taking run, it is again suggested that on-call experts inspect the turn-on curves for each L1 jet trigger item to see if they have a *Green* DQ flag and there are no reductions in efficiency.

[5]Generally, the trigger items with a hadronic veto have a poorer performance due to hadronic candidates entering the data sample.

6.4.3 Results from Tier 0

6.4.3.1 Electromagnetic Efficiencies

Figures 6.16 and 6.17 show typical results for turn on curves and η-ϕ maps in 2011 data as produced at Tier-0. There is a sharp rise of the turn on curve and the plateau of the curve reaches 100% for L1_EM16V, reflecting the good performance of the trigger towers to find electrons and photons in η and ϕ.

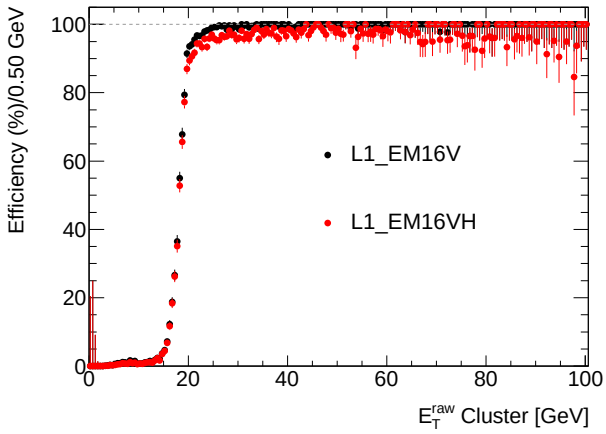

Figure 6.16: Efficiency with respect to clusters of tight offline electrons and photons as a function of the raw cluster E_{T} for the L1_EM16V and L1_EM16VH electromagnetic trigger items using the *JetTauEtmiss* stream for run 203876.

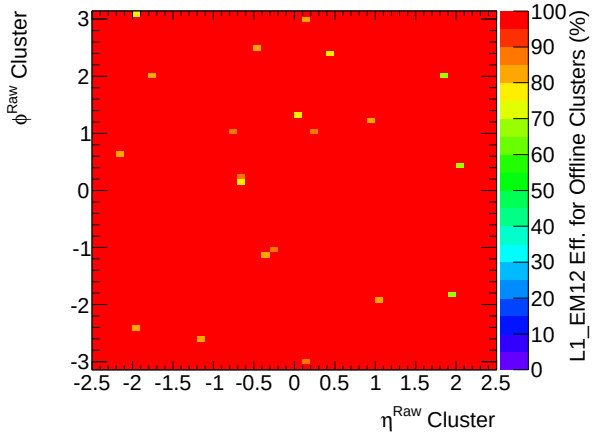

Figure 6.17: L1_EM12 efficiency map in η-ϕ for offline clusters with $E_{\mathrm{T}}^{\mathrm{raw}}$ greater than 30 GeV using the *JetTauEtmiss* stream for run 203876.

The express stream proved useful in identifying noise bursts in the EM calorimeter. The noise is reconstructed by the ATLAS reconstruction software as electrons and photons

over a wide range of transverse energies, but is not triggered on by L1Calo. Figure 6.18 shows the effects of noise bursts spread across the electromagnetic end-cap on the C side of the detector ($\eta < -1.5$) in a 2012 run.

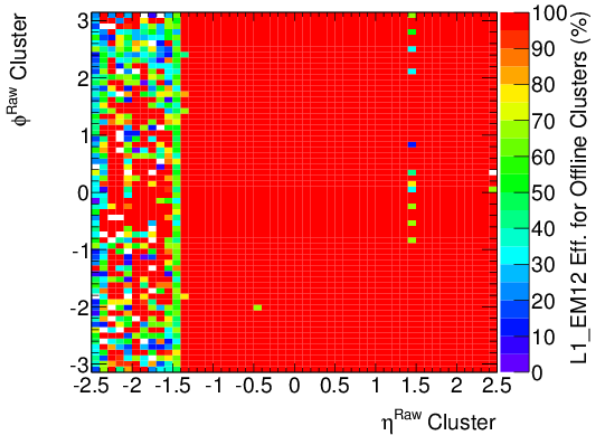

Figure 6.18: L1_EM12 efficiency map in η-ϕ for offline clusters with $E_{\text{T}}^{\text{raw}}$ greater than 30 GeV using the *express* stream for run 203636. The noise bursts observed at $\eta^{\text{raw}} < -1.5$ result in reduced apparent efficiencies.

6.4.3.2 Jet Efficiencies

Figure 6.19 shows example turn-on curves for the six lowest L1 jet trigger items made by doing tests with single runs of 2011 data to replicate what is done at Tier-0. These results match expectations for L1 efficiencies in terms of the shapes, with the plateau of the curves reaching 100% at sufficiently large E_{T}. Jet trigger items with an energy threshold above 150 GeV are likely to be too high in energy to be able to study properly on a run-by-run basis due to a lack of statistics.

Figure 6.20 shows results for an η-ϕ map, from studies of 2011 data. Based on the turn-on curves for the jet trigger items, the lowest suitable jet E_{T} cut for the η-ϕ maps was 50 GeV . On a run-by-run basis, the statistics potentially do not cover the most forward jets. Generally the efficiencies are very high, but for higher energy threshold items, it may be seen that the region which corresponds to the transition between the electromagnetic barrel and end-caps has reduced efficiency. This is partly due to some energy loss by L1Calo and higher levels of jet energy calibration to correct for the difficulty in the energy measurement here.

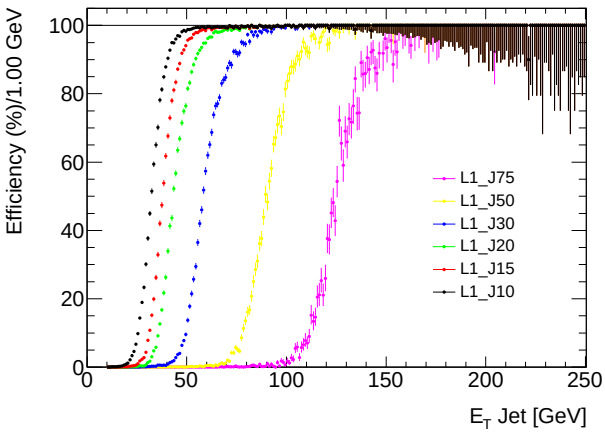

Figure 6.19: Efficiency with respect to $R = 0.4$ anti-k_t jets as a function of the electromagnetic scale jet E_T for the L1_J10, L1_J15, L1_J20, L1_J30, L1_J50 and L1_J75 jet trigger items in the run 191933 *Egamma* stream.

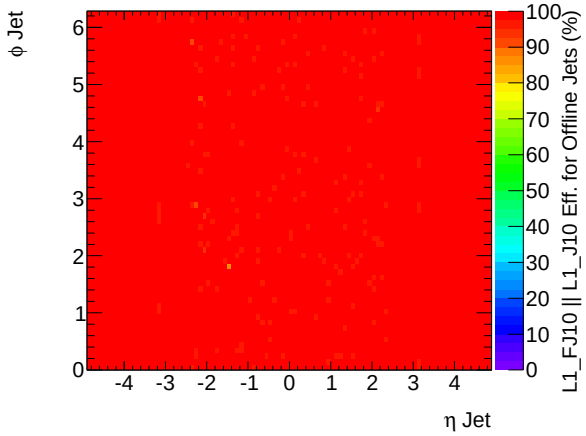

Figure 6.20: An efficiency map in η-ϕ for the combination of the L1_J10 and L1_FJ10 trigger items for $R = 0.4$ anti-k_t jets with an electromagnetic scale jet E_T greater than 50 GeV for the run 191190 *Egamma* stream.

Although the algorithm to produce Jet RoIs uses jet elements, the jet η-ϕ maps are binned using trigger towers so that it is possible to compare regions with lower efficiency with 'dead' towers or those with bad calorimeter connections.

6.4.4 Future Work

For future collisions, the Tier-0 analysis code is open to improvements in order to become more useful and to accommodate different L1Calo conditions as they change. More

sophisticated and sensitive Data Quality algorithms can be developed to check for low statistics, to avoid false flagging of errors and make the existing parameters tighter. New DQ algorithms could also be developed for the η-ϕ maps.

In 2015, L1Calo is expected to use much higher granularity digital data to select high energy deposits and the pile-up levels will increase. There will be improved EM trigger isolation definitions, implemented as a function of E_{T} rather than a single fixed value to select candidates, meaning all of the thresholds are likely to change. With the prescales becoming higher and the bandwidths for single electron or jet triggers becoming limited, the default Tag-and-Probe methods e.g. $Z \rightarrow ee$ may become more suitable for candidate selection.

6.5 Summary

A strategy has been developed to monitor the ATLAS L1Calo electromagnetic trigger items with respect to offline reconstructed electron and photon candidates, in order to determine and improve the performance of the L1Calo hardware. In order to to this, a new method for measuring triggering efficiencies using an independently triggered jet Tag-and-Probe has been proposed and developed. The majority of the time, the L1Calo hardware works very well in triggering on the candidates it sees. The efficiency turn-on curves generally have the expected shape with well above 95% of electron and photon candidates of sufficiently high energy being able to produce a trigger. Improvements in the reconstruction and selection of candidates will make the rise in the turn-on curves sharper in the future.

Although the digital electronics within L1Calo are well under control, there are many opportunities for noise build up and other problems with the propagation of analogue signals from the electromagnetic and hadronic calorimeter front-ends into the many stages of the L1Calo electronics.

One effect of this, seen in early 2010 running, is the unexpected bump in the trigger efficiencies at low transverse energies. The causes for the bump in the efficiency for the

L1_EM2, L1_EM3 and L1_EM5 trigger items have been investigated thoroughly and are attributed to 5 effects, with propagation of noise being dominant.

A further effect is a reduced amount of energy seen by L1Calo for high E_{T} clusters in some regions, resulting in trigger thresholds not being passed and EmTau RoIs not being produced. In 2010, Trigger Towers with poor performance were identified and reported to hardware exports, who followed (and mostly fixed) the problems. Tools have now been developed which allow the trigger towers with poorer performance for producing RoIs to be identified automatically so that the hardware experts can be informed of them.

The results for 2011 data show that the jet Tag-and-Probe method provides good statistics for checking the electron and photon efficiencies with sufficient coverage across the EM trigger towers. Apart from the electromagnetic trigger towers that were known to have issues in 2011, the L1Calo electromagnetic trigger towers work very well. Inverting this procedure, an electromagnetic Tag-and-Probe method is used to measure L1 jet efficiencies. The efficiencies for triggering on both jets and forward jets are very high in 2011 and 2012.

Using Tier-0 software, a set of plots is automatically produced for each data run to monitor the L1Calo efficiencies for identifying electrons, photons and jets. For each run in 2012, the results of these analyses were checked by L1Calo on-call shifters so that regions of poor trigger tower performance were identified quickly.

CHAPTER 7

Diffractive Dijet Production

Perturbative QCD (pQCD) has been very successful in describing many areas of hadron collider physics, but is limited to the regime of hard scattering where the strong coupling is small. Diffraction is usually associated with lower energies, where gluon interactions are very strong, making it non-perturbative and a subject whose description is based on phenomenology or effective theories. Hard diffraction is a subset of diffraction, in which a hard scatter takes place in the interaction, providing a bridge between non-perturbative and perturbative QCD. It is an interesting field to study experimentally, leading to a greater understanding of the nature of high energy scattering processes and the dynamics of hadron collisions.

7.1 Quantum Chromodynamics and Jet Production

Quantum chromodynamics (QCD) describes the strong interaction between quarks and gluons. Quarks and gluons carry an additional charge, related to the symmetry of the

SU(3) group, known as colour. In quantum electrodynamics, the coupling that determines the strength of the interaction (α_{EM}) is small and increases slowly with the energy scale of the interaction. By contrast in QCD, the running coupling α_s varies strongly with the energy scale of the interaction. The value of the strong coupling is small at high energy (very small distance scales), a regime known as asymptotic freedom, which means that the interactions between quarks and gluons are weak and perturbative QCD can be used to describe the interactions.

At low energy scales, the strength of the coupling is large and so non-perturbative approaches have to be adopted to describe interactions. A property of QCD at low energy scales is confinement. Both quarks and gluons carry colour but they are not found as single free objects in nature. Unlike the Coulomb force or gravity where the potential diminishes with distance, $V(r) \propto 1/r$, for the strong force the potential behaves as $V(r) \sim r$ such that the force is constant with increased separation. It would require infinite energy to separate two quarks, which means that quarks stay in colour-bound states such as mesons and baryons.

QCD hard scattering processes create high transverse momentum quarks or gluons. These particles radiate as they emerge from the hard interaction, producing lower p_T particles which are approximately collinear with their parents (fragmentation). Thus a parton shower is created, where one parton will radiate gluons, which will in turn produce $q\bar{q}$ pairs and so on. The resulting collection of highly energetic partons is known as a jet. Perturbative QCD calculations may have coloured partons in the final state, but only the combination of coloured partons into bound states of colourless hadrons (hadronisation) are observed experimentally. Parton showering produces partons of successively lower energy, and must ultimately exit the region of validity for perturbative QCD. Different phenomenological models are applied to describe the showering process, and the combination of coloured partons into bound states of colourless hadrons, which is inherently non-perturbative.

The probability of creating a certain set of jets is described by the jet production cross section, which from the QCD factorisation theorem, can be split up into the perturbative parton cross section ($\hat{\sigma}$) and non-perturbative parts such as the parton distribution

functions ($f_{i/p}(x_i, Q^2)$), giving the likelihood for partons to be found within the proton for given kinematics. The general hard scattering produces a cross section of the form

$$\sigma_{pp\to j_1 j_2 X} = \int dx_i dx_k f_{i/p}(x_i, Q^2) f_{k/p}(x_k, Q^2) \hat{\sigma}_{ik\to j_1 j_2} \tag{7.1}$$

where x is the fraction of the momentum carried by partons i and k from their respective protons, Q^2 is the squared energy of the hard partonic interaction, $j_1 j_2$ represents the dijets and X represents the remnants of the two protons. There are numerous ways this can proceed at LO: $pp \to jjX = gg \to gg$, $qg \to qg$, $qq \to qq$, $q\bar{q} \to q\bar{q}$, $q\bar{q} \to gg$, $gg \to q\bar{q}$.

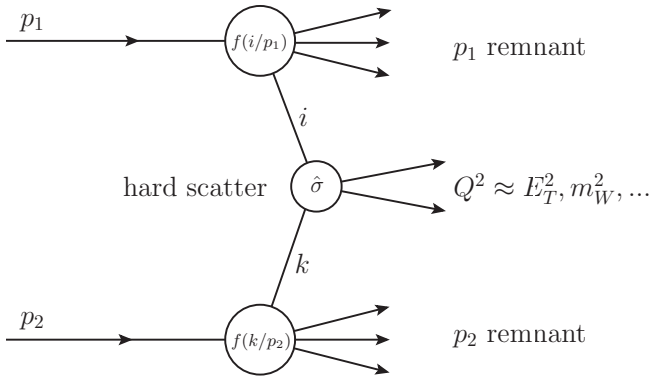

Figure 7.1: Feynman diagram of a generic hard scattering.

The parton distributions, $f_{i/p}(x_i, Q^2)$, used in these hard-scattering calculations are solutions of the DGLAP (Dokshitzer-Gribov-Lipatov-Altarelli-Parisi) equations [81–83], which determine the Q^2 dependence of the PDFs. The x-dependence has to be obtained from fits to DIS and other hard scattering data. Additional perturbative corrections (higher orders of the perturbative expansion) can be included in the calculation to better account for effects of gluon radiation.

7.2 Diffraction

The total proton-proton cross section can be divided into elastic ($pp \to pp$ in the LHC context) and inelastic (all other processes) components. Elastic collisions involve the incoming protons interacting usually with only a very small 4-momentum transfer (typically

$|t| < 1.0$ GeV^2) and staying intact. The protons may be detected at very forward η with no new particles being observed in the centre of a detector. Inelastic collisions, which make up all other types of collision, cause the protons to break up with further particles being produced. Inelastic proton-proton collisions can happen in many ways and are often classified into three major categories: single diffractive (SD, $pp \to Xp$ or $pp \to pX$), double diffractive (DD, $pp \to XY$) and non-diffractive (ND), based on the rapidity (y) distribution of the products, as shown in Figure 7.2. The ATLAS measurement of the total inelastic proton-proton cross section at the LHC suggests that diffraction makes up approximately 30% of all inelastic interactions [84].

The outputs are classified in terms of the dissociated systems, most generally X and Y, where X has a larger invariant mass than Y by convention ($M_X > M_Y$). In the case of single diffractive events, system Y would contain the intact proton, meaning $M_Y = m_p$, or a low mass excited state just above m_p. There is also central diffractive (CD, $pp \to pXp$) production in which both protons are left intact by the scattering process but produce activity in the central region and two rapidity gaps occur in forward regions. At Tevatron energies, the CD cross section was seen to be suppressed relative to SD by a factor of about 10 [85].

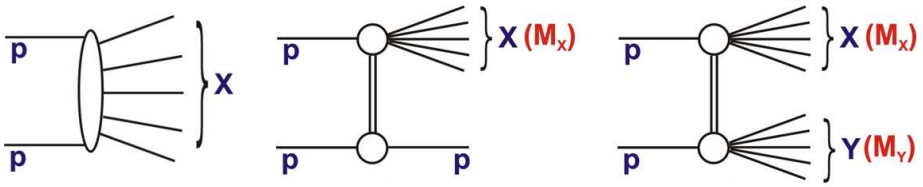

(a) Non diffractive (b) Single diffractive (c) Double diffractive

Figure 7.2: Diffractive and non-diffractive processes [86].

Elastic and diffractive scattering are well-described by the phenomenology of a strongly interacting colour singlet exchange (as described by Regge theory [87], Section 7.2.1), with the quantum numbers of the vacuum. A strong colourless exchange produces no gluon radiation, resulting in a region of the detector ($\Delta\eta$ or Δy) in which there is an absence of associated hadronic activity, known as a 'rapidity gap' or Large Rapidity Gap (LRG). In SD and DD events, the momentum exchange associated with this colour singlet particle causes the dissociation to happen but in elastic events the protons remain intact after the momentum transfer. In ND events, there is a coloured exchange between the

protons, resulting in many particles being produced across the detector as the colour neutralises. This division is illustrated in Figure 7.3 where a rough sketch of typical rapidity distributions of the particles produced in each type of collision is presented.

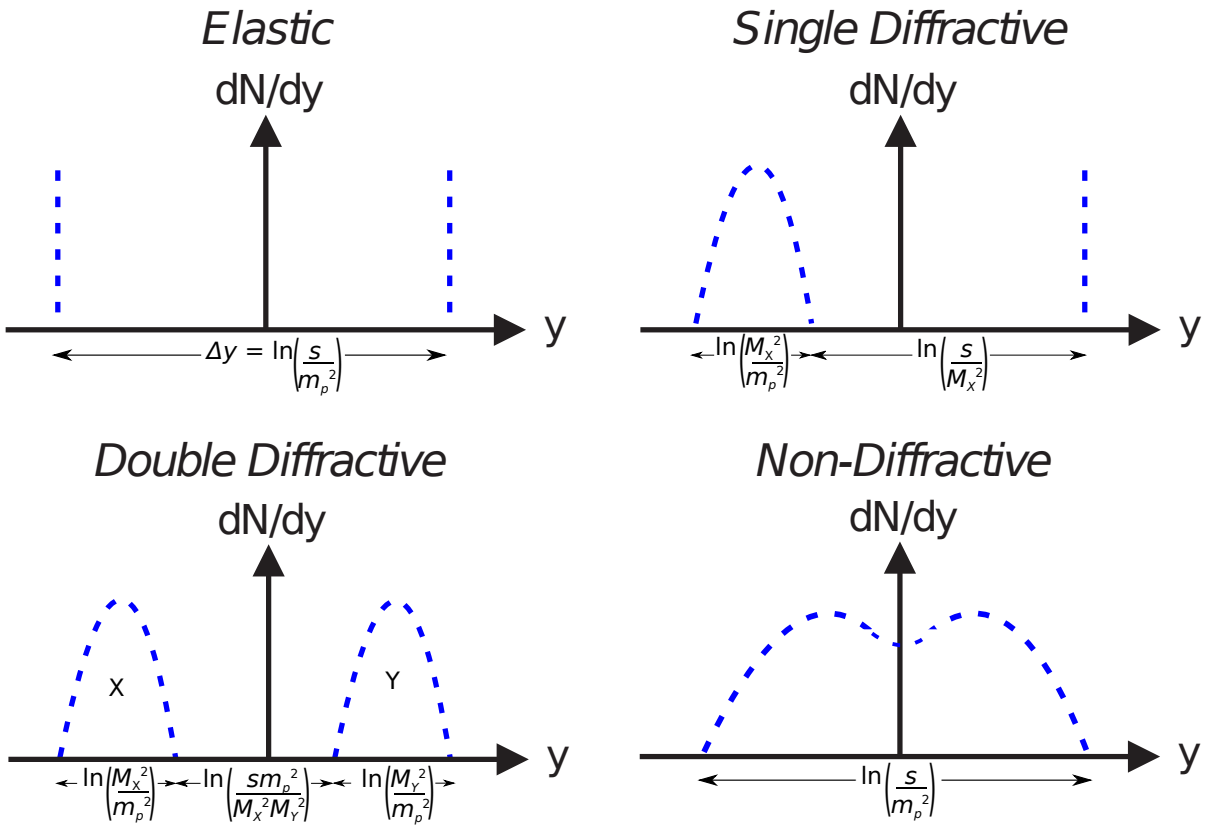

Figure 7.3: Rapidity distributions for particles in events involving elastic collisions, non-diffractive, single diffractive and double diffractive production.

Large rapidity gaps may also occur in non-diffractive collisions due to fluctuations in the hadronisation process. The size of the gap can be related to the density of particles, ρ, by Poisson statistics, as

$$P(\Delta\eta) = e^{-\rho\Delta\eta} \ , \tag{7.2}$$

implying that larger gap sizes are exponentially suppressed.

Figure 7.4 shows a Feynman diagram of a single diffractive event involving two protons, similar to Figure 7.2(b) but with a few additional details. In this case, t is the four-momentum transfer squared between the two protons and ξ, often referred to as $x_{\mathbb{P}}$, is the fractional momentum loss of the proton that remains intact. It is related to the invariant

mass of diffractive system X as

$$\xi_X = \frac{M_X^2}{s} \tag{7.3}$$

and similar relations hold for the double diffractive case, where there is an additional variable for the Y system,

$$\xi_Y = \frac{M_Y^2}{s} \ . \tag{7.4}$$

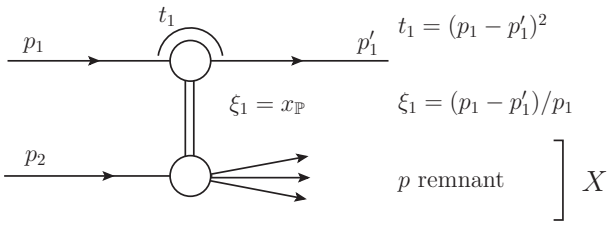

Figure 7.4: Feynman diagram of a soft single diffractive scattering.

For diffractive processes, increasing gap sizes are not exponentially suppressed. For SD events, the size of the gap between the intact proton and diffractive system X varies as $\Delta\eta \simeq \ln(s/M_X^2) = -\ln(\xi)$.

7.2.1 Regge Theory and the Pomeron

The most commonly adopted theory of diffractive interactions comes from Regge theory, which predates QCD in trying to describe soft hadron-hadron interactions.

As mentioned in 1, an electromagnetic interaction is mediated by the exchange of a photon. Regge theory works in a similar way to describe cases where particles such as protons are scattered via the strong force, but now the exchange is made by whole families of related particles. An example is the vector (spin-1) ρ meson, followed by its counterparts with higher spin and mass (ρ_3, ρ_5 with spin-3, spin 5, etc.). Each such set of exchange particles can be described by a experimentally determined, t-dependent Regge trajectory of the form

$$\alpha(t) = \alpha(0) + \alpha' t \ . \tag{7.5}$$

The trajectory corresponds to a straight line in the plane of spin versus mass squared with

an intercept, $\alpha(0)$, and slope, α'. The value of the trajectory at $t = 0$ is important in Regge theory for describing the energy dependence of the total cross section via $\sigma_{tot} \propto s^{\alpha(0)-1}$.

The pomeron, $\mathbb{P}$, is a special trajectory with the quantum numbers of the vacuum, and the intercept of slightly above unity[1] is often expressed as

$$\alpha_{\mathbb{P}}(0) = 1 + \epsilon \ . \tag{7.6}$$

Donnachie and Landshoff found, from fitting total cross sections of pp and $p\bar{p}$ data, the pomeron to be described by $\epsilon = 0.08$ and $\alpha'_{\mathbb{P}} = 0.25$ GeV^{-2} [88]. This can be compared with mesons, such as the ρ, where $\alpha(0) = 0.55$. The exchange of a pomeron in QCD can be interpreted as a multi-gluon exchange, and has been used to describe elastic and diffractive scattering.

Regge theory defines the probability of a pomeron being emitted from a proton, known as the pomeron flux factor, of the form

$$f_{\mathbb{P}/p}(t, \xi) = A_{\mathbb{P}} e^{b_{\mathbb{P}} t} / \xi^{2\alpha_{\mathbb{P}}(t)-1} \tag{7.7}$$

where the $e^{b_{\mathbb{P}} t}$ is an experimentally determined parametrisation of the t dependence.

The cross section as a function of ξ follows from this and is given as:

$$\frac{d\sigma}{d\xi} \propto \left(\frac{1}{\xi}\right)^{2\alpha_{\mathbb{P}}(t)-\alpha_{\mathbb{P}}(0)} \ . \tag{7.8}$$

For further details, see [89].

7.2.2 Experimentally Searching for Diffraction

There are two methods used to identify diffraction, that exploit as much of the rapidity acceptance of an experiment as possible. One involves identifying and measuring the rapidity gap based on calorimetry and tracking detectors and the other is to tag the intact scattering protons using a proton tagger placed hundreds of metres down the beam

[1] If $\epsilon = 0$ then the pomeron is called a "critical" pomeron, if $\epsilon > 0$ it is "super-critical".

pipe, away from the central detector.

The rapidity gap method is capable of measuring large gaps, provided there is high efficiency to trigger on events with limited activity in the detector and pile-up rates are negligible. Depending on the number of rapidity gaps and their separation, it is possible to distinguish between the different diffractive processes. Ideally, a proton tagger would be used in conjunction with searching for rapidity gaps to identify the intact proton. This removes the potential contamination of rapidity fluctuations in the hadronisation and/or low multiplicity in non-diffractive events. A proton tagger could also identify if the scattered proton remains intact or dissociates into a very low mass state that could go straight down the beam pipe (separating DD and SD topologies), and if the proton trajectory can be measured then the values of ξ and t can be inferred.

7.3 Hard Diffraction and Diffractive Dijets

From soft diffractive and elastic interactions, it is not possible to determine the underlying parton dynamics of the process and understand the composition of the pomeron. Ingelman and Schlein introduced the idea of hard diffractive scattering [90], by proposing jets in diffractive events as a way of probing the nature of the exchanged object, corresponding to a pomeron with its own partonic substructure that varies depending on the energy scale Q^2. They assumed that the pomeron can be treated as an object that couples to the a proton, with the probability for radiating a pomeron from the proton defined by the pomeron flux factor based on Regge theory (Equation 7.7).

Hard diffractive processes involve the production of a high mass or large p_T state that can be calculated perturbatively and provides information on the proton Diffractive Parton Distribution Functions (DPDFs). Based on the success of the QCD factorisation theorem [91] proven for diffractive electron-proton interactions, in the Ingelman-Schlein model the cross section factorizes into a DPDF, f^D, and the standard QCD partonic cross section of the hard sub-process, $\hat{\sigma}$, as

$$\sigma = f^D(x, Q^2, \xi, t) \otimes \hat{\sigma}(x, Q^2) \ . \tag{7.9}$$

The diffractive parton distribution function for the proton can be further decomposed into the pomeron flux factor and the probability of finding a parton i in the pomeron

$$f^D(x, Q^2, \xi, t) = f_{\mathbb{P}/p}(t, \xi) f_{i/\mathbb{P}}(Q^2, x) \ . \tag{7.10}$$

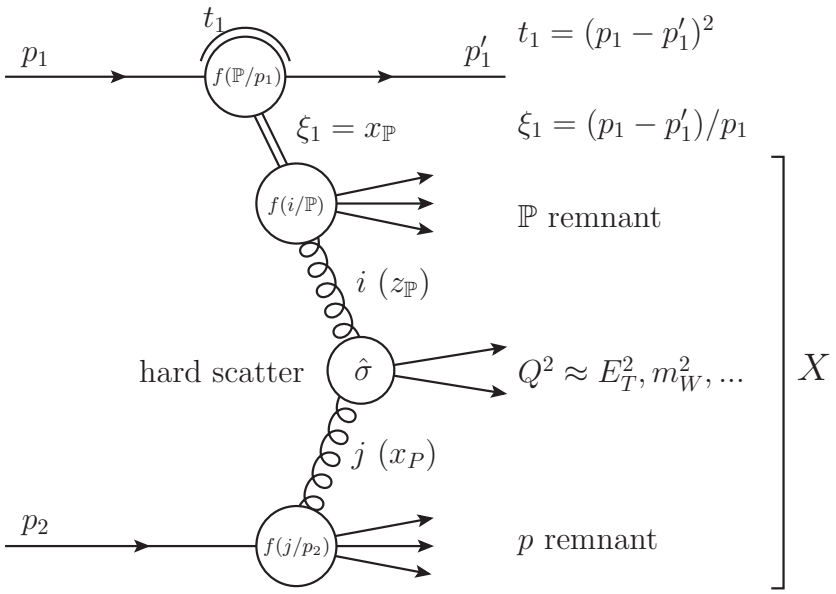

Figure 7.5: Feynman diagram of hard single diffractive scattering.

Figure 7.5 shows a Feynman diagram for a general single diffractive process including a hard scatter, producing a scattered proton, and a rapidity gap. QCD factorisation means that this diagram can be thought of as the combination of Figures 7.1 and 7.4. The new variable that aids the description of the hard diffractive interaction is $z_{\mathbb{P}}$, also known as β, which measures the fraction of the pomeron momentum that is transferred to the parton entering the hard interaction.

7.3.1 Diffractive Parton Density Functions

The first evidence of dijets in single diffractive events was found by the UA8 Collaboration in proton-antiproton collisions at $\sqrt{s} = 630$ GeV and was interpreted in terms of DPDFs [92, 93].

The DPDFs have since been determined precisely by the HERA experiments by performing NLO QCD fits at H1 [94], using inclusive diffractive deep inelastic scattering data ("H1 2006 DPDF Fits A and B"). There is also a leading order DPDF Fit B which produces similar distributions to the NLO fit. This result was added to by performing a simultaneous fit of diffractive inclusive and dijet production data ("H1 2007 DPDF Fit Jets") [95]. ZEUS [96] also produced similar fits in 2010. The DPDFs in these fits assume a general form for gluon and quark densities of $A_i z^{B_i}(1-z)^{C_i}$, with Fit A omitting the B term for gluons only and Fit B omitting the B and C gluon terms. All three fits have been successfully used to describe different hard-diffractive processes in ep collisions.

The 2006 fits gave an effective pomeron trajectory with $\alpha_{I\!P}(0) = 1.118 \pm 0.008\,(\text{exp.})^{+0.029}_{-0.010}\,(\text{sys})$. Fit B has since been adopted as standard due to its slightly better description of final state DIS data. The 2007 fits to jet data are compatible with 2006 Fit B and improve the accuracy for describing the gluon and quark content of the pomeron for $0.05 \leq z_{I\!P} \leq 0.9$, giving a pomeron intercept of $\alpha_{I\!P}(0) = 1.104 \pm 0.007$ (exp.). In all of these DPDFs the majority of the pomeron momentum is carried by gluons with a small quark contribution.

7.4 Factorisation Breaking and Rapidity Gap Survival Probability

QCD diffractive factorisation works very well in diffractive ep DIS collisions but at hadron-hadron colliders, this factorisation is broken due to soft interactions and rescatterings among spectator particles in the interaction that result in the loss of the rapidity gap and diffractive signature, suppressing the visible diffractive cross section, σ^D. The amount of suppression for σ^D is quantified as a factor, S^2 (also known as $\langle S \rangle^2$), known as the 'rapidity gap survival probability' [97].

This factorisation breaking was first observed at the Tevatron when studying diffractive dijets in $p\bar{p}$ collisions. The CDF (Collider Detector at Fermilab) diffractive dijet data (see Section 7.5.1) were compared with NLO predictions with H1 DPDFs, extrapolated to the ξ range covered by the Tevatron using the Regge flux factor (Equation 7.7). As shown

in Figure 7.6, there was disagreement between the data and the predictions by a factor of approximately 10 ($S^2 \sim 0.1$), with some dependence on $z_{\mathbb{P}}$ [98]. In 2009, the results were re-evaluated at next to leading order [99] and confirmed that S^2 is dependent on $z_{\mathbb{P}}$, varying from 0.05 at $z_{\mathbb{P}} = 10^{-1}$ to 0.3 at $z_{\mathbb{P}} = 10^{-3}$.

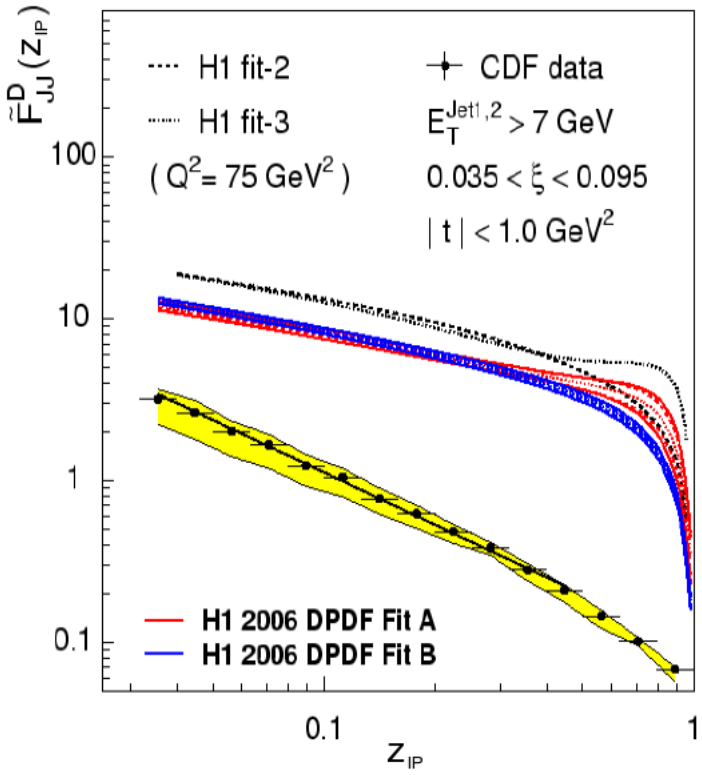

Figure 7.6: Comparison of H1 DPDF based predictions to Tevatron data, as a function of the fraction of momentum transferred from the pomeron to the parton involved in the hard scatter. The disagreement between the data and the predictions from H1 data, extrapolated to Tevatron energies, suggests that factorisation is broken [98].

The KKMR model (Kaidalov et al. [100]) predicts the QCD factorisation breaking based on multi-pomeron exchanges, and is able to reproduce the observations at the Tevatron for single diffractive dijets. Other KMR models [101] suggest that S^2 is approximately 0.04 at LHC energies.

7.5 Recent results

As well as trying to determine the structure of the pomeron, the aims of studying diffractive dijets include the determination of the gap survival probability at LHC energies.

7.5.1 Tevatron Diffractive Dijets

The Tevatron studied diffraction in proton-antiproton collisions in Run I at $\sqrt{s} = 630$ GeV and 1.8 TeV [102], and also in Run II at 1.96 TeV [103], at the CDF experiment with $|t| < 1$ GeV^2 and $0.035 < \xi < 0.095$. In addition to confirming that QCD factorisation is broken in hadron-hadron collisions (Figure 7.6), other interesting results were obtained.

A measurement of the single diffractive structure function, $F_{jj}^{SD}(x, Q^2)$, is calculated based on the ratio, $R_{SD/ND}$ of the diffractive and non-diffractive distributions and knowledge of the normal proton structure function as

$$R_{SD/ND}(x, Q^2, \xi, t) = \frac{n_{jj}^{SD}(x, Q^2, \xi, t)}{n_{jj}^{ND}(x, Q^2)} \simeq \frac{F_{jj}^{SD}(x, Q^2, \xi, t)}{F_{jj}^{ND}(x, Q^2)} \tag{7.11}$$

where n_{jj}^{SD} and n_{jj}^{ND} are uncorrected numbers of single diffractive and non-diffractive dijet events $F_{jj}^{ND}(x, Q^2)$ is known from inclusive deep inelastic scattering data. $R_{SD/ND}$ was found to be consistent at $\sqrt{s} = 630$ GeV and 1.8 TeV.

In Run I, the $z_{\mathbb{P}}$, Q^2 and t dependence was tested and the results were confirmed by Run II. Over the range $10 < Q^2 < 10^4$ GeV^{-2}, there was no significant Q^2 or t dependence to the ratio and this suggested that the pomeron behaves similarly to a proton.

7.5.2 CMS Diffractive Dijets

At CMS, the measurement of diffraction, as a contribution to dijet production, was performed in early 2010 running with low pile-up, corresponding to an integrated luminosity of 2.7 nb^{-1} [104]. This is the first measurement of diffractive dijets at the LHC.

The data were selected by triggering on at least one jet with an uncorrected $p_T > 6$ GeV and then the off-line selection involved at least two anti-k_{t} jets reconstructed with $R = 0.5$ with $p_T > 20$ GeV in the range $|\eta| < 4.4$. For the diffractive selection, the detector covers the range $|\eta| < 4.9$ so it was required that there be at least 1.9 units of pseudorapidity from one edge of the detector with no activity ($|\eta_{max}| > 3$ or $|\eta_{min}| > -3$), where η_{max} (η_{min}) is the pseudorapidity of the most forward (backward) object per event. The data were

compared against different Monte Carlo models. Non-diffractive dijets were generated with PYTHIA6 [105] and PYTHIA8 [106] and diffractive dijets, using DPDFs from H1 2006 fit B, are generated at leading order (LO) by using POMPYT (SD) [107], POMWIG (SD) [108] and PYTHIA8 (SD+DD) and at next-to-leading order (NLO) with POWHEG [109].

The measurements of inclusive dijets are presented as a function of $\widetilde{\xi}$ before and after requiring the diffractive selection, over the range $0.0003 < \widetilde{\xi} < 0.01$. $\widetilde{\xi}$ is an approximation to the generated ξ, calculated from the sum of E and p_z of particles reconstructed within the detector acceptance, with a correction factor derived from Monte Carlo applied to data accounting for truth particles that are not reconstructed. The data were best described by a normalised mixture of non-diffractive PYTHIA8 and single diffractive POMPYT as shown in Figure 7.7.

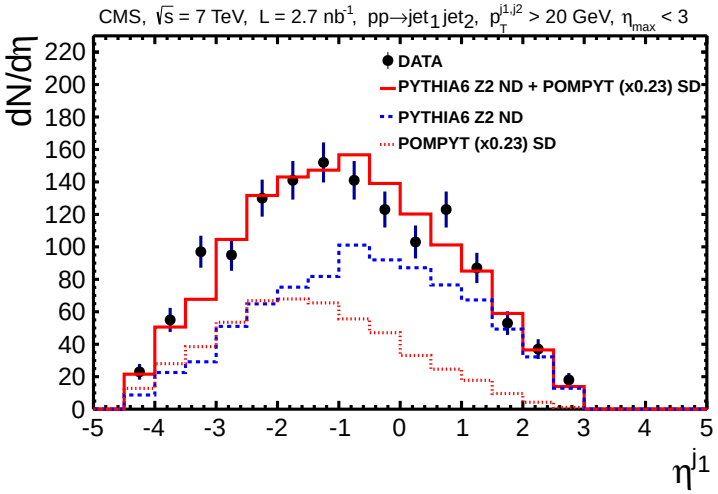

Figure 7.7: Distribution of the leading jet η, after applying the gap and jet requirements. The CMS data are best described by a combination of PYTHIA8 ND and 0.23× PYTHIA8 SD [104].

As shown in Figure 7.8, the various non-diffractive models underestimate the data in the lowest bin $\widetilde{\xi}$ ($0.0003 < \widetilde{\xi} < 0.002$), but all of the diffractive models (LO and NLO) overestimate the data by an approximate factor of 5. The overestimation is attributed to the gap survival probability, which was measured by comparison with the LO predictions to be 0.12 ± 0.05 and at NLO as 0.08 ± 0.04, assuming 41% of proton dissociation in data. The central results at LO and NLO are closer to the Tevatron results rather than the LHC predictions from KMR, although a different ξ range is being probed.

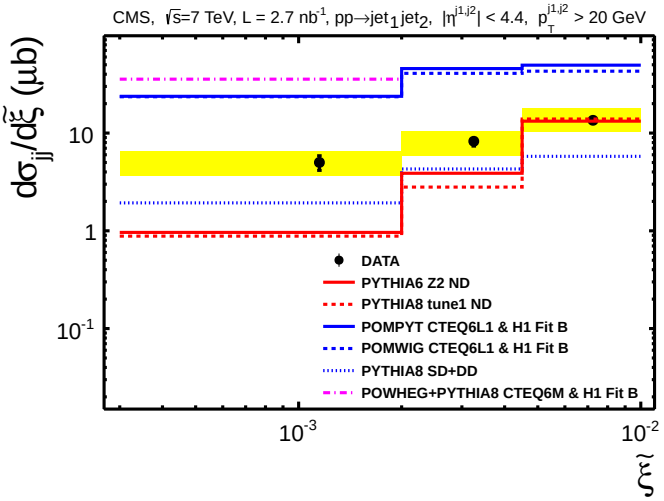

Figure 7.8: Differential cross section as a function of $\widetilde{\xi}$, after applying the gap and jet requirements. The non-diffractive models underestimate the data in the lowest bin but the diffractive models overestimate the data [104].

7.6 Relevant ATLAS results

Although diffractive dijets have not been studied at ATLAS until now, there are several analyses that influence what can be measured.

7.6.1 2010 Inclusive Dijet Analysis

An inclusive dijet analysis was performed over the full 2010 dataset, corresponding to an integrated luminosity of 37.1 pb^{-1} [110]. The dijet selection required at least two anti-k_t jets reconstructed from topological clusters either with $R = 0.4$ or $R = 0.6$ within $|\eta| < 4.4$, with the leading jet having $p_T > 30$ GeV and the sub-leading jet having $p_T > 20$ GeV and both jets passing the jet cleaning procedures. Dijet events were selected by using fully efficient triggers.

The asymmetry in the p_T cuts for the leading and sub-leading jets was needed to compare with NLO pQCD predictions from NLOJET++ 4.1.2, to which non-perturbative corrections have been applied. POWHEG was also used for predictions, with the showering applied using PYTHIA8 and HERWIG++. The data were presented as a function of the dijet mass, m_{12}, up to masses of 4 TeV and showed good agreement with NLO

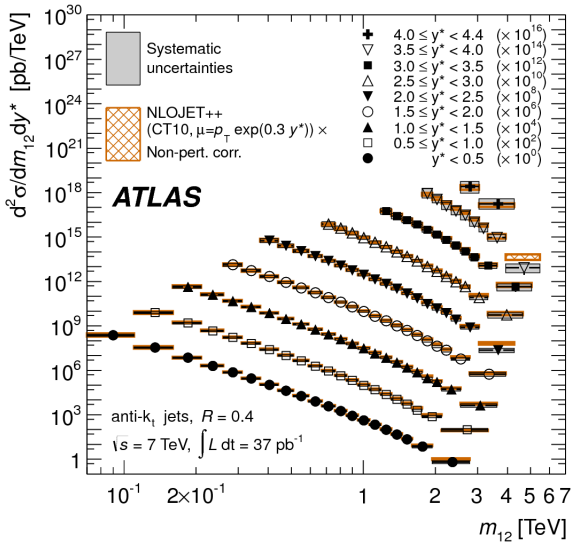

(a) $R = 0.4$ dijets

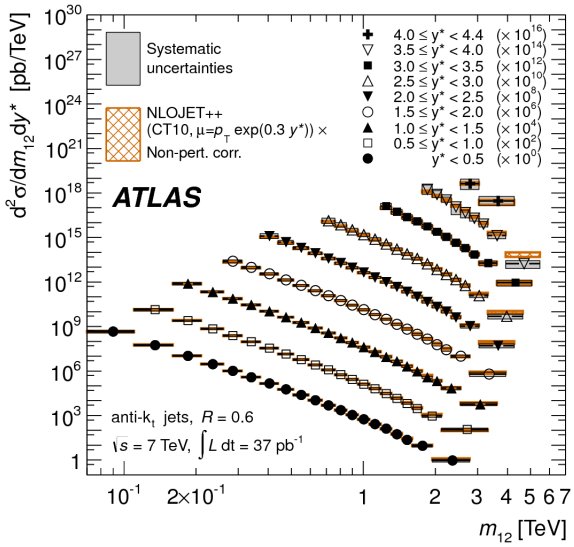

(b) $R = 0.6$ dijets

Figure 7.9: Double-differential dijet cross section as a function of dijet mass, binned as a function of half the rapidity separation between the two leading jets, $y^* = |y_1 - y_2|/2$. The results are shown for jets identified using the anti-k_t algorithm with $R = 0.4$ and $R = 0.6$. For visibility, the cross sections are multiplied by the factors indicated in the legend [110].

predictions within statistical and systematic uncertainties, as shown in Figure 7.9. The dominant systematic uncertainty came from the uncertainty on the jet energy scale.

7.6.2 Rapidity Gaps Analysis

The rapidity gap analysis [86] measured the diffractive contribution to the inelastic cross-section, using the first stable run of 2010 data running. The data contained negligible pile-up and corresponded to an integrated luminosity of 7.1 μb^{-1}. The diffractive selection involved measuring the largest forward rapidity gap ($\Delta\eta^F$) from the edge of the detector acceptance without any particle activity. Particles above $p_T > 200$ MeV at the reconstructed level or truth level were considered.

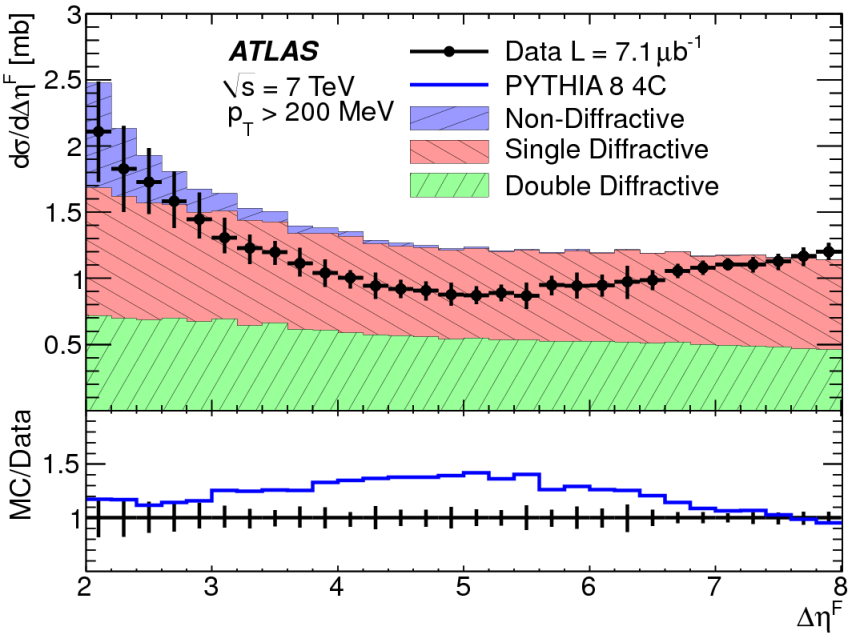

Figure 7.10: Inelastic cross section differential in forward gap size, $\Delta\eta^F$, for particles with $p_T > 200$ MeV and $\Delta\eta^F > 2$. The error bars on the data represent the total uncertainties. The full areas show the predictions of PYTHIA8 contributions of the ND, SD and DD components [86].

The unfolded $\Delta\eta^F$ distributions were compared to Monte Carlo models (PYTHIA6, PYTHIA8, PHOJET and HERWIG++) based on Regge phenomenology, assuming different parametrisations for the pomeron flux. The data are compared with different models with the PYTHIA8 predictions showing the contributions of the non-diffractive, single diffractive and double diffractive components in Figure 7.10. At small $\Delta\eta^F$, the cross section is dominated by non-diffractive events but these are exponentially suppressed as $\Delta\eta^F$ increases, becoming only a small contribution in the region shown. At large $\Delta\eta^F$ values, single-diffractive events dominate and are accompanied by double-diffractive events

with $M_Y < 7$ GeV, for which the Y system travels down the beam-pipe without being detected by ATLAS. For $\Delta\eta^F > 3.5$, the diffractive cross section has been measured as $\frac{d\sigma}{d\Delta\eta^F} \approx 1.0$ mb per unit of rapidity. This approximately constant behaviour of the forward gap size is known as a rapidity gap plateau.

CHAPTER 8

Monte Carlo Simulation of Inclusive and Diffractive Dijets

There are many Monte Carlo event generators but the physics process being studied determines which ones can be used, and are better to perform studies with. In this analysis, the generation of single and non-diffractive dijets is performed using the multi-purpose leading order event generators, PYTHIA8 and HERWIG++, chosen for their different models of diffractive dijet production and hadronisation models. PYTHIA8 is also used to generate double diffractive dijets. For further details of the actual samples, refer to Appendix A.

Multi-purpose event generators are used to simulate an entire event, including the hard process (if there is one) and showering of the particles as shown schematically in Figure 8. PDFs for the proton are used to determine probabilistically which particles are involved in the hard scattering, which is calculated by a LO perturbative QCD matrix element. The products from the hard scatter will either decay or emit radiation, potentially creating parton showers, which are usually modelled using a leading logarithmic DGLAP approach. After the particles in the showers get to a small enough energy, the process of hadronisation begins to turn coloured states into colourless mesons and baryons that can subsequently

decay.

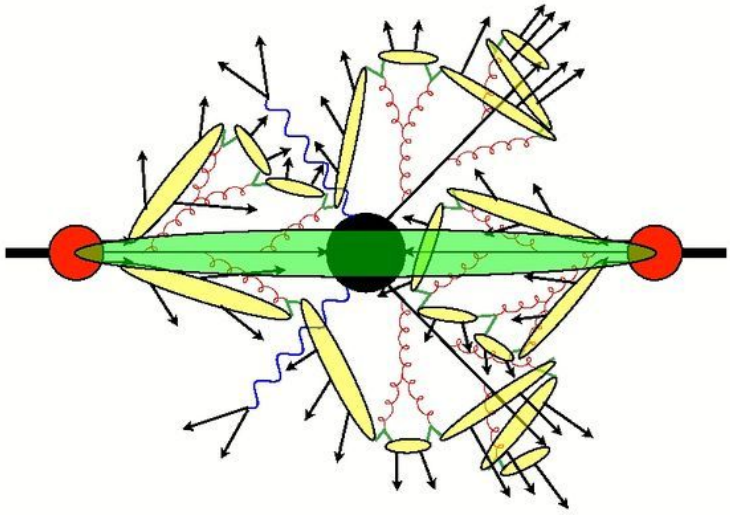

Figure 8.1: Simulation of a Monte Carlo hadron-hadron collision with a hard scatter. It starts with a hard sub-process (black) which then produces outgoing objects that radiate gluons and photons, leading to a parton shower. As the scale decreases and the strong interaction strength increases, hadronisation starts (yellow). Other partons in the hadrons (red) not directly involved in the hard scatter, may undergo additional interactions producing the underlying event (green) [111].

8.1 PYTHIA8

The PYTHIA8 MC is used to model ND, DD and SD processes as described in the following sections.

The hadronisation model used by PYTHIA8 [106] is the Lund String model [112] and is common to all of the ND, SD and DD models. At short distance, QCD acts similarly to QED but at long distances, the gluon self-interaction makes colour field lines that produce a tube of colour flux. For a $q\bar{q}$ pair moving apart from each other, the tube gets stretched out like a string under tension, with the potential $V(r) = kr$ where $k \sim 1$ GeV/fm $\sim$ 0.2 GeV^2 up to a cut-off point where the tube breaks and new $q\bar{q}$ pairs are made.

PYTHIA8 also has a prescription to model the underlying event using multiple parton interactions (MPI), which are set by tunes to LHC data, and the parton showering models

additional radiation using p_T-ordering (DGLAP approximation) [113].

8.1.1 Non-Diffractive Dijets

Non-diffractive dijet events are generated using the approach illustrated in Figure 8. The hard interaction follows the prescription for QCD $2 \rightarrow 2$ LO processes, using leading order MRST LO* PDFs [114] by default. The minimum and maximum k_T (transverse momentum) for the outgoing partons from the hard interaction can be set by the user.

8.1.2 Single and Double Diffractive Dijets

PYTHIA8 generates diffraction based on models of both soft and hard interactions. These cannot be separated, so inclusive (all k_T) samples were produced. The soft interaction model comes from its predecessor, PYTHIA6 [105], which generates cross sections for the single and double diffractive processes using a Regge theory based model developed by Schuler and Sjöstrand [115]. Cross sections are calculated as a function of the diffractive mass, M_X (M_Y), and momentum transfer, t, as

$$\frac{\mathrm{d}^2\sigma_{\mathrm{sd}(AX)}(s)}{\mathrm{d}t\mathrm{d}M_X^2} = \frac{g_{3\mathbb{P}}}{16\pi}\beta_{A\mathbb{P}}^2\beta_{B\mathbb{P}}\frac{1}{M_X^2}e^{B_{\mathrm{sd}(AX)}t}F_{\mathrm{sd}} \ , \tag{8.1}$$

$$\frac{\mathrm{d}^2\sigma_{\mathrm{sd}(XB)}(s)}{\mathrm{d}t\mathrm{d}M_X^2} = \frac{g_{3\mathbb{P}}}{16\pi}\beta_{A\mathbb{P}}\beta_{B\mathbb{P}}^2\frac{1}{M_X^2}e^{B_{\mathrm{sd}(XB)}t}F_{\mathrm{sd}} \ , \tag{8.2}$$

$$\frac{\mathrm{d}^3\sigma_{\mathrm{dd}}(s)}{\mathrm{d}t\mathrm{d}M_X^2\mathrm{d}M_Y^2} = \frac{g_{3\mathbb{P}}^2}{16\pi}\beta_{A\mathbb{P}}\beta_{B\mathbb{P}}\frac{1}{M_X^2}\frac{1}{M_Y^2}e^{B_{\mathrm{dd}}t}F_{\mathrm{dd}} \ . \tag{8.3}$$

In Equations 8.1-8.3 above, $g_{3\mathbb{P}}$ represents the triple-pomeron vertex coupling and $\beta_{X\mathbb{P}}$ is the coupling of particle X to the pomeron. For diffractive masses (M_X, M_Y) that are less than 1.2 GeV above the mass of the incoming beam particles, there is an isotropic decay into a two-body state. Above this, the diffractive system decays to final state hadrons according to the Lund string model with empirical corrections (F_{sd} and F_{dd}) required to make this model cover the full phase space.

The PYTHIA6 approach had no model to generate hard diffraction. PYTHIA8 follows

earlier models such as POMPYT [107], in using the Ingleman-Schlein method [90] to give the pomeron a partonic structure, making it possible for high p_T jets to be found in the diffractive system. For $M_X > m_{min} = 10$ GeV, a perturbative element based on partonic pomeronproton scattering is introduced with the standard machinery for multiple partonic interactions, parton showers and hadronisation. For the M_X values relevant to this analysis, the perturbative model dominates.

Pomeron-proton collisions can use a choice of DPDFs including H1 2007 DPDF Fit Jets and H1 2006 Fits A and B (LO and NLO), and there is no gap survival model.

There are multiple models implemented for the pomeron flux, as seen in Figure 8.1.2. The choice of flux influences how key distributions are generated. Section 7.6.2 showed for soft diffractive interactions that there is an approximately constant differential cross section $\frac{\mathrm{d}\sigma}{\mathrm{d}\,\Delta\eta}$ at large gap sizes, known as a rapidity gap plateau. However, the requirement of a hard scale will prevent a rapidity gap plateau from being observed, favouring large ξ values, corresponding to larger M_X, with more phase space for jet production.

The default flux model in PYTHIA8 is that devised by Schuler and Sjöstrand [115] which has a critical pomeron ($\epsilon = 0$). The mass spectrum varies like $\mathrm{d}M^2/M^2$ and there is an exponential t dependence. The t dependence is different for double and single diffraction. The Bruni and Ingelman flux [116] also uses a critical pomeron but uses a t distribution based on the sum of two exponentials.

Other models use a more conventional description using a super-critical ($\epsilon > 0$) pomeron. The first available in PYTHIA8 is from Berger et al. [117] and Streng [118], with a mass-dependent exponential t slope. Donnachie and Landshoff [88] use a power-law t distribution.

In the hard diffractive model in PYTHIA8, the diffractive mass distributions are derived from these flux parametrisations, but the final state hadron distributions depend more on what the products of the hard scatters are. To get samples of jets from PYTHIA8 SD and DD, inclusive samples have to be produced and filtered at the hadron level.

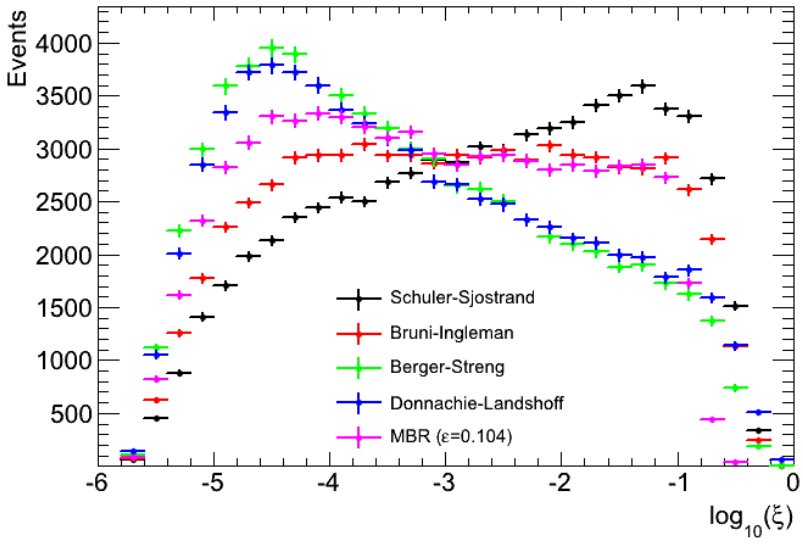

Figure 8.2: Comparison of ξ distributions in PYTHIA8 soft diffractive events using different models of the pomeron flux. The Berger-Streng and Donnachie-Landshoff models were generated using the default $\epsilon = 0.085$ and $\alpha'_{\mathbb{P}} = 0.25$ GeV^{-2} values.

8.2 HERWIG++

HERWIG++ [119] simulates fully inclusive minimum bias collisions in a similar fashion to PYTHIA8, but using angular ordering (in E and θ) in the generation of the parton shower and different hadronisation and MPI models.

The hadronisation stage in HERWIG++ is accomplished by a cluster fragmentation model. At the end of the parton shower, all gluons are split into quark-antiquark pairs. Neighbouring $q\bar{q}$ pairs form color neutral clusters, with hadrons chosen based on the invariant masses of the particles forming the clusters, which (usually) decay into lighter hadrons.

8.2.1 Non-Diffractive Dijets

HERWIG++ generates the matrix elements for hard $2 \rightarrow 2$ proton-proton collisions, and allows cuts to be applied to the generation of the hard process including the minimum or maximum invariant mass of the outgoing process, the momentum fractions of the partons from the protons involved and the k_T of the outgoing partons. There are interfaces to

different proton PDF sets and tunes for the underlying event, treated as additional semi-hard and soft partonic scatters.

8.2.2 Single Diffractive Dijets

HERWIG++ generates single diffractive dijets using the Ingleman-Schlein approach, assuming the that the $2 \rightarrow 2$ pomeron-proton hard scattering can be factorised out from the pomeron flux factor. It can also generate central diffraction on this basis, but not double diffraction. The model does not include the gap survival probability factors which need to be taken into account in hadron-hadron collisions.

The pomeron flux is implemented in the form derived from Ingleman and Schlein with default values of $\alpha_{\mathbb{P}}(0) = 1.104$ and $\alpha'_{\mathbb{P}} = 0.06$ GeV^{-2}, but these can be adjusted. The DPDFs implemented are the H1 2006 A, 2006 B and 2007 Jets fits. Unlike the non-diffractive scenario, no additional underlying event model is used.

CHAPTER 9

Diffractive Dijet Analysis

This chapter describes how the study of diffractive dijets was performed. This includes the choices of data and Monte Carlo samples used for the analysis, event selection cuts, the kinematic reconstruction of diffractive quantities and the evaluation of the uncertainty in the measurement.

The general aim of the selection is to identify events in which two jets are reconstructed and a large rapidity gap is found starting from either edge of the detector acceptance. An example of this type of event is shown in Figure 9.1, using ATLANTIS and Virtual Point 1 [120]. From these events, differential cross sections of diffractive variables and jet properties are calculated in Chapter 10.

9.1 Data Samples

The data used for this analysis were grouped by data taking period. This grouping is organised according to the date of collection and the LHC beam conditions. To study

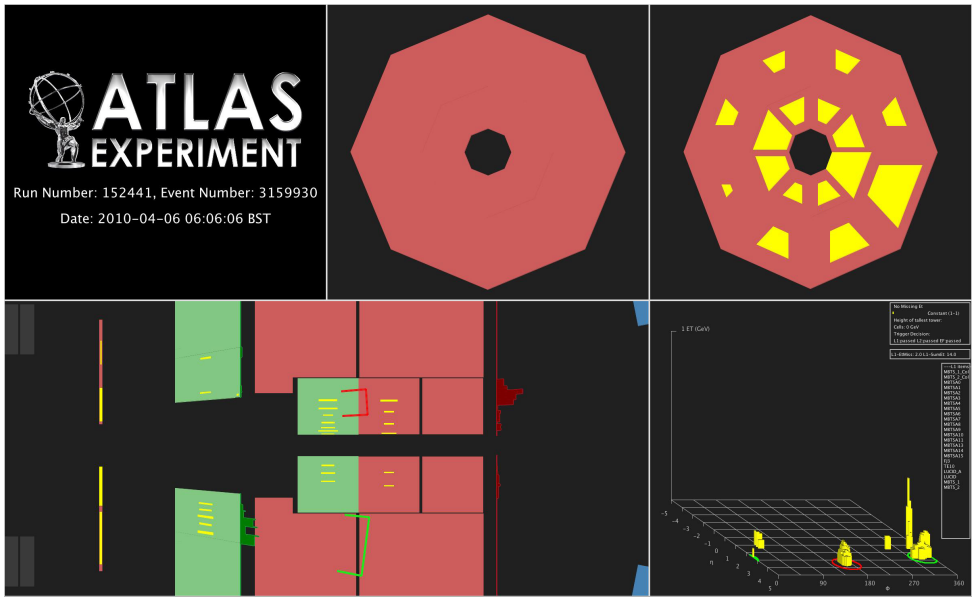

(a) ATLANTIS

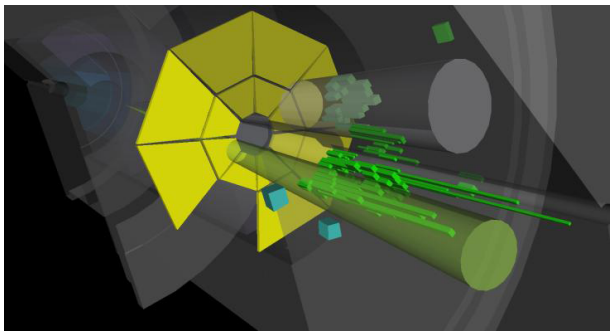

(b) Virtual Point 1

Figure 9.1: Example of a candidate diffractive dijet event, containing two jets in the A side of the detector, and a large rapidity gap, starting from the C side of the detector, as seen using different event visualisation software. In (a) the jets are represented by the two brackets and in (b) they are represented by cones.

rapidity gap production properly, the experiment needs to be run in an environment with zero or low pile-up. For $\sqrt{s} = 7$ TeV collisions, the conditions to do this were available in the early runs in 2010.

The Period B dataset, which consists of runs 153565-155160, contains data collected with the first squeezed stable beams in the LHC. This involves beams with $\beta* = 2$ m, and a typical beam spot width in x and y of 30-40 μm. It was chosen over Period A (runs 152166-153200) which used unsqueezed stable beam data ($\beta* = 10$ m, beam spot width of 50-60 μm in x, y). Despite the fact that Period A had negligible levels of in-time pile-up and that run 152166 was exclusively used for the ATLAS rapidity gaps

analysis [86], the unsqueezed beams produced collisions with a relatively small number of hard scatterings, yielding few dijet events meeting the selection criteria. Period B does have slightly increased pile-up levels overall compared to Period A, but that is accounted for in Section 9.3.1.

Data are selected using two physics streams, L1Calo and MinBias. The L1Calo stream contains events triggered by L1Calo (on the basis of e/γ, jets, τ or energy sums) and the MinBias stream contains events triggered by the MBTS and forward detectors.

9.1.1 Detector Status

The data to be studied were required to be taken in conditions where the appropriate ATLAS sub-detectors were working properly. A Good Run List (GRL) is a list of runs, and in particular the portions of runs, that meet certain quality conditions. For data quality selection, the requirements recommended by the Jet/Missing Energy performance group were used, requiring *green* data-quality flags for L1Calo, CTP, the solenoid magnet, tracking (Pixel, SCT, and TRT) and calorimeters (barrel, end-caps and forward calorimeters), as well as for the jet reconstruction and luminosity performance. After applying the data quality requirements, the runs in the GRL are 153565, 155073, 155112, 155116 and 155160. Selected properties for these runs, after passing the GRL requirements, can be seen in Table 9.1.

Run Number	Peak $\langle\mu\rangle$	Luminosity delivered after GRL (μb^{-1})
153565	0.044	715.2
155073	0.108	1120.7
155112	0.144	3279.6
155116	0.114	453.6
155160	0.123	1263.3

Table 9.1: Luminosity and peak average number of interactions per bunch crossing ($\langle\mu\rangle$) for the selected runs in 2010 Period B, after meeting data quality requirements. The error on each luminosity measurement is $\pm 3.5\%$.

9.2 Monte Carlo Samples

Samples of dijet events in proton-proton collisions at $\sqrt{s} = 7$ TeV were produced using HERWIG++ and PYTHIA8. For HERWIG++, samples of non-diffractive and single-diffractive dijet productions were generated. For PYTHIA8, samples of non-diffractive, single-diffractive and double diffractive dijets were generated. All diffractive samples were generated with DPDFs based on the HERA DPDF Fits (see Section 7.3.1) but PYTHIA8 uses an outdated pomeron flux parametrisation (from the Schuler-Sjöstrand model, see Section 8.1.2) for its diffractive samples, which does not match the HERA results. All samples were simulated to have a response to the layout of the ATLAS geometry in 2010 and to have no pile-up interactions.

The samples of ND, SD and DD collisions were generated to have jets using two different generator filters, a dijet filter and a forward gap filter. The dijet filter generates a flat p_T spectrum for the leading jet. The forward gap filter, produces a flat spectrum of events with smaller rapidity gap sizes, in order to maximise the statistics of events with larger gaps. For this reason, samples generated with the forward gap filter are the primary samples in this analysis. Details of how the filters work and the main properties of each of the generated samples are found in Appendix A.

9.2.1 HERWIG++ Problems

It was initially planned to use HERWIG++ and PYTHIA8 as different models in order to assess theoretical and model uncertainties since they have many differences, including different clustering algorithms at the truth level. Unfortunately, the HERWIG++ samples were found to be unsuitable for this analysis.

HERWIG++ produces events with unexpectedly large gap sizes, such that the non-diffractive samples do not fall away exponentially as expected. This was first observed in the ATLAS rapidity gaps analysis when compared to data and the other generators tested. This is attributed to how HERWIG++ generates the initial $2 \rightarrow 2$ interaction, and then uses a Poisson-statistics-based underlying event model to produce the remaining

activity, in which there is a finite possibility of interaction taking place. The model fails in the clustering of high mass clusters resulting in large regions of rapidity without any activity, which occur more frequently than with underlying event models in other generators. Due to this serious problem in its gap production, HERWIG++ could not be used at this time.

A consequence of the rapidity fluctuations in HERWIG++ can be seen in the single diffractive samples. It is expected that in the vast majority of single diffractive events, the larger forward rapidity gap (see Section 9.5.1) is between the intact proton and the X system. In the generated samples it was found that approximately half of the events had their larger forward gap in the opposite hemisphere to that where the intact proton was found, regardless of how large the gap was and the choice of generator filter, as shown in Figure 9.2. These events are known as mismatched gap start (MGS) events and can also occur in PYTHIA8 SD samples but at a significantly smaller rate to HERWIG++ SD samples.

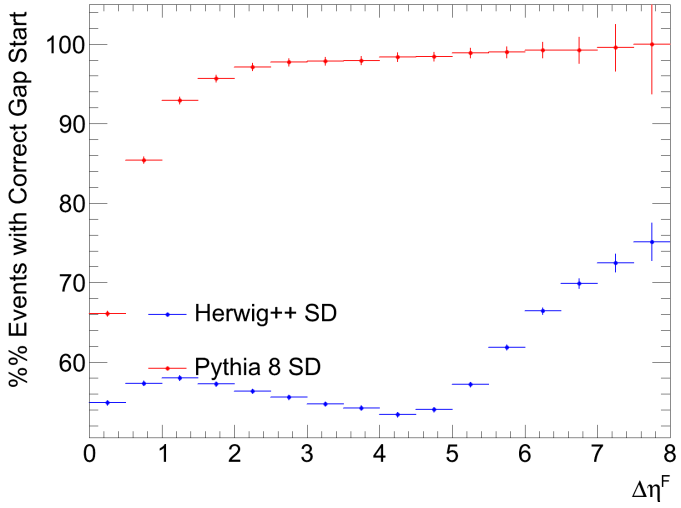

Figure 9.2: Percentage of events in which the truth forward gap starting position is found to be on the same side as the intact proton for PYTHIA8 and HERWIG++ samples. For single diffractive HERWIG++, approximately only half of the events produce a forward gap on the same side as the intact proton.

MGS events may be expected to occur more frequently at small forward gap sizes but should not be common once the gap size becomes at least 2 or 3 units of rapidity. An example of an MGS event with a truth $\Delta\eta^F > 6$ is shown in Figure 9.3. MGS events are generated with large ξ values, typically associated with smaller gaps, and this can be seen

in Figure 9.4, where two separate ξ bands are seen as the gap size increases.

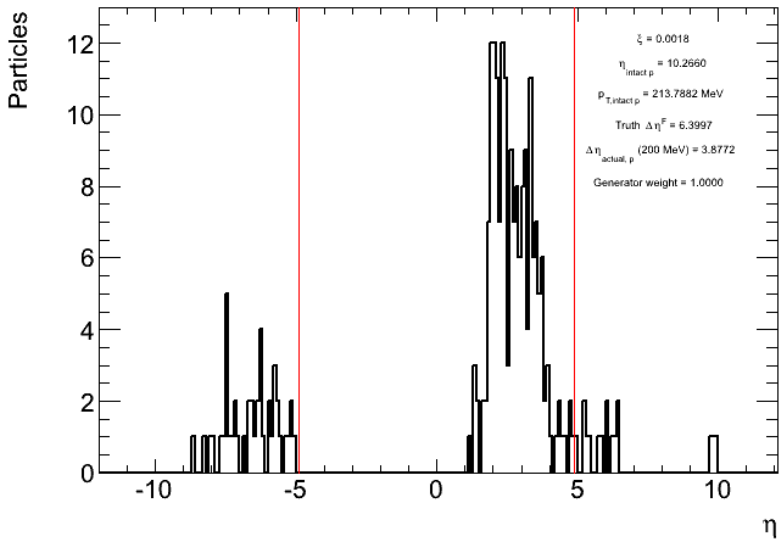

Figure 9.3: Rapidity distribution of particles in a HERWIG++ single diffractive event with a truth forward gap greater than 6 units in pseudorapidity. The red lines indicate the range $|\eta| < 4.9$ considered by the forward rapidity algorithm used in the rapidity gaps analysis. The intact proton is located at $\eta \simeq 10$, from which the distance to the nearest stable particle is much smaller than that found by the rapidity gap algorithm in the opposite hemisphere.

9.3 Event Selection

In data, events are selected with a GRL, as mentioned in 9.1.1. A cut to exclude events with noise bursts in the LAr calorimeters is covered by the GRL. For both reconstructed level Monte Carlo and data, there is a cut on the reconstructed vertices in the event.

9.3.1 Reconstructed Event Vertex

It is possible for diffractive events not to have a reconstructed vertex if ξ is small and all hadrons are produced very forward in the detector or not enough tracks reconstructed close enough to each other in the inner detector to make vertices [121]. However, events were required to have a primary vertex with at least five associated tracks, and the primary vertex location was constrained by the reconstruction to be consistent with the beam-spot position. These requirements are designed to reject events due to cosmic ray muons and

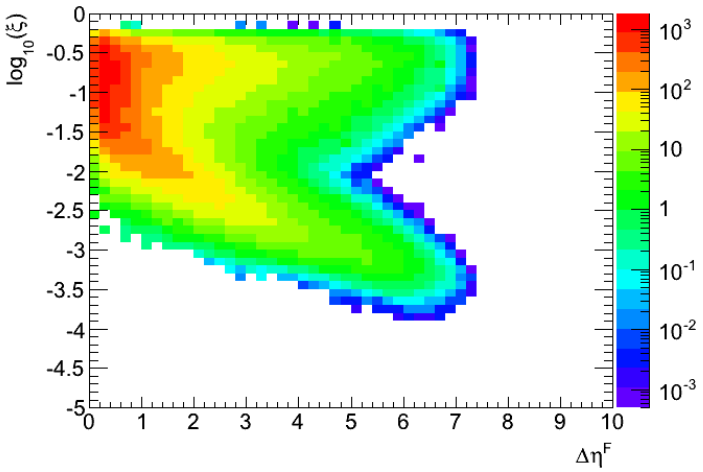

Figure 9.4: Correlation of the actual truth ξ value with truth $\Delta\eta^F$ for HERWIG++ single diffractive events generated with a gap filter. A decrease of ξ with increasing gap size is expected but there is a significant subset of events where the gap starting position is incorrectly matched, meaning that ξ stays constantly large.

beam-induced backgrounds (see Section 9.4.3).

As the instantaneous luminosity is high enough that the potential for multiple collisions inside the same bunch crossing is not completely negligible, it was also required that there should be no "pile-up" vertices in the event that have two or more associated tracks.

Events with a reconstructed primary vertex and no pile-up vertices, with the required number of associated tracks, are dominant in both data and MC. The probability of there being zero, one or more interactions in the same bunch crossing can be calculated using Poisson statistics. After asking that a primary vertex is reconstructed, and taking the mean number of interactions per bunch crossing to be 0.144, corresponding to the peak $\langle\mu\rangle$ value in run 155112 (Table 9.1), $P(2+ \text{ excluding } 0) = (1-P(0)-P(1))/(1-P(0)) = 7.0\%$. From a sample with at least one primary vertex with 5 associated tracks, the fraction of events with more than one interaction in the same bunch crossing is measured to be approximately 5.4% for combined L1Calo and MinBias stream data, and determined from MC to be 0.6%. The MC samples are generated with defined p_T ranges and without pile-up, meaning that the difference in the percentage between data and MC with multiple reconstructed vertices is expected.

Figure 9.5 shows that the overall primary and pile-up vertex requirement removes approx-

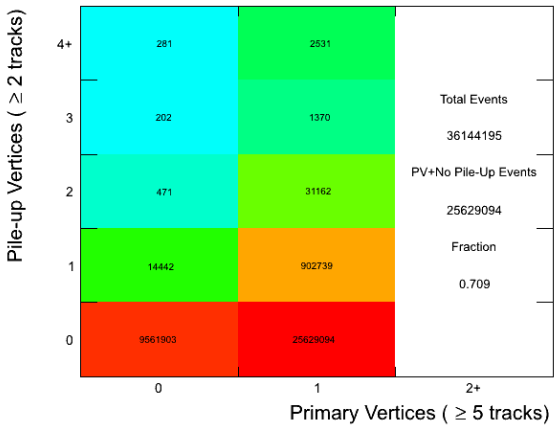

(a) MinBias stream data

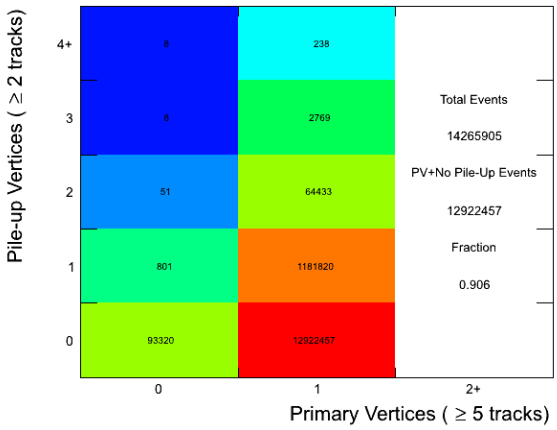

(b) L1Calo stream data

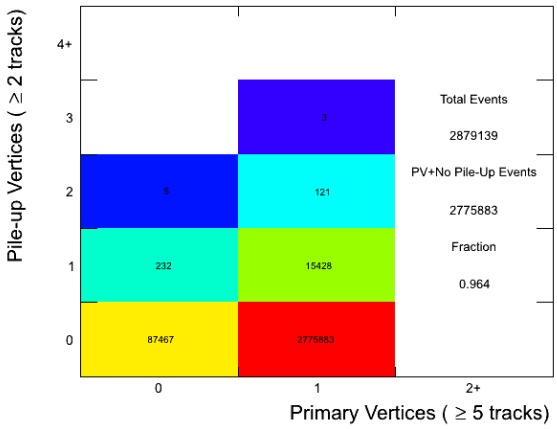

(c) PYTHIA8 SD+DD+ND Gap Filtered

Figure 9.5: Distribution of primary vertices against pile-up vertices after GRL and LAr noise burst cuts are applied for 2010 Period B data and the combined PYTHIA8 SD+DD+ND samples generated with the forward gap filter. The difference between MC and data comes from the preselection of samples.

imately 29.1% of events passing the GRL and noise burst requirements in the MinBias stream. This is dominated by not having 1 primary vertex with 5 associated tracks, however, once an event is triggered and the dijet selection criteria is met, the actual number of events rejected is 5.5% primarily due to events with one or more pile-up vertex. For the L1Calo stream, the vertex requirement rejects 9.5% of events, primarily due to pile-up vertices. This percentage remains the same once events are triggered and the dijet selection criteria is met.

9.4 Dijet Selection

The basis of the dijet selection comes from the ATLAS 2010 inclusive dijet analysis [110], as mentioned in Section 7.6.1. Jets are selected using the anti-k_{t} algorithm, as discussed in Section 5.5.1, reconstructed from topological clusters at the ATLAS EM+JES scale. To compare with the truth level, jets are formed with the anti-k_{t} algorithm from stable final state particles ($c\tau > 10$ mm) [122]. The analysis is performed with both possible jet cone radius parameters available in ATLAS, $R = 0.4$ for narrow jets and $R = 0.6$ for wider jets.

9.4.1 Jet Selection

The standard dijet selection used in the inclusive analysis [110] required at least two anti-k_{t} jets with the jet barycentre within $|\eta| < 4.4$, with the leading jet having $p_T > 30$ GeV and the sub-leading jet having $p_T > 20$ GeV. The η and lower p_T limits are defined by the regions in which the jet energy scale and jet energy resolutions are well measured and the η cut also ensures that parts of the jets will not fall out of the detector acceptance. The asymmetric p_{T} cut was designed to enable meaningful NLO comparisons, as the NLO cross sections become non-physical when the p_T of the jets approach each other. To ensure good quality of the reconstructed jets, both the leading and the sub-leading jet were required to pass medium quality cleaning cuts.

For studying diffractive dijets, the η and cleaning cuts remain unchanged but the p_T cuts

for both jets are set to $p_T > 20$ GeV, because the theory comparisons made to data are with Monte Carlo models, which are generated at LO. Going to lower p_T increases statistics of dijet pairs and the kinematic range accessible in M_X or ξ. Ideally the jet p_T would go down to the reconstruction limit, 7 GeV, but that would have required a large undertaking to understand the low p_T jet energy scale and the associated systematic uncertainties.

Figure 9.6 shows a comparison of jets reconstructed at $R = 0.4$ and $R = 0.6$. Across the η range, the ratio of events reconstructed with $R = 0.4$ to $R = 0.6$ is roughly one half. However, when this is observed as a function of p_T, the ratio of $R = 0.4$ to $R = 0.6$ approaches unity as p_T increases.

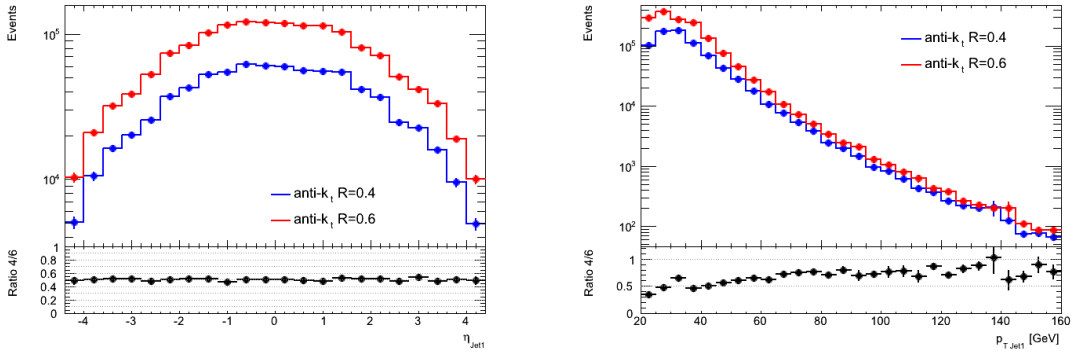

(a) Leading jet η (b) Leading jet p_T

Figure 9.6: Comparison of the leading jet (a) η and (b) p_T distributions for anti-k_t jets reconstructed with $R = 0.4$ and $R = 0.6$ in data.

9.4.2 Trigger

The trigger selection is adapted from the 2010 inclusive dijet analysis and uses a mixture of two triggers, L1_MBTS_1 and the lowest threshold central jet trigger, L1_J5. Whilst L1_MBTS_1 has large prescales, L1_J5 is unprescaled across the entire data set being studied, after passing the GRL requirement. The trigger selection has been modified to select enhanced numbers of events with low p_T jets.

The choice of trigger depends on the p_T and η range for both the leading and sub-leading jet in the dijet pair. Based on the jet η, the jets are classified as being in one of two regions covered by different triggers: central ($|\eta| < 2.9$) or forward ($3.3 < |\eta| < 4.4$). For

kinematic regions where the jet p_T is too low to fire any of the available jet triggers with sufficient efficiency, ($\epsilon < 80\%$), the L1_MBTS_1 trigger is used, as for dijet events it is found to be fully efficient apart from prescales. Otherwise, central jets are tested to see if a L1 jet trigger (L1_J5) was created for the jet by matching the jet η and ϕ coordinates to a L1 Jet RoI with $\Delta R = \sqrt{(\eta_{RoI} - \eta_{Jet})^2 + (\phi_{RoI} - \phi_{Jet})^2} < 0.5$. In the forward region, the MBTS is always used as for 2010 data periods A-C, the L1 forward jet triggers had not yet been commissioned. For jets in the HEC-FCAL transition, if a jet can be matched to a L1 Jet RoI it is classed as central, otherwise it is treated as forward. Central jets falling in the region of the transition between the EM barrel and end-caps ($1.3 < |\eta| < 1.6$) were allowed to be triggered with reduced efficiency.

As the MinBias and L1Calo physics streams can have a small overlap, events are kept in the L1Calo stream only if the jets are triggered on central jet triggers, else the MinBias stream is used. L1_MBTS_1 is prescaled in Period B, as shown in Table 9.2. For data events triggered by L1_MBTS_1, the value of the trigger prescale is applied as a weight.

Run Number	Average L1_MBTS_1 Prescale
153565	4.17
155073	20.69
155112	68.70
155116	55.20
155160	53.11

Table 9.2: Luminosity weighted average prescale for L1_MBTS_1 for parts of selected runs in 2010 Period B passing the GRL requirement, calculated using the ATLAS luminosity calculator. The prescale can vary throughout the run, explaining why the averages are non-integer values.

9.4.2.1 L1_J5 Efficiency

Similarly to how efficiencies were measured for the Level-1 Calorimeter Trigger jet trigger items in Section 6.3, the efficiency of L1_J5, ϵ, was measured in 2010 Period B using a sample of events selected with the L1_MBTS_1 trigger in the MinBias stream. The efficiency is measured separately for the EM transition region ($1.3 < |\eta| < 1.6$) and the remainder of the central detector range (up to $|\eta| < 2.9$), as

$$\epsilon\,(\text{L1\_J5}) = \frac{\text{N}^{\text{o}}(\text{Jet \& } \Delta R \text{ to Jet RoI} < 0.5 \text{ \& RoI passes L1\_J5})}{\text{N}^{\text{o}}(\text{Jet})}\,, \tag{9.1}$$

where the $\Delta R < 0.5$ matching uses the 2010 inclusive dijet analysis recommendations. To characterise the performance of the trigger efficiencies of L1_J5, the turn-on curves were fitted with a sigmoid of the form $f(x) = a_0(1 + Erf((x - a_1)/a_2)$, with a_0, a_1 and a_2 as fit parameters.

The L1_J5 turn-on curves for MinBias data are shown in Figure 9.7. Due to the jet triggers not being fully commissioned during Period B, the fit overestimates the data in the range where the turn-on curve approaches the plateau, but describes the remaining data well enough to be used. Based on these results, the 80% efficiency mark was determined to be at 27 GeV for $R = 0.4$ jets and 32 GeV for $R = 0.6$ jets. These p_{T} cuts for the use of L1_J5 are also applied in the EM transition region, meaning the efficiency is reduced in this relatively small portion of the η range.

The trigger requirement was not applied to MC as the inefficiencies are accounted for by weighting each data event by $1/\epsilon$ if the event was triggered by L1_J5, with ϵ depending on the jet p_T and η. Nonetheless, the L1_J5 trigger efficiency was determined from the Monte Carlo to check for dependencies on other variables such as $\Delta\eta^F$ as shown in Figure 9.8. The efficiencies as a function of p_T for PYTHIA8 are similar to 2010 data Period B and there is no evidence for strong dependences on other variables other than the expected performance drop in the transition region $1.3 < |\eta| < 1.6$.

9.4.3 Backgrounds

The backgrounds for this analysis are typically from cosmic rays, "beam-gas" or "beam-halo" events rather than from any particular physics signal. Beam-gas collisions are ones where the proton beam interacts with the residual beam gas within the beam pipe over the length of ATLAS. Beam-halo events occur when muons or pions travel as a halo around the proton beam due to interactions of protons having been produced well upstream. There is also a small background component of cosmic ray muons overlapping with actual collision events.

To study background levels, the analysis is repeated using bunch crossings in which one bunch crossing is deliberately kept empty. The jet triggers used are L1_J5_UNPAIRED or

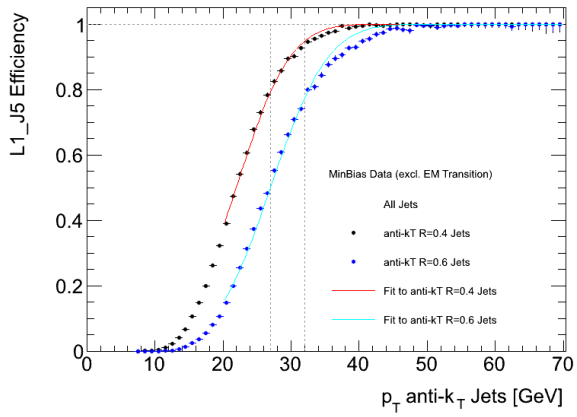

(a) EM Transition region excluded

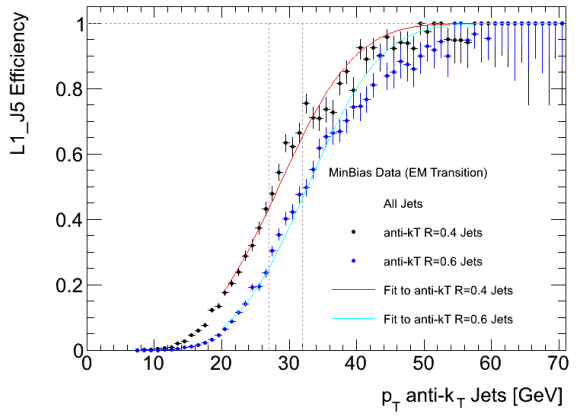

(b) EM Transition region only

Figure 9.7: L1_J5 efficiency in data as a function of the jet p_T for anti-k_t jets with $R = 0.4$ and $R = 0.6$, for (a) the calorimeters up to $|\eta| < 2.9$ excluding the EM transition range ($1.3 < |\eta| < 1.6$) and (b) the EM transition range only. The dashed lines indicate the p_T cuts applied in the analysis. Refer to the text for details of the fits.

L1_MBTS_1_UNPAIRED. Empty triggers (from bunch crossings in which both bunches are empty e.g. L1_J5_EMPTY) are also studied in order to see if noise processes could produce dijet pairs.

After the data-quality and trigger selections described above, no jets are found that satisfied the event and jet selection criteria using the unpaired or empty triggers. Given this, the background rates across the entire data period are taken to be negligible.

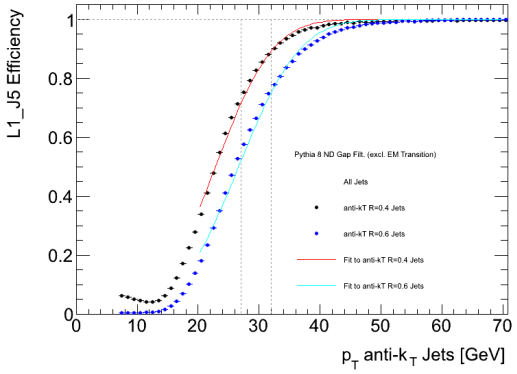

(a) p_{T} (excluding EM transition region)

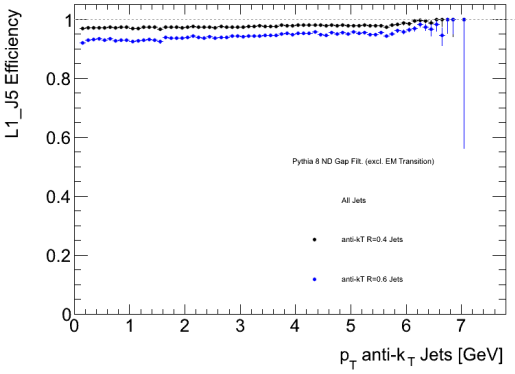

(b) $\Delta\eta^F$ (excluding EM transition region)

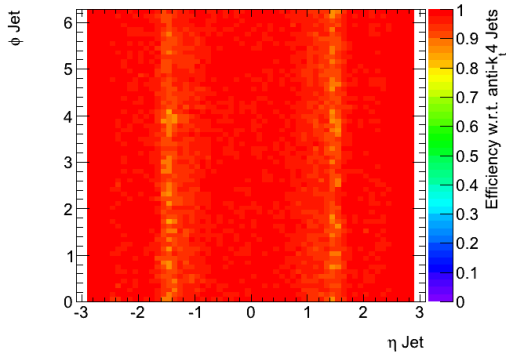

(c) η-ϕ map for anti-k_{t} $R = 0.4$ jets with $p_{\mathrm{T}} > 30$ GeV

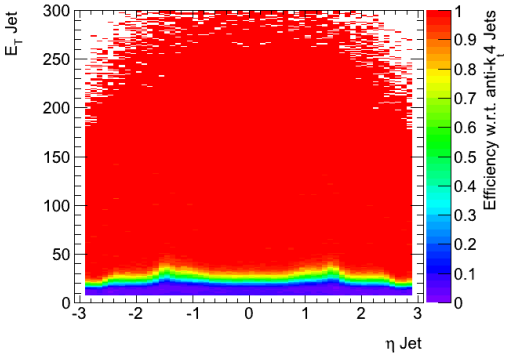

(d) η-p_T map for anti-k_{t} $R = 0.4$ jets

Figure 9.8: L1_J5 efficiency for PYTHIA8 ND samples generated with a gap filter. The efficiency is calculated as a function of p_{T}, $\Delta\eta^F$, η-ϕ and η-p_T to determine if there are unexpected strong dependencies.

9.4.4 Integrated Luminosity

The effective integrated luminosity for each trigger after accounting for prescales was calculated using the ATLAS luminosity calculation tool. The tool uses the GRL for the selected runs and then uses a luminosity tag which has records of the luminosities recorded in time steps of approximately one minute for each run. The calculation uses a "L1-live fraction" trigger, which determines the fraction of luminosity that ATLAS could record after correcting for dead-time or pausing of the triggering to process backlogs of events.

L1_MBTS_2 was chosen as the live fraction trigger, for its high rate and low prescale across Period B. The effective integrated luminosities for L1_J5 and L1_MBTS_1 were calculated as $\int \mathcal{L}dt = 6.753$ and 0.303 nb^{-1}, respectively, based on the final 2010 pp luminosity determination [123]. To combine the results for the different data streams, the MinBias

stream data is weighted by the prescale of L1_MBTS_1 per event, making the integrated luminosity of the MinBias stream match that of the L1Calo stream. The uncertainty on the luminosity is $\delta\mathcal{L}/\mathcal{L} = \pm 3.5\%$ and will be taken account of in the systematics.

9.4.5 Jet Transverse Momentum Correction

As mentioned in Section 5.5.2, the EM+JES scale is intended to optimise the jet response so that the truth p_T in MC equals the reconstructed p_T on average. This calibration is not perfect, and is optimised for higher p_T jets so the scale calibration was checked and re-optimised based on the data available.

To re-optimise the jet response, jets were first matched in MC between the truth and reconstructed levels using $\Delta R = \sqrt{(\eta_{truth} - \eta_{recon})^2 + (\phi_{truth} - \phi_{recon})^2} \leq 0.15R$, where R is the jet cone size. The analysis was restricted to cases where the reconstructed dijets pass the selection criteria, regardless of whether the truth jets pass their respective criteria or not.

The p_T response shift for matched jets, $(p_T^{recon} - p_T^{truth})/p_T^{truth}$, is measured as a function of the p_T and η of the reconstructed jet as a two-dimensional distribution. From this, a one-dimensional projection is taken for shifts in the range between -0.4 and 0.4, the most populated part of the distribution, for each bin in p_T or η. From this projection, the distribution is fitted with a Gaussian, from which the average p_T response shift is determined as a function of p_T and η. The error on the average p_T response shift is calculated as $1/\sqrt{w}$, where w is the sum of the weights for a given bin in the projection. This error corresponds to the standard deviation of weighted mean where each measurement is uncorrelated and has an error σ, which is expressed in the weight used to fill the original distribution ($w = 1/\sigma^2$). An estimate of the overall mean shift and any variation is obtained from the average p_T shift response is obtained from a linear fit.

Figure 9.9 shows the two-dimensional response shifts and resulting average p_T response shifts as a function of η for the leading jet, sub-leading jet and the average of the dijet pair for the combined PYTHIA8 SD+DD+ND samples, created with the dijet filter. Although the final corrections are taken from the gap weighted samples, the results for the dijet

filter show the structure in the variations more clearly. The biggest shift occurs in the central regions, up to $|\eta| < 1.5$, and is typically a 5% over-reconstruction. The shifts were found to change by less than 0.5%, when the size of ΔR matching cone is loosened to $0.25R$ or tightened to $0.05R$.

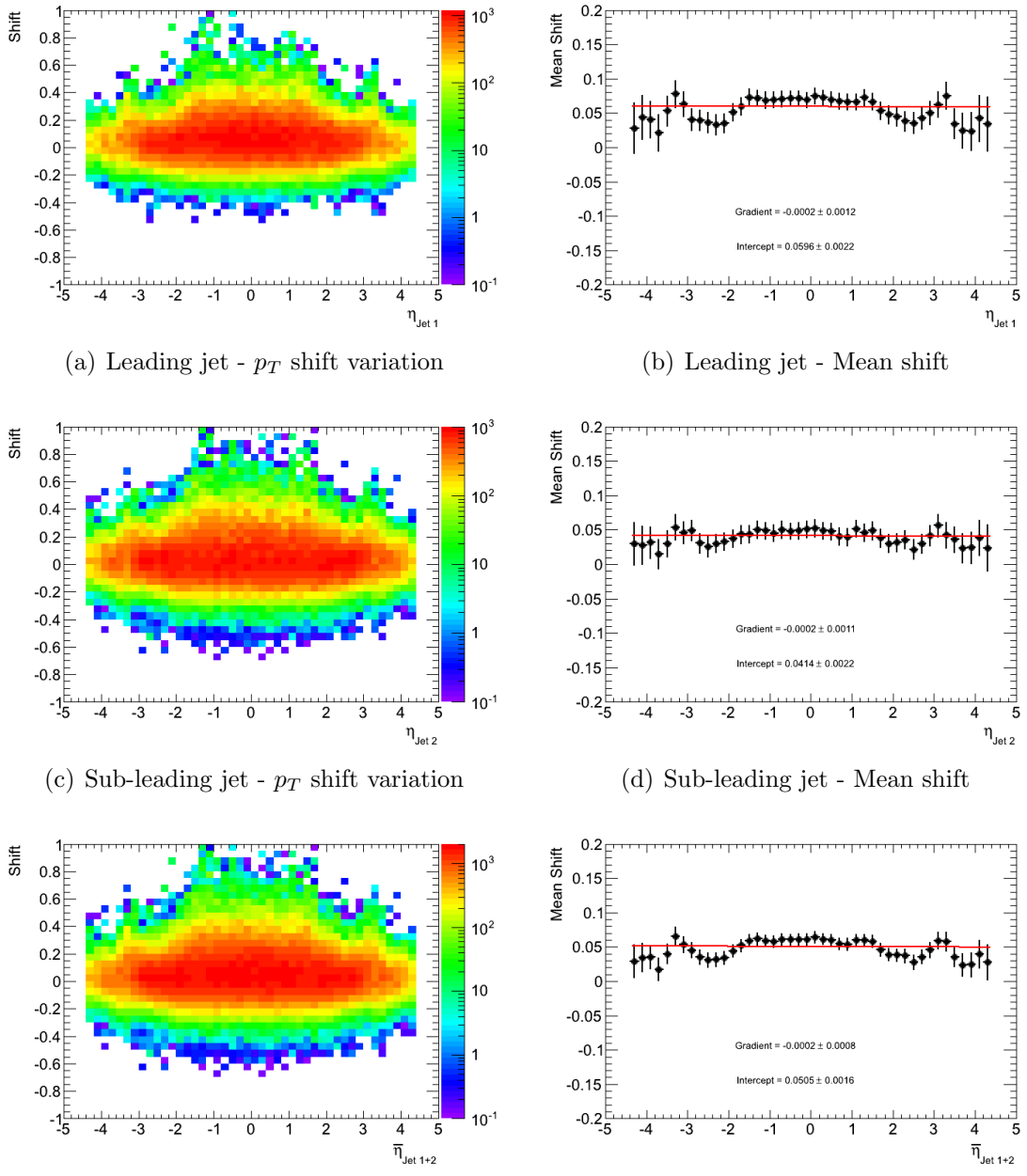

(a) Leading jet - p_T shift variation

(b) Leading jet - Mean shift

(c) Sub-leading jet - p_T shift variation

(d) Sub-leading jet - Mean shift

(e) Mean of jets - p_T shift variation

(f) Mean of jets - Mean shift

Figure 9.9: p_{T} response shift, $(p_T^{recon} - p_T^{truth})/p_T^{truth}$, as a function of reconstructed level η for the leading jet, sub-leading jet and mean η of the dijets, reconstructed with anti-k_{t} $R = 0.6$ for the combined PYTHIA8 SD+DD+ND samples obtained with the dijet filter. In (b), (d) and (f) the range of the y-axis has been reduced in order to better observe the mean shift variation.

The response shifts measured as a function of the reconstructed level p_T are shown in

Figure 9.10. The response shift is largest at low p_{T}, such that many truth jets with $p_T < 20$ GeV migrate into the sample with the default calibration. Although the response shifts get smaller with increasing p_T, there remains an over-reconstruction.

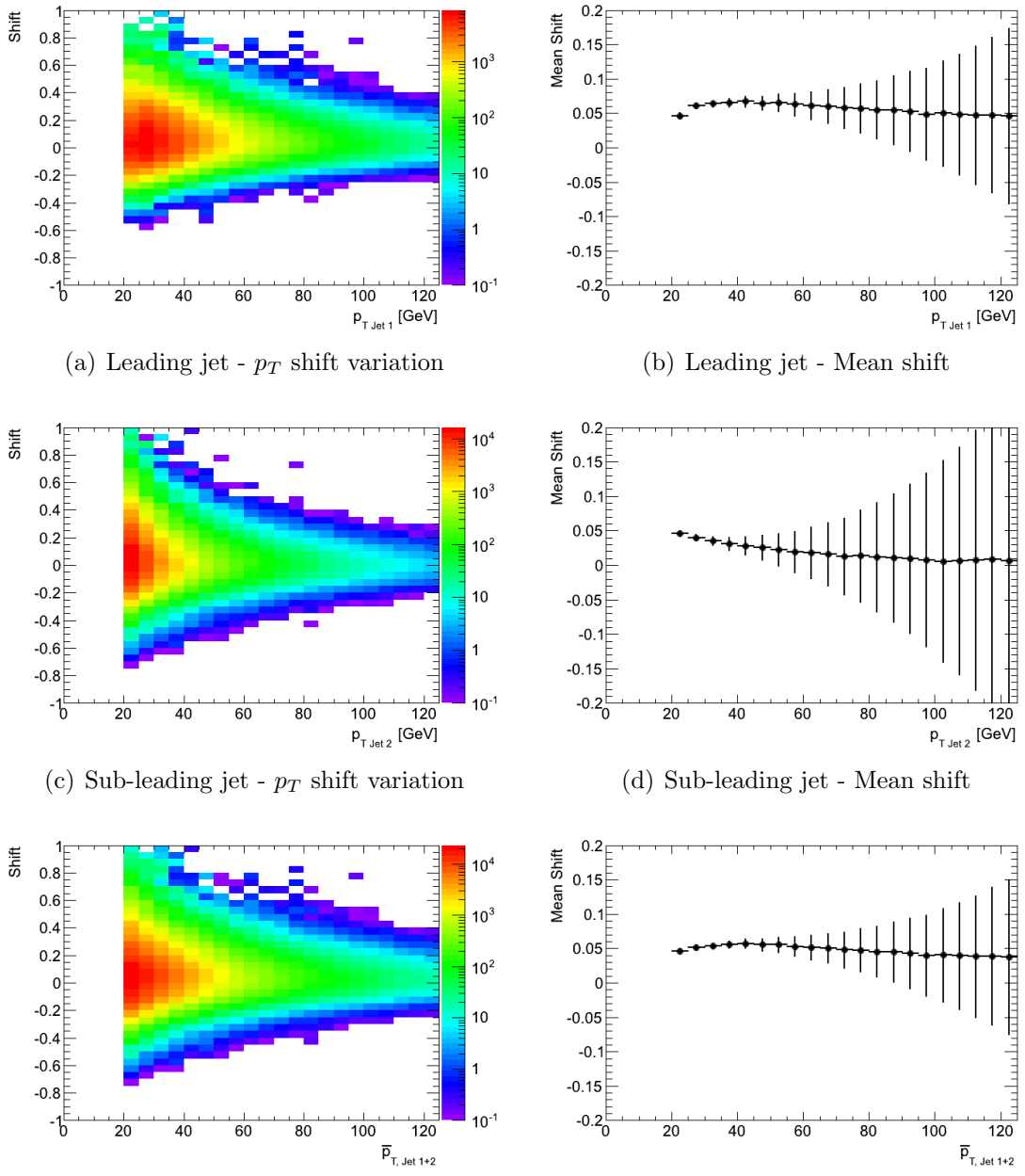

(a) Leading jet - p_T shift variation

(b) Leading jet - Mean shift

(c) Sub-leading jet - p_T shift variation

(d) Sub-leading jet - Mean shift

(e) Mean of jets - p_T shift variation

(f) Mean of jets - Mean shift

Figure 9.10: p_{T} response shift, $(p_T^{recon} - p_T^{truth})/p_T^{truth}$, as a function of the reconstructed level p_T for the leading jet, sub-leading jet and mean p_T of the dijets, reconstructed with anti-k_{t} $R = 0.6$ for the combined PYTHIA8 SD+DD+ND samples obtained with the dijet filter. In (b), (d) and (f) the range of the y-axis has been reduced in order to better observe the mean shift variation.

Since the p_T dependence of the response shift only varies by 1-2% across the p_T range

studied and is poorly constrained at large p_T due to limited statistics, it was decided to correct the jet p_T based on a single number derived from the mean response shift of the η distribution for the average of the leading jet and sub-leading jet (Figure 9.9(f)). This is favoured over a two-dimensional correction in p_T and η to have a single response correction for all jets in both data and MC.

9.5 Diffractive Selection

After requiring a dijet, the diffractive selection involves the steps necessary for the measurement of cross sections as functions of rapidity gap sizes and the fractional proton longitudinal momentum transferred to the pomeron, ξ, using the information available within the detector acceptance. Tests with diffractive MC samples show that events with small diffractive systems e.g. with $M_X \leq 7$ GeV, or $M_Y \leq 7$ GeV in the case of double diffractive events, are not observed as they fall out of the range of the detector acceptance ($|\eta| < 4.9$). As large forward rapidity gaps are a focus of this analysis, the single and double diffractive results are combined, apart from a few cases where the behaviour of the individual samples need to be studied separately.

9.5.1 Forward Rapidity Gap

The forward rapidity gap algorithm was originally developed for the rapidity gaps analysis [86]. It makes use of the full tracking ($|\eta| < 2.5$) and calorimetric ($|\eta| < 4.9$) range of the ATLAS detector.

9.5.1.1 Calorimeter Electronic Noise Suppression

The primary concern in performing a gap analysis with ATLAS is from the electronic noise produced by the calorimeters. As mentioned in Section 5.5, the standard method for measuring the jet energy is through topological clustering of cells (TopoClusters). TopoClusters require that the seed cell has an energy significance, $S = |E|/\sigma_{\text{noise}}$, above

a threshold seed (t_{seed}). The significance determines the probability

$$P(t_{seed}) = \sqrt{\frac{1}{2\pi}} \int_{t_{seed}}^{\infty} e^{-S^2/2} \mathrm{d}S \tag{9.2}$$

that the noise energy in a cell exceeds t_{seed}, assuming that the noise is described by a Gaussian distribution. This works for all of the calorimeters other than the Tile calorimeter where the cell noise is better described by a double Gaussian distribution [124]. With $t_{seed} = 4$ in ATLAS, and with 187616 cells in the detector, it is expected that an average of six TopoClusters with positive energy and six TopoClusters with negative energy per event are produced purely from the fluctuations of noise in the calorimeters.

Any cluster produced through noise fluctuations has the capacity to destroy a rapidity gap. This requires higher noise suppression thresholds, S_{th}, to be applied to the cells, but if the thresholds are too high then low energy deposits are neglected and the reconstructed gap artificially becomes too large.

To optimise the noise algorithm, the full calorimeter acceptance is split into 98 rings of 0.1 in η. With N cells per ring, the probability of a noise cell in the ring having significance above the threshold (P_{noise}) is given by

$$\frac{P_{\text{noise}}}{N} = \sqrt{\frac{1}{2\pi}} \int_{S_{th}}^{\infty} e^{-S^2/2} \mathrm{d}S \ . \tag{9.3}$$

The threshold S_{th} in each ring was influenced by the determination of the gap resolution, the RMS spread of the gap size as measured in the calorimeter as a function of the truth level gap definition (Section 9.5.1.2). The choice of S_{th} should aim to minimise the RMS for all truth level gap sizes. The P_{noise} that minimises the effect of noise was optimised using only the calorimeter and truth information. Figure 9.11 shows the gap noise resolution for various noise thresholds tested above t_{seed}: 4.1, 4.5, 5.0, 5.5 and 6.0.

While a fixed threshold of 4.1 underestimates the gap size yielding large gap resolution for gaps greater than $\Delta\eta^F > 4$, the resolutions are similar for thresholds fixed at 5.0, 5.5 and 6.0 with similar stability of the resolution for intermediate values. Thresholds based on a fixed value of 5.5 are therefore used for the nominal noise probability, with the number

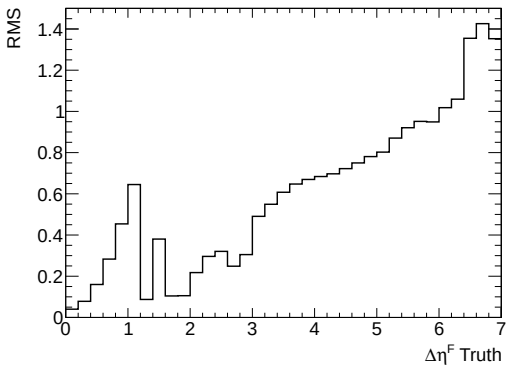

(a) Threshold fixed at 4.1

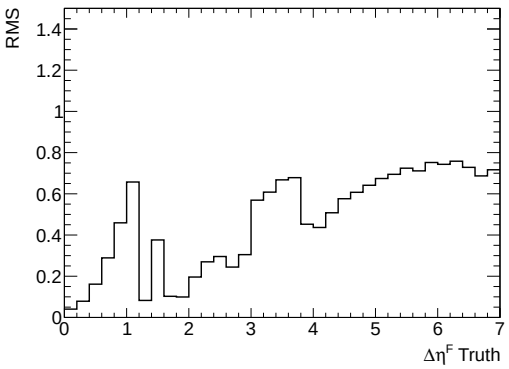

(b) Threshold fixed at 4.5

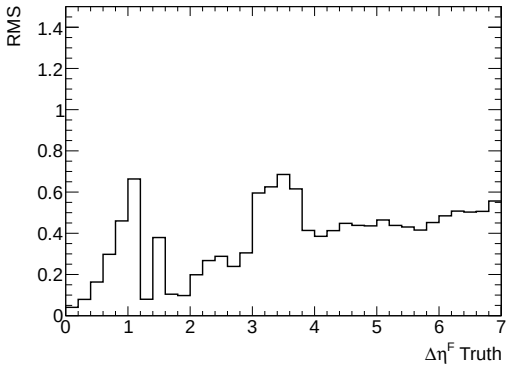

(c) Threshold fixed at 5.0

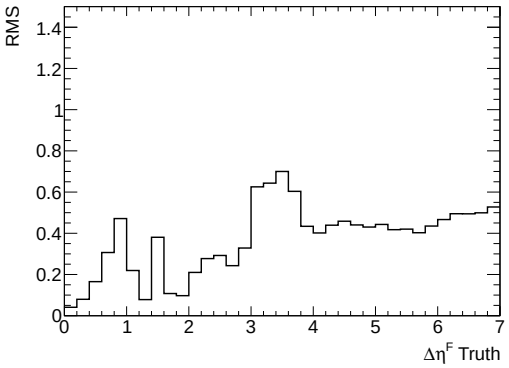

(d) Threshold fixed at 5.5

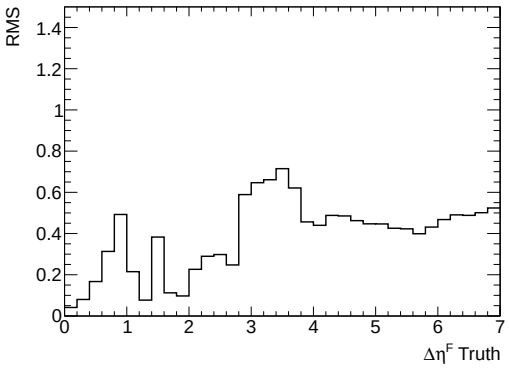

(e) Threshold fixed at 6.0

Figure 9.11: Gap resolution as a function of truth forward gap size for ring noise probabilities, observed in PYTHIA8 for different significance thresholds.

of cells (N) and electronic noise (Figure 5.3) for a given ring also taken in account such that the probability of having a noisy cell in a ring is $P_{\text{noise}} = 500 \times P(5.5) = 1.4 \times 10^{-4}$. The resulting S_{th} values can be seen in Figure 9.12. The thresholds in the centre of the detector are higher to account for the greater cell density (and consequently cluster density) in these regions (Figure 5.4).

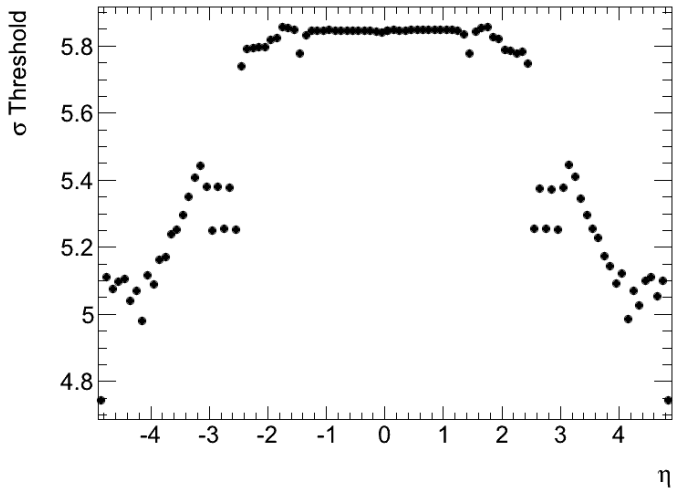

Figure 9.12: Significance thresholds S_{th} for clusters (c.f. Equation 9.3).

9.5.1.2 Rapidity Gap Algorithm

The ATLAS rapidity gaps analysis [86] selected clusters reconstructed at the EM scale, across the detector acceptance with $p_{\mathrm{T}} > 200$ MeV if they contained cells that exceed the significance threshold for the η ring that the cluster barycentre η position falls within (Figure 9.12). The shape of the cell noise distribution in the ATLAS calorimeter is well described by a Gaussian distribution, apart from the TileCal layers where the noise is better described by a double Gaussian. The algorithm is based on Gaussian probability so using the TileCal can complicate this and is excluded. This deteriorates the gap resolution but can be recovered by using the track information in conjunction with the calorimeter information to increase the sensitivity to charged particles.

Good tracks are selected within $|\eta| < 2.5$, with $p_{\mathrm{T}} > 200$ MeV, matching the cluster p_T cut. The requirements for being a good track are:

- At least 1 hit from the Pixel layer, including the B-layer.
- 4 hits in the SCT layer for $p_{\mathrm{T}} > 200$ MeV, increasing to 6 hits in the SCT layer for $p_{\mathrm{T}} > 300$ MeV.
- $d_0 \geq 1.5$ mm with respect to the primary vertex.
- $z_0 \times \sin(\theta_0) \geq 1.5$ mm, with θ_0 measured with respect to the primary vertex.

If there is no reconstructed primary vertex (see Section 9.8.3.2) then the last two requirements change to $d_0 \geq 1.8$ mm with respect to the beam spot.

The algorithm works by using the symmetry of the detector to calculate the gap size starting from each side of the detector, at $\eta = \pm 4.9$, and finding the region without activity, which is terminated by the first track or cluster satisfying the above requirements. The larger gap from either side is denoted $\Delta\eta^F$. At the truth level, the same algorithm is used, based on ($c\tau > 10$ mm) final state particles with $p_{\mathrm{T}} > 200$ MeV.

9.5.1.3 Modifications to Algorithm Selection

The $p_{\mathrm{T}} > 200$ MeV requirement at $|\eta| = 4.9$ corresponds to a cluster or truth particle with $E > 12$ GeV[1], meaning that clusters and stable generator particles at the edge of the detector acceptance are required to be much more energetic than those in the barrel, typically exceeding the S_{th} values for the forward regions. For this analysis, the cluster selection was changed to that used for the measurement of the pseudorapidity dependence of the total transverse energy [125], hereafter referred to as the "E_T flow" analysis, to better reflect what actually gets reconstructed in the detector.

The tracking cuts remain unchanged, as there were none for the E_T flow analysis, but the cluster requirements change to having $p > 0$ MeV and $|\eta| < 4.8$, as very few clusters are reconstructed close to the edge of the detector acceptance. $p > 0$ MeV is necessary because noisy cells can lead to clusters being reconstructed with negative energy, as discussed in Section 5.3.1. Only in the region $1.3 < |\eta| < 1.32$ is there an additional calorimeter requirement of $E_{had}/E_{total} < 0.4$, where $E_{total} = E_{had} + E_{em}$, because the TopoClusters had the potential for a much larger hadronic energy fraction here. The effect of the cuts on the cluster selection from the two analyses can be seen in Figure 9.13.

At the truth level, instead of a universal $p_{\mathrm{T}} > 200$ MeV selection up to $|\eta| = 4.9$ for stable particles, the cuts are changed to $p > 200$ MeV for neutral particles and $p > 500$ MeV for charged particles, up to $|\eta| < 4.8$. The difference in the momentum cuts for neutral and charged particles matches the range over which the simulation indicates that the

[1]Using the relationship $|p| = p_T \cosh\eta$ as clusters are reconstructed as massless objects.

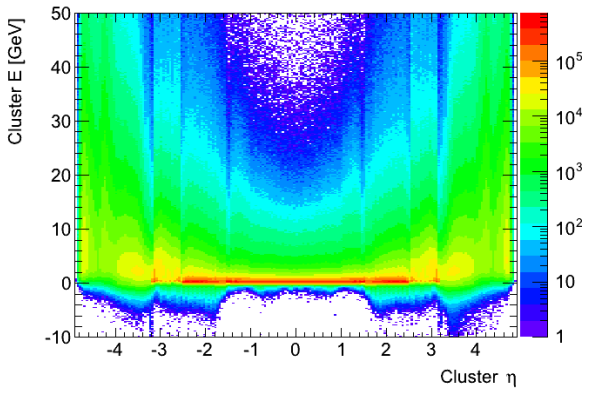

(a) Before cuts

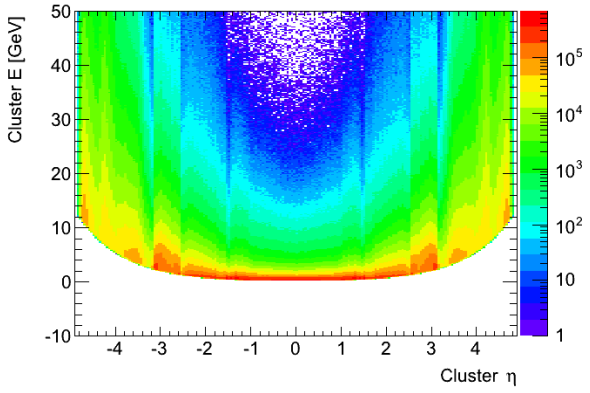

(b) Rapidity Gaps selection

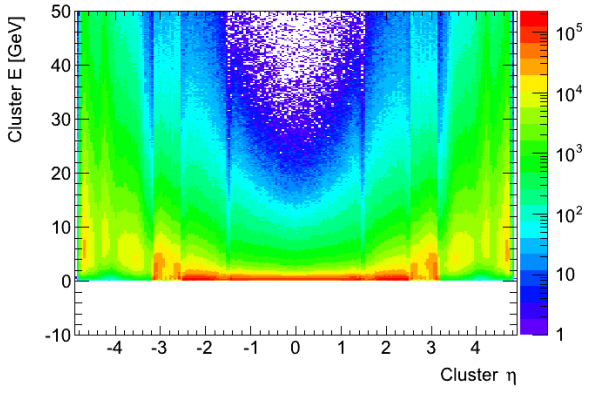

(c) E_T Flow selection

Figure 9.13: Energies of all reconstructed clusters as a function of η, before applying cuts and after applying the cluster cuts for the rapidity gap and E_{T} flow selections.

particles are likely to reach the calorimeter, accounting for the solenoidal magnetic field surrounding the Inner Detector.

The E_T flow analysis also applies scaling factors to the cluster energies in MC to have a better response to low energy particles and what is observed in data. The shifts, α, are

listed in Table 9.3 with their uncertainties, such that the energies are scaled by $1 + \alpha$. The shifts are based on fits to the reconstructed neutral pion decay to two photons, with extensive details listed in [126], and the uncertainties on the α values are from various sources including test-beam studies and single particle energy responses [127, 128].

η bin	α	σ (EM-particles)	σ (Hadrons)	σ (Combined)
$-4.8 < \eta < -4.2$	0.04	-0.023, +0.023	-0.023, +0.093	-0.023, +0.074
$-4.2 < \eta < -3.5$	-0.017	-0.032, +0.034	-0.032, +0.096	-0.032, +0.079
$-3.5 < \eta < -3.2$	0.01	-0.098, +0.11	-0.098, +0.14	-0.098, +0.13
$-3.2 < \eta < -2.8$	-0.027	-0.023, +0.025	-0.023, +0.06	-0.023, +0.051
$-2.8 < \eta < -2.37$	-0.089	-0.025, +0.029	-0.025, +0.062	-0.025, +0.053
$-2.37 < \eta < -1.52$	-0.022	-0.021, +0.02	-0.05, +0.05	-0.042, +0.042
$-1.52 < \eta < -1.37$	-0.073	-0.17, +0.18	-0.05, +0.05	-0.084, +0.085
$-1.37 < \eta < -0.8$	-0.017	-0.031, +0.025	-0.05, +0.05	-0.045, +0.043
$-0.8 < \eta < 0.0$	-0.017	-0.031, +0.025	-0.035, +0.035	-0.034, +0.032
$0.0 < \eta < 0.8$	-0.013	-0.031, +0.025	-0.035, +0.035	-0.034, +0.032
$0.8 < \eta < 1.37$	-0.013	-0.031, +0.025	-0.05, +0.05	-0.045, +0.043
$1.37 < \eta < 1.52$	-0.013	-0.17, +0.18	-0.05, +0.05	-0.084, +0.085
$1.52 < \eta < 2.37$	-0.031	-0.021, +0.02	-0.05, +0.05	-0.042, +0.042
$2.37 < \eta < 2.8$	-0.107	-0.025, +0.029	-0.025, +0.062	-0.025, +0.053
$2.8 < \eta < 3.2$	-0.054	-0.023, +0.024	-0.023, +0.06	-0.023, +0.051
$3.2 < \eta < 3.5$	0.04	-0.092, +0.1	-0.092, +0.14	-0.092, +0.13
$3.5 < \eta < 4.2$	-0.042	-0.032, +0.034	-0.032, +0.096	-0.032, +0.079
$4.2 < \eta < 4.8$	0.01	-0.023, +0.023	-0.023, +0.093	-0.023, +0.074

Table 9.3: α values and systematic uncertainties in each η bin for EM and hadronic particles. The combined uncertainty assumes 27% of particles are EM with the remainder being hadronic [125].

9.5.1.4 Noise Clusters

Any residual noise passing the rapidity gap thresholds could destroy a gap. The influence of these clusters can be estimated by triggering on the random empty triggers, L1_RD0_EMPTY and L1_RD1_EMPTY, which pick out events randomly in empty bunch crossings. For each data run, a noise map is built to see if significant noise is observed in any specific region of η-ϕ, that could then be masked out for the run to ensure that gaps are terminated due to actual particles, rather than noise, with negligible impact on the physics. The noise maps obtained by this method for the first and last runs of Period B, 153565 and 155160, can be seen in Figure 9.14.

Run 155116 could not be tested as no random empty triggers were available for that run,

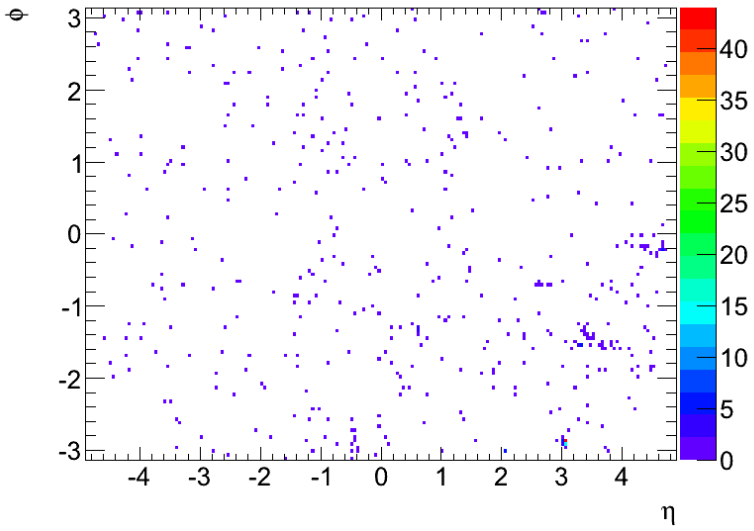

(a) Run 153565

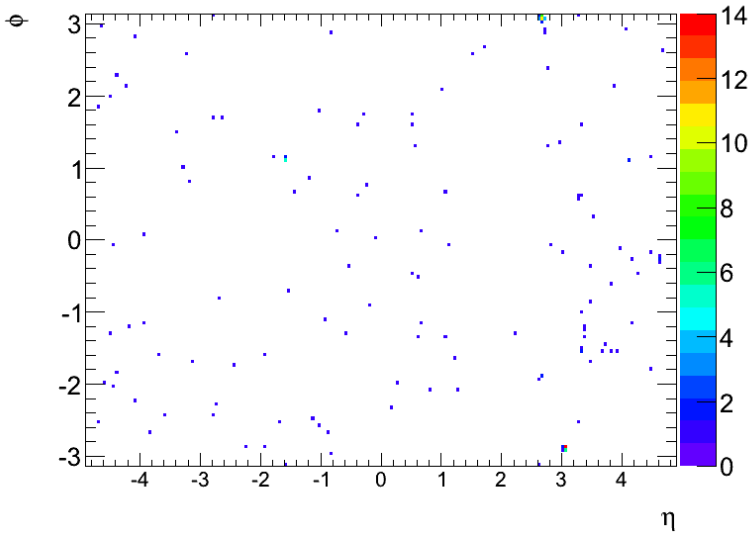

(b) Run 155160

Figure 9.14: η-ϕ maps of clusters, triggered in empty bunch crossings, that pass the rapidity gap selection.

but for all other runs around 0.5% of events contain at least one noise cluster (Table 9.4). The noise suppression cut on the cell significance was tuned to give a 1.4% probability per event of a noise cluster destroying the gap (on average once all η regions are combined), so the observed noise rate is currently smaller than expected when dijets are selected.

Looking more closely at Figure 9.14, there are a few towers at positive η that appear to have more activity than others, but comparing with the integral over the full phase space, a maximum of 10% of all noise clusters are from these regions, so they affect only 0.05%

Run	Events triggered	Events with 1+ EM cluster above threshold	Total clusters above threshold
153565	101629	520	561
155073	35328	188	190
155112	50878	320	330
155116	0	-	-
155160	28545	176	185

Table 9.4: Details of events passing random empty trigger and containing noise clusters for the 2010 Period B random physics stream.

of events. The low probability means that no regions are masked off in any of the runs.

9.5.1.5 Resolution and Acceptance

The PYTHIA8 samples were studied separately to determine the bias and resolution of the measurement of $\Delta\eta^F$ at the truth and detector levels. The $\Delta\eta^F$ response was calculated as (Detector $\Delta\eta^F$ − Truth $\Delta\eta^F$) and fitted with a Gaussian over the peak of the distribution (-0.3 to +0.3). As seen in Figure 9.15, the sample with the worst resolution in $\Delta\eta^F$ comes from the PYTHIA8 double diffractive sample, and is used to set an appropriate bin width of 0.5 units for studying the distributions.

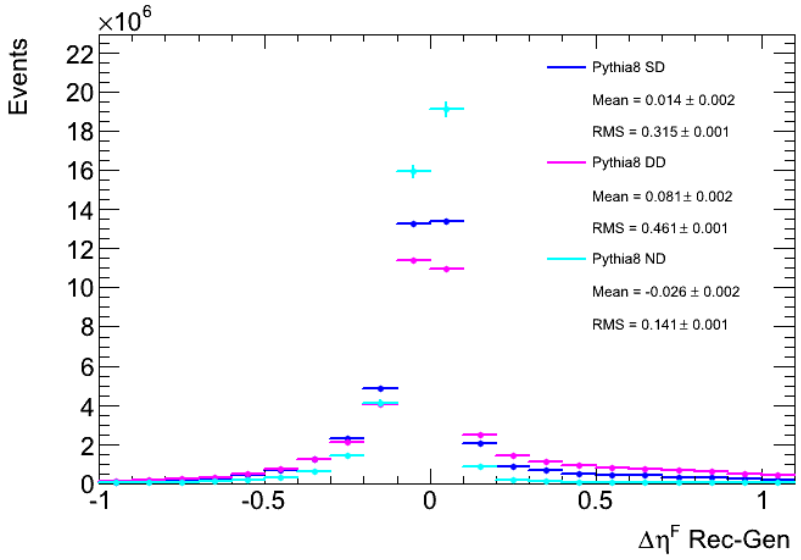

Figure 9.15: Resolution in $\Delta\eta^F$ after requiring 2 anti-k_t $R = 0.6$ jets passing selection criteria, for PYTHIA8 non, single and double diffractive samples generated with the forward gap filter (Gaussian fits not shown).

To determine the range over which $\Delta\eta^F$ can be studied, for each Monte Carlo sample a bin-by-bin ratio is calculated of the number of events independently passing the reconstructed level dijet cuts to the number of events passing the truth level dijet cuts (Figure 9.16). Ideally this should be equal to unity across the entire range of the distribution but the ratio is large for gap sizes less than two units of rapidity, and follows the structure of where the clusters are reconstructed in the detector (Figure 9.13). The lower limit of the range is still set at $\Delta\eta^F = 0.0$ in order to study the contribution of all the different samples at small $\Delta\eta^F$. The bin-by-bin ratio drops below 50% beyond $\Delta\eta^F = 6.5$, so this sets the upper limit of where there is sufficient reconstructed level information and the range to study.

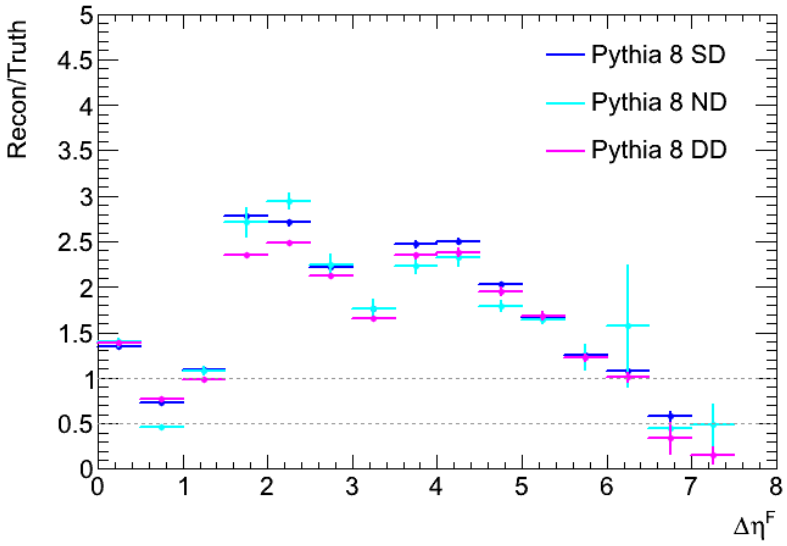

Figure 9.16: Bin-by-bin ratio of reconstructed events to truth events in $\Delta\eta^F$ after requiring 2 anti-k_t $R = 0.6$ jets passing selection criteria independently at the truth and reconstructed levels, for PYTHIA8 non, single and double diffractive samples generated with the forward gap filter.

Influenced by the results seen in Chapter 10 (refer to Figure 10.1), around $\Delta\eta^F = 2.0$, there is a transition where the distribution of the combined single and double diffractive Monte Carlo is above the distribution of the non-diffractive sample. It is decided that an appropriate forward gap requirement for studying distributions with a larger proportion of single diffractive dijets is to select events with $3.0 < \Delta\eta^F < 6.5$.

9.5.1.6 Comparison of Data and Monte Carlo

The shapes of the distributions from data and the different MC samples are compared against each other by scaling them all to have the same integral. As can be seen in Figure 9.17, the data is better described by non-diffractive Monte Carlo, especially at small $\Delta\eta^F$. The single and double diffractive Monte Carlo samples alone cannot describe the data.

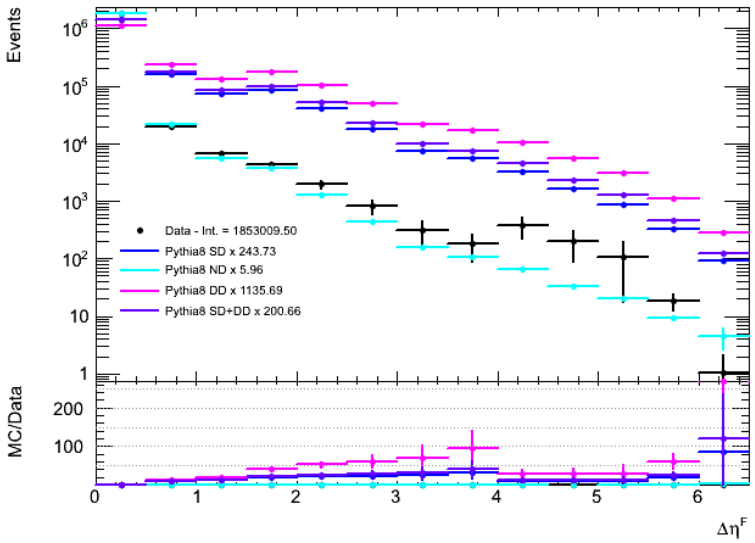

Figure 9.17: Comparison of PYTHIA8 non, single and double diffractive samples generated with the forward gap filter with 2010 Period B data after requiring two anti-k_t $R = 0.6$ jets. All distributions are scaled to have the same area.

9.5.2 Kinematic Reconstruction of Diffractive Variables

With the acceptance of the ATLAS detector restricted to $|\eta| < 4.9$, many particles in the system X of $pp \to Xp$ SD events are not observed and the variable $\xi = M_X^2/s$ is not directly calculable. Additionally, $z_{\mathbb{P}}$ is a parton level quantity and is not directly observable[2]. Approximations allow observables closely related these quantities to be calculated from the information available.

[2]The way PYTHIA8 and HERWIG++ SD events are generated prevents the actual $z_{\mathbb{P}}$ value from being measured in this analysis.

9.5.2.1 Calculation of ξ

For PYTHIA8 SD events, it is possible to use the momentum loss of the intact proton in order to calculate ξ, according to $\xi = 1 - E'_p/E_p$. The truth level correlation of ξ with $\Delta\eta^F$ is shown in Figure 9.18. This shows that in less than 5% of events the gap-finding algorithm selects the incorrect gap starting position (MGS events, compared to 45% with HERWIG++ SD in Figure 9.4).

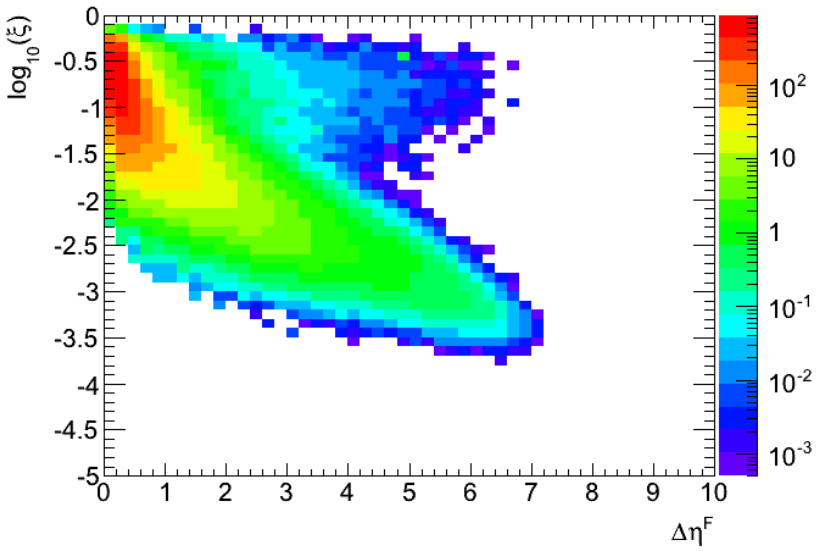

Figure 9.18: Correlation of the actual truth ξ value with truth $\Delta\eta^F$ for PYTHIA8 single diffractive events generated with the forward gap filter.

As $\xi = M_X^2/s$, it can be obtained by reconstructing M_X. However, particles from the X system may fall out of the detector acceptance, meaning some information about it is lost. The influence of this problem can be minimised by using an alternate expression. Assuming the emitted pomeron travels down the beam line, and in the low Q^2 and t limit, M_X can be expressed as

$$M_X^2 \simeq 2E_p \sum (E \pm p_z)_X \ . \tag{9.4}$$

If the forward rapidity gap position starts at $\eta = -4.8$ then the sum is $\sum(E - p_z)$, and $\sum(E + p_z)$ is chosen for gaps starting at $\eta = +4.8$. The benefit of this calculation is that for particles in the X system travelling in the very forward directions, the longitudinal momentum will be very close to the energy, and the sign of the sum causes it cancel out. This approximation to M_X is therefore most sensitive to particles in the detector

acceptance and relatively insensitive to those outside. The diffractive contribution to dijet production should then be largest when $\sum(E \pm p_z)$ is small.

As the detector has a finite acceptance, a "fiducial" ξ ($\xi^{\pm}$) is calculated as

$$\xi^{\pm} \simeq M_X^2/s \simeq 1/\sqrt{s}\sum(E \pm p_z)_X \ , \tag{9.5}$$

taking $2E_p$ to be $\sqrt{s}$, and only considering particles in the region $|\eta| < 4.8$ at both the detector and truth levels[3] in MC.

The selection of stable truth particles follows that from the E_{T} flow analysis, up to $|\eta| < 4.8$. The correlation of the actual truth ξ value with the truth $\xi^{\pm}$ is determined using PYTHIA8 SD events reconstructed with the gap filter, and shown in Figure 9.19 for events with a truth forward gap $\Delta\eta^F > 3$ and two jets. Most events have the truth ξ and $\xi^{\pm}$ values agree within 2-3% but there is a small subset of events, however, where the wrong choice of ξ^+ or ξ^- is chosen as the forward gap algorithm incorrectly identifies the gap starting position.

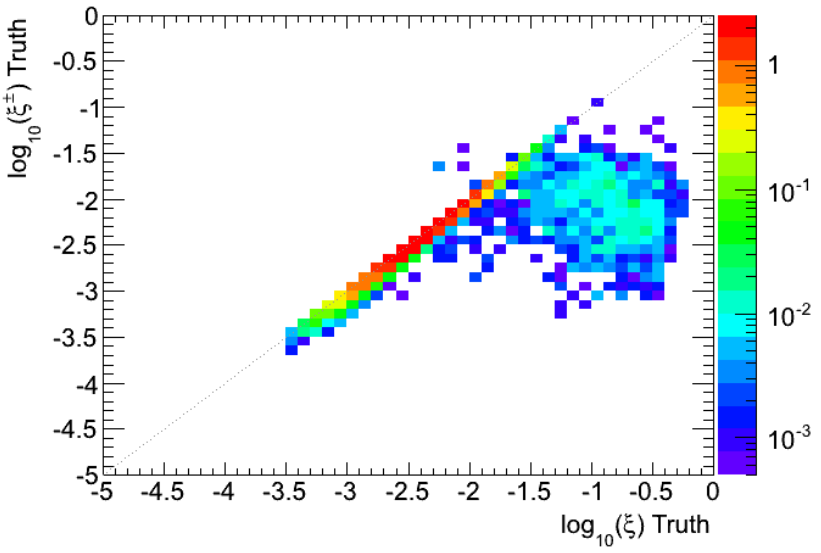

Figure 9.19: Correlation of the truth ξ value with the truth $\xi^{\pm}$ for PYTHIA8 samples generated with a gap filter, after requiring a forward gap of 3 units and two anti-k_{t} $R = 0.6$ jets in the event.

At the reconstructed level, all TopoClusters up to $|\eta| < 4.8$ are included as for the $E \pm p_z$

[3]The truth level is often referred as the "hadron level".

sum, every negative energy noise cluster used in the calculation will statistically, over many events, cancel similar positive noise contributions (provided that the momentum of negative energy clusters is also negative). For data, ξ is reconstructed as

$$\xi^{\pm} = \frac{C}{\sqrt{s}} \sum_{\text{clusters, } i} (E_i \pm p_{z,i}) \tag{9.6}$$

where C is a single correction factor accounting for losses at the detector level from particles falling out of the detector acceptance, not reaching the calorimeters or losing most of their energy traversing the inner detector. The resolution from MC events, $(\xi^{\pm}_{recon} - \xi^{\pm}_{truth})/\xi^{\pm}_{truth}$, is fitted over the peak of the distribution with a Gaussian and the correction factor is determined from the mean of the fit, μ, as $C = 1/(1-\mu)$.

For PYTHIA8 SD events with a gap requirement and two anti-k_{t} $R = 0.6$ jets, $\mu = -0.4535 \pm 0.0008$ and $C = 1.832 \pm 0.003$ where the errors are purely statistical. Figure 9.20 shows the resolution, before and after applying the correction. For anti-k_{t} $R = 0.4$ jets, the number of events passing the dijet and gap requirements is different, resulting in a resolution with $\mu = -0.4397 \pm 0.0010$ and $C = 1.785 \pm 0.003$.

Figure 9.21 shows the correlation between the reconstructed and truth $\xi^{\pm}$ for PYTHIA8 SD events with a gap requirement and two anti-k_{t} $R = 0.6$ jets. The correlation between variables is best in the range $-3.5 < \log_{10}(\xi^{\pm}) < -2.0$. However, there is a tail at truth $\log_{10}(\xi^{\pm}) \simeq -3.0$, for which the reconstructed $\xi^{\pm}$ value is $\log_{10}(\xi^{\pm}) \leq -3.5$. As the reconstructed and truth $\xi^{\pm}$ are not as well correlated originally, applying the correction factor will not significantly improve the reconstruction.

9.6 Cut Flow

For the MinBias and L1Calo stream data, the numbers of events remaining after successive application of the analysis cuts are listed in Table 9.5. Despite containing more events overall, the MinBias stream provides fewer diffractive dijets, before weighting events by the prescale of the L1_MBTS_1 trigger. All events passing the cuts down to "overlap removal" are considered in the measurement of the $\Delta\eta^F$ distribution.

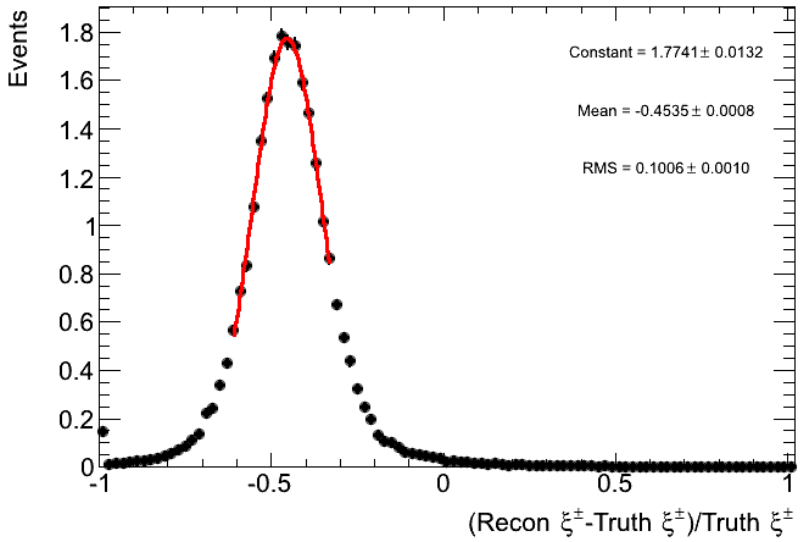

(a) Original

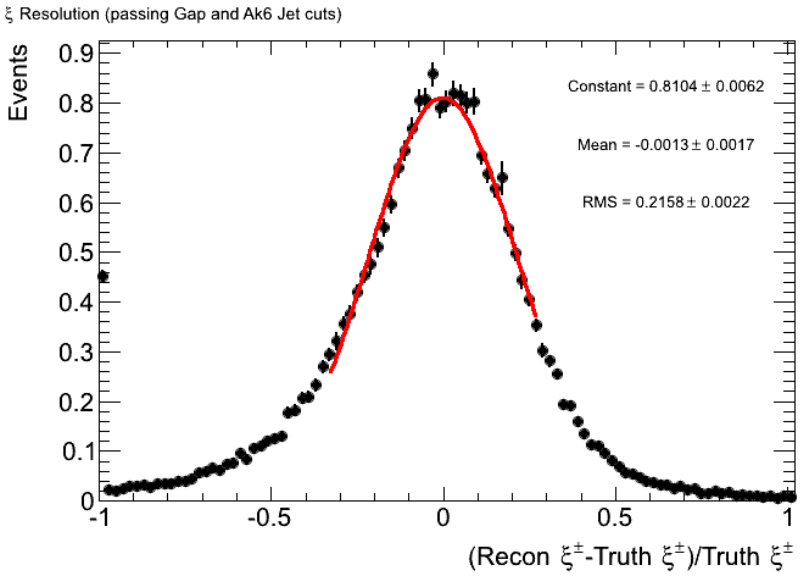

(b) Corrected

Figure 9.20: $\xi^{\pm}$ resolution for a PYTHIA8 SD sample generated with a gap filter, before and after the correction factor C is applied.

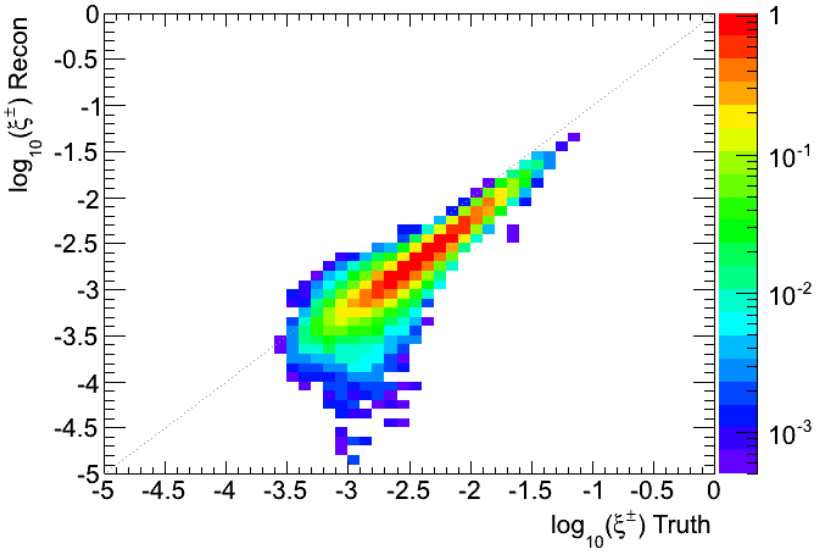

(a) Original

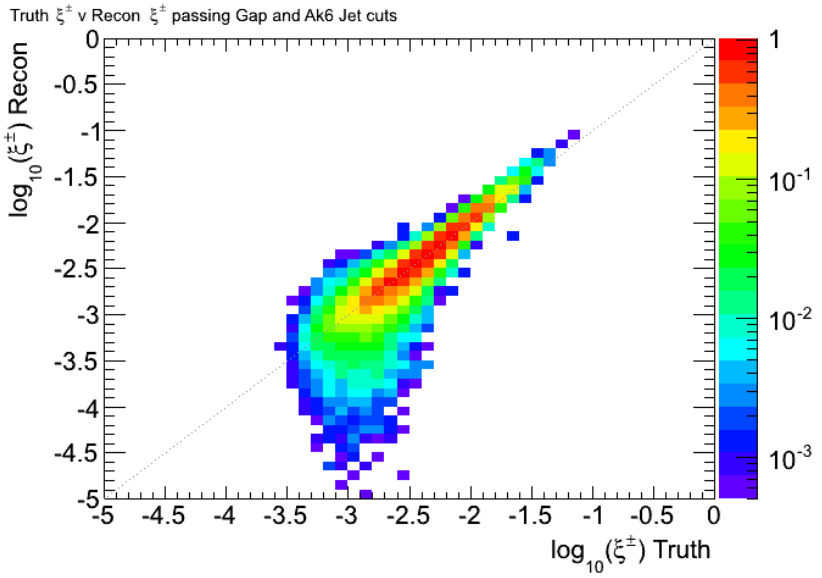

(b) Corrected

Figure 9.21: Correlation of truth and reconstructed $\xi^{\pm}$ for a PYTHIA8 SD sample generated with a gap filter, before and after the correction factor C is applied.

Cut	L1Calo $R = 0.4$	L1Calo $R = 0.6$	MinBias $R = 0.4$	MinBias $R = 0.6$
Total Events	15932908	15932908	38206244	38206244
GRL & LAr Noise	14265905	14265905	36144195	36144195
Primary Vertex	14171717	14171717	26566896	26566896
Pile-up	12922457	12922457	25629094	25629094
Dijets	7299913	10150429	1803584	3977192
Medium Cleaning	6216127	8690840	1549472	3430117
p_{T}, η cuts	592561	1197228	59991	138686
Triggered	369303	468253	45425	81046
Overlap Removal	323110	358833	19386	53002
$\Delta\eta^F > 3$	206	201	6	32
$\Delta\eta^F > 4$	86	84	3	17
$\Delta\eta^F > 5$	25	24	0	4
$\Delta\eta^F > 6$	3	1	0	0

Table 9.5: Events remaining after analysis selection criteria are successively applied for the 2010 Period B L1Calo and MinBias stream data with anti-k_{t} jets reconstructed using $R = 0.4$ and $R = 0.6$.

9.7 Unfolding

The raw data distributions for the $\Delta\eta^F$, ξ and dijet variables are affected by the experimental effects arising from the response of the detector including efficiencies, biases and resolutions for reconstructing jets, clusters and tracks. To measure cross sections, the data have to be corrected for these effects through a process called unfolding. Unfolding of the raw data distributions is performed with the RooUnfold package [129], using a single iterative Bayesian method, developed by d'Agostini [130].

For a given variable e.g. $\Delta\eta^F$, the procedure involves taking Monte Carlo events and constructing a one-dimensional distribution, at both the reconstructed level and the truth hadron level. The reconstructed and truth one-dimensional distributions for the variables are filled independently of each other, in order to account for the migrations in and out of each bin of the measurement. This also allows the unfolding to correct for events which pass at the reconstructed level and fail at the truth level (and vice versa). To determine the migration effects, a two-dimensional response matrix representing the reconstructed quantity against the true physical quantity is built from MC using events which pass the selection criteria at both the truth and reconstructed levels. The response matrix can also be turned into a folding (probability) matrix, giving the probability for a value of the reconstructed quantity to be originally from another value of the true physical quantity, by normalising the sum of the entries in a bin of the reconstructed quantity to unity.

To verify that the unfolding package works, "closure tests" were performed on the Monte Carlo samples to check that the measured MC could be unfolded to reproduce the truth distributions, as shown for ξ and $\Delta\eta^F$ in Figure 9.22. Other than some very small statistical shifts, the truth distribution was perfectly reproduced.

By default, the data are unfolded using a 1.0:1.0:1.0 mixture of ND:SD:DD PYTHIA8 samples[4]. The response matrices and the effect of the unfolding on data are shown for $\Delta\eta^F$ and $\xi^{\pm}$ in Figures 9.23 and 9.24, respectively. The unfolding procedure shifts events between the bins based on the truth distribution, and in the process changes the definition

[4]A 1.0:1.0:1.0 mixture of PYTHIA8 ND, SD and DD samples means that the samples are still scaled by their effective cross sections. The ND, SD and DD samples are then scaled by factors of 1.0, 1.0 and 1.0, respectively before producing the combined PYTHIA8 ND+SD+DD sample.

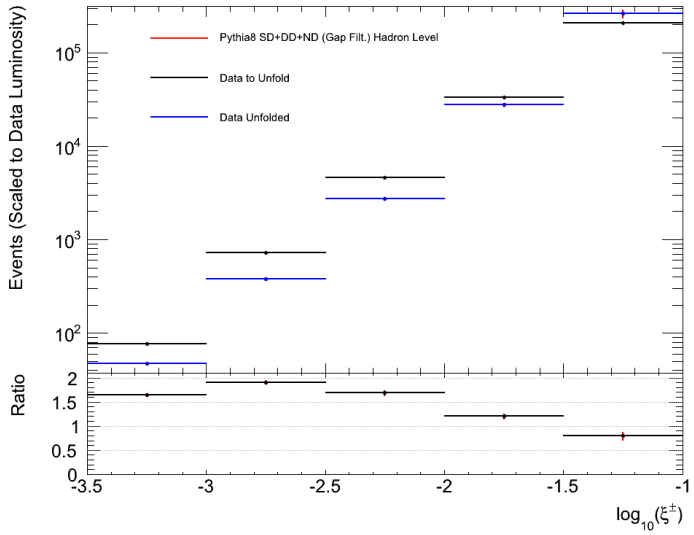

(a) ξ

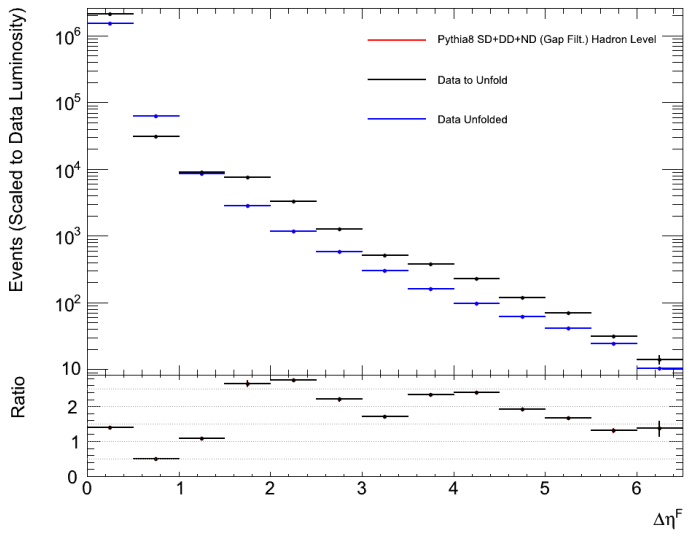

(b) $\Delta\eta^F$

Figure 9.22: Closure tests for $\xi^{\pm}$ and $\Delta\eta^F$. The "data" (black) is a combined PYTHIA8 ND+SD+DD sample generated with a gap filter at the reconstructed level and is unfolded (blue) by a 1.0:1.0:1.0 mixture of ND:SD:DD PYTHIA8 back to the original truth distribution (red), often not visible since it coincides with the blue, unfolded data points. Aside from small statistical variations, unfolding the reconstructed "data" reproduces the original truth (hadron level) distribution.

of the statistical error, no longer reflecting what was collected in the raw data.

Figures 9.23(b) and 9.23(c) show that the response and folding matrices are approximately diagonal. For $\Delta\eta^F$, a significant fraction of the events at the detector level originate from smaller gap sizes at the truth level. It also shows events where there is a very large forward gap at either the detector or truth level and then a small one at the opposite

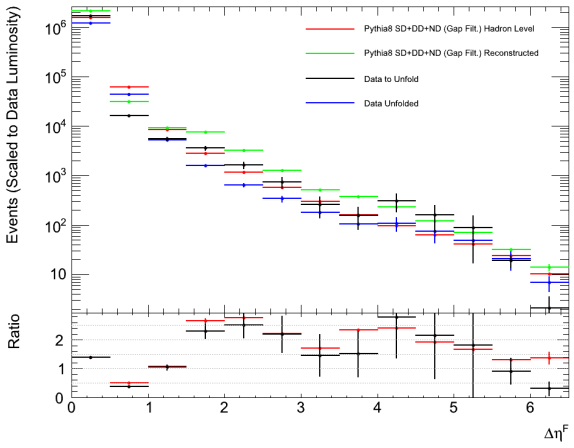

(a) Unfolding data by MC sample

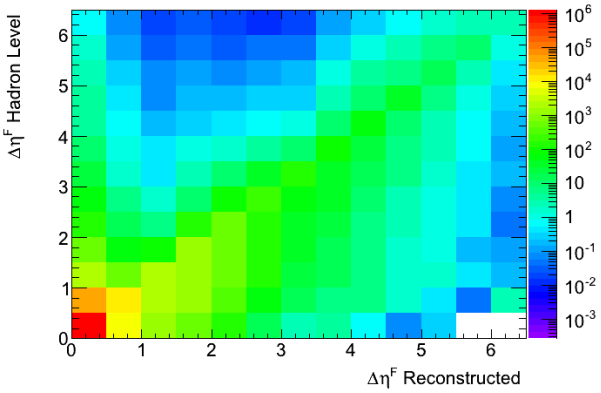

(b) Response matrix showing all MC events

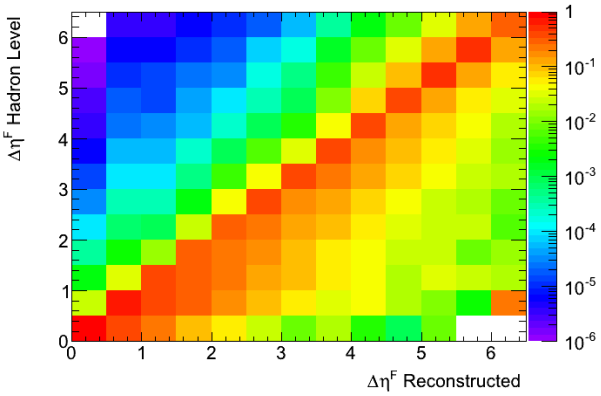

(c) Folding matrix showing all MC events

Figure 9.23: Unfolding for $\Delta\eta^F$ for jets selected with $R = 0.6$. (a) The top of the plot shows the real raw data (black) being unfolded using a 1.0:1.0:1.0 mixture of ND:SD:DD PYTHIA8 samples (blue). The raw and unfolded data distributions are compared against the PYTHIA8 ND+SD+DD sample at the reconstructed level (green) and the truth level (red). The bottom of the plot shows the ratios of raw to unfolded data (black) and the reconstructed to truth level MC (red). (b) Response matrix showing all MC events passing selection criteria at both the truth level and detector level. (c) Folding matrix.

level, which most often occurs when the forward gap algorithm selects the opposite edge of the detector. The effect of statistical errors in the response matrix was evaluated by removing events with very large generator filter weights, that fall significantly off the diagonal of the matrix e.g. those contributing to the bin at reconstructed $\Delta\eta^F = 6.5$ and truth $\Delta\eta^F = 0.5$. The resulting difference in the unfolded data distribution from the original result was found to be at most 1% everywhere.

Figures 9.24(b) and 9.24(c) show that with the correction C applied to $\xi^{\pm}$ at the detector level (Section 9.5.2.1), the majority of $\xi^{\pm}$ calculations fall mainly along the diagonal.

9.8 Systematic Uncertainties

The reconstruction of jets, gaps and $\xi^{\pm}$ introduce systematic errors into the analysis that have to be accounted for when producing the differential cross sections.

9.8.1 Jet Systematics

The measurement of jets from TopoClusters at the EM scale is subject to uncertainties on the influence of dead material, leakage, triggering on jets, the non-compensation of the calorimeter for hadrons and the inefficiencies in reconstructing clusters and jets. In evaluating these uncertainties, a similar approach is taken to that in the 2010 ATLAS inclusive dijet analysis [110].

9.8.1.1 L1_J5 Trigger Efficiency Uncertainty

The L1_J5 trigger efficiency (ϵ) for data is calculated in the range $|\eta| < 2.9$, excluding the EM transition range ($1.3 < |\eta| < 1.6$) which is studied separately (Section 9.4.2.1). The efficiency as a function of p_T is fitted by a sigmoid function for $p_T > 20$ GeV, in order to extract the value of the efficiency for a given value of p_T and η and apply it as a weight of $1/\epsilon$ to the data. For all η values, the fit does not describe the data perfectly, with the worst agreement just before the efficiency approaches 100%. The disagreement

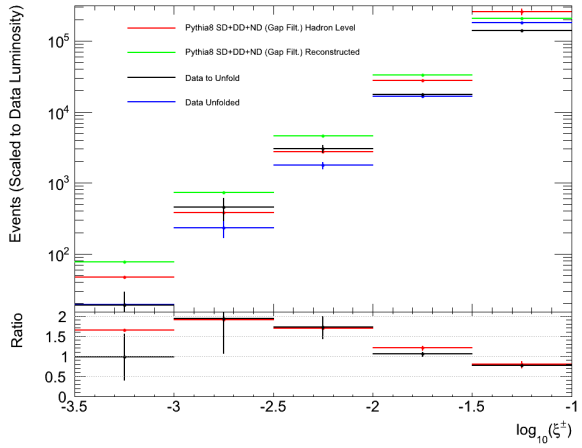

(a) Unfolding data by MC sample

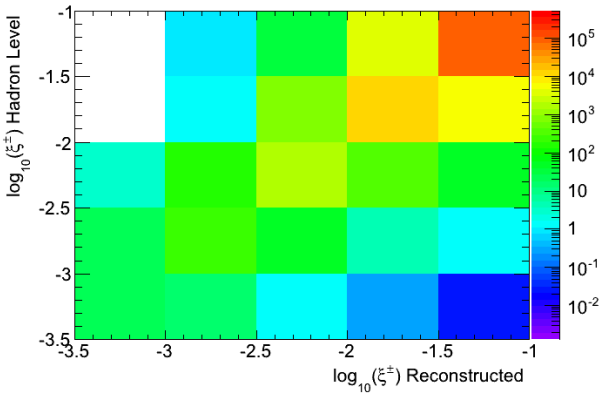

(b) Response matrix showing MC events passing detector and truth selection criteria

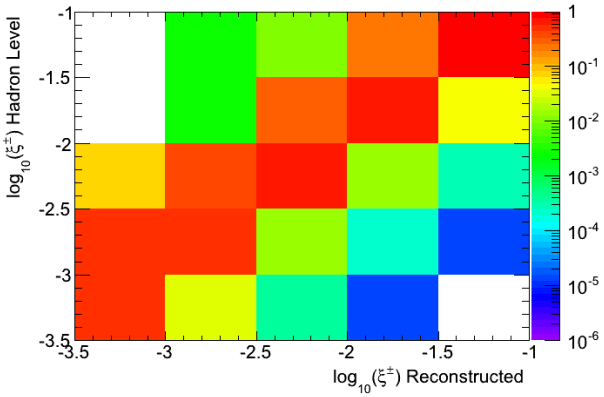

(c) Folding matrix showing all MC events

Figure 9.24: Unfolding for $\xi^{\pm}$ for jets selected with $R = 0.6$. (a) The top of the plot shows the real raw data (black) being unfolded using a 1.0:1.0:1.0 mixture of ND:SD:DD PYTHIA8 samples (blue). The raw and unfolded data distributions are compared against the PYTHIA8 ND+SD+DD sample at the reconstructed level (green) and the truth level (red). The bottom of the plot shows the ratios of raw to unfolded data (black) and the reconstructed to truth level MC (red). (b) Response matrix showing all MC events passing selection criteria at both the truth level and detector level. (c) Folding matrix.

is also larger for anti-k_t $R = 0.6$ jets rather than $R = 0.4$ jets.

To evaluate the resulting uncertainty, the analysis is rerun and instead of extracting the value of the trigger efficiency from the fit, it is taken directly from the calculated efficiency. The resulting change in the differential cross section is typically 4% for anti-k_t $R = 0.4$ jets and 6% for $R = 0.6$ jets.

9.8.1.2 Jet Energy Scale

The EM+JES jet energy scale determination is based on comparing reconstructed and truth jets in MC and providing a correction as a function of η and p_T[5]. The uncertainty on the jet energy scale accounts for uncertainties in a number of factors including the absolute EM scale (e.g. dead material, electronic noise, different responses of the LAr and Tile calorimeters), the simulation of particle showers in the calorimeters, pile-up and the models of fragmentation used by different MC generators [131].

The various components of the jet energy scale uncertainty are combined such that the uncertainty is evaluated by single p_T and η dependent shifts of the jet p_T up and down in the MC, whilst keeping the data fixed. The uncertainty for EM+JES jets reconstructed from topological clusters, in zero pile-up conditions, is taken from [110]. It is shown in Figure 9.25, as a function of jet p_T for the different η regions. It is largest at low p_T and in the forward region.

Diffractive dijets with very large gaps are constrained to be forward-going and are mostly found at the low p_T limit where the JES uncertainty is largest. As in the 2010 inclusive dijet analysis, this is the dominant systematic and resulting change in the differential cross section is typically between 25-40%.

9.8.1.3 Jet Energy Resolution

The jet energy resolution causes fluctuations in the value of the energy measured for each jet. If it is incorrectly modelled, the measured cross sections are influenced. The

[5] p_T is preferred for the jet energy scale rather than E_T despite the name of the uncertainty

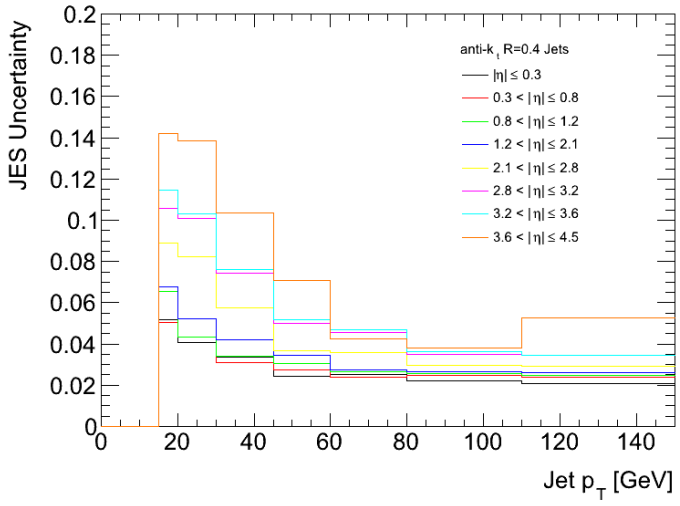

Figure 9.25: Jet Energy Scale uncertainty for EM+JES jets reconstructed from topological clusters using the anti-k_t algorithm with $R = 0.4$ without pile-up corrections.

resolution was determined from data using in-situ techniques and Monte Carlo [132]. The nominal fractional jet energy resolution, $\sigma_{nominal}(p_T)/p_T$, and its associated uncertainty, $\Delta\sigma(p_T)/p_T$, are shown in Figure 9.26 for anti-k_t $R = 0.4$ jets.

The resulting uncertainty on the measurement is evaluated by smearing the p_T of the reconstructed jets in the MC with a Gaussian defined by σ_{smear}, using the formula

$$\sigma^2_{smear} = (\sigma_{nominal} + \Delta\sigma)^2 - \sigma^2_{nominal} \ . \tag{9.7}$$

The resulting change in the differential cross section is typically 8-10%.

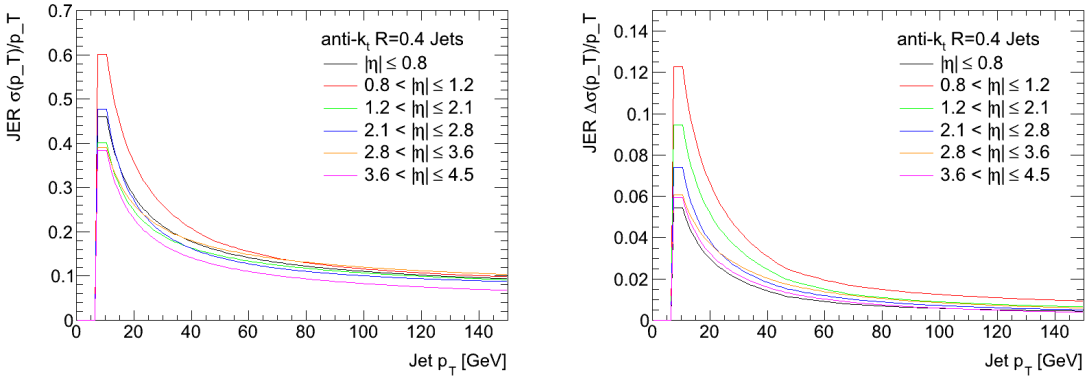

(a) Nominal resolution

(b) Uncertainty on nominal resolution

Figure 9.26: Jet energy resolution $\sigma_{nominal}$, and its associated uncertainty $\Delta\sigma$, for EM+JES jets reconstructed from topological clusters using the anti-k_t algorithm with $R = 0.4$.

9.8.1.4 Jet Angular Resolution

The reconstruction of jets also introduces an uncertainty due to resolution of the jet ϕ and η. It is measured using data and Monte Carlo using the same techniques as that used for the jet energy resolution. The resolution is at most 0.05 in η or ϕ for jets with $p_T = 20$ GeV, becoming smaller than 0.01 for jets above 100 GeV, due to the η correction applied as part of the calibration to the EM+JES scale.

The systematic uncertainty was determined for the inclusive dijet analysis with anti-k_t $R = 0.4$ and $R = 0.6$ jets. The angular resolution, $\sigma_{nominal}$, is shown as a function of the η and E of the jet in Figure 9.27. As the uncertainty on the resolution, $\Delta\sigma$, is very small, $\Delta\sigma$ is fixed at 0.1 for all jets. This is chosen based on the prescription of the inclusive dijet analysis, to increase the effect of applying the systematic. The systematic is propagated through the analysis in a similar fashion to that for the jet energy resolution and the resulting change in the differential cross section is typically around 1-2%, which is small when compared with the uncertainties related to jet energy, and mostly affects jets close to the $|\eta| = 4.4$ limit.

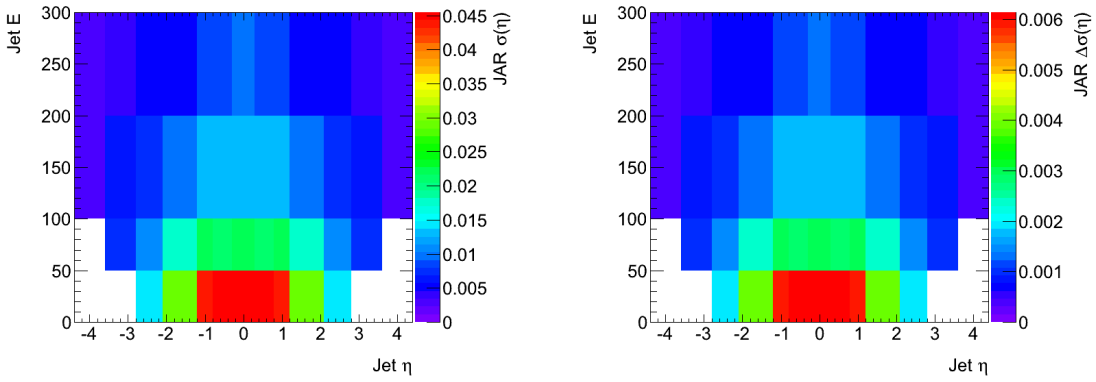

(a) Nominal resolution

(b) Uncertainty on nominal resolution

Figure 9.27: Jet angular resolution and its associated uncertainty for EM+JES jets reconstructed from topological clusters using the anti-k_t algorithm with $R = 0.4$.

9.8.1.5 Jet Reconstruction Efficiency

The efficiency of reconstructing a jet from the calorimeter information is determined by reference to a sample of jets reconstructed from inner detector tracks (track jets). The

uncertainty on the jet reconstruction efficiency was determined for the 2010 inclusive dijet analysis from the difference between the measured efficiency to reconstruct a calorimeter jet if a track jet is nearby from data and MC. The difference is 2% for $p_{\mathrm{T}}^{jet} < 20$ GeV, becoming less than 1% for $p_{\mathrm{T}}^{jet} > 30$ GeV, and is applied to the reconstructed MC jet p_T. The resulting change in the differential cross section is at most 2%.

9.8.1.6 Jet Cleaning Efficiency

The cuts for "cleaning" the jets to medium quality (Section 5.5.3) have an η and p_T dependent efficiency. Many of the jet cleaning variables are not modelled well in the MC and so the jet cleaning efficiency, defined as the number of jets remaining after cleaning compared to the total number of jets, has been studied in ATLAS in-situ using a tag-and-probe technique [133].

Many of the cleaning cuts to remove cosmic and beam background jets make use of the presampler, which covers $|\eta| < 1.8$, so the tag jets are required to be within $|\eta| < 2.0$ and the probe jets are made to balance the tag jet in p_T and ϕ. For jets with $|\eta| < 2.1$, the efficiency is greater than 99% for jets with $p_T > 90$ GeV and for jets with $|\eta| > 2.1$, the efficiency is greater than 99% as there is no presampler requirement. The efficiency in p_T for different η ranges is shown in Figure 9.28. Systematic uncertainties on the jet cleaning efficiency were derived by applying looser and tighter selections to the tag jet, and are less than 2% across p_T and η.

The difference to the central differential cross section result by applying this efficiency is typically 5%, much smaller than that from the jet energy scale uncertainty.

9.8.1.7 Jet Transverse Momentum Correction Uncertainty

To control the migrations into the sample at low p_T, a single factor was applied to the p_T of all detector level Monte Carlo jets (see Section 9.4.5), based on a fit to the mean p_T response shift as a function of η. The uncertainty in this procedure is covered by the existing JES uncertainty as the shifts applied in this analysis are within the JES uncertainties shown in Figure 9.25.

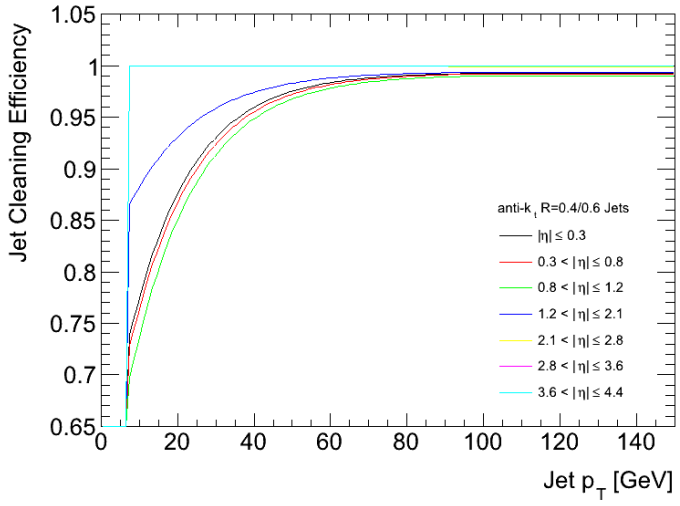

Figure 9.28: Jet cleaning efficiency correction for EM+JES jets reconstructed from topological clusters using the anti-k_t algorithm.

9.8.2 Diffractive Systematics

The systematic errors for the measurements of ξ and $\Delta\eta^F$ are evaluated using similar procedures to those applied in the rapidity gaps analysis [86] and the E_T flow analysis [125].

9.8.2.1 Forward Gap Left-Right Start Asymmetry

After correcting for detector effects, the forward gap algorithm should produce compatible results regardless of whether the forward gap starting position is on the A or the C side of the detector.

Figure 9.29 shows the ratio of the gap distribution when split into events selected with a gap starting separately at $\eta = +4.8$ and $\eta = -4.8$, for anti-k_t $R = 0.6$ jets, in data before the unfolding of the $\Delta\eta^F$ distribution. Across the bins studied, the ratio shows a small shift from unity, but it is negligible on the scale of the major jet uncertainties. The unfolding procedure does not have a significant impact on this comparison. This uncertainty is neglected, as was the case for the minimum bias rapidity gaps analysis.

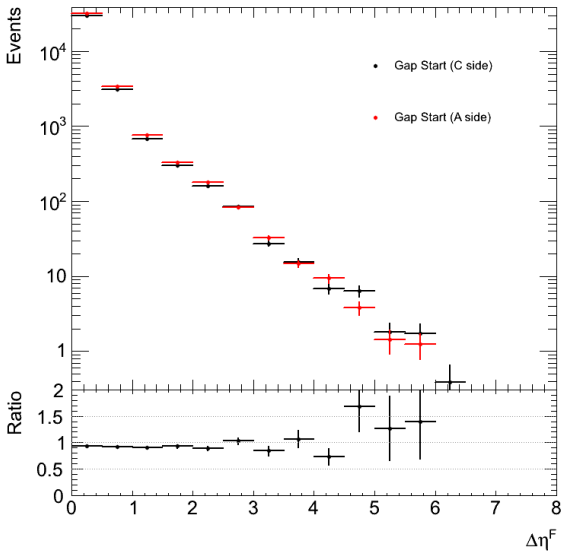

Figure 9.29: Comparison of the $\Delta\eta^F$ distribution in data, before unfolding, for gaps starting at $\eta = +4.8$ and $\eta = -4.8$ after requiring that two anti-k_t $R = 0.6$ jets matching all selection criteria are found.

9.8.2.2 Cluster Energy Scale

The uncertainty on the energy scale of the individual clusters used to determine $\Delta\eta^F$ and ξ is tested by adjusting the cluster energy correction factor, $1 + \alpha$, for combined EM and hadronic objects (refer to the "combined uncertainty" column in Table 9.3). The change in α values after applying the combined uncertainty can be seen in Figure 9.30. The resulting change in the differential cross section is typically 5% for $\Delta\eta^F$ and 10% for $\xi^{\pm}$.

9.8.2.3 Ring Threshold Uncertainty

Following the rapidity gaps analysis, the η ring significance thresholds, S_{th}, for clusters to exceed the noise fluctuation requirement were shifted up and down by 10% to observe the effect on the forward gap size distribution, a systematic reflecting the stability of the gap thresholds.

The systematic effect on the final result in the rapidity gaps cross section measurement was less than 5%, due to the fact that the clusters at $\eta = \pm 4.9$ had an energy cut of 12 GeV resulting from the p_T cut of 200 MeV. For the diffractive dijets analysis, the

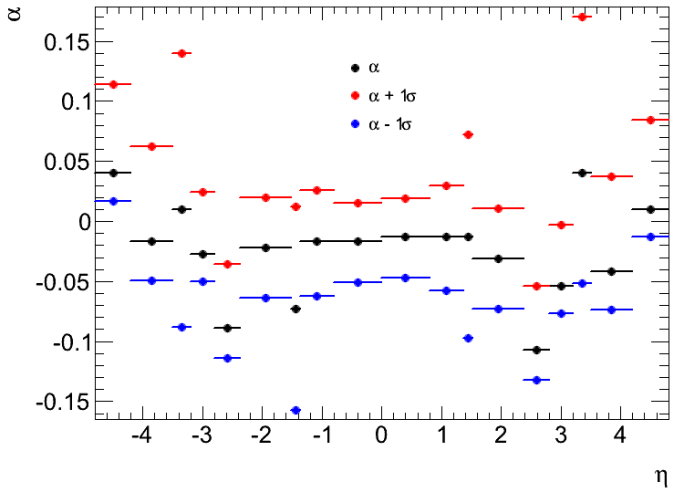

Figure 9.30: Cluster energy shift using the central α values and after applying the "combined uncertainty".

requirement of clusters with $p > 0$ across the whole of the detector is more sensitive to this shift, particularly in the forward regions, and the resulting change in the differential cross section is typically 10%.

9.8.2.4 Tracking

After the selection criteria for tracks are applied, the tracking efficiency has little effect on the reconstruction of rapidity gaps. The uncertainty is taken from the rapidity gaps analysis and is negligible.

9.8.2.5 ξ Correction Uncertainty

A correction factor derived from PYTHIA8 SD (Section 9.5.2.1), C, is applied to the detector level $\xi^{\pm}$ to account for particles that do not reach the calorimeter or are not reconstructed into clusters. As the correction factor was designed to help primarily in aligning the $\xi^{\pm}$ distribution between the truth and reconstructed level, and since the JES and cluster energy scale uncertainties already account for this effect to a large extent, only the statistical error of the mean of the shift was applied as a systematic error. The resulting change in the differential cross section is typically 1-2% and only applied for the

cross section differential in $\xi^{\pm}$.

9.8.3 Other Systematics Uncertainties

The following uncertainties cannot be directly classed as belonging solely to the calculation of diffractive quantities or the jet reconstruction.

9.8.3.1 Luminosity

The uncertainty on the luminosity is taken from the final 2010 luminosity determination [123] to be $\pm 3.5\%$, which is applied as a normalisation uncertainty to all of the results.

9.8.3.2 Reconstructed Vertex Requirement and Pile-up

The requirement of exactly one primary vertex and no additional pile-up vertices creates a clean sample for analysing diffractive events. This results in an inefficiency, whose uncertainty is evaluated by loosening the requirement in data to allow events that have a primary vertex with fewer than 5 associated tracks but still not allow pile-up vertices (see Section 9.3.1). The increase of events from this cut results in a change to the differential cross section of 3%.

9.8.3.3 Additional Material

The effect of dead material requires an understanding of the detector geometry. Properly evaluating the corresponding uncertainties requires special samples to be generated in which the material budget of the inner detector, services and calorimeters are modified. The uncertainty was not directly evaluated but instead taken from the rapidity gaps analysis [86] as a symmetric shift of $\pm 3.0\%$ to be applied to all of the results.

9.8.3.4 Unfolding Uncertainty

Since only PYTHIA8 MC samples are available in the analysis, the uncertainty on the unfolding procedure was tested by adjusting the relative contributions of the ND, SD and DD samples from the default 1.0:1.0:1.0 ratio.

After studying multiple variations of the relative normalisations of the non-diffractive and diffractive PYTHIA8 samples, two selections were chosen, reflecting both the quality of the comparisons of the raw Monte Carlo and data distributions (Figure 9.17) and the range of variations allowed by the measurements presented in Chapter 10. The first choice was to unfold the data with a purely non-diffractive sample of PYTHIA8 (ND:SD:DD = 1.0:0.0:0.0), and the second choice was to keep the contribution of SD and DD the same and halve the ND contribution (ND:SD:DD = 0.5:1.0:1.0). The effect of these modifications can be seen in Figures 9.31 and 9.32, where the default unfolded data are compared in shape with the truth level MC with default ND:SD:DD mixing and with the systematic variations.

It can be seen from these figures that the central 1.0:1.0:1.0 ratio produces the best overall match to the shape of the unfolded data. The systematic variations change the shape such that the agreement becomes much worse. The resulting change in the differential cross section as a result of applying the unfolding uncertainty is small in parts of the distribution that are dominated by the non-diffractive contribution. In other areas, the change to the differential cross section can become as large as 20%.

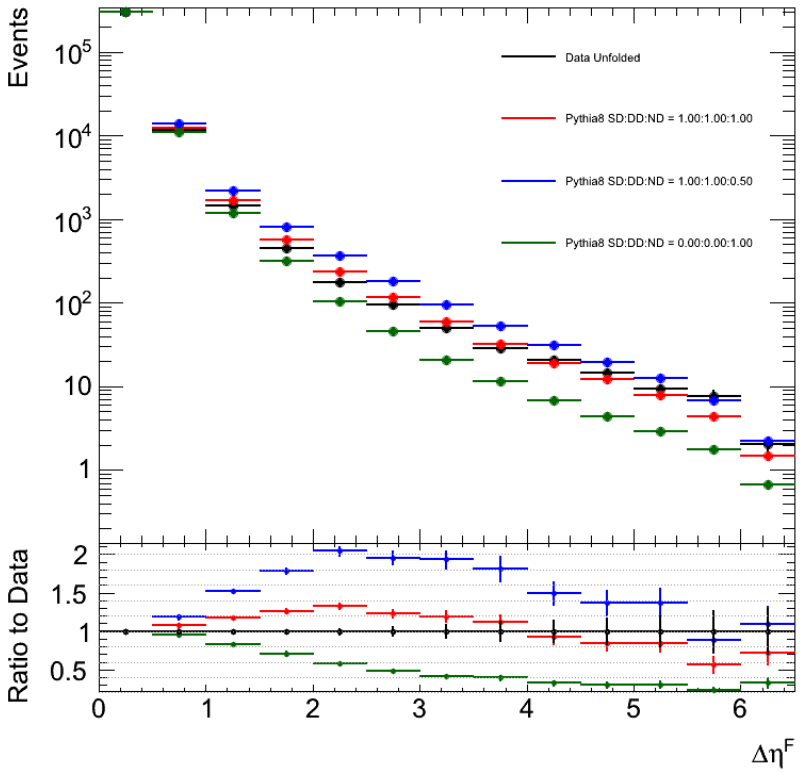

Figure 9.31: Distribution of $\Delta\eta^F$ after requiring two anti-k_{t} $R = 0.6$ jets. The data, unfolded with PYTHIA8 ND+SD+DD with the components scaled in the ratio ND:SD:DD = 1.0:1.0:1.0, are compared to truth level PYTHIA8 ND+SD+DD distributions combined in the ratios ND:SD:DD = 1.0:1.0:1.0, 0.5:1.0:1.0 and 1.0:0.0:0.0. The data and MC are normalised to the first bin ($0.0 < \Delta\eta^F < 0.5$).

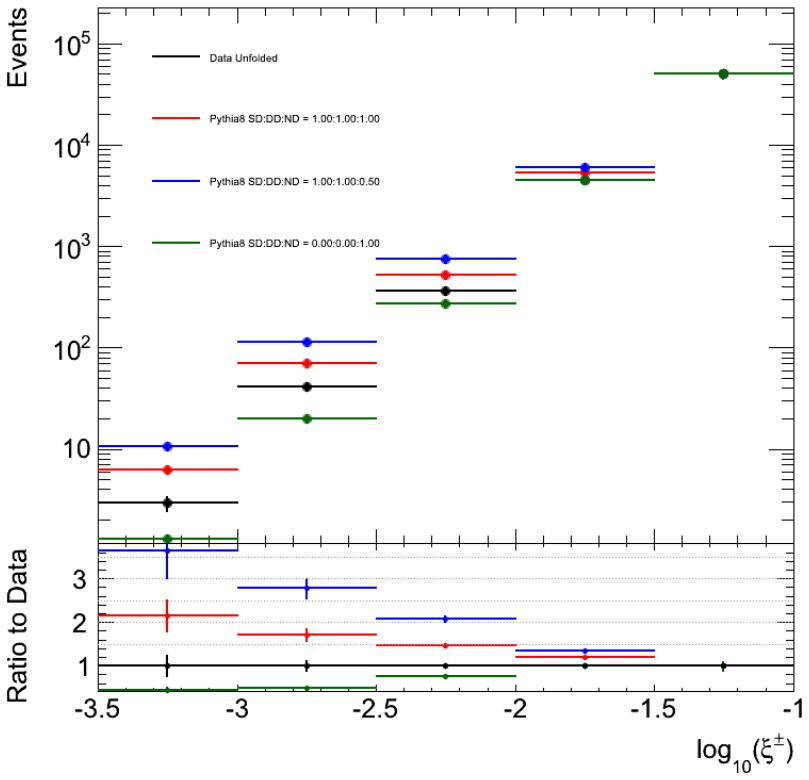

Figure 9.32: Distribution of $\xi^{\pm}$ after requiring two anti-k_{t} $R = 0.6$ jets. The data, unfolded with PYTHIA8 ND+SD+DD with the components scaled in the ratio ND:SD:DD = 1.0:1.0:1.0, are compared to truth level PYTHIA8 ND+SD+DD distributions combined in the ratios ND:SD:DD = 1.0:1.0:1.0, 0.5:1.0:1.0 and 1.0:0.0:0.0. The data and MC are normalised to the last bin ($-1.5 < \log_{10}(\xi^{\pm}) < -1.0$).

CHAPTER 10

Diffractive Dijet Results

This chapter presents the results of the analysis described in Chapter 9. The main results are cross sections presented differentially in the key diffractive variables, $\Delta\eta^F$ and $\xi^{\pm}$. The differential cross sections in p_T and η of the leading jet are also shown. From the differential cross sections in $\Delta\eta^F$ and $\xi^{\pm}$, the relative contributions of the ND, SD and DD components in data are estimated in Section 10.2.

The differential cross section definition requires two jets with $p_T > 20$ GeV and $|\eta| < 4.4$ plus, where appropriate, a forward gap size requirement of $3.0 < \Delta\eta^F < 6.5$. The cross sections are defined in terms of final state truth particles with $|\eta| < 4.8$ and $p > 200$ MeV for neutral particles, $p > 500$ MeV for charged particles.

10.1 Differential Cross Sections

The differential cross sections are presented as a function of $\Delta\eta^F$ and of $\xi^{\pm}$ before and after applying the forward rapidity gap size cut. The differential cross sections are determined

for a variable X, in bins of width ΔX, as

$$\frac{\mathrm{d}\sigma}{\mathrm{d}X} = \frac{N^{weighted}}{\mathcal{L}\Delta X} \tag{10.1}$$

where $\mathcal{L}$ is the luminosity of the data and $N^{weighted}$ is the number of data events after accounting for the efficiency ϵ, trigger prescale per data event and the unfolding. The unfolding corrects the data for experimental effects and migrations between bins, allowing the results to be compared to the truth level Monte Carlo samples.

For Figures 10.1-10.6, the data are shown as black points with error bars representing the statistical errors, in front of yellow bands representing the total statistical and systematic uncertainties added in quadrature.

10.1.1 Forward Rapidity Gap Size

The differential cross section is shown for data as a function of $\Delta\eta^F$ for anti-k_t dijets with $R = 0.4$ and $R = 0.6$ in Figures 10.1 and 10.2, respectively. The data are compared with PYTHIA8 samples generated with the forward gap filter.

For $R = 0.4$, Figure 10.1(a) shows the comparison of data with the combined PYTHIA8 ND+DD+SD sample and 10.1(b) shows the comparison with the PYTHIA8 ND and SD+DD samples separated, suggesting that both non-diffractive and diffractive contributions are present in the data. For the truth level MC "out of the box", the total PYTHIA8 non-diffractive and diffractive cross section is approximately a factor of 1.5 larger than the data cross section, taken as an average over the bins. If the integrals, dominated by the bins at small gap size, of the MC and data distributions are compared then the difference is approximately 1.3. The combined non-diffractive and diffractive samples describe the overall shape reasonably across the entire $\Delta\eta^F$ range, with the largest difference coming around $\Delta\eta^F = 3$ where the ND and SD+DD contributions are similar. These differences may be sensitive to the choice of MC steering and tunes. It can also be seen that unlike the ATLAS minimum bias rapidity gaps analysis [86], where softer diffraction is studied, there is no $\frac{d\sigma}{d\Delta\eta^F} \simeq constant$ behaviour at large gap sizes. Instead the cross section falls away with increasing forward gap size due to kinematic constraints on the jets. However,

like the minimum bias rapidity gaps analysis, non-diffractive dijet events make up the majority of the cross-section at low gap size and the diffractive contribution contributes more after gap sizes of 2 units in rapidity.

In comparing the results with the anti-k_t algorithm for $R = 0.4$ and $R = 0.6$ (Figures 10.1 and 10.2), the larger cone size roughly doubles the cross section for data but keeps the ratio between data and PYTHIA8 MC approximately at a factor of 1.5 up to $\Delta\eta^F = 4.0$, showing that the shape of the distribution is not changed significantly by the choice of jet cone size. Beyond this point the data show a hint of a diffractive plateau but this may be attributed to limited statistics in these bins. The differences in trigger efficiencies for L1_J5 between $R = 0.4$ and $R = 0.6$ jets (Section 9.4.2.1) leads to a greater proportion of events selected in data from the MinBias stream for $R = 0.6$ jets, particularly for $\Delta\eta^F > 4.0$ (Table 9.5). The large prescale weights for these events makes the statistical uncertainties very large. Figures 10.1(c) and 10.2(c) show the sizes of the systematic uncertainties relative to the central result. It can be observed that the jet energy scale uncertainty dominates the total uncertainty, which increases from 30% to 40% over the range of the measurement.

The CMS diffractive dijet analysis used anti-k_t $R = 0.5$ jets while previous experiments have used jet cone sizes (with different algorithms) up to $R = 1.0$ [134] but all focused on a single cone size. The ATLAS inclusive dijet analysis [110] showed no significant variation in quality of description with different cone sizes but made comparisons with NLO, not LO, calculations (and without trying to measure rapidity gaps). This analysis shows good consistency between cone sizes, like the inclusive ATLAS dijet measurement, where statistics are not limited.

The presence of a significant ND prediction throughout the measured range matches observations by CMS [104] and can be expected somewhat from the minimum bias rapidity gaps analysis [86]. The requirement of dijets with p_T above 20 GeV inside the X system, even at larger gap sizes, increases the ND component relative to the total MC contribution. However, this contribution is very sensitive to the rapidity fluctuations in the Lund hadronisation model, which are not well constrained.

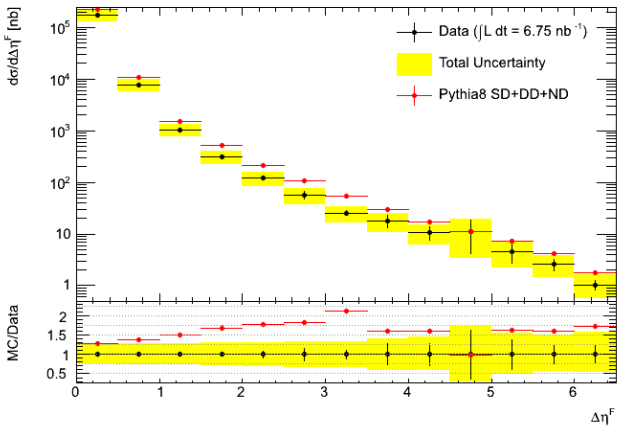

(a) Differential cross section compared to PYTHIA8 SD+DD+ND.

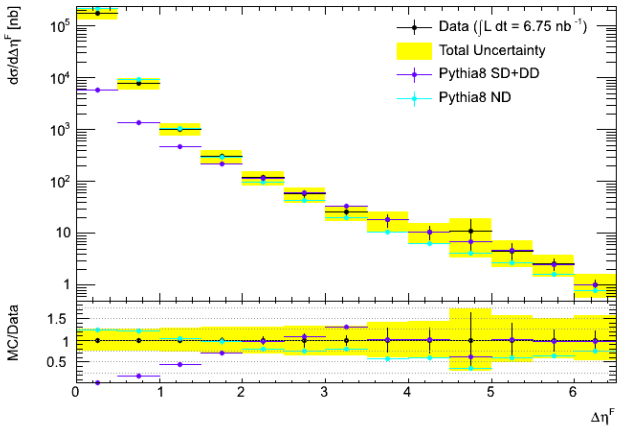

(b) Differential cross section compared to PYTHIA8 SD+DD and PYTHIA8 ND.

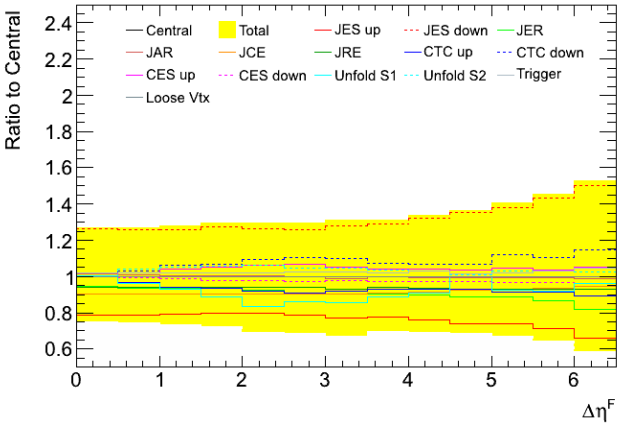

(c) Summary of systematic uncertainties.

Figure 10.1: Differential cross section and systematic uncertainties as a function of $\Delta\eta^F$ for anti-k_t dijets with $R = 0.4$. The data are compared to PYTHIA8 samples generated with the gap filter.

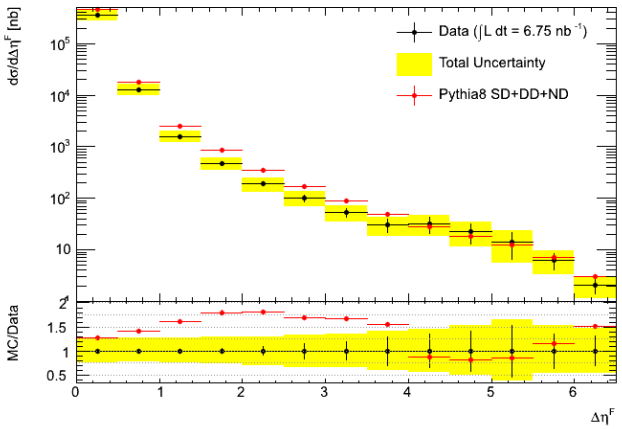

(a) Differential cross section compared to PYTHIA8 SD+DD+ND.

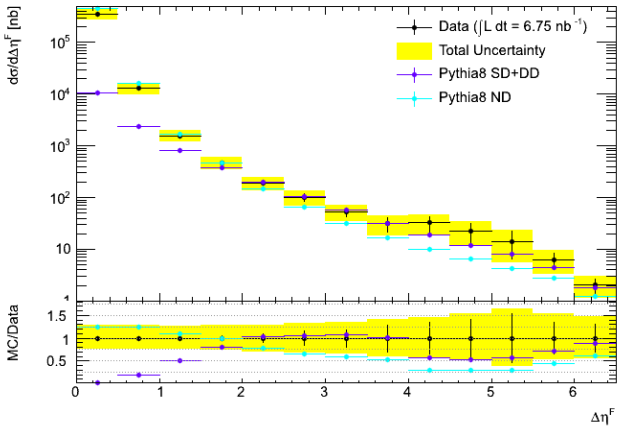

(b) Differential cross section compared to PYTHIA8 SD+DD and PYTHIA8 ND.

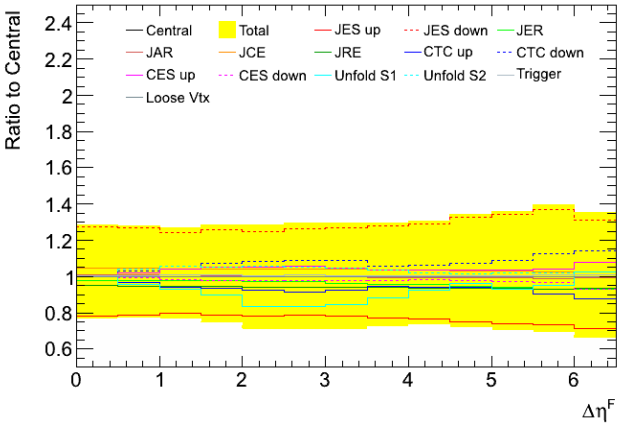

(c) Summary of systematic uncertainties.

Figure 10.2: Differential cross section and systematic uncertainties as a function of $\Delta\eta^F$ for anti-k_t dijets with $R = 0.6$. The data are compared to PYTHIA8 samples generated with the gap filter.

10.1.2 Proton Fractional Longitudinal Momentum Loss

The differential cross sections for $\xi^{\pm}$ are shown for anti-k_{t} $R = 0.6$ jets, with and without the forward gap requirement, in Figures 10.3 and 10.4, respectively. The chosen range over which the cross sections are presented, $-3.5 < \log_{10}(\xi^{\pm}) < -1.0$, excludes events with very small gaps.

Figures 10.3(a) and 10.3(b) show that the difference between the combined PYTHIA8 ND+SD+DD model and data increases steadily as $\xi^{\pm}$ decreases and this can be attributed to the SD+DD model component, which is heavily dominant in the lowest $\xi^{\pm}$ bin. The non-diffractive component dominates for $-2.0 < \log_{10}(\xi^{\pm}) < -1.0$ such that a similar MC/data ratio is seen here to that in Figure 10.2 for non-zero gaps. After the more stringent forward gap requirement is applied, as in Figure 10.4, the non-diffractive contribution reduces significantly.

A possible explanation for the excess of MC over data in the small $\xi^{\pm}$ (large forward gap) region is having rapidity gap destruction effects in data, which are not modelled in PYTHIA8. However, the choice of pomeron flux, from Schuler and Sjöstrand, used for the SD and DD samples (with a pomeron intercept of unity) shifts the diffractive mass distribution, and consequently ξ, to larger values than would be expected for more conventional pomeron flux descriptions. Therefore, the data in these figures are also sensitive to the choice of pomeron flux. The ratio of the data to the diffractive MC samples increases as $\xi^{\pm}$ gets smaller. This suggests that the MC cross section needs to fall away more steeply. Referring back to Figure 8.1.2, the default Schuler-Sjöstrand model used here generates far more large-ξ (high diffractive mass) events compared to samples generated with more conventional flux parametrisations such as those from the Donnachie-Landshoff or Berger-Streng models. Had these more conventional models been chosen, fewer diffractive events would be generated between $-3.5 < \log_{10}(\xi^{\pm}) < -2.0$ possibly improving the overall description of the data. This kind of behaviour was observed in the CMS diffractive dijet production result [104], where using the default pomeron flux in PYTHIA8 resulted in a significantly larger normalisation for PYTHIA8 SD+DD than for the other similar models, POMPYT SD and POMWIG SD, which use a pomeron intercept above unity (super-critical pomeron).

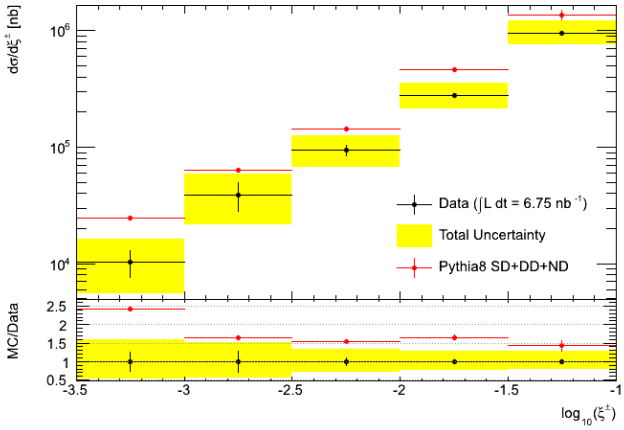

(a) Differential cross section compared to PYTHIA8 SD+DD+ND.

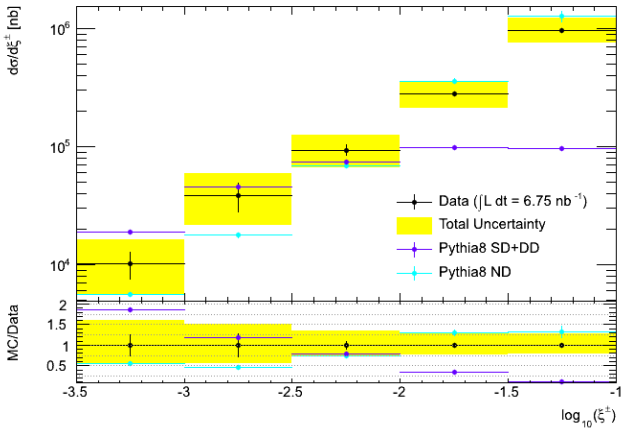

(b) Differential cross section compared to PYTHIA8 SD+DD and PYTHIA8 ND.

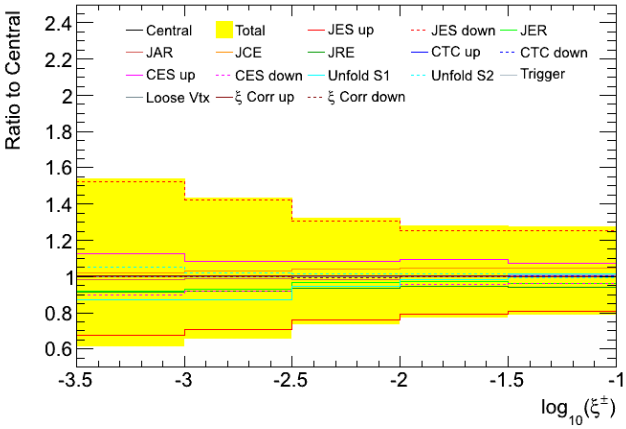

(c) Summary of systematic uncertainties.

Figure 10.3: Differential cross section and systematic uncertainties as a function of $\xi^{\pm}$ for anti-k_{t} dijets with $R = 0.6$. The data are compared to PYTHIA8 samples generated with the forward gap filter.

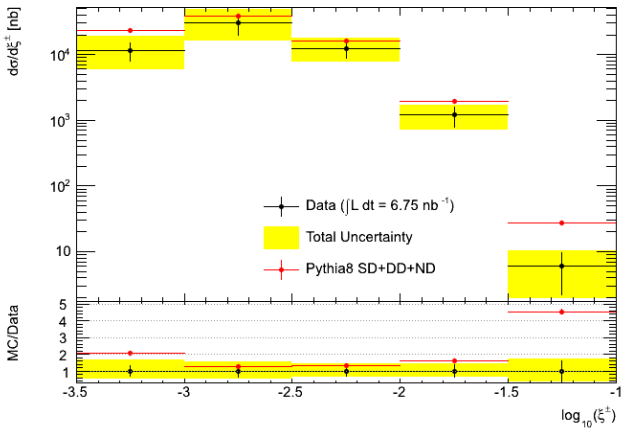

(a) Differential cross section compared to PYTHIA8 SD+DD+ND.

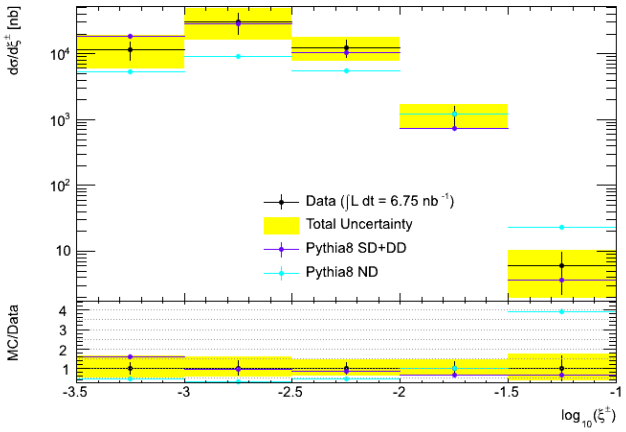

(b) Differential cross section compared to PYTHIA8 SD+DD and PYTHIA8 ND.

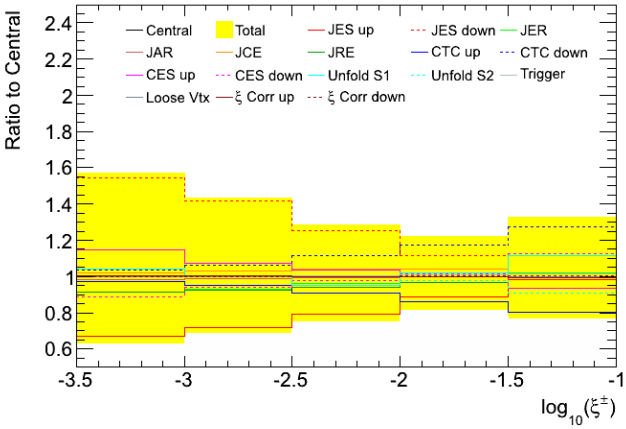

(c) Summary of systematic uncertainties.

Figure 10.4: Differential cross section and systematic uncertainties as a function of $\xi^{\pm}$ for anti-k_{t} dijets with $R = 0.6$ and a forward gap requirement of $3.0 < \Delta\eta^{F} < 6.5$. The data are compared to PYTHIA8 samples generated with the forward gap filter.

The hadron level cross section definition of $\xi^{\pm}$ in this analysis is different from the $\widetilde{\xi}$ definition in the CMS analysis, which means they are not directly comparable. The CMS $\widetilde{\xi}$ definition corrects the data to all stable truth particles in the range $-4.9 < \eta < +\infty$ ($-\infty < \eta < +4.9$) to include more of the X system, at the expense of more MC extrapolation, and the forward gap cut is 1.9 units in pseudorapidity. In this analysis, the forward gap range is $3.0 < \Delta\eta^F < 6.5$ and the cross sections are defined by $p > 200$ MeV for neutral particles and $p > 500$ MeV for charged particles in the range $|\eta| < 4.8$ to better match what can be observed experimentally. Although the cross section definitions are different, the cross sections are similar in magnitude.

Like CMS, once the sensitivity to the flux model is determined, it may be possible to look at the smallest $\xi^{\pm}$ ($\widetilde{\xi}$) bin, specifically the ratio of SD+DD to data, to provide some insight into rapidity gap survival. The CMS results found the diffractive models overestimate the data by an approximate factor of 5 for the range $0.0003 < \widetilde{\xi} < 0.002$. For this analysis, with the different cross section definition and the unconventional pomeron flux used to measure this factor, the factor is between 2-3 for $0.0003 < \xi^{\pm} < 0.001$ depending on whether the forward gap cut requirement is required and the choice of cone size.

10.1.3 Dijet variables

The differential cross sections as functions of the leading jet p_T and η, after applying the forward gap requirement, are presented in Figures 10.5 and 10.6, respectively. Before asking for the gap requirement the cross sections can be described well using only the non-diffractive samples.

The p_T differential cross section (Figure 10.5(a)) shows that, after requiring $3.0 < \Delta\eta^F < 6.5$, the MC and data agree reasonably well within statistical and systematic errors. A factor of about 1.4 is obtained when comparing the integrated data and MC, consistent with that obtained for $\Delta\eta^F$ and $\xi^{\pm}$. After splitting the total MC into its diffractive and non-diffractive components, Figure 10.5(b), a higher cross section is observed at low p_T for the diffractive MC samples compared to the non-diffractive ones and the distribution falls away faster for the diffractive than the non-diffractive MC. The data agree more with

the diffractive prediction at low p_T and the ND model is more consistent with what is seen in data for $p_T > 60$ GeV, after the statistical and systematic errors are taken into account. At higher p_T there is a hint that the ND model falls away faster than data, suggesting a diffractive component is also necessary in this region.

The measured cross section as a function of η (Figure 10.6(a)) is statistically limited throughout the full range. The total MC cross section rises from the edges of the η acceptance to become approximately flat over several units of rapidity and the data almost replicates this within errors, apart from some of the central bins. Once the MC is split into its components, Figure 10.6(b), the shape of the data cross section is better described by the diffractive samples than the non-diffractive model. However, the precision of the data is currently insufficient to distinguish between these two cases as the trigger selection in data uses the MinBias stream for forward jets and central jets with $p_T \lesssim 30$ GeV, introducing events with large prescale weights which significantly increase the statistical errors in most bins.

After asking for a forward gap, the non-diffractive PYTHIA8 model is characterised by a curve peaking in the centre of the η acceptance, which then falls away with increasing $|\eta|$. The diffractive samples show a double peak structure with maxima around $|\eta| = 2.5$, reflecting the fact that once a large gap is required the diffractive system and the jets within it tend to be forward in the detector, whereas in a non-diffractive event particles are produced more uniformly across the detector.

After a forward gap requirement of $3.0 < \Delta\eta^F < 6.5$, the statistics of both MC and data are approximately 10% of the total that passed the full selection criteria. The difference in the differential cross section between the central result and after the systematics are applied is typically less than 10% (apart from the jet energy scale systematic at forward pseudorapidity, as seen in Figure 10.6(c)). Combined with the large prescale weights entering the distribution, this results in some bins where the systematic uncertainties are much smaller that the fluctuations of the measurements. This also applies to the differential cross section as a function of p_T (Figure 10.5) once the forward gap requirement is applied, but is less pronounced.

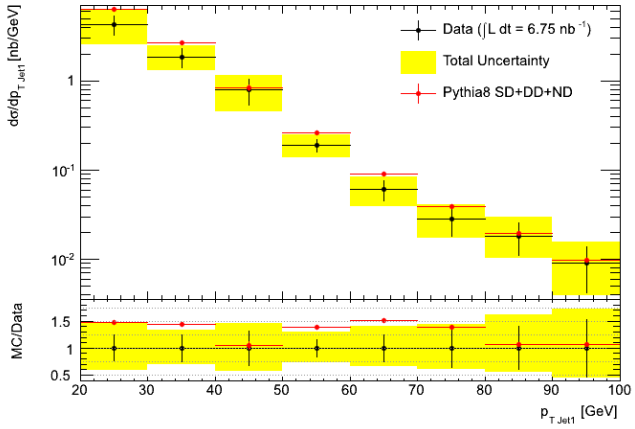

(a) Differential cross section compared to PYTHIA8 SD+DD+ND.

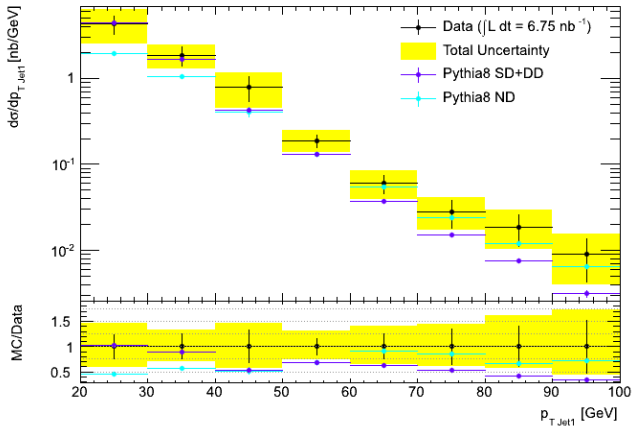

(b) Differential cross section compared to PYTHIA8 SD+DD and PYTHIA8 ND.

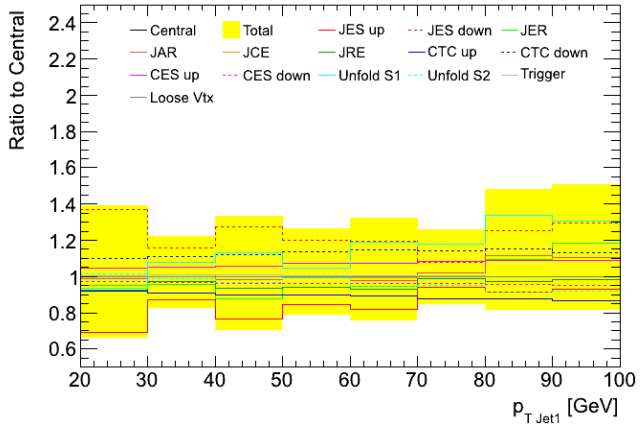

(c) Summary of systematic uncertainties.

Figure 10.5: Differential cross section and systematic uncertainties as a function of the leading jet p_T for anti-k_t dijets with $R = 0.6$ and a forward gap requirement of $3.0 < \Delta\eta^F < 6.5$. The data are compared to PYTHIA8 samples generated with the gap filter.

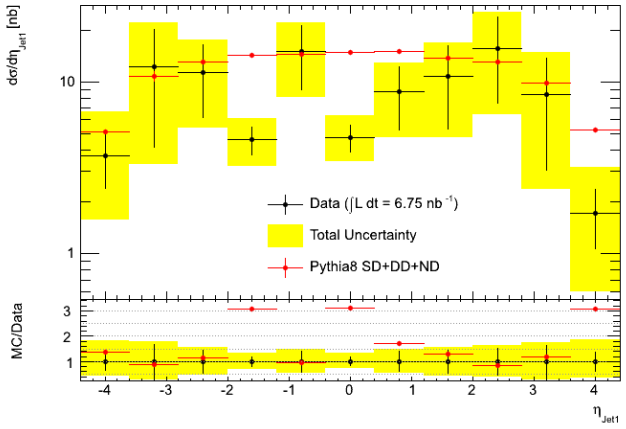

(a) Differential cross section compared to PYTHIA8 SD+DD+ND.

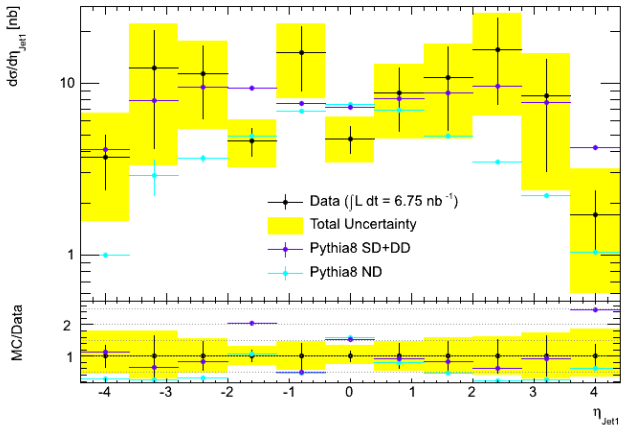

(b) Differential cross section compared to PYTHIA8 SD+DD and PYTHIA8 ND.

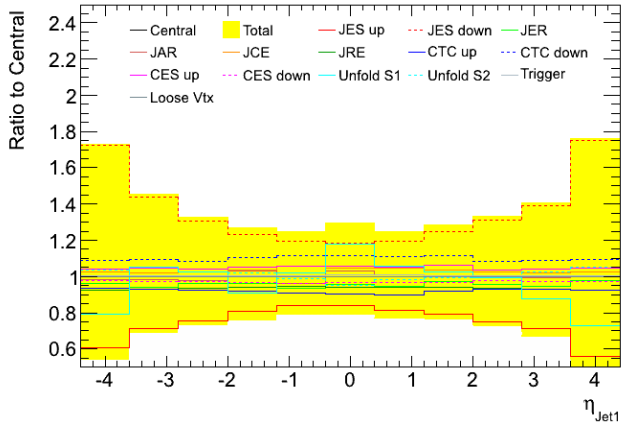

(c) Summary of systematic uncertainties.

Figure 10.6: Differential cross section and systematic uncertainties as a function of the leading jet η for anti-k_t dijets with $R = 0.6$ and a forward gap requirement of $3.0 < \Delta\eta^F < 6.5$. The data are compared to PYTHIA8 samples generated with the gap filter.

10.2 Fitting Non-Diffractive and Diffractive Monte Carlo Components to Data

The normalisations of the diffractive and non-diffractive components of the PYTHIA8 sample can be fitted to the data to constrain the fractions of each component present. This is not a rigorous process, and no attempt is made to evaluate systematic uncertainties, but is a useful exercise to see if the the data description can be optimised by varying the contributions from each subprocess in the MC.

The extracted fractions of ND and SD+DD components are found to depend slightly on the variable studied and the method of scaling the combined PYTHIA8 ND+SD+DD sample to the overall data. The scaling is either done by making the integrated areas of the curves match over the entire sample (default), a portion of the sample where the single and double diffractive components are larger than the non-diffractive component, or a single bin.

Figure 10.7 illustrates the fitting procedure for the cross section measured as a function of $\Delta\eta^F$ for anti-k_t dijets with $R = 0.6$. The shapes of each distribution are kept fixed and the relative fractions of ND:(SD+DD) are optimised. The fit is not quite as good at large gap sizes as at small sizes. It yields a 0.988:0.012 ratio of ND:(SD+DD), constrained mainly by the dominance of the non-diffractive contribution to PYTHIA8 at small gap sizes. For $R = 0.4$ jets, the fitting procedure gives a similar ratio of 0.985:0.015. By changing to different types of fitting, the contributions of the relative functions are changed by 1% at most.

Determining the components from the $\xi^{\pm}$ distribution (Figure 10.8) produces a different result compared to $\Delta\eta^F$, due to the restriction of the $\xi^{\pm}$ range to $-3.5 < \log_{10}(\xi^{\pm}) < -1.0$, excluding the region $\log_{10}(\xi^{\pm}) > -1.0$ which is dominated by the non-diffractive sample. This changes the SD+DD fit component from 0.012 ± 0.001 in $\Delta\eta^F$ to 0.122 ± 0.001. If a forward gap cut is applied to these distributions, then the ratio of the non-diffractive to diffractive components is approximately 0.5:0.5 for ND:(SD+DD). The factors by which the PYTHIA8 SD+DD predictions have to be downscaled to match the data are approximately 3.2 for $\Delta\eta^F$, which is broadly consistent for most cases where the full data and

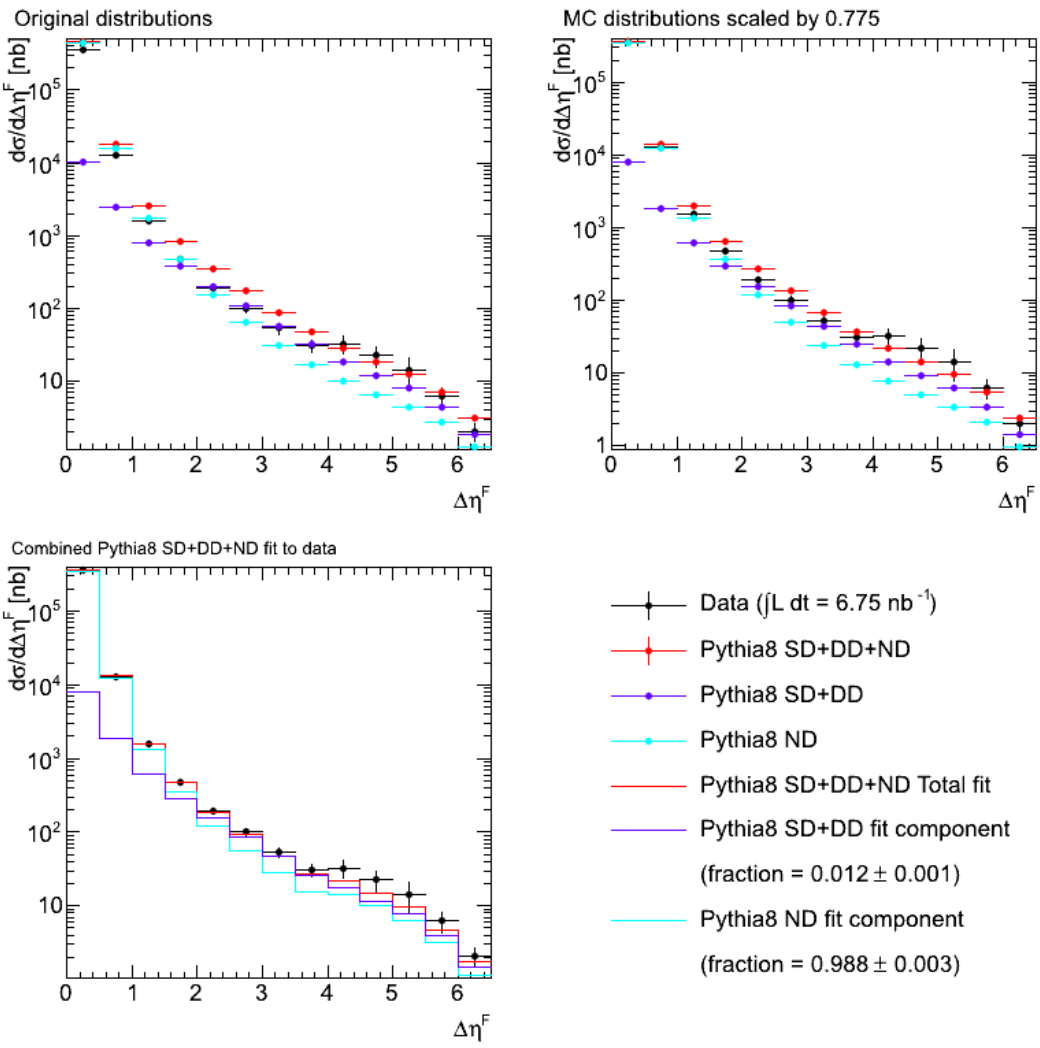

Figure 10.7: Cross section decomposition as a function of $\Delta\eta^F$ for anti-k_t dijets with $R = 0.6$. (Top left) The data cross section is compared to PYTHIA8 samples generated with the gap filter. (Top right) The combined PYTHIA8 ND+SD+DD sample is scaled to the area of the data. (Bottom left) The ND and SD+DD components of the combined PYTHIA8 sample are adjusted to fit the data. (Bottom right) Legend and fractional components of PYTHIA8 ND and SD+DD according to fit, with statistical uncertainties.

MC are studied (i.e. without any forward rapidity gap cuts). The only case where this does not hold is for the $\xi^{\pm}$ distributions, where the downscaling factor is approximately 1.9 as a result of excluding a large proportion of the ND distribution. This agrees more with the factors obtained once the forward rapidity gap cut is applied as the increase in the amount of SD+DD relative to ND means this downscaling factor becomes closer to 2.1. The differences in these factors may be explained by how well the models predict the behaviour at large gap size (small $\xi^{\pm}$).

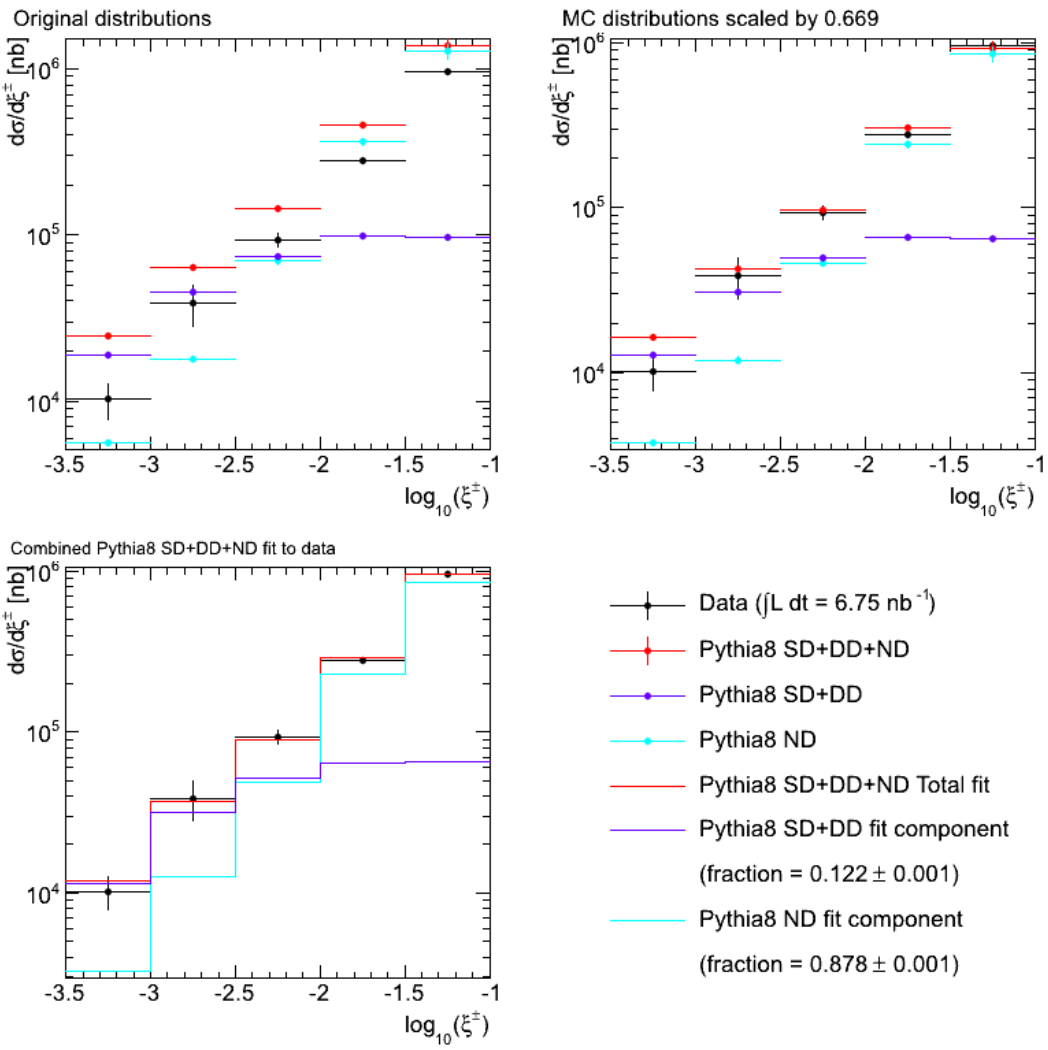

Figure 10.8: Cross section decomposition as a function of $\xi^{\pm}$ for anti-k_t dijets with $R = 0.6$. (Top left) The data cross section is compared to PYTHIA8 samples generated with the gap filter. (Top right) The combined PYTHIA8 ND+SD+DD sample is scaled to the area of the data. (Bottom left) The ND and SD+DD components of the combined PYTHIA8 sample are adjusted to fit the data. (Bottom right) Legend and fractional components of PYTHIA8 ND and SD+DD according to fit, with statistical uncertainties.

This information could potentially be interpreted as a gap survival factor. This might be misleading as there may be problems with the SD and DD normalisations, due to the flux choice (see Section 10.1.2). However, without an improved model for PYTHIA8 and an alternative model, e.g. HERWIG++ to test the effects of hadronisation, it is premature to attach any significant meaning to these numbers.

CHAPTER 11

Conclusions

The first measurement of the cross section for diffractive dijet production using forward rapidity gaps at the ATLAS experiment has been made possible by analysing low pile-up LHC data taken in 2010, with negligible background.

Forward rapidity gaps, quantified by $\Delta\eta^F$, are a useful tool in distinguishing between non-diffractive and diffractive interactions of protons at high energy. The relationship between $\Delta\eta^F$ and the mass of the diffractive system allows the results to also be represented as a function of $\xi^{\pm}$, which for the single diffractive case approximates the fractional longitudinal momentum loss of the scattered proton from the information available within the detector acceptance.

By correcting the data for experimental effects and comparing to Monte Carlo samples of non-diffractive, single-diffractive and double-diffractive PYTHIA8, it is shown that the non-diffractive component of the Monte Carlo model is capable of describing a significant portion of data, via large fluctuations in the hadronisation. However, a diffractive component is also required for a more complete description of the data, especially once

a large forward rapidity gap is required in an event. The requirement of a hard scale in diffractive interactions changes the nature of the $\Delta\eta^F$ distribution from flattening out at large gap sizes (forward rapidity gap plateau) in the minimum bias case to exponentially falling for the dijet analysis.

The problems encountered in generating the Monte Carlo samples prevent a complete interpretation of the data. The HERWIG++ samples were not usable and the PYTHIA8 samples used an outdated pomeron flux description compared with what was measured at HERA, overestimating the diffractive contribution. Being limited to one model prevents the uncertainty on hadronisation being determined and limits the ability to estimate the rapidity gap survival probability.

11.1 Potential Improvements and Extensions to the Analysis

While the analysis has provided a first measurement of the large rapidity gap contribution to dijet production, it would benefit from additional studies that would increase the precision of the analysis and allow the pomeron structure and gap survival effects to be probed.

By generating new Monte Carlo samples with different models for diffractive dijet production, a more realistic model dependence uncertainty could be obtained. Also modifying PYTHIA8 to use a more appropriate pomeron flux parametrisation, such as that from Donnachie and Landshoff, will help. This would allow the rapidity gap survival probability to be measured. A generator such as POMWIG may allow a better assessment of model dependences and would permit the $z_{\mathbb{P}}$ distribution to be unfolded.

The correction process currently unfolds the different distributions separately but there are two exponentially falling distributions in this analysis, $\Delta\eta^F$ and jet p_T, both of which produce a net migration into the large rapidity gap analysis region. By using a simultaneous unfolding procedure for both of these variables, the migrations will be better controlled and there should not be a necessity to correct the jet p_T scale as was done in

this analysis.

One of the main causes for a loss in precision for this result comes from the trigger requirement to select jets using the L1_J5 trigger down to 80% in order to increase statistics and avoid overlap of events in different streams. The trigger strategy in data should be modified to use fully efficient triggers while maintaining or increasing the existing statistics. In particular, the L1_MBTS_2 trigger could be used for the MinBias stream, given it is unprescaled and has a very high trigger rate for the data used in this analysis and there is currently a small return from using the MinBias stream with L1_MBTS_1. L1_MBTS_2 could either be used exclusively or allow the p_T cuts on L1_J5 to be increased to select jets at full efficiency. Finally, rather than trying to assign triggers to both jets, a single trigger could be assigned to the event. If the existing trigger scheme remains, the p_T cut at which central jets are selected down to 80% should be set by anti-k_{t} $R = 0.6$ jets, and also be used for anti-k_{t} $R = 0.4$ jets so that the relative proportion of events selected using the MinBias and L1Calo streams is consistent.

This analysis can be extended to use dedicated ALFA runs taken in 2011 and 2012, in which ALFA can be used as a proton tagger, where the beam optics are optimised for elastic and diffractive interactions. This would completely remove the ambiguity between single diffractive and non-diffractive events in data, allowing the diffractive distributions to be clearly obtained and interpreted in terms of pomeron structure and rapidity gap survival probabilities. Furthermore, the t distribution in diffractive dijet production could then be measured for the first time at the LHC, potentially setting new constraints on the gluon and quark densities in the pomeron.

Bibliography

[1] P. De Laplace, F. Truscott, and F. Emory, *A Philosophical Essay on Probabilities*. COSIMO CLASSICS, 2007.

[2] I. J. R. Aitchison and A. J. G. Hey, *Gauge Theories in Particle Physics: A Practical Introduction: Volume 2 Non-Abelian Gauge Theories: Qcd and the Electroweak Theory*. Institute of Physics Publishing, January 2004. 3rd edition.

[3] J. Beringer *et al.*, "Review of particle physics," *Phys. Rev. D*, vol. 86, p. 010001, Jul 2012.

[4] G. Bernardi, M. Carena, and T. Junk, "Higgs bosons: theory and searches," *Particle Data Group*, 2007.

[5] A. Djouadi, "Higgs Physics: Theory," *Pramana*, vol. 79, pp. 513–539, 2012.

[6] LHC Higgs Cross Section Working Group, S. Heinemeyer, C. Mariotti, G. Passarino, and R. Tanaka (Eds.), "Handbook of LHC Higgs Cross Sections: 3. Higgs Properties," *CERN-2013-004*, CERN, Geneva, 2013.

[7] The ATLAS Collaboration, "Observation of a new particle in the search for the Standard Model Higgs boson with the ATLAS detector at the LHC," *Phys. Lett.*, vol. B716, pp. 1–29, 2012.

[8] S. Chatrchyan *et al.*, "Observation of a new boson at a mass of 125 GeV with the CMS experiment at the LHC," *Phys.Lett.*, vol. B716, pp. 30–61, 2012.

[9] G. Aad *et al.*, "Measurements of Higgs boson production and couplings in diboson final states with the ATLAS detector at the LHC," 2013.

[10] G. Aad *et al.*, "Evidence for the spin-0 nature of the Higgs boson using ATLAS data," 2013.

[11] S. Chatrchyan *et al.*, "Study of the Mass and Spin-Parity of the Higgs Boson Candidate Via Its Decays to Z Boson Pairs," *Phys.Rev.Lett.*, vol. 110, p. 081803, 2013.

[12] P. Ade *et al.*, "Planck 2013 results. I. Overview of products and scientific results," 2013.

[13] S. Dimopoulos, S. Raby, and F. Wilczek, "Supersymmetry and the scale of unification," *Phys. Rev. D*, vol. 24, pp. 1681–1683, Sep 1981.

[14] A. Collaboration, "Atlas physics summary plots." `https://twiki.cern.ch/twiki/pub/AtlasPublic/CombinedSummaryPlots`.

[15] S. Gilardoni, D. Manglunki, J.-P. Burnet, C. Carli, M. Chanel, R. Garoby, M. Giovannozzi, S. Hancock, H. Haseroth, K. Hbner, D. Kchler, J. Lewis, A. Lombardi, M. Martini, S. Maury, E. Mtral, D. Mhl, G. Plass, L. Rinolfi, R. Scrivens, R. Steerenberg, C. Steinbach, M. Vretenar, and T. Zickler, *Fifty years of the CERN Proton Synchrotron: Volume 2*. Geneva: CERN, 2013.

[16] CERN, "Big science - the lhc in pictures." `http://bigscience.web.cern.ch/bigscience/en/lhc/lhc2.html`.

[17] D. J. Simon, "The CERN PS complex: a versatile particle factory," 1996. CERN-PS-96-019-DI.

[18] O. S. Bruning, P. Collier, P. Lebrun, S. Myers, R. Ostojic, J. Poole, and P. Proudlock, *LHC Design Report*. Geneva: CERN, 2004.

[19] S. Baird, "Accelerators for pedestrians; rev. version," Tech. Rep. AB-Note-2007-014. CERN-AB-Note-2007-014. PS-OP-Note-95-17-Rev-2. CERN-PS-OP-Note-95-17-Rev-2, CERN, Geneva, Feb 2007.

[20] L. Evans and P. Bryant, "Lhc machine," *Journal of Instrumentation*, vol. 3, no. 08, p. S08001, 2008.

[21] J. M. Campbell, J. Huston, and W. Stirling, "Hard Interactions of Quarks and Gluons: A Primer for LHC Physics," *Rept.Prog.Phys.*, vol. 70, p. 89, 2007.

[22] A. Collaboration, "Public results for atlas luminosity measurements." `https://twiki.cern.ch/twiki/bin/view/AtlasPublic/LuminosityPublicResults`.

[23] The ALICE Collaboration, "The ALICE experiment at the CERN LHC," *Journal of Instrumentation*, vol. 3, no. 08, p. S08002, 2008.

[24] The LHCb Collaboration, *LHCb reoptimized detector design and performance: Technical Design Report*. Technical Design Report LHCb, CERN, 2003.

[25] The CMS Collaboration, *CMS Physics Technical Design Report Volume I: Detector Performance and Software*. Technical Design Report CMS, CERN, 2006.

[26] G. Latino, "The TOTEM Experiment at LHC," pp. 631–646, 2008.

[27] The LHCf Collaboration, "Technnical Proposal for the CERN LHCf Experiment: Measurement of Photons and Neutral Pions in the Very Forward Region of LHC," 2005. CERN-LHCC-2005-032. LHCC-P-007.

[28] C. Eck, J. Knobloch, L. Robertson, I. Bird, K. Bos, N. Brook, D. Dllmann, I. Fisk, D. Foster, B. Gibbard, C. Grandi, F. Grey, J. Harvey, A. Heiss, F. Hemmer, S. Jarp, R. Jones, D. Kelsey, M. Lamanna, H. Marten, P. Mato-Vila, F. Ould-Saada, B. Panzer-Steindel, L. Perini, Y. Schutz, U. Schwickerath, J. Shiers, and T. Wenaus, *LHC computing Grid: Technical Design Report. Version 1.06 (20 Jun 2005)*. Technical Design Report LCG, Geneva: CERN, 2005.

[29] *ATLAS: technical proposal for a general-purpose pp experiment at the Large Hadron Collider at CERN*. LHC Tech. Proposal, Geneva: CERN, 1994.

[30] G. Aad *et al.*, "The atlas experiment at the cern large hadron collider," *JINST*, vol. 3, p. S08003, 2008.

[31] U. Egede, *The search for a Standard Model Higgs at the LHC and electron identification using transition radiation in the ATLAS tracker*. PhD thesis, Lund U., Lund, 1998. Presented on 16 Jan 1998.

[32] "Atlas liquid argon calorimeter: Technical design report," 1996.

[33] G. Aad *et al.*, "Electron performance measurements with the ATLAS detector using the 2010 LHC proton-proton collision data," *Eur.Phys.J.*, vol. C72, p. 1909, 2012.

[34] *ATLAS calorimeter performance: Technical Design Report*. Technical Design Report ATLAS, Geneva: CERN, 1996.

[35] A. Artamonov, D. Bailey, G. Belanger, M. Cadabeschi, T. Y. Chen, V. Epshteyn, P. Gorbounov, K. K. Joo, M. Khakzad, V. Khovanskiy, P. Krieger, P. Loch, J. Mayer, E. Neuheimer, F. G. Oakham, M. O'Neill, R. S. Orr, M. Qi, J. Rutherfoord, A. Savine, M. Schram, P. Shatalov, L. Shaver, M. Shupe, G. Stairs, V. Strickland, D. Tompkins, I. Tsukerman, and K. Vincent, "The atlas forward calorimeter," *Journal of Instrumentation*, vol. 3, no. 02, p. P02010, 2008.

[36] C. W. Fabjan and F. Gianotti, "Calorimetry for Particle Physics," *Rev. Mod. Phys.*, vol. 75, pp. 1243–1286. 96 p, Oct 2003.

[37] E. Abat *et al.*, "Combined performance studies for electrons at the 2004 atlas combined test-beam," *Journal of Instrumentation*, vol. 5, no. 11, p. P11006, 2010.

[38] T. Davidek and the Atlas Tilecal system, "Atlas tile calorimeter performance for single particles in beam tests," *Journal of Physics: Conference Series*, vol. 160, no. 1, p. 012057, 2009.

[39] B. Dowler *et al.*, "Performance of the ATLAS hadronic end-cap calorimeter in beam tests," *Nucl.Instrum.Meth.*, vol. A482, pp. 94–124, 2002.

[40] "The atlas magnet system." `http://atlas-magnet.web.cern.ch/atlas-magnet/`.

[41] "The atlas luminosity task force." `http://project-atlas-lucid.web.cern.ch/project-atlas-lucid/taskforce/main.html`.

[42] G. Aad *et al.*, "Luminosity Determination in *pp* Collisions at $\sqrt{s} = 7$ TeV Using the ATLAS Detector at the LHC," *Eur.Phys.J.*, vol. C71, p. 1630, 2011.

[43] "Atlas first level trigger: Technical design report," 1998.

[44] S. Klous, "Event streaming in the online system," 2010.

[45] R. Achenbach *et al.*, "The atlas level-1 calorimeter trigger," *Journal of Instrumentation*, vol. 3, no. 03, p. P03001, 2008.

[46] P. Amaral, N. Ellis, P. Farthouat, P. Gallno, J. Haller, T. Maeno, T. Pauly, H. Lima, I. Arcas, J. deSeixas, G. Schuler, R. Spiwoks, R. Teixeira, and T. Wengler, "The atlas level-1 central trigger system," *Nuclear Science, IEEE Transactions on*, vol. 52, pp. 1217 – 1222, August 2005.

[47] N. J. Buchanan *et al.*, "Atlas liquid argon calorimeter front end electronics," *Journal of Instrumentation*, vol. 3, no. 09, p. P09003, 2008.

[48] A. Hamilton, "The ATLAS Trigger System Commissioning and Performance," *ArXiv e-prints*, Sept. 2010.

[49] B. sman *et al.*, "The atlas level-1 calorimeter trigger: Preprocessor implementation and performance," *Journal of Instrumentation*, vol. 7, no. 12, p. P12008, 2012.

[50] L. Collaboration *et al.*, "Atlas level-1 calorimeter trigger algorithms," tech. rep., ATL-DAQ-2004-011, Version 1.0, 2004.

[51] "Performance of the ATLAS Electron and Photon Trigger in p-p Collisions at sqrts = 7 TeV in 2011," 2012.

[52] M. Stockton, "The ATLAS level-1 central trigger," *J.Phys.Conf.Ser.*, vol. 331, p. 022041, 2011.

[53] P. Calafiura, W. Lavrijsen, C. Leggett, M. Marino, and D. Quarrie, "The athena control framework in production, new developments and lessons learned," pp. 456–458, 2005.

[54] G. Barrand, I. Belyaev, P. Binko, M. Cattaneo, R. Chytracek, G. Corti, M. Frank, G. Gracia, J. Harvey, E. Herwijnen, P. Maley, P. Mato, S. Probst, and F. Ranjard, "GAUDI - A software architecture and framework for building HEP data processing applications," *Computer Physics Communications*, vol. 140, no. 12, pp. 45 – 55, 2001. CHEP2000.

[55] S. Agostinelli *et al.*, "Geant4 a simulation toolkit," *Nuclear Instruments and Methods in Physics Research Section A: Accelerators, Spectrometers, Detectors and Associated Equipment*, vol. 506, no. 3, pp. 250–303, 2003.

[56] V. Lacuesta, "Track and vertex reconstruction in the ATLAS experiment," *Journal of Instrumentation*, vol. 8, no. 02, p. C02035, 2013.

[57] M. Limper, S. Bentvelsen, and A. P. Colijn, *Track and vertex reconstruction in the ATLAS inner detector*. PhD thesis, Amsterdam U., Amsterdam, 2009. Presented on 12 Oct 2009.

[58] "Electron and photon reconstruction and identification in atlas: expected performance at high energy and results at 900 gev," Tech. Rep. ATLAS-CONF-2010-005, CERN, Geneva, Jun 2010.

[59] C. Collard, "Electronic calibration of the ATLAS LAr calorimeter," *Nucl. Instrum. Methods Phys. Res., A*, vol. 623, pp. 246–248. 3 p, Apr 2009. Conference proceedings deadline : 20/04/2009.

[60] M. Kuna, "Electron and photon reconstruction and identification with the ATLAS detector," *Nucl.Phys.Proc.Suppl.*, vol. 215, pp. 176–178, 2011.

[61] G. Pospelov, "Recent results on jets from ATLAS," Apr 2011.

[62] W. Lampl, S. Laplace, D. Lelas, P. Loch, H. Ma, S. Menke, S. Rajagopalan, D. Rousseau, S. Snyder, and G. Unal, "Calorimeter clustering algorithms: Description and performance," Tech. Rep. ATL-LARG-PUB-2008-002. ATL-COM-LARG-2008-003, CERN, Geneva, Apr 2008.

[63] "Properties of Jets and Inputs to Jet Reconstruction and Calibration with the ATLAS Detector Using Proton-Proton Collisions at $\sqrt{s} = 7$ TeV," 2010.

[64] K. Perez, "Jet Software: From the Users Point of View." ATLAS Hadronic Calibration Workshop, 2009.

[65] M. Cacciari, G. P. Salam, and G. Soyez, "The anti-k$_t$ jet clustering algorithm," *Journal of High Energy Physics*, vol. 2008, no. 04, p. 063, 2008.

[66] "Data-quality requirements and event cleaning for jets and missing transverse energy reconstruction with the atlas detector in proton-proton collisions at a center-of-mass energy of $sqrts = 7$ tev," Tech. Rep. ATLAS-CONF-2010-038, CERN, Geneva, Jul 2010.

[67] W. Bell, "Minimum bias physics at the LHC with the ATLAS detector," pp. 109–116, 2009.

[68] G. Aad *et al.*, "Performance of the ATLAS Trigger System in 2010," *Eur.Phys.J.*, vol. C72, p. 1849, 2012.

[69] A. Collaboration, "Level-1 calorimeter trigger public results." `https://twiki.cern.ch/twiki/bin/view/AtlasPublic/L1CaloTriggerPublicResults`.

[70] T. Liu, "Optical links for atlas liquid argon calorimeter front-end electronics readout," *Journal of Instrumentation*, vol. 6, no. 01, p. C01013, 2011.

[71] "ATLAS Monte Carlo tunes for MC09," Tech. Rep. ATL-PHYS-PUB-2010-002, CERN, Geneva, Mar 2010.

[72] A. Collaboration, "Public results for the atlas trigger system." `https://twiki.cern.ch/twiki/bin/view/Atlas/TriggerPublicResults`.

[73] H. S. Bansil, "Monitoring the ATLAS Level-1 Calorimeter Trigger Electromagnetic Trigger Items using Proton-Proton Collision Data." Midterm Report, University of Birmingham, `http://epweb2.ph.bham.ac.uk/user/bansil/Files/MidtermReport/hsb_midterm.pdf`, 2010.

[74] A. Collaboration, "Atlantis - event display for atlas." `http://www.hep.ucl.ac.uk/atlas/atlantis/`.

[75] J.-B. Sauvan, "ATLAS level-1 trigger energy estimation and calibration for energy recovery in the liquid argon calorimeter," Tech. Rep. ATL-COM-LARG-2010-041, CERN, Geneva, Sep 2010.

[76] "Probing the material in front of the atlas electromagnetic calorimeter with energy flow from sqrt(s)=7 tev minimum bias events," Tech. Rep. ATLAS-CONF-2010-037, CERN, Geneva, Jul 2010.

[77] H. S. Bansil, J. Bracinik, R. D. Mudd, and P. R. Newman, "Tier-0 Monitoring of the ATLAS Level-1 Calorimeter Trigger Jet and Electromagnetic Trigger Item Efficiencies," Tech. Rep. ATL-DAQ-INT-2012-002, CERN, Geneva, Jul 2012.

[78] M. Elsing, L. Goossens, A. Nairz, and G. Negri, "The atlas tier-0: Overview and operational experience," *Journal of Physics: Conference Series*, vol. 219, no. 7, p. 072011, 2010.

[79] N. Nikiforou, "Performance of the ATLAS Liquid Argon Calorimeter after three years of LHC operation and plans for a future upgrade," 2013.

[80] T. Golling, H. Hayward, P. Onyisi, H. Stelzer, and P. Waller, "The atlas data quality defect database system," *The European Physical Journal C*, vol. 72, pp. 1–6, 2012.

[81] Y. L. Dokshitzer, "Calculation of the Structure Functions for Deep Inelastic Scattering and e+ e- Annihilation by Perturbation Theory in Quantum Chromodynamics.," *Sov.Phys.JETP*, vol. 46, pp. 641–653, 1977.

[82] V. Gribov and L. Lipatov, "Deep inelastic ep scattering in perturbation theory," *Sov.J.Nucl.Phys.*, vol. 15, pp. 438–450, 1972.

[83] G. Altarelli and G. Parisi, "Asymptotic Freedom in Parton Language," *Nucl.Phys.*, vol. B126, p. 298, 1977.

[84] G. Aad *et al.*, "Measurement of the Inelastic Proton-Proton Cross-Section at $\sqrt{s} = 7$ TeV with the ATLAS Detector," *Nature Commun.*, vol. 2, p. 463, 2011.

[85] D. Acosta *et al.*, "Inclusive double pomeron exchange at the Fermilab Tevatron $\bar{p}p$ collider," *Phys.Rev.Lett.*, vol. 93, p. 141601, 2004.

[86] G. Aad *et al.*, "Rapidity gap cross sections measured with the ATLAS detector in pp collisions at $\sqrt{s} = 7$ TeV," *Eur.Phys.J.*, vol. C72, p. 1926, 2012.

[87] P. Collins, "An Introduction to Regge Theory and High-Energy Physics," 1977.

[88] A. Donnachie and P. Landshoff, "Elastic scattering and diffraction dissociation," *Nuclear Physics B*, vol. 244, no. 2, pp. 322 – 336, 1984.

[89] K. A. Goulianos, "Diffraction in QCD," 2002.

[90] G. Ingelman and P. Schlein, "Jet structure in high mass diffractive scattering," *Physics Letters B*, vol. 152, no. 34, pp. 256 – 260, 1985.

[91] J. C. Collins, "Proof of factorization for diffractive hard scattering," *Phys. Rev. D*, vol. 57, pp. 3051–3056, Mar 1998.

[92] R. Bonino, A. Brandt, J. Cheze, S. Erhan, G. Ingelman, M. Medinnis, P. Schlein, J. Zsembery, J. Zweizig, A. Clark, and J. Hansen, "Evidence for transverse jets in high-mass diffraction: UA8 Experiment," *Physics Letters B*, vol. 211, no. 12, pp. 239 – 246, 1988.

[93] A. Brandt, S. Erhan, A. Kuzucu, M. Medinnis, N. Ozdes, P. Schlein, M. Zeyrek, J. Zweizig, J. Cheze, and J. Zsembery, "Evidence for a super-hard pomeron structure," *Physics Letters B*, vol. 297, no. 34, pp. 417 – 424, 1992.

[94] A. Aktas *et al.*, "Measurement and QCD analysis of the diffractive deep-inelastic scattering cross-section at HERA," *Eur.Phys.J.*, vol. C48, pp. 715–748, 2006.

[95] A. Aktas *et al.*, "Dijet Cross Sections and Parton Densities in Diffractive DIS at HERA," *JHEP*, vol. 0710, p. 042, 2007.

[96] S. Chekanov *et al.*, "A QCD analysis of ZEUS diffractive data," *Nuclear Physics B*, vol. 831, no. 12, pp. 1 – 25, 2010.

[97] J. D. Bjorken, "Rapidity gaps and jets as a new-physics signature in very-high-energy hadron-hadron collisions," *Phys. Rev. D*, vol. 47, pp. 101–113, Jan 1993.

[98] T. Affolder *et al.*, "Diffractive dijets with a leading antiproton in $\bar{p}p$ collisions at $\sqrt{s} = 1800$GeV," *Phys. Rev. Lett.*, vol. 84, pp. 5043–5048, May 2000.

[99] M. Klasen and G. Kramer, "Survival probability for diffractive dijet production in $p\bar{p}$ collisions from next-to-leading order calculations," *Phys. Rev. D*, vol. 80, p. 074006, Oct 2009.

[100] A. Kaidalov, V. Khoze, A. Martin, and M. Ryskin, "Factorization breaking in diffractive dijet production," *Phys.Lett.*, vol. B559, pp. 235–238, 2003.

[101] V. Khoze, A. Martin, and M. Ryskin, "Soft diffraction and the elastic slope at tevatron and lhc energies: a multi-pomeron approach," *The European Physical Journal C - Particles and Fields*, vol. 18, no. 1, pp. 167–179, 2000.

[102] D. Acosta *et al.*, "Diffractive dijet production at $\sqrt{s} = 630$ and 1800 gev at the fermilab tevatron," *Phys. Rev. Lett.*, vol. 88, p. 151802, Mar 2002.

[103] T. Aaltonen *et al.*, "Diffractive Dijet Production in $\bar{p}p$ Collisions at $\sqrt{s} = 1.96$ TeV," *Phys.Rev.*, vol. D86, p. 032009, 2012.

[104] S. Chatrchyan *et al.*, "Observation of a diffractive contribution to dijet production in proton-proton collisions at $\sqrt{s} = 7$ TeV," *Phys. Rev. D*, vol. 87, p. 012006, Jan 2013.

[105] T. Sjstrand, S. Mrenna, and P. Skands, "Pythia 6.4 physics and manual," *Journal of High Energy Physics*, vol. 2006, no. 05, p. 026, 2006.

[106] T. Sjostrand, S. Mrenna, and P. Z. Skands, "A Brief Introduction to PYTHIA 8.1," *Comput.Phys.Commun.*, vol. 178, pp. 852–867, 2008.

[107] P. Bruni and G. Ingelman, "Diffractive hard scattering at e p and p anti-p colliders," *Conf.Proc.*, vol. C930722, pp. 595–596, 1993.

[108] B. E. Cox and J. R. Forshaw, "POMWIG: HERWIG for diffractive interactions," *Comput.Phys.Commun.*, vol. 144, pp. 104–110, 2002.

[109] S. Alioli, K. Hamilton, P. Nason, C. Oleari, and E. Re, "Jet pair production in POWHEG," *JHEP*, vol. 1104, p. 081, 2011.

[110] G. Aad *et al.*, "Measurement of inclusive jet and dijet production in *pp* collisions at $\sqrt{s} = 7$ TeV using the ATLAS detector," *Phys.Rev.*, vol. D86, p. 014022, 2012.

[111] B. Webber, "Parton shower monte carlo event generators," vol. 6, no. 12, p. 10662, 2011.

[112] B. Andersson, G. Gustafson, G. Ingelman, and T. Sjstrand, "Parton fragmentation and string dynamics," *Physics Reports*, vol. 97, no. 23, pp. 31 – 145, 1983.

[113] S. Navin, "Diffraction in pythia," 2010.

[114] A. Sherstnev and R. Thorne, "Parton Distributions for LO Generators," *Eur.Phys.J.*, vol. C55, pp. 553–575, 2008.

[115] G. A. Schuler and T. Sjöstrand, "Hadronic diffractive cross sections and the rise of the total cross section," *Phys. Rev. D*, vol. 49, pp. 2257–2267, Mar 1994.

[116] P. Bruni and G. Ingelman, "Diffractive w and z production at pp colliders and the pomeron parton content," *Physics Letters B*, vol. 311, no. 14, pp. 317 – 323, 1993.

[117] E. L. Berger, J. C. Collins, D. E. Soper, and G. Sterman, "Diffractive hard scattering," *Nuclear Physics B*, vol. 286, no. 0, pp. 704 – 728, 1987.

[118] K. H. Streng, "Hard QCD scatterings in diffractive reactions at HERA," p. 27 p, Jan 1988.

[119] S. Gieseke, D. Grellscheid, K. Hamilton, A. Papaefstathiou, S. Platzer, *et al.*, "Herwig++ 2.5 Release Note," 2011.

[120] T. Kittelmann, V. Tsulaia, J. Boudreau, and E. Moyse, "The virtual point 1 event display for the atlas experiment," *Journal of Physics: Conference Series*, vol. 219, no. 3, p. 032012, 2010.

[121] E. Nurse and S. Sen, "Methods to Select Soft Diffraction Dissociation at the LHC," 2011.

[122] C. Buttar, J. D'Hondt, M. Kramer, G. Salam, M. Wobisch, *et al.*, "Standard Model Handles and Candles Working Group: Tools and Jets Summary Report," pp. 121–214, 2008.

[123] G. Aad *et al.*, "Improved luminosity determination in *pp* collisions at $\sqrt{s} = 7$ tev using the atlas detector at the lhc," *The European Physical Journal C*, vol. 73, no. 8, pp. 1–39, 2013.

[124] "Atlas public tile calorimeter noise plots." `https://twiki.cern.ch/twiki/bin/view/AtlasPublic/ApprovedPlotsTileNoise`.

[125] G. Aad *et al.*, "Measurements of the pseudorapidity dependence of the total transverse energy in proton-proton collisions at $\sqrt{s} = 7$ TeV with ATLAS," *JHEP*, vol. 1211, p. 033, 2012.

[126] F. Colecchia, J. Monk, E. Nurse, R. Prabhu, and P. Wijeratne, "Validation of the calorimeter energy response with $\pi^0 \to \gamma\gamma$ candidates," Tech. Rep. ATL-COM-CAL-2011-003, CERN, Geneva, Aug 2011.

[127] G. Aad *et al.*, "Single hadron response measurement and calorimeter jet energy scale uncertainty with the ATLAS detector at the LHC," *Eur.Phys.J.*, vol. C73, p. 2305, 2013.

[128] J. Pinfold *et al.*, "Evaluation of the local hadronic calibration with combined beam-test data for the endcap and forward calorimeters of ATLAS in the pseudorapidity region $2.5 < |\eta| < 4.0$," *Nucl.Instrum.Meth.*, vol. A693, pp. 74–97, 2012.

[129] T. Adye, "Unfolding algorithms and tests using RooUnfold," 2011.

[130] G. D'Agostini, "A Multidimensional unfolding method based on Bayes' theorem," *Nucl.Instrum.Meth.*, vol. A362, pp. 487–498, 1995.

[131] "Update on the jet energy scale systematic uncertainty for jets produced in proton-proton collisions at $\sqrt{s} = 7$ TeV measured with the ATLAS detector," Tech. Rep. ATLAS-CONF-2011-007, CERN, Geneva, Feb 2011.

[132] G. Aad *et al.*, "Jet energy resolution in proton-proton collisions at $\sqrt{s} = 7$ TeV recorded in 2010 with the ATLAS detector," *Eur.Phys.J.*, vol. C73, p. 2306, 2013.

[133] K. M. Perez, *Inclusive jet cross sections in proton-proton collisions at 7.0 TeV center-of-mass energy with the ATLAS detector at the Large Hadron Collider*. PhD thesis, Caltech, 2011. presented 13 May 2011.

[134] F. Aaron *et al.*, "Inelastic Production of J/psi Mesons in Photoproduction and Deep Inelastic Scattering at HERA," *Eur.Phys.J.*, vol. C68, pp. 401–420, 2010.

[135] R. D. Field, "The Underlying event in hard scattering processes," *eConf*, vol. C010630, p. P501, 2001.

[136] "Summary of ATLAS Pythia 8 tunes," 2012.

[137] H.-L. Lai, M. Guzzi, J. Huston, Z. Li, P. M. Nadolsky, *et al.*, "New parton distributions for collider physics," *Phys.Rev.*, vol. D82, p. 074024, 2010.

[138] R. Corke and T. Sjostrand, "Interleaved Parton Showers and Tuning Prospects," *JHEP*, vol. 1103, p. 032, 2011.

[139] "Measurement of diffraction dissociation cross sections at $\sqrt{s} = 7$ TeV at the LHC," Tech. Rep. CMS-PAS-FSQ-12-005, CERN, Geneva, 2013.

[140] S. Gieseke, C. Rohr, and A. Siodmok, "Colour reconnections in Herwig++," *Eur.Phys.J.*, vol. C72, p. 2225, 2012.

[141] J. Pumplin, D. Stump, J. Huston, H. Lai, P. M. Nadolsky, *et al.*, "New generation of parton distributions with uncertainties from global QCD analysis," *JHEP*, vol. 0207, p. 012, 2002.

[142] A. Sherstnev and R. Thorne, "Different PDF approximations useful for LO Monte Carlo generators," p. 149, 2008.

APPENDIX A

Monte Carlo Samples used in Diffractive Dijets Analysis

Samples of dijet events in proton-proton collisions at $\sqrt{s} = 7$ TeV were produced using HERWIG++ 6.21 and PYTHIA8. All samples were simulated to match the layout of the ATLAS geometry in 2010 and to have no pile-up interactions. Individual tunes are used to describe the underlying event in a proton-proton collision [135].

The PYTHIA8 samples of non-diffractive, single-diffractive and double diffractive dijets use the tune "ATLAS UE Tune AU2-CT10" [136]. This uses the CTEQ10 PDFs [137] and is based on a previous tune (Tune 4C [138]) which was based to give good agreement to CDF data, then is modified to the be more suited to LHC conditions which include a reduced relative cross section for diffraction (10% reduction for SD, 12% for DD [139]), increased multiparton interactions and a charged particle η distribution that better matches that observed by ATLAS. The PYTHIA8 single and double diffractive samples use the H1 2006 Fit B LO pomeron DPDF, but unfortunately, they are generated with the default Schuler-Sjöstrand pomeron flux, which does not describe the pomeron used in the determination of the DPDFs.

For HERWIG++, samples of non-diffractive dijet production were generated with the UE-EE-3-CTEQ6L1 tune [140]. This is the third version of the energy-extrapolation (EE) underlying event tune, used to better describe the ATLAS data at $\sqrt{s} = 900$ GeV and 7 TeV. The modelling of the underlying event depends on the choice of PDF used for the proton, here being CTEQ6L1 [141] (MRST LO** [142] being the other). For single diffractive events, the CTEQ6L1_H12007 tune is used. This uses the CTEQ6L1 PDFs and H1 2007 Fit Jets DPDFs and a super-critical pomeron (Section 8.2.2).

A.1 Generator Filters

The samples of ND, SD and DD collisions were generated using two different filters, a dijet filter and a forward gap filter, in order to obtain adequate statistics across both the jet p_T and forward gap spectra.

A.1.1 Forward Gap Filter

Large gaps are exponentially suppressed for non-diffractive events, and are kinematically restricted by the requirement of a dijet system within the detector acceptance for single and double diffractive events. The forward gap filter is designed to generate a flat gap spectrum up to a pre-defined threshold, in order to reduce the number of events at small gap sizes relative to the amount at large gap sizes.

The filter starts from the standard MC truth level generation. For each generated event, it requires that at least two truth jets, reconstructed using anti-k_{t} jets with $R = 0.4$ or $R = 0.6$, above or between predefined p_T thresholds ($p_T^{\mathrm{jet\_threshold}}$), are contained within the event. The filter then determines the truth gap size, from either edge of the detector η acceptance ($|\eta| < 4.9$), using particles with p_T above a defined threshold ($p_T^{\mathrm{parton\_threshold}}$), as in the ATLAS rapidity gaps analysis (see Section 9.5.1.2). By default, $p_T^{\mathrm{jet\_threshold}}$ for the leading and sub-leading jet are set to 12 GeV. This is chosen to produce samples designed for high purity (events containing dijets) but not necessarily high efficiency (creating dijets meeting the p_T and η requirements for the analysis).

All events with a gap greater than $\Delta\eta^F_{\text{threshold}}$ are then retained. Each event with $\Delta\eta^F < \Delta\eta^F_{\text{threshold}}$ gets a weight calculated using a fit of the gap spectrum from unfiltered events, of the form, $f(x) = Ae^{(B+Cx)} + De^{E+Fx)} + Gx^H$, where $x = \Delta\eta^F$ and A-H are fit parameters. Events are then retained for simulation and use in the analysis with probability based on the weight, which is recorded along with the event for use in the analysis.

A.1.2 Dijet Filter

The dijet filter selects events such that the p_T distribution for the leading jet is flat before the weights are applied. For the dijet-filtered samples, the filtering is performed on the p_T and η of the leading jet in the event to see that it fits within the detector acceptance ($|\eta| < 4.9$) and that the p_T falls between in the range $p_T^{min} < p_T < p_T^{max}$. The weights in this case take the form, $f(x) = Ax^{B+Cx+Dx^2}(1 - Ex)^F x^G$, where $x = p_T$ and A-G are fit parameters.

A.2 Sample Details

For the gap filtered samples, the options were set to produce anti-k_{t} jets with $R = 0.4$ so that they could also be reconstructed with $R = 0.6$. Both leading hadron level jets in the event are filtered to have at least 12 GeV, well below the lower p_T cut of 20 GeV in the analysis, to account for migrations in and out of the sample.

For PYTHIA8 SD and DD, jets are products in high mass diffractive states rather than originating from the hard scatter so the p_T thresholds for the two hadron level jets are set in order to filter them out. For HERWIG++ and PYTHIA8 ND, the k_T of the partons from the hard scatter can be set to guide how energetic the hadron jets become. The forward gap distributions were calculated using all stable final state truth particles with $p_T^{\text{parton\_threshold}} > 0$ MeV, in order to be fully sensitive to the real forward rapidity gap in the event. The remaining parameters of the fit and the size of the $\Delta\eta^F_{\text{threshold}}$ were produced separately for every Monte Carlo sample. Details of these samples are listed in Tables A.1-A.5. These are the primary samples for the analysis.

For the dijet filter, all samples are filtered using anti-k_t $R = 0.6$ jets, in the p_T ranges listed in the Tables A.6-A.10. There were problems with the filtering being very inefficient for some samples, so the simulation had to be stopped. These samples have zero events in the tables.

The effective cross section for each Monte Carlo sample is calculated from the mean generator filter efficiency multiplied by the generated cross section for the process. Throughout the analysis, each event is weighted appropriately in all distributions at both the reconstructed and truth levels.

k_T range (GeV)	Jet range	Run number	$\Delta\eta^F$ Thresh.	Events generated	Events reconstructed	Cross section [nb]	Mean Gen. Filter Eff.
8-17	J0	147236	5.0	200000	200000	5.249×10^6	6.754×10^{-5}
17-35	J1	147237	6.0	600000	599949	4.131×10^5	6.363×10^{-4}
35-70	J2	147238	5.0	200000	199998	2.456×10^4	1.881×10^{-3}
70-140	J3	147239	5.0	100000	100000	1.301×10^3	9.717×10^{-4}
140-280	J4	147240	4.0	100000	99999	5.264×10^1	1.702×10^{-3}

Table A.1: Details for HERWIG++ 2.61 non-diffractive samples generated with the forward gap filter.

k_T range (GeV)	Jet range	Run number	$\Delta\eta^F$ Thresh.	Events generated	Events reconstructed	Cross section [nb]	Mean Gen. Filter Eff.
8-17	$+z$ J0	147241	6.0	100000	100000	5.822×10^5	1.639×10^{-4}
17-35	$+z$ J1	147242	6.0	300000	300000	4.122×10^4	3.915×10^{-3}
35-70	$+z$ J2	147243	5.0	100000	100000	2.140×10^3	9.476×10^{-3}
70-140	$+z$ J3	147244	5.0	50000	49950	9.468×10^1	4.570×10^{-3}
140-280	$+z$ J4	147245	4.5	50000	50000	2.917×10^0	5.302×10^{-3}
7-18	$-z$ J0	147246	6.0	100000	99997	5.821×10^5	1.646×10^{-4}
18-35	$-z$ J1	147247	6.0	300000	300000	4.122×10^4	3.917×10^{-3}
35-70	$-z$ J2	147248	5.0	100000	99949	2.140×10^3	9.517×10^{-3}
70-140	$-z$ J3	147249	5.0	50000	50000	9.476×10^1	4.568×10^{-3}
140-280	$-z$ J4	147250	4.5	50000	50000	2.917×10^0	5.275×10^{-3}

Table A.2: Details for HERWIG++ 2.61 single-diffractive samples generated with the forward gap filter. For the jet range, $+z$ indicates that the intact proton is located at positive η and $-z$ indicates that the intact proton ends up at negative η.

k_T range (GeV)	Jet range	Run number	$\Delta\eta^F$ Thresh.	Events generated	Events reconstructed	Cross section [nb]	Mean Gen. Filter Eff.
8-17	J0	147251	3.0	200000	199848	6.803×10^6	2.286×10^{-6}
17-35	J1	147252	4.0	600000	600000	5.210×10^5	2.217×10^{-4}
35-70	J2	147253	4.0	200000	198948	3.392×10^4	2.364×10^{-4}
70-140	J3	147254	4.0	100000	100000	1.923×10^3	1.694×10^{-4}
140-280	J4	147255	4.0	100000	99949	8.136×10^1	1.849×10^{-4}

Table A.3: Details for PYTHIA8 non-diffractive samples generated with the forward gap filter.

p_T range (GeV)	Jet range	Run number	$\Delta\eta^F$ Thresh.	Events generated	Events reconstructed	Cross section [nb]	Mean Gen. Filter Eff.
12-20	J0	147256	5.0	300000	293950	1.238×10^7	4.980×10^{-6}
20-30	J1	147257	4.5	500000	400599	1.238×10^7	3.112×10^{-6}
30+	J2	147258	3.5	299300	179250	1.238×10^7	2.348×10^{-6}

Table A.4: Details for PYTHIA8 single-diffractive samples generated with the forward gap filter.

p_T range (GeV)	Jet range	Run number	$\Delta\eta^F$ Thresh.	Events generated	Events reconstructed	Cross section [nb]	Mean Gen. Filter Eff.
12-20	J0	147259	4.5	300000	269947	8.105×10^6	1.044×10^{-5}
20-30	J1	147260	4.5	408600	339647	8.105×10^6	4.026×10^{-6}
30+	J2	147261	3.5	300000	196950	8.105×10^6	2.343×10^{-6}

Table A.5: Details for PYTHIA8 double-diffractive samples generated with the forward gap filter.

p_T range (GeV)	Jet range	Run number	Events generated	Events reconstructed	Cross section [nb]	Mean Gen. Filter Eff.
10-20	J0	147262	400000	0	1.551×10^2	-
20-80	J1	147263	600000	599949	3.014×10^6	1.313×10^{-3}
80-200	J2	147264	200000	199998	1.496×10^4	2.382×10^{-3}

Table A.6: Details for HERWIG++ 2.61 non-diffractive samples generated with the forward gap filter.

p_T range (GeV)	Jet range	Run number	Events generated	Events reconstructed	Cross section [nb]	Mean Gen. Filter Eff.
0-20	$+z$ J0	147265	200000	0	1.429×10^1	-
20-80	$+z$ J1	147266	300000	300000	3.243×10^5	7.188×10^{-4}
80-200	$+z$ J2	147267	100000	99950	1.253×10^3	1.511×10^{-3}
0-20	$-z$ J0	147268	200000	0	1.430×10^1	-
20-80	$-z$ J1	147269	300000	299950	3.243×10^5	7.159×10^{-4}
80-200	$-z$ J2	147270	100000	99949	1.253×10^3	1.508×10^{-3}

Table A.7: Details for HERWIG++ 2.61 single-diffractive samples generated with the dijet filter. For the jet range, $+z$ indicates that the intact proton is located at positive η and $-z$ indicates that the intact proton ends up at negative η.

p_T range (GeV)	Jet range	Run number	Events generated	Events reconstructed	Cross section [nb]	Mean Gen. Filter Eff.
10-20	J0	147271	400000	399844	5.091×10^7	1.349×10^{-1}
20-80	J1	147272	600000	598896	5.091×10^7	1.414×10^{-4}
80-200	J2	147273	200000	199848	2.103×10^4	3.360×10^{-3}

Table A.8: Details for PYTHIA8 non-diffractive samples generated with the dijet filter.

p_T range (GeV)	Jet range	Run number	Events generated	Events reconstructed	Cross section [nb]	Mean Gen. Filter Eff.
10-20	J0	147274	400000	399948	1.238×10^7	1.789×10^{-2}
20-80	J1	147275	456500	401400	1.238×10^7	1.181×10^{-5}
80-200	J2	147276	0	0	-	-

Table A.9: Details for PYTHIA8 single-diffractive samples generated with the dijet filter.

p_T range (GeV)	Jet range	Run number	Events generated	Events reconstructed	Cross section [nb]	Mean Gen. Filter Eff.
10-20	J0	147277	400000	399947	8.105×10^6	6.975×10^{-3}
20-80	J1	147278	576600	402699	8.105×10^6	3.429×10^{-6}
80-200	J2	147279	0	0	-	-

Table A.10: Details for PYTHIA8 double-diffractive samples generated with the dijet filter.

APPENDIX B

Glossary

β: Beam envelope function, giving a measure of the size of the beam at a given point. Typically measured in metres.

β^*: Beam envelope function at the interaction point, characterises the beam size and focusing distance at the collision point.

$\langle\mu\rangle$: Average number of interactions per bunch crossing.

ξ: Fractional momentum loss of the proton that remains intact in a single diffractive proton-proton collision.

A-side: The two ends of ATLAS are called the 'A-side' and the 'C-side' ('B' is the central barrel). The A-side is along the positive z-axis.

ADC: Analogue-to-Digital Converter.

ALFA: Absolute Luminosity For ATLAS. Sub-detector located at 240 m from the ATLAS interaction point, used for measurements of elastic proton-proton scattering and absolute

luminosity calibration.

ALICE: A Large Ion Collider Experiment. A particle physics experiment at the Large Hadron Collider designed to study heavy ion collisions.

AOD: Analysis Object Data. Reduced size output of physics quantities from the reconstruction.

Athena: ATLAS offline software framework.

Atlantis: ATLAS standalone event display.

ATLAS: A Toroidal LHC ApparatuS. A general-purpose particle physics experiment at the Large Hadron Collider.

barrel: The central-rapidity region of the ATLAS detector.

BLK: Full processing of ATLAS raw data at Tier-0, after initial processing (ES1).

BC: Bunch crossing. Proton-proton bunch crossing in the the LHC.

BCID: Bunch crossing identification. The assignment of detector data to a specific bunch crossing.

BG: Bunch group. Collection of BCIDs grouped based on whether both beams, one of the beams or neither beam passes through ATLAS experiment in a bunch crossing.

***B*-layer**: The innermost layer of the Pixel Detector. The B stands for b quark, as this layer allows b-tagging.

calorimeter cell: The smallest unit of calorimeter information to be read out.

CD: Central diffractive process, $pp \rightarrow pXp$, where protons remain intact and are separated from centrally produced system X by rapidity gaps.

CERN: European Laboratory for Particle Physics.

CMM: Common Merger Module of the Level-1 Calorimeter Trigger.

CMS: Compact Muon Solenoid. A general-purpose particle physics experiment at the Large Hadron Collider.

CondDB: Conditions Database. Contains records of the detector conditions for all data taking. This includes calibration and any other parameters required for the data analysis.

ConfDB: Configuration Database. Stores the parameters necessary to describe the experiment's architecture, hardware and software components.

CP: Cluster Processor. The part of the Level-1 Calorimeter Trigger that carries out the electron/photon and τ/hadron triggers.

CPM: Cluster Processor Module of the Level-1 Calorimeter Trigger.

CSC: Cathode Strip Chamber. Muon chambers in the end-caps, used for both triggering and precision reconstruction.

CTP: Central Trigger Processor. The part of the Level-1 Trigger System that combines results from the Level-1 Calorimeter Trigger and Level-1 Muon Trigger to make the global yes/no Level-1 Trigger decision for each bunch crossing.

C-side: The two ends of ATLAS are called the 'A-side' and the 'C-side' ('B' is the central barrel). The C-side is along the negative z-axis.

DAC: Digital-to-analogue converter.

DAQ: Data Acquisition System. System responsible for the assembly and permanent storage of events accepted by all three levels of the trigger system (Level-1, Level-2 and Event Filter).

Dead-time: Time after each event during which the system is not able to record another event.

dijet: A system of two jets (or two leading momentum jets) in an event.

Dijet filter: Generator level filter used in MC to create samples with a flat transverse momentum spectrum for jets.

DD: Double diffraction ($pp \rightarrow XY$). Physics process in which both protons decay into systems X and Y, separated by a rapidity gap due to a colourless exchange between partons.

DPDF: Diffractive Parton Density Function. Give the probability to find a parton in a hadron if the hadron is diffractively scattered.

DQ: Data Quality. Checks to assign which data is suitable for performance and physics analysis in ATLAS.

DQM: Data Quality monitoring. The process by which Data Quality is checked for ATLAS data.

ECAL: Liquid argon Electromagnetic Calorimeter.

Egamma stream: ATLAS data samples containing events triggered on electrons and photons up to HLT level.

EM scale: Electromagnetic energy scale. Baseline energy scale used in ATLAS determined from the response of electrons in the LAr and Tile calorimeters in test beam data.

EM+JES scale: Combined electromagnetic and jet energy scale. Corrects the energy and transverse momentum as measured in the calorimeter to the hadron level.

EMB: Liquid argon Electromagnetic Barrel calorimeter.

EMEC: Liquid argon Electromagnetic End-cap Calorimeter.

end-caps: The high-rapidity regions of the ATLAS detector.

ES1: Initial processing of ATLAS raw data at Tier-0 for fast calibration and error checking.

ESD: Event Summary Data. Provides sufficient information to re-run parts of the reconstruction, as AOD information may not be enough

event: The data resulting from a particular bunch-crossing.

EB: Event Builder. The subsystem that combines data corresponding to one event from all the subdetectors. This takes place after acceptance by the Level-2 Trigger.

EF: Event Filter. The third level of event selection, responsible for reducing the trigger rate to a value acceptable for permanent storage as well as doing data monitoring and calibration, using offline-style algorithms operating on complete events accepted by the Level-2 Trigger.

express stream: Small subset of ATLAS data for a given run, used primarily for fast calibration and error checking.

FADC: Flash Analogue-to-digital Converter.

FCAL: Liquid argon Forward Calorimeter.

FEB: Front End Board. FEBs of ATLAS LAr calorimeter readout contain preamplifiers/preshapers, shapers, analog memories, ADCs, and associated control logic, and contain 128 readout channels.

FIR filter: Finite-Impulse Response filter. A type of digital filter, used in Bunch crossing identification.

front-end electronics (FE): The detector subsystems which generate and send trigger data to the Level-1 Trigger, and event data to their RODs for transmission to the data acquisition system.

Forward gap: A measure of the largest region without activity above defined thresholds from either edge of the ATLAS detector acceptance. Also known as a forward rapidity gap and given the symbol $\Delta\eta^F$.

Forward gap filter: Generator level filter used in MC to create samples with a flat forward gap spectrum up to a defined threshold, enhancing the number of events at larger gap sizes relative to the amount at smaller gap sizes.

Forward gap requirement: A requirement of a forward gap of at least 3 units of rapidity, used to improve the selection of diffractive events.

GAUDI: Data processing applications framework.

GEANT4: A general Monte Carlo simulation package for describing detector geometry and tracking particles through detector material. Used to simulate the response of the ATLAS detector.

GRL: Good Runs List. Defines a set of ATLAS full data runs (or parts of runs) meeting Data Quality requirements for performing analyses with.

HCAL: Hadronic Calorimeter (Tile Calorimeter barrel, Liquid-argon Hadronic End-cap Calorimeter).

HEC: Liquid-argon Hadronic End-cap Calorimeter.

HEP: High-energy physics.

HERWIG: A Monte Carlo package for simulating Hadron Emission Reactions With Interfering Gluons.

HLT: High-Level Trigger. Collective term for the Level-2 Trigger and the Event Filter, the two trigger levels that are implemented primarily in software.

ID: Inner Detector. The inner tracking detector of ATLAS, made up of the Pixel, Semiconductor and Transition Radiation Trackers.

IP: Interaction Point. Point at which bunches collide, located at the centre of the ATLAS detector.

ITC: Inter TileCal Scintillator. Scintillators located between the Tile barrel and extended barrels, used to account for energy losses in dead material.

JEM: Jet/Energy Module of the Level-1 Calorimeter Trigger.

jet: Depending on their energy, the quarks and gluons emerging from a collision will materialize into 5-30 particles (mostly mesons and baryons). At high momentum, these particles will appear in clusters called "jets", that is, in groups of particles moving in roughly the same direction, centred about the original quark or gluon.

jet element: The smallest elements, 0.2×0.2 in η-ϕ, used to form transverse-energy sums for the jet trigger. They are summed over the combined depth of the electromagnetic and hadronic calorimeters.

JEP: Jet/Energy-sum Processor. The part of the Level-1 Calorimeter Trigger that carries out jet, missing-E_T and total-E_T triggers.

JetTauEtmiss stream: ATLAS data samples containing events triggered on jets, τ-leptons and missing energy up to HLT level.

L1Calo stream: ATLAS data samples containing events triggered using the Level-1 Calorimeter Trigger.

L1A: Level-1 Accept. A signal generated by Central Trigger Processor when an event has met the Level-1 Trigger criteria. It is distributed by the TTC system.

Level-1 buffer: Buffer (analogue or digital) in the front-end electronics that retains the event data until the Level-1 Accept result is received.

L1Calo: Level-1 Calorimeter Trigger. The part of the Level-1 Trigger System based on information from the calorimeters. Trigger objects are e.m. (electron/photon) showers, taus, jets, missing-E_T and total-E_T.

L1Muon: Level-1 Muon Trigger. The part of the Level-1 Trigger System based on information from the muon detectors. Trigger objects are high-p_T muons.

L1: Level-1 Trigger System. The first level of event selection, consisting of the Level-1 Calorimeter and Muon Triggers and the Central Trigger Processor, responsible for reducing the event rate from the bunch-crossing rate of 40 MHz to no more than 75 kHz. Based on custom hardware and uses a subset of detector data. For accepted events, it issues Level-1 Accept to the front-end electronics.

L2: Level-2 Trigger System. The second level of event selection, responsible for reducing the trigger rate from about 75 kHz (upgradeable to 100 kHz) to a rate acceptable to the Event Filter, 2.5 kHz. Uses Regions-of-Interest from the Level-1 Trigger to selectively read out only certain parts of the detector.

LHC: Large Hadron Collider. Particle physics collider capable of colliding opposing beams of protons or heavy ions.

LHCb: Large Hadron Collider beauty. A particle physics experiment focussed on the study of B-mesons at the Large Hadron Collider.

LHCf: Large Hadron Collider forward. A particle physics experiment used to study cosmic ray shower development at the Large Hadron Collider.

LAr: Liquid Argon Calorimeters. The barrel (EMB) and end-cap (EMEC) electromagnetic calorimeters, the end-cap hadronic calorimeters (HEC), and the forward calorimeters (FCAL).

LO: Leading Order. Lowest order diagrams (tree level) that can be drawn for a given process based on perturbative theory.

LRG: Large Rapidity Gap. A rapidity gap spanning at least two or three units in rapidity.

LUCID: LUminosity measurement using Cerenkov Integrating Detector. Used for instantaneous luminosity monitoring in ATLAS.

LUT: Lookup Table. Used for energy calibration of digitised signal in the Level-1 Calorimeter Trigger.

MBTS: Minimum Bias Trigger Scintillators. Scintillators located at ± 3.56 m from interaction point, used as the primary minimum bias triggers for ATLAS.

MC: Monte Carlo simulation.

MinBias stream: ATLAS data samples containing events triggered using minimum bias triggers (MBTS, ZDC, etc.).

MDT: Monitored Drift Tube. Muon chambers used for precision reconstruction, in both barrel and end-caps.

MGS: Mismatched Gap Start. A simulated single diffractive event in which the forward gap algorithm calculates that the rapidity gap is in the opposite hemisphere in rapidity

to where the actual rapidity gap was.

MS: Muon Spectrometer. The combined muon trigger and tracking system, consisting of the Resistive Plate Chambers, Monitored Drift Tubes, Cathode Strip Chambers and Thin Gap Chambers.

MPI: Multiple Parton Interaction. A phenomenon where multiple quark and gluon collisions occur from the same proton-proton collision.

ND: Non-diffraction. Physics process in which the interaction involves a colour exchange between partons, resulting in final states with large particle multiplicity and unlikely to contain large rapidity gaps.

NLO: Next to Leading Order. Next highest order of diagrams above tree level that can be drawn for a given process based on perturbative theory.

OFC: Optimal Filtering Coefficients. Coefficients used in the reconstruction of energy from Liquid argon calorimeter signals, important for distinguishing between noise and physics signals.

OTX: Liquid Argon front-end board optical transmitters. Used for sending information from calorimeters to data acquisition systems.

PDF: Parton density function. Defined as the probability density for finding a particle with a certain longitudinal momentum fraction x at resolution scale Q^2.

Pixel Tracker: Semiconductor pixel detector used for tracking in the innermost layers of the Inner Detector.

PMT: Photomultiplier tube.

PPM: PreProcessor Module of the Level-1 Calorimeter Trigger.

PPr: PreProcessor. The part of the Level-1 Calorimeter Trigger that digitizes the calorimeter signals, does bunch-crossing identification, and uses a lookup table to do final ET calibration.

prescale factor: Reduces the rate of events accepted by a specific Level-1 Trigger or HLT logic item.

PV: Primary vertex. Position of the primary interaction point in an event, determined from the reconstruction of vertices from associated reconstructed tracks in the Inner Detector.

PYTHIA: A Monte Carlo program used to generate simulated proton-proton interactions for various physics processes.

QCD: Quantum Chromodynamics. Theory of strong interactions.

RG: Rapidity Gap. Large angular (rapidity) region in which no outgoing particles are detected.

ROB: Readout Buffer. A standard module that receives data from one or more RODs via standard Readout Links, passes on request a subset of the data to the Level-2 Trigger, and buffers the data until a Level-2 Trigger decision has been reached. It then sends the data to the Event Builder.

ROD: Readout Driver. The detector-specific last element in the readout chain that is still considered part of the front-end electronics. Collects data streams from data pipelines and merges them into a single stream which is fed via a standard Readout Link into a Readout Buffer.

ROL: Readout Link. The ATLAS-standard data-transmission link between a ROD and a ROB.

ROS: Readout System. The first element in the readout chain that is considered part of the Data Acquisition System. Collects data from Readout Drivers via Readout Links and supplies it to the Level-2 Trigger and the Event Builder.

Receiver Station: Modules into which analogue trigger-tower signals from the calorimeters are received, and their gains adjusted to be on a calibrated scale proportional to ET. Signals are also available for waveform monitoring by the calorimeter groups.

RoI: Region of Interest. A geographical region of the experiment, identified by the Level-1 Trigger System as containing candidates for Level-2 Trigger objects requiring further computation. Come in three different types to identify electrons/photons, jets and muons.

RoIB: Region of Interest Builder. A unit that collects and formats level-1 Region-of-Interest information and sends it to the Level-2 Supervisor for use by the Level-2 Trigger.

RPC: Resistive Plate Chamber. Muon chamber used for the Level-1 Muon Trigger in the barrel region.

run: Each period of data acquisition.

SCT: Semiconductor Tracking detector. Silicon microstrip detector used for tracking in the intermediate radial range of the Inner Detector.

SD: Single diffraction ($pp \to pX$). Physics process in which one proton decays into system X and other proton remains intact, separated by a rapidity gap due to colourless exchange between partons.

SM: Standard Model. Name for the theory of fundamental particles and their interactions.

Tag-and-probe: A selection method where one reconstructed object (jet, electron, etc.) in an event meeting certain requirements (tag) is used to study another reconstructed object (probe).

TAN: Target Absorber Neutral. Zero degree neutral absorbers located in the proximity of ATLAS in order to protect the outer superconducting beam separation dipoles from neutral particle debris originating from the interaction point.

TDAQ: Collective term for Trigger, Data Acquisition and Detector Control systems.

TDR: Technical Design Report.

TGC: Thin Gap Chamber. Muon chamber used for the Level-1 Muon Trigger and precision muon tracking in the end-cap regions.

Tier-0: Data centre at CERN, mainly responsible for prompt processing and archiving

of the raw data coming from the online data acquisition system.

TileCal: Tile Calorimeter. Hadronic barrel and extended-barrel calorimeters of ATLAS, using scintillating tiles as active medium.

TTC: Timing, Trigger and Control. The system that provides and distributes trigger signals (e.g. Level-1 Accept), timing signals (e.g. LHC clock), and fast control signals to the various subsystems of ATLAS.

Topological clustering: Clustering algorithm used in ATLAS, groups cells into clusters (TopoClusters) based on their neighbour relations and on the significance of their energy contents.

TOTEM: TOTal cross section, Elastic scattering and diffraction dissociation Measurement at the LHC. An experiment at the LHC focussed on forward particle production and luminosity measurements.

track: The record of the path of a particle traversing a detector.

tracking: The reconstruction of a "track" left in a detector by the passage of a particle through the detector.

Trigger menu: The set of trigger conditions in use at any particular time. They specify a list of items, each with its transverse energy threshold and multiplicity, and the logic to be applied to them.

TT: Trigger Tower. The smallest element of calorimeter information used in the Level-1 Calorimeter Trigger, with dimensions of approximately 0.1×0.1 in η-ϕ and summed over the full depth of either the electromagnetic or hadronic calorimeter.

TRT: Transition Radiation Tracker. Combined tracking and electron identification detector, which is part of the ATLAS Inner Detector.

US15: ATLAS underground service area. On the positive-x side of UX15, i.e. inside the LHC ring.

USA15: Main ATLAS underground electronics cavern. On the negative-x side of UX15,

i.e. outside the LHC ring.

UX15: ATLAS underground experimental cavern containing the detector.

vdM scan: van der Meer scan. A method to measure and optimise the luminosity of colliding beams.

VP1: Virtual Point One. The interactive three-dimensional event display for the ATLAS experiment.

ZDC: Zero-Degree Calorimeter. Detector located ± 140 m away from ATLAS interaction point used to detect forward neutrons and photons in both proton-proton and heavy-ion collisions.